MAGNETIC RELAXATION DURING OSCILLATING FIELD CURRENT DRIVE IN A REVERSED FIELD PINCH

by

Douglas R. Stone

A dissertation submitted in partial fulfillment of

the requirements for the degree of

Doctor of Philosophy

(Physics)

at the

University of Wisconsin – Madison

2013

Date of final oral examination: October 23, 2013

The dissertation is approved by the following members of the Final Oral Committee:
John S. Sarff, Professor, Physics
Karsten J. McCollam, Scientist, Physics
Cary B. Forest, Professor, Physics
Jan Egedal, Assistant Professor, Physics
Carl R. Sovinec, Professor, Engineering Physics

Abstract

Magnetic relaxation has been measured during partial Oscillating Field Current Drive (OFCD) experiments on the Madison Symmetric Torus (MST) reversed field pinch (RFP). Ohm's law terms have been measured in the edge of MST during OFCD for a range of OFCD phases. The dynamo, $< \tilde{\mathbf{E}} \cdot \tilde{\mathbf{B}} > /B$, is shown to balance $\mathbf{E} - \eta \mathbf{J}$ to within a standard deviation during the majority of the OFCD cycle. The dynamo is a few volts per meter except during discrete relaxation events where it can be as large as a few tens of volts per meter.

Previous work measuring the dynamo in an RFP has shown that the dynamo is a result of the inductive toroidal electric field peaking the radial current profile, which linearly destabilizes the core-resonant m=1 tearing modes. These modes nonlinearly couple with the m=0 tearing modes, which are resonant at the reversal surface. Mode interactions produce a dynamo that supports the parallel current in the edge and opposes it in the core.

The tearing modes are primarily responsible for producing the flows and electromagnetic fields that interact to create the dynamo electromotive force. During partial OFCD experiments, the m=0 modes resonant at the reversal surface appear to become linearly unstable, become large, and stop rotating periodically during the OFCD cycle. Times when the dynamo is not measured to balance might be due to issues with the measurement technique when the modes are locked. Alternately, the measured imbalance during part of the OFCD cycle could be due to a contribution from one of the terms in Ohm's law that are not measured in this thesis and assumed to be small. The diamagnetic dynamo, $<\widetilde{\nabla P_e} \cdot \tilde{\mathbf{B}}> /(n_e e)$, is the most likely candidate.

We find that when OFCD adds excess current in the edge, the modes are capable of interacting to create a dynamo that opposes the parallel current in the edge. This demonstrates the robustness of the RFP's tendency to relax toward the minimum energy state. It is also the first time that the dynamo has been observed to oppose the current in the RFP edge. The dynamo oscillates between ~ -3 V/m and ~ 3 V/m except at the sawtooth crash where it spikes to 10-15 V/m.

The contribution to the dynamo from $<\tilde{\mathbf{E}}_{\|} \cdot \tilde{\mathbf{B}}_{\|}> /B_0 \approx <\tilde{\mathbf{U}}_{\perp} \times \tilde{\mathbf{B}}_{\|} \cdot \tilde{\mathbf{B}}_{\perp}>$ is measured for the first time in MST along with the contribution from $<\tilde{\mathbf{E}}_{\perp} \cdot \tilde{\mathbf{B}}_{\perp}> /B_0$. Contrary to expectations, the contribution to the dynamo from $<\tilde{\mathbf{E}}_{\|} \cdot \tilde{\mathbf{B}}_{\|}> /B_0$ is found to be significant at the sawtooth crash, while in between crashes it is small but not completely negligible.

The Hall dynamo opposes the current while the MHD dynamo supports the current in the edge of MST during RFPs with OFCD. They are generally individually large in magnitude relative to their net effect. The Hall dynamo is measured directly while the MHD dynamo is measured indirectly. Similar behavior is observed for the Hall dynamo and MHD dynamo for RFPs without OFCD, which is consistent with previous results on MST. The magnetic helicity flux is also measured in the edge of MST. The helicity flux during OFCD is generally outward except for a short period during the OFCD cycle when it becomes slightly inward, which is consistent with expectations for magnetic relaxation.

Measurements of dynamo terms are conducted with a novel insertable probe that can simultaneously measure $\tilde{V}_{plasma}$, $\tilde{\mathbf{E}}$, $\mathbf{B}$, and $\mathbf{J}$. This probe uses secondary emission capacitive probes to measure the plasma voltages and electric fields. To the author's knowledge, this is the first time capacitive probes have been used to measure electric fields in MST or other plasmas.

Acknowledgements

I would like to thank the many people who have assisted me throughout my graduate studies. This research would not have happened without the entire MST research group. I have learned so much from so many people who were always generous with their time and willing to help me through my research problems.

Thanks to the engineers, hackers, and administrative staff for keeping MST running. Without you, those of us focusing on the scientific results would have a lot less time for experiments and data analysis. I probably won't have a full appreciation of all you have done for me until I begin my postdoc.

Thanks to all the professors, scientists and postdocs who have helped me wrestle through all the challenges of running OFCD, making and using probes, and analyzing data. Particular thanks to Karsten McCollam for all that he has taught me and for all the work he has put into this thesis. To all of my fellow graduate students, thank you for your solidarity and friendship.

Lastly, I'd like to thank my family and friends for all their love and support. It has been a long road, but the road would have felt much longer without you, and I might not have made it to the end. In particular, I'd like to thank my loving, patient wife Sara. You have been with me through the toughest part of graduate school and have had to deal with just as much stress and frustration as I have these final months. Thank you for giving me space when I needed it and being there when I needed you.

Contents

Abstract **i**

Acknowledgements **iv**

1 Introduction **1**

1.1 Magnetic Relaxation 2

1.1.1 The Dynamo and Ohm's Law 3

1.1.2 Development of the $< \tilde{\mathbf{E}} \cdot \tilde{\mathbf{B}} > /B_0$ Term 5

1.1.3 Development of the $< \tilde{\mathbf{E}}_\perp \cdot \tilde{\mathbf{B}}_\perp > /B_0$ and $< \tilde{\mathbf{E}}_\parallel \cdot \tilde{\mathbf{B}}_\parallel > /B_0$ Terms 7

1.1.4 Magnetic Helicity and the Taylor Hypothesis 10

1.1.5 Tearing Modes 13

1.2 The Madison Symmetric Torus 15

1.3 Oscillating Field Current Drive 19

2 Oscillating Field Current Drive on MST **23**

2.1 Hardware 24

2.2 Current Drive Results 28

2.3 The Sawtooth Crash During OFCD 31

2.4 Magnetic Relaxation During OFCD 33

3 Tearing Modes on MST **38**
3.1 Mode Measurements Using the Toroidal Array 39
3.2 Tearing Mode Amplitudes and Velocities 41
3.3 Tearing Mode Phases 48

4 Probes **53**
4.1 Measurement Techniques 54
    4.1.1 Mirnov Coils 54
    4.1.2 Langmuir Probes 54
    4.1.3 Secondary Emission Capacitive Probes 57
        4.1.3.1 Secondary Electron Emission 58
        4.1.3.2 Capacitive Probes 60
4.2 Probe Designs 64
    4.2.1 Dynamo Probe 64
    4.2.2 Helicity Probe 65
    4.2.3 Electrostatic Probe 66
4.3 Data Analysis Technique 68
    4.3.1 Random Phase Approximation 68
    4.3.2 The OFCD Cycle and Fluctuation Analysis in MST 70

5 Magnetic Relaxation During the Standard RFP **74**
5.1 Measurement of $\mathbf{E} - \eta\mathbf{J}$ 75
5.2 The Dynamo and Ohm's Law Balance 79
5.3 Hall Dynamo and MHD Dynamo 86
5.4 Magnetic Helicity Flux 91
5.5 Analysis Variation: Unfiltered Signals 93

6 Magnetic Relaxation During OFCD 97

6.1 OFCD $\delta = \pi/2$ 100

6.1.1 Measurement of $\mathbf{E} - \eta\mathbf{J}$ 100

6.1.2 The Dynamo and Ohm's Law Balance 103

6.1.3 Hall Dynamo and MHD Dynamo 111

6.1.4 Helicity Flux 112

6.2 Other OFCD Phases 114

6.2.1 The Dynamo and Ohm's Law 115

6.2.2 Hall Dynamo and MHD Dynamo 117

6.2.3 Helicity Flux 121

6.3 Addressing Data Analysis Issues During OFCD 121

6.3.1 OFCD Sawteeth 121

6.4 Diamagnetic Dynamo 125

7 Conclusions and Future Work 130

7.1 Ohm's Law During Partial OFCD Experiments 130

7.2 Sawteeth During OFCD 132

7.3 The Dynamo and Magnetic Relaxation 133

7.4 Ohm's Law During the Standard RFP 134

7.5 Oscillating Field Current Drive 135

7.6 Future Work 135

A OFCD Complete Circuit Schematic 143

B Probe Hardware 145

C Average Electric Field Near MST Inner Wall 150

D Additional Data For Probe Ensembles **153**

D.1 OFCD $\delta = \pi/2$ 154

D.1.1 Sawtooth Ensemble 154

D.2 OFCD $\delta = +\pi/4$ 162

D.2.1 Cycle Ensemble 162

D.2.2 Sawtooth Ensemble 175

D.3 OFCD $\delta = 0$ 183

D.3.1 Cycle Ensemble 183

D.3.2 Sawtooth Ensemble 196

D.4 OFCD $\delta = -\pi/4$ 204

D.4.1 Cycle Ensemble 204

D.4.2 Sawtooth Ensemble 217

D.5 Standard 250 kA, $F \approx -0.5$ 225

List of Tables

1.1 MST Parameters 16

5.1 RFP Parameters For Thesis 75

6.1 OFCD Cycle Regions 98

List of Figures

1.1 The RFP magnetic field configuration 12
1.2 The Madison Symmetric Torus 15
1.3 MST q profile 17
1.4 Directions in MST 18

2.1 OFCD circuit conceptual schematic 24
2.2 OFCD tank circuit waveforms 25
2.3 OFCD good and bad ignitron commutation 27
2.4 OFCD current and voltage oscillations 28
2.5 Current resulting from OFCD on MST 29
2.6 Mode amplitude dependence on OFCD phase in MST 30
2.7 Comparison of OFCD $\Delta < I_\phi > (\delta)$ on MST and in DEBS simulations 32
2.8 OFCD sawtooth entrainment 33
2.9 $\mathbf{E}_{parallel}$, $\eta \mathbf{J}_{\|}$, and dynamo EMF radial profiles during OFCD 35
2.10 OFCD electric field, current, and implied dynamo 36

3.1 Standard plasma tearing mode amplitudes and velocities. 42
3.2 q(a) during OFCD 43
3.3 OFCD $\delta = +\pi/2$ m=0 and m=1 mode amplitudes and velocities 44
3.4 OFCD $\delta = +\pi/2$ m=1, +n and -n mode amplitudes and velocities . . . 46

3.5 Standard RFP m=1, +n and -n mode amplitudes and velocities 50
3.6 Tearing mode phase distribution during the standard RFP 51
3.7 Tearing mode phase distribution during the OFCD $\delta = \pi/2$ ensemble . 52

4.1 Plasma sheath around probe 56
4.2 Boron nitride floating potential 60
4.3 Capacitive probe circuit 61
4.4 Example capacitive probe calibration data 62
4.5 Dynamo probe 64
4.6 Dynamo Probe cartoon 65
4.7 Helicity Probe 66
4.8 Electrostatic Probe 67
4.9 Tearing mode frequencies in the standard RFP 70
4.10 Tearing mode frequencies during OFCD $\delta = +\pi/2$ 73

5.1 Average electric field at the probe minor radius 77
5.2 Average current and resistivity at the probe minor radius 78
5.3 Ensemble averaged Dynamo Probe signals 80
5.4 Ensemble averaged Dynamo Probe fluctuation RMS amplitudes 82
5.5 The dynamo measured by the Dynamo Probe 83
5.6 The dynamo from perpendicular or parallel fluctuations 84
5.7 Comparison of the dynamo and $\mathbf{E} - \eta\mathbf{J}$ 85
5.8 Comparison of the dynamo and $\mathbf{E} - \eta\mathbf{J}$ 87
5.9 Ensemble averaged Dynamo Probe fluctuation RMS amplitudes 89
5.10 The Hall dynamo and implied MHD dynamo 90
5.11 Magnetic helicity flux 92
5.12 Ensemble averaged Dynamo Probe fluctuation RMS amplitudes 93

5.13 The dynamo, $\mathbf{E}-\eta\mathbf{J}$, Hall dynamo, implied MHD dynamo, and helicity flux 94

6.1 OFCD $\delta = +\pi/2$ global parameters 99
6.2 Average electric field at the probe minor radius 100
6.3 Average current and resistivity at the probe minor radius 102
6.4 Ensemble averaged Dynamo Probe signals 104
6.5 Ensemble averaged Dynamo Probe fluctuation RMS amplitudes 105
6.6 Dynamo and components during OFCD $\delta = +\pi/2$ 107
6.7 Perpendicular and parallel contributions to dynamo - OFCD $\delta = +\pi/2$ 108
6.8 Comparison of the dynamo and $\mathbf{E} - \eta\mathbf{J}$ 110
6.9 Ensemble averaged Dynamo Probe fluctuation RMS amplitudes 112
6.10 The Hall dynamo and implied MHD dynamo 113
6.11 Magnetic helicity flux 114
6.12 Comparison of the dynamo and $\mathbf{E} - \eta\mathbf{J}$ 116
6.13 Parallel field contribution to $< \tilde{\mathbf{E}} \cdot \tilde{\mathbf{B}} > /B_0$ 118
6.14 The Hall dynamo and implied MHD dynamo 119
6.15 Magnetic helicity flux 120
6.16 Comparison of the dynamo from filtered signals with $\mathbf{E} - \eta\mathbf{J}$ 123
6.17 The Hall dynamo and implied MHD dynamo 124
6.18 Comparison of the dynamo and $\mathbf{E} - \eta\mathbf{J}$ 126
6.19 Electron normalized mean free path 128

A.1 OFCD circuit schematic (complete) 144

B.1 Capacitive probe circuit 146
B.2 Operational amplifier circuit diagram for capacitive probe circuit 147

B.3 Theoretical capacitive probe gain (amplitude) 148

B.4 Theoretical capacitive probe gain (phase) 148

B.5 Circuit diagram for circuit used with triple Langmuir probe. 149

D.1 Parallel electric field data, OFCD $\delta = +\pi/2$ sawtooth. 154

D.2 Probe $\eta\mathbf{J}$ data, OFCD $\delta = +\pi/2$ sawtooth. 155

D.3 Dynamo Probe $< \mathbf{E} >$ and $< \mathbf{B} >$, OFCD $\delta = +\pi/2$ sawtooth. 156

D.4 Dynamo Probe $\tilde{\mathbf{E}}_{RMS}$ and $\tilde{\mathbf{B}}_{RMS}$, OFCD $\delta = +\pi/2$ sawtooth. 157

D.5 Dynamo contributions from $\tilde{\mathbf{E}}$ and $\tilde{\mathbf{B}}$ components, OFCD $\delta = +\pi/2$ sawtooth. 158

D.6 Ohm's law ($\mathbf{E} - \eta\mathbf{J}$ and $- < \tilde{\mathbf{E}} \cdot \tilde{\mathbf{B}} > /B$), OFCD $\delta = +\pi/2$ sawtooth. . 159

D.7 Dynamo Probe $\tilde{\mathbf{J}}_{RMS}$ and $\tilde{\mathbf{B}}_{RMS}$, OFCD $\delta = +\pi/2$ sawtooth. 160

D.8 Hall Dynamo and MHD Dynamo, OFCD $\delta = +\pi/2$ sawtooth. 161

D.9 Edge safety factor, OFCD $\delta = +\pi/4$ cycle. 162

D.10 Tearing mode amplitudes and velocities, OFCD $\delta = +\pi/4$ cycle. 163

D.11 Tearing mode +n and -n amplitudes and velocities, OFCD $\delta = +\pi/4$ cycle. 164

D.12 Tearing mode phase distribution, OFCD $\delta = +\pi/4$ cycle. 165

D.13 Global and edge parameters, OFCD $\delta = +\pi/4$ cycle. 166

D.14 Parallel electric field data, OFCD $\delta = +\pi/4$ cycle. 167

D.15 Probe $\eta\mathbf{J}$ data, OFCD $\delta = +\pi/4$ cycle. 168

D.16 Dynamo Probe $< \mathbf{E} >$ and $< \mathbf{B} >$, OFCD $\delta = +\pi/4$ cycle. 169

D.17 Dynamo Probe $\tilde{\mathbf{E}}_{RMS}$ and $\tilde{\mathbf{B}}_{RMS}$, OFCD $\delta = +\pi/4$ cycle. 170

D.18 Dynamo contributions from $\tilde{\mathbf{E}}$ and $\tilde{\mathbf{B}}$ components, OFCD $\delta = +\pi/4$ cycle. 171

D.19 Ohm's law ($\mathbf{E} - \eta\mathbf{J}$ and $- < \tilde{\mathbf{E}} \cdot \tilde{\mathbf{B}} > /B$), OFCD $\delta = +\pi/4$ cycle. . . . 172

D.20 Dynamo Probe $\tilde{\mathbf{J}}_{RMS}$ and $\tilde{\mathbf{B}}_{RMS}$, highpass filtered, OFCD $\delta = +\pi/4$ cycle. 173

D.21 Hall Dynamo and MHD Dynamo, OFCD $\delta = +\pi/4$ cycle. 174

D.22 Parallel electric field data, OFCD $\delta = +\pi/4$ sawtooth. 175

D.23 Probe $\eta\mathbf{J}$ data, OFCD $\delta = +\pi/4$ sawtooth. 176

D.24 Dynamo Probe $< \mathbf{E} >$ and $< \mathbf{B} >$, OFCD $\delta = +\pi/4$ sawtooth. 177

D.25 Dynamo Probe $\tilde{\mathbf{E}}_{RMS}$ and $\tilde{\mathbf{B}}_{RMS}$, OFCD $\delta = +\pi/4$ sawtooth. 178

D.26 Dynamo contributions from $\tilde{\mathbf{E}}$ and $\tilde{\mathbf{B}}$ components, OFCD $\delta = +\pi/4$ sawtooth. 179

D.27 Ohm's law ($\mathbf{E} - \eta\mathbf{J}$ and $- < \tilde{\mathbf{E}} \cdot \tilde{\mathbf{B}} > /B$), OFCD $\delta = +\pi/4$ sawtooth. . 180

D.28 Dynamo Probe $\tilde{\mathbf{J}}_{RMS}$ and $\tilde{\mathbf{B}}_{RMS}$, OFCD $\delta = +\pi/4$ sawtooth. 181

D.29 Hall Dynamo and MHD Dynamo, OFCD $\delta = +\pi/4$ sawtooth. 182

D.30 Edge safety factor, OFCD $\delta = 0$ cycle. 183

D.31 Tearing mode amplitudes and velocities, OFCD $\delta = 0$ cycle. 184

D.32 Tearing mode +n and -n amplitudes and velocities, OFCD $\delta = 0$ cycle. 185

D.33 Tearing mode phase distribution, OFCD $\delta = 0$ cycle. 186

D.34 Global and edge parameters, OFCD $\delta = 0$ cycle. 187

D.35 Parallel electric field data, OFCD $\delta = 0$ cycle. 188

D.36 Probe $\eta\mathbf{J}$ data, OFCD $\delta = 0$ cycle. 189

D.37 Dynamo Probe $< \mathbf{E} >$ and $< \mathbf{B} >$, OFCD $\delta = 0$ cycle. 190

D.38 Dynamo Probe $\tilde{\mathbf{E}}_{RMS}$ and $\tilde{\mathbf{B}}_{RMS}$, OFCD $\delta = 0$ cycle. 191

D.39 Dynamo contributions from $\tilde{\mathbf{E}}$ and $\tilde{\mathbf{B}}$ components, OFCD $\delta = 0$ cycle. . 192

D.40 Ohm's law ($\mathbf{E} - \eta\mathbf{J}$ and $- < \tilde{\mathbf{E}} \cdot \tilde{\mathbf{B}} > /B$), OFCD $\delta = 0$ cycle. 193

D.41 Dynamo Probe $\tilde{\mathbf{J}}_{RMS}$ and $\tilde{\mathbf{B}}_{RMS}$, highpass filtered, OFCD $\delta = 0$ cycle. 194

D.42 Hall Dynamo and MHD Dynamo, OFCD $\delta = 0$ cycle. 195

D.43 Parallel electric field data, OFCD $\delta = 0$ sawtooth. 196

D.44 Probe $\eta\mathbf{J}$ data, OFCD $\delta = 0$ sawtooth. 197

D.45 Dynamo Probe $< \mathbf{E} >$ and $< \mathbf{B} >$, OFCD $\delta = 0$ sawtooth. 198

D.46 Dynamo Probe $\tilde{\mathbf{E}}_{RMS}$ and $\tilde{\mathbf{B}}_{RMS}$, OFCD $\delta = 0$ sawtooth. 199

D.47 Dynamo contributions from $\tilde{\mathbf{E}}$ and $\tilde{\mathbf{B}}$ components, OFCD $\delta = 0$ sawtooth. 200

D.48 Ohm's law ($\mathbf{E} - \eta\mathbf{J}$ and $- < \tilde{\mathbf{E}} \cdot \tilde{\mathbf{B}} > /B$), OFCD $\delta = 0$ sawtooth. . . . 201

D.49 Dynamo Probe $\tilde{\mathbf{J}}_{RMS}$ and $\tilde{\mathbf{B}}_{RMS}$, OFCD $\delta = 0$ sawtooth. 202

D.50 Hall Dynamo and MHD Dynamo, OFCD $\delta = 0$ sawtooth. 203

D.51 Edge safety factor, OFCD $\delta = -\pi/4$ cycle. 204

D.52 Tearing mode amplitudes and velocities, OFCD $\delta = -\pi/4$ cycle. 205

D.53 Tearing mode +n and -n amplitudes and velocities, OFCD $\delta = -\pi/4$ cycle. 206

D.54 Tearing mode phase distribution, OFCD $\delta = -\pi/4$ cycle. 207

D.55 Global and edge parameters, OFCD $\delta = -\pi/4$ cycle. 208

D.56 Parallel electric field data, OFCD $\delta = -\pi/4$ cycle. 209

D.57 Probe $\eta\mathbf{J}$ data, OFCD $\delta = -\pi/4$ cycle. 210

D.58 Dynamo Probe $< \mathbf{E} >$ and $< \mathbf{B} >$, OFCD $\delta = -\pi/4$ cycle. 211

D.59 Dynamo Probe $\tilde{\mathbf{E}}_{RMS}$ and $\tilde{\mathbf{B}}_{RMS}$, OFCD $\delta = -\pi/4$ cycle. 212

D.60 Dynamo contributions from $\tilde{\mathbf{E}}$ and $\tilde{\mathbf{B}}$ components, OFCD $\delta = -\pi/4$ cycle. 213

D.61 Ohm's law ($\mathbf{E} - \eta\mathbf{J}$ and $- < \tilde{\mathbf{E}} \cdot \tilde{\mathbf{B}} > /B$), OFCD $\delta = -\pi/4$ cycle. . . . 214

D.62 Dynamo Probe $\tilde{\mathbf{J}}_{RMS}$ and $\tilde{\mathbf{B}}_{RMS}$, highpass filtered, OFCD $\delta = -\pi/4$ cycle. 215

D.63 Hall Dynamo and MHD Dynamo, OFCD $\delta = -\pi/4$ cycle. 216

D.64 Parallel electric field data, OFCD $\delta = -\pi/4$ sawtooth. 217

D.65 Probe $\eta\mathbf{J}$ data, OFCD $\delta = -\pi/4$ sawtooth. 218

D.66 Dynamo Probe $< \mathbf{E} >$ and $< \mathbf{B} >$, OFCD $\delta = -\pi/4$ sawtooth. 219

D.67 Dynamo Probe $\tilde{\mathbf{E}}_{RMS}$ and $\tilde{\mathbf{B}}_{RMS}$, OFCD $\delta = -\pi/4$ sawtooth. 220

D.68 Dynamo contributions from $\tilde{\mathbf{E}}$ and $\tilde{\mathbf{B}}$ components, OFCD $\delta = -\pi/4$ sawtooth. 221

D.69 Ohm's law ($\mathbf{E} - \eta\mathbf{J}$ and $- < \tilde{\mathbf{E}} \cdot \tilde{\mathbf{B}} > /B$), OFCD $\delta = -\pi/4$ sawtooth. . 222

D.70 Dynamo Probe $\tilde{\mathbf{J}}_{RMS}$ and $\tilde{\mathbf{B}}_{RMS}$, OFCD $\delta = -\pi/4$ sawtooth. 223

D.71 Hall Dynamo and MHD Dynamo, OFCD $\delta = -\pi/4$ sawtooth. 224

D.72 Tearing mode amplitudes and velocities, deeply reversed standard sawtooth. 227

D.73 Tearing mode +n and -n amplitudes and velocities, deeply reversed standard sawtooth. 228

D.74 Tearing mode phase distribution, deeply reversed standard sawtooth. . 229

D.75 Parallel electric field data, deeply reversed standard sawtooth. 230

D.76 Probe $\eta\mathbf{J}$ data, deeply reversed standard sawtooth. 231

D.77 Dynamo Probe $< \mathbf{E} >$ and $< \mathbf{B} >$, deeply reversed standard sawtooth. 232

D.78 Dynamo Probe $\tilde{\mathbf{E}}_{RMS}$ and $\tilde{\mathbf{B}}_{RMS}$, deeply reversed standard sawtooth. . 233

D.79 Dynamo contributions from $\tilde{\mathbf{E}}$ and $\tilde{\mathbf{B}}$ components, deeply reversed standard sawtooth. 234

D.80 Dynamo contributions from $< \tilde{\mathbf{E}}_{\perp} \cdot \tilde{\mathbf{B}}_{\perp} > /B_0$ and $< \tilde{\mathbf{E}}_{\parallel} \cdot \tilde{\mathbf{B}}_{\parallel} > /B_0$, deeply reversed standard sawtooth. 235

D.81 Ohm's law ($\mathbf{E} - \eta\mathbf{J}$ and $- < \tilde{\mathbf{E}} \cdot \tilde{\mathbf{B}} > /B$), deeply reversed standard sawtooth. 236

D.82 Dynamo Probe $\tilde{\mathbf{J}}_{RMS}$ and $\tilde{\mathbf{B}}_{RMS}$, deeply reversed standard sawtooth. . 237

D.83 Hall Dynamo and MHD Dynamo, deeply reversed standard sawtooth. . 238

D.84 Magnetic helicity flux, deeply reversed standard sawtooth. 239

Chapter 1

Introduction

Magnetic relaxation is a process in which a plasma moves from a higher magnetic-energy state to a lower one. It often involves breaking and reconnecting magnetic field lines, which is known as magnetic reconnection. In magnetic confinement fusion, it is most often negatively associated with decreased confinement of energy and particles. However, in the reversed field pinch (RFP) with current driven via an inductive toroidal electric field, magnetic relaxation also has the positive effect of maintaining the current profile and magnetic field profile. This is accomplished even though the toroidal electric field is larger than required for the current in the core of the plasma and opposes the current in the plasma's edge.

Inductive electric fields are relatively efficient and inexpensive for sustaining the RFP current profile against resistive dissipation compared to options such as neutral beam injection or launching rf-waves from an antenna. However, a DC inductive toroidal electric field cannot be maintained in a plasma indefinitely because the primary transformer has a finite flux swing. Oscillating Field Current Drive (OFCD) is a proposed method of sustaining an RFP indefinitely solely through AC magnetic fields [1]. It would drive current in the edge of the RFP and rely on magnetic relaxation to sustain the current profile and the magnetic field profile [2]. In this thesis, the term "DC field" will refer to a field that is constant during the quasi-steady state plasma current flat top while "AC field" will refer to a time-dependent field with a time average of zero over the flat top.

This thesis is a study of magnetic relaxation during OFCD experiments on the Madison Symmtric Torus (MST) RFP. In these experiments, OFCD and MST's inductive toroidal electric field are applied in tandem, and the plasma is sustained primarily by MST's inductive toroidal electric field. The benefits of this study are twofold. First, understanding magnetic relaxation in these experiments provides insight into the viability of sustaining the plasma in an RFP using OFCD. Secondly, these measurements will strengthen our understanding of the physcis of magnetic relaxation.

The principle result is localized measurements of the dynamo electromotive fields in the edge of MST, which is the mechanism through which magnetic relaxation is accomplished. The local magnetic helicity flux, which is related to the dynamo, is examined in the edge. Global measurements of the behavior of the plasma are also presented, including observations of tearing modes, which are the primary source of the spatial fluctuations in magnetic fields and particle velocities that produce the dynamo, and sawteeth, which are spontaneous discrete magnetic relaxation events produced by the tearing modes.

1.1 Magnetic Relaxation

Magnetic relaxation is the process in which a magnetically confined plasma such as an RFP moves to a lower magnetic-energy state. In the RFP, this is accomplished primarily by the electromagnetic fluctuations associated with tearing modes, which interact to produce a dynamo EMF that drives or opposes current in different parts of the plasma [3]. In the standard MST RFP, magnetic relaxation can be empirically separated into two periods, the quasi-steady state dynamo EMF that attempts to maintain a flat current profile and the rapid sawtooth crash that flattens the current profile on the tearing time scale.

In between MST sawtooth crashes, linearly unstable core m=1 tearing modes grow and produce non-axisymmetric fluctuations that interact to create a dynamo. This dynamo attempts to maintain the relaxed state but the current profile peaks over the course of a few milliseconds in spite of the dynamo. The peaked current profile provides more energy to the tearing modes, leading to the sawtooth crash.

During the MST sawtooth crash, core m=1 tearing modes couple nonlinearly to the m=0 tearing modes resonant at the reversal surface. The magnitude of the dynamo is substantially enhanced from the growth of these tearing modes relative to before and after the sawtooth. Magnetic reconnection throughout the plasma during the sawtooth crash creates stochastic fields throughout the plasma, which leads to enhanced transport of energy and particles during the crash, and also rapidly flattens the current profile.

1.1.1 The Dynamo and Ohm's Law

The specific physical mechanisms by which electromagnetic fields, current, particle velocities, and pressure interact to produce the dynamo EMF in the RFP are described by a two-fluid Ohm's law [4],

$$\mathbf{E} + \mathbf{v} \times \mathbf{B} - \frac{\mathbf{J} \times \mathbf{B}}{n_e e} + \frac{\nabla p_e}{n_e e} - \frac{m_e}{e^2 n_e} \frac{\partial \mathbf{J}}{\partial t} = \eta \mathbf{J} \tag{1.1}$$

which is one equation in the two-fluid resistive magnetohydrodynamic (MHD) model for a plasma. A two-fluid Ohm's law has accurately explained measurements of electric fields and current in plasmas including MST RFP experiments. Measuring terms in Ohm's law during OFCD provide another case to test the model in addition to the standard RFP.

Before examining Ohm's law in more detail it is necessary to define the notation used in this thesis. For the RFP, it is useful to consider the averages and spatial variations of measured quantities on a given flux surface by separating a quantity X into $X =< X > +\tilde{X}$, where $< X >$ represents the flux surface average of X and $\tilde{X}$ is the spatial fluctuation on the flux surface. Note that $< \tilde{X} >= 0$ and $< XY >=< X >< Y > + < \tilde{X}\tilde{Y} >$. Also, $\mathbf{X}_0 \equiv< \mathbf{X} >$, $X_0 \equiv \mid < \mathbf{X} > \mid$, and the unit vector $\hat{\mathbf{x}}_0 \equiv \mathbf{X}_0 / \mid X_0 \mid$. Finally, $\mathbf{x} = \mathbf{x}_\parallel + \mathbf{x}_\perp$ where parallel and perpendicular components are defined with respect to the mean equilibrium magnetic field $\mathbf{B}_0$ as $\mathbf{x}_\parallel \cdot \mathbf{B}_0 = x_\parallel B_0$ and $\mathbf{x}_\perp \cdot \mathbf{B}_0 = 0$.

Consider the flux surface average of Ohm's law in the direction parallel to the average magnetic field on the surface. First, separate all quantities X in Ohm's law into mean and fluctuating parts. Then take the flux surface average and finally dot it with the unit vector magnetic field direction to derive the flux surface average of Ohm's law parallel to $\mathbf{B_0}$, known as parallel mean-field Ohm's law:

$$\mathbf{E}_{0\parallel} + < \tilde{\mathbf{v}} \times \tilde{\mathbf{B}} >_\parallel - \frac{< \tilde{\mathbf{J}} \times \tilde{\mathbf{B}} >_\parallel}{n_e e} = \eta_\parallel \mathbf{J}_{0\parallel} \tag{1.2}$$

The mean diamagnetic term, $< \nabla p_e/(n_e e) >_\parallel$, is zero if the plasma is isothermal along the field line and the inertial term $< \partial \mathbf{J}/\partial t >\approx 0$. What remains is the average electric field, the current, and two dynamo terms, the MHD dynamo $< \tilde{\mathbf{v}} \times \tilde{\mathbf{B}} >_\parallel$ and the Hall dynamo $< \tilde{\mathbf{J}} \times \tilde{\mathbf{B}} >_\parallel /(n_e e)$ (assuming $\tilde{n}_e = 0$).

Note that $\mathbf{j} = en(\mathbf{v_i} - \mathbf{v_e})$ and $\mathbf{v} = (m_i \mathbf{v_i} + m_e \mathbf{v_e})/(m_i + m_e) \approx \mathbf{v_i}$ so mean-field Ohm's law becomes:

$$\eta_\parallel \mathbf{J}_{0\parallel} - \mathbf{E}_{0\parallel} =< \tilde{\mathbf{v}}_\mathbf{i} \times \tilde{\mathbf{B}} >_\parallel - < (\tilde{\mathbf{v}}_\mathbf{i} - \tilde{\mathbf{v}}_\mathbf{e}) \times \tilde{\mathbf{B}} >_\parallel \approx < \tilde{\mathbf{v}}_\mathbf{e} \times \tilde{\mathbf{B}} >_\parallel \tag{1.3}$$

Of course, $\mathbf{J_{0\parallel}}$ is primarily due to the electrons since $m_e \ll m_i$. Therefore, to a good approximation mean-field Ohm's law is actually an electron force balance equation. Physically, this implies that the current and dynamo electric field are due almost completely to the electrons.

Historically, the dynamo has been studied experimentally in MST in several ways. The MHD dynamo has been measured in the core using line-averaged spectroscopic measurements of impurity ions [5, 6] and localized spectroscopic measurements of impurity ions from charge exchange recombination [7]. The Hall dynamo has also been measured in the core using a fast Faraday rotation diagnostic [8].

In the edge, dynamo terms have been measured locally with insertable probes. The MHD dynamo was measured using two probes, one to measure $\tilde{B}_\phi$ and $\tilde{B}_r$ fluctuations using magnetic pickup coils, and second to measure local $\tilde{v}_\phi$ and $\tilde{v}_r$ fluctuations spectroscopically using impurity ion emission lines [9]. The Hall dynamo was measured using a probe with magnetic pickup coils [10] and contributions of individual m=0 tearing modes to the Hall dynamo were isolated using magnetic pickup coil measurements and a pseudospectral technique [11]. Probe measurements of electromagnetic fluctuations ($\mathbf{\tilde{E}}$, $\mathbf{\tilde{B}}$, and $\tilde{V}_{plasma}$) have also been used to measure the dynamo in the edge of MST [12], as well as the magnetic helicity flux [13], which is related to the dynamo [14]. This final method using electromagnetic fluctuations is the same method used in this thesis and will be described in the following subsections.

1.1.2 Development of the $< \mathbf{\tilde{E}} \cdot \mathbf{\tilde{B}} > /B_0$ Term

It is possible to derive an equivalent expression for the mean-field dynamo $< \mathbf{\tilde{E}} \cdot \mathbf{\tilde{B}} > /B_0 \approx < \mathbf{\tilde{v}_e} \times \mathbf{\tilde{B}} >_\parallel$ that is easier to measure with probes. Previous work on MST used $< \mathbf{\tilde{E}}_\perp \cdot \mathbf{\tilde{B}}_\perp > /B_0$ as an equivalent expression for the dynamo [12]. However, according to more recent work, that is only an approximation. The complete version,

$< \tilde{\mathbf{E}} \cdot \tilde{\mathbf{B}} > /B_0$, will be derived first from simple arguments [15]. Then it will be derived again from a more detailed analysis to illuminate the differences between the two versions. The physical meaning of this equivalent expression for the dynamo will be discussed.

Begin with two-fluid Ohm's law (Eq. 1.1) where $\boldsymbol{\varepsilon}$ has been defined for convenience and $< \partial \mathbf{J}/\partial t > \approx 0$ is assumed again

$$\mathbf{E} + \boldsymbol{\varepsilon} + \frac{\nabla p_e}{n_e e} = \eta \mathbf{J} \tag{1.4}$$

$$\boldsymbol{\varepsilon} \equiv \left(\mathbf{v} - \frac{\mathbf{J}}{n_e e} \right) \times \mathbf{B} \tag{1.5}$$

Note that $\boldsymbol{\varepsilon}$ is a vector with the property

$$\boldsymbol{\varepsilon} \cdot \mathbf{B} = 0 \tag{1.6}$$

$$< \boldsymbol{\varepsilon} \cdot \mathbf{B} > = < \boldsymbol{\varepsilon} > \cdot < \mathbf{B} > + < \tilde{\boldsymbol{\varepsilon}} \cdot \tilde{\mathbf{B}} > = 0 \tag{1.7}$$

For the simple derivation method, take the flux-surface average of Eq. 1.4 dotted with $< \mathbf{B} >$, then use Eq. 1.7, and finally the fluctuating part of Eq. 1.4 as follows

$$\begin{aligned} \left\langle \eta \mathbf{J} - \mathbf{E} - \frac{\nabla p_e}{n_e e} \right\rangle \cdot < \mathbf{B} > &= < \boldsymbol{\varepsilon} > \cdot < \mathbf{B} > \\ &= - < \tilde{\boldsymbol{\varepsilon}} \cdot \tilde{\mathbf{B}} > \\ &= \left\langle \left(\tilde{\mathbf{E}} - \widetilde{\eta \mathbf{J}} + \widetilde{\frac{\nabla p_e}{n_e e}} \right) \cdot \tilde{\mathbf{B}} \right\rangle \end{aligned} \tag{1.8}$$

$< \nabla p_e/(n_e e) > \cdot < \mathbf{B} > = 0$ should be true if the plasma is isothermal along a field line. $< \eta\tilde{\mathbf{J}}\cdot\tilde{\mathbf{B}} >$ is measured to be small for all cases in this thesis. Dropping these terms and dividing by B_0 gives

$$\eta\mathbf{J}_{\parallel} - \mathbf{E}_{\parallel} = < \boldsymbol{\varepsilon} >_{\parallel} = \frac{< \tilde{\mathbf{E}}\cdot\tilde{\mathbf{B}} >}{B_0} + \left\langle \frac{\widetilde{\nabla P_e}}{n_e e}\cdot\frac{\tilde{\mathbf{B}}}{B_0} \right\rangle \tag{1.9}$$

The term due to electron pressure fluctuations, sometimes called the diamagnetic dynamo, is a contribution from the fluctuating diamagnetic drift [12]. It was measured previously to be substantial in RFP plasmas with high collisionality in the edge (REPUTE, TPE-1RM20 at high density) but small in standard RFP plasmas in MST [16]. The diamagnetic dynamo is not measured in this thesis but could be significant.

Substituting Eq. 1.5 into Eq. 1.9 for $\boldsymbol{\varepsilon}$ and assuming that the diamagnetic dynamo is negligible gives

$$\frac{< \tilde{\mathbf{E}}\cdot\tilde{\mathbf{B}} >}{B_0} = < \tilde{\mathbf{v}}\times\tilde{\mathbf{B}} >_{\parallel} - \frac{< \tilde{\mathbf{J}}\times\tilde{\mathbf{B}} >_{\parallel}}{n_e e} \tag{1.10}$$

In this thesis, the dynamo is measured with a probe in the edge of MST using the term on the left. The Hall dynamo, $- < \tilde{\mathbf{J}}\times\tilde{\mathbf{B}} >_{\parallel} /(n_e e)$, is also measured with the probe and the MHD dynamo, $< \tilde{\mathbf{v}}\times\tilde{\mathbf{B}} >_{\parallel}$, is calculated using the other two dynamo terms and Eq. 1.10.

1.1.3 Development of the $< \tilde{\mathbf{E}}_{\perp}\cdot\tilde{\mathbf{B}}_{\perp} > /B_0$ and $< \tilde{\mathbf{E}}_{\parallel}\cdot\tilde{\mathbf{B}}_{\parallel} > /B_0$ Terms

Ohm's law has been demonstrated to balance in the edge of MST solely using $< \tilde{\mathbf{E}}_{\perp}\cdot\tilde{\mathbf{B}}_{\perp} > /B_0$ and $\mathbf{E} - \eta\mathbf{J}$ [12]. However, it is possible that this previous work was not precise enough to show an imbalance in Ohm's law. In order to explore the meaning of $< \tilde{\mathbf{E}}_{\perp}\cdot\tilde{\mathbf{B}}_{\perp} > /B_0$ and $< \tilde{\mathbf{E}}_{\parallel}\cdot\tilde{\mathbf{B}}_{\parallel} > /B_0$, begin by defining $\mathbf{U} \equiv \mathbf{v} - \mathbf{J}/(n_e e)$ for convenience and substituting into Eq. 1.5:

$$\begin{aligned}\boldsymbol{\varepsilon} &= \left(\mathbf{v} - \frac{\mathbf{J}}{n_e e}\right) \times \mathbf{B} \equiv \mathbf{U} \times \mathbf{B} \\ &= (<\mathbf{U}>_\parallel + <\mathbf{U}>_\perp + \tilde{\mathbf{U}}_\parallel + \tilde{\mathbf{U}}_\perp) \times (<\mathbf{B}> + \tilde{\mathbf{B}}_\parallel + \tilde{\mathbf{B}}_\perp)\end{aligned} \tag{1.11}$$

To find the contribution to $<\tilde{\mathbf{E}} \cdot \tilde{\mathbf{B}}>/B$ due to perpendicular electromagnetic contributions, consider the fluctuating part of Ohm's law

$$\tilde{\mathbf{E}} - \eta\tilde{\mathbf{J}} = -\tilde{\mathbf{U}}_\perp \times <\mathbf{B}> - \mathbf{U} \times \tilde{\mathbf{B}} - <\tilde{\mathbf{U}} \times \tilde{\mathbf{B}}> \tag{1.12}$$

Next, take the cross product with $<\mathbf{B}>$

$$(\tilde{\mathbf{E}}_\perp - \eta\tilde{\mathbf{J}}_\perp) \times <\mathbf{B}> = B_0^2\tilde{\mathbf{U}}_\perp - (\mathbf{U} \times \tilde{\mathbf{B}}) \times <\mathbf{B}> + <\tilde{\mathbf{U}} \times \tilde{\mathbf{B}}> \times <\mathbf{B}> \tag{1.13}$$

Now take the cross product with $\tilde{\mathbf{B}}_\perp$

$$[(\tilde{\mathbf{E}}_\perp - \eta\tilde{\mathbf{J}}_\perp) \cdot \tilde{\mathbf{B}}_\perp] <\mathbf{B}> = B_0^2\tilde{\mathbf{U}}_\perp \times \tilde{\mathbf{B}}_\perp - [(\mathbf{U} \times \tilde{\mathbf{B}}_\parallel) \cdot \tilde{\mathbf{B}}_\perp] <\mathbf{B}> + [<\tilde{\mathbf{U}} \times \tilde{\mathbf{B}}> \cdot \tilde{\mathbf{B}}_\perp] <\mathbf{B}> \tag{1.14}$$

Then take the flux surface average and dot with $<\mathbf{B}>$

$$<(\tilde{\mathbf{E}}_\perp - \eta\tilde{\mathbf{J}}_\perp) \cdot \tilde{\mathbf{B}}_\perp> = <\tilde{\mathbf{U}}_\perp \times \tilde{\mathbf{B}}_\perp> \cdot <\mathbf{B}> + <\mathbf{U}_\perp \times \tilde{\mathbf{B}}_\perp \cdot \tilde{\mathbf{B}}_\parallel> \tag{1.15}$$

Dividing by B_0 and dropping the $\eta\tilde{\mathbf{J}}_\perp \cdot \tilde{\mathbf{B}}_\perp$ term, which is negligible, gives the result for the perpendicular contribution to $<\tilde{\mathbf{E}} \cdot \tilde{\mathbf{B}}>/B$:

$$\frac{<\tilde{\mathbf{E}}_\perp \cdot \tilde{\mathbf{B}}_\perp>}{B_0} = <\tilde{\mathbf{U}}_\perp \times \tilde{\mathbf{B}}_\perp>_\parallel + \frac{<\mathbf{U}_\perp \times \tilde{\mathbf{B}}_\perp \cdot \tilde{\mathbf{B}}_\parallel>}{B_0} \tag{1.16}$$

The first term on the right, $<\tilde{\mathbf{U}}_\perp \times \tilde{\mathbf{B}}_\perp>_\parallel$, is the desired MHD dynamo and Hall dynamo. The last term on the right can be divided into two parts. The first part, $<<\mathbf{U}>_\perp \times \tilde{\mathbf{B}}_\parallel \cdot \tilde{\mathbf{B}}_\perp>/B_0$, is a mean flow effect due to $<\mathbf{U}>_\perp$. There is no source for a large flow perpendicular to the mean magnetic field so it is not surprising that this term is small. The second part, $<\tilde{\mathbf{U}}_\perp \times \tilde{\mathbf{B}}_\parallel \cdot \tilde{\mathbf{B}}_\perp>/B_0$, is a three wave effect. It may be small because $\tilde{\mathbf{B}} \lll <\mathbf{B}>$ and also because on MST it has been experimentally observed that the coherence between fluctuations is typically around 10% e.g. [12]. Therefore, it is not surprising that this assumption has worked in the past in the edge of the standard MST RFP when showing that Ohm's law is balanced by $<\tilde{\mathbf{E}}_\perp \cdot \tilde{\mathbf{B}}_\perp>/B_0$, $\mathbf{E}$, and $\eta\mathbf{J}$ [12]. However, it is also possible that previous measurements were not precise enough to show any imbalance caused by not including $<\tilde{\mathbf{E}}_\parallel \cdot \tilde{\mathbf{B}}_\parallel>/B_0$ in Ohm's law.

Now consider the contribution to $<\tilde{\mathbf{E}}\cdot\tilde{\mathbf{B}}>/B_0$ from the parallel electromagnetic fluctuations in a similar manner as the contribution from perpendicular fluctuations. Begin with the fluctuating part of Ohm's law

$$\tilde{\mathbf{E}} - \eta\tilde{\mathbf{J}} = -\tilde{\mathbf{U}}_\perp \times <\mathbf{B}> - \mathbf{U} \times \tilde{\mathbf{B}} - <\tilde{\mathbf{U}} \times \tilde{\mathbf{B}}> \tag{1.17}$$

Next, take the dot product with $<\mathbf{B}>$

$$\tilde{\mathbf{E}}_\parallel - \eta\tilde{\mathbf{J}}_\parallel = -\mathbf{U}_\perp \times \tilde{\mathbf{B}}_\perp + <\tilde{\mathbf{U}}_\perp \times \tilde{\mathbf{B}}_\perp> \tag{1.18}$$

Then take the dot product with $\tilde{\mathbf{B}}_\parallel$ and flux surface average

$$< (\tilde{\mathbf{E}}_{\parallel} - \eta\tilde{\mathbf{J}}_{\parallel}) \cdot \tilde{\mathbf{B}}_{\parallel} >= - < \mathbf{U}_{\perp} \times \tilde{\mathbf{B}}_{\perp} \cdot \tilde{\mathbf{B}}_{\parallel} > \tag{1.19}$$

The term $< \eta\tilde{\mathbf{J}}_{\perp} \cdot \tilde{\mathbf{B}}_{\perp} >$ is small. Dividing by B_0 gives the contribution from the parallel electromagnetic fluctuations

$$\frac{< \tilde{\mathbf{E}}_{\parallel} \cdot \tilde{\mathbf{B}}_{\parallel} >}{B_0} = -\frac{< \mathbf{U}_{\perp} \times \tilde{\mathbf{B}}_{\perp} \cdot \tilde{\mathbf{B}}_{\parallel} >}{B_0} \tag{1.20}$$

The contribution $- < \mathbf{U}_{\perp} \times \tilde{\mathbf{B}}_{\perp} \cdot \tilde{\mathbf{B}}_{\parallel} > /B_0$ from $< \tilde{\mathbf{E}}_{\parallel} \cdot \tilde{\mathbf{B}}_{\parallel} > /B_0$ cancels the identical term in $< \tilde{\mathbf{E}}_{\perp} \cdot \tilde{\mathbf{B}}_{\perp} > /B_0$, giving that $< \tilde{\mathbf{E}} \cdot \tilde{\mathbf{B}} > /B_0 =< \tilde{\mathbf{U}}_{\perp} \times \tilde{\mathbf{B}}_{\perp} >_{\parallel}$, as expected. This confirms that $< \tilde{\mathbf{E}}_{\perp} \cdot \tilde{\mathbf{B}}_{\perp} > /B_0$ is equivalent to the dynamo only if $< \mathbf{U}_{\perp} \times \tilde{\mathbf{B}}_{\perp} \cdot \tilde{\mathbf{B}}_{\parallel} > /B_0$ is small.

The complete dynamo term includes contributions from all three components of $\tilde{\mathbf{E}}$ and $\tilde{\mathbf{B}}$. Therefore, in this thesis $< \tilde{\mathbf{E}} \cdot \tilde{\mathbf{B}} > /B_0$ will be measured as the dynamo. The contributions from the perpendicular and parallel electromagnetic field fluctuations, $< \tilde{\mathbf{E}}_{\perp} \cdot \tilde{\mathbf{B}}_{\perp} > /B_0$ and $< \tilde{\mathbf{E}}_{\parallel} \cdot \tilde{\mathbf{B}}_{\parallel} > /B_0$, will be compared to see if $< \mathbf{U}_{\perp} \times \tilde{\mathbf{B}}_{\perp} \cdot \tilde{\mathbf{B}}_{\parallel} > /B_0$ is unexpectedly large. Any contribution from $< \tilde{\mathbf{E}}_{\parallel} \cdot \tilde{\mathbf{B}}_{\parallel} > /B_0 =< \mathbf{U}_{\perp} \times \tilde{\mathbf{B}}_{\perp} \cdot \tilde{\mathbf{B}}_{\parallel} > /B_0$ is expected to be due to a three wave effect, $< \tilde{\mathbf{U}}_{\perp} \times \tilde{\mathbf{B}}_{\parallel} \cdot \tilde{\mathbf{B}}_{\perp} >$.

1.1.4 Magnetic Helicity and the Taylor Hypothesis

The Taylor hypothesis predicts the RFP relaxed state particularly well through minimizing the global magnetic energy while simultaneously holding the global magnetic helicity constant [17]. The gauge-independent magnetic helicity K in a torus of volume v is defined as [18, 19]

$$K = \int \mathbf{A} \cdot \mathbf{B} dv - \Phi\Psi \tag{1.21}$$

where $\mathbf{B}$ is the magnetic field, $\mathbf{A}$ is the vector potential defined as $\nabla \times \mathbf{A} \equiv \mathbf{B}$, and Ψ and Φ are the poloidal flux penetrating through the hole in the torus and toroidal flux in the volume, respectively. The magnetic helicity is due to electrical currents $\mathbf{J}$ flowing along magnetic field lines, which results in interconnected loops of magnetic field. It is a measure of the knottedness of magnetic field lines and can be heuristically understood as the amount of linked flux enclosed in the volume. The time derivative of magnetic helicity is

$$\frac{\partial K}{\partial t} = 2V_\phi \Phi - 2\int \mathbf{E} \cdot \mathbf{B} dv - 2\int \chi \mathbf{B} \cdot d\mathbf{s} \tag{1.22}$$

where V_ϕ is the toroidal loop voltage and χ is the electrostatic potential.

Magnetic helicity is perfectly conserved everywhere in ideal MHD but is only approximately conserved globally in resistive MHD. Taylor expected that the decay rate of magetic energy in a plasma should be at least as fast as the decay rate of magnetic helicity [20], which has been confirmed in RFP experiments [13]. He suggested that the relaxed state of a plasma could be derived by minimizing the energy of a plasma and allowing the local magnetic helicity $\mathbf{A} \cdot \mathbf{B}$ to change while holding the global magnetic helicity constant. This became known as the Taylor Hypothesis, which predicts the resulting state in a cylinder, known as the Taylor state,

$$\nabla \times \mathbf{B} = \lambda \mathbf{B} \tag{1.23}$$

$$\lambda = \frac{\mu_0 J_\parallel}{B} \tag{1.24}$$

where λ is uniform over the volume. The solutions to Eq. 1.23 are $B_\phi = B_0 J_0(\lambda r)$ and $B_\theta = B_0 J_1(\lambda r)$ where J_0 and J_1 are Bessel functions of the first kind. Note that,

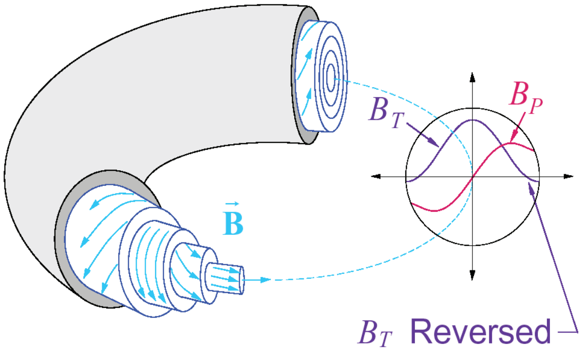

Figure 1.1: The RFP magnetic field configuration. The magnetic field, represented by arrows, is toroidal in the core, solely poloidal at the reversal surface, and points in the opposite toroidal direction in the edge.

by Ampere's law, Eq. 1.23 implies that the magnetic field and current density $\mathbf{J}$ are parallel, so the Taylor state is also called a force-free state since $\mathbf{J} \times \mathbf{B} = 0$.

This model produces a good prediction of the RFP relaxed state, shown in Fig. 1.1, particularly after accounting for the presence of the wall by modifying λ such that it goes to zero at the edge of the plasma $(r = a)$ [21]

$$\lambda(r) = \lambda_0(1 - (r/a)^{\alpha}) \tag{1.25}$$

$$\nabla \times \mathbf{B}(r) = \lambda(r)\mathbf{B}(r) \tag{1.26}$$

where λ_0 and α are constants. This is called the alpha model. The λ_0 parameter will be used later in this thesis to characterize the ratio of the parallel current to the magnetic field and α to characterize the peakedness of the current profile.

The success of the Taylor hypothesis suggests that magnetic relaxation keeps the global magnetic helicity approximately constant but changes the local magnetic helicity. It is possible to measure the fluctuation-induced transport of magnetic helicity across a flux surface at $r = b$ using the time rate of change of magnetic helicity $\partial K/\partial t$

(Eq. 1.22). This is accomplished by breaking the magnetic helicity K into three parts: K inside the flux surface (core helicity), K outside the flux surface (edge helicity), and K due to the toroidal flux inside the flux surface and the poloidal flux outside the flux surface (linkage helicity). The edge helicity and linkage helicity will both be assigned to the edge. Then the time rate of change in the edge helicity can be written as [13]

$$\begin{aligned} \frac{dK_{edge}}{dt} + \frac{dK_{linkage}}{dt} = & + 2\Phi_\phi(a)V_\phi(a) - 2\Phi_\phi(b)V_\phi(b) \\ & - 2\int_b^a \eta \mathbf{j_0} \cdot \mathbf{B_0} dv + 2\int < \tilde{V}_{plasma}\tilde{B}_r > dS_b \end{aligned} \tag{1.27}$$

where $\Phi_\phi(a)$ is the total toroidal flux within the volume and $V_\phi(a)$ is the toroidal loop voltage at $r = a$. Ohm's law has been used to substitute for $\mathbf{E}$ in the third term on the right.

The first two terms on the right are the change in K in the entire plasma $r < a$ minus the change in helicity in the sub-volume $r < b$. The third term is resistive dissipation in the outer annular volume $b < r < a$ while the last term is the helicity flux due to fluctuations, which does not appear at $r = a$ since B_r vanishes there, assuming a perfectly conducting wall. It was demonstrated previously that the helicity flux term was necessary to explain the helicity balance between the core helicity and edge helicity in the MST standard RFP. The helicity flux during partial OFCD sustainment and in standard plasmas will be presented in this thesis.

1.1.5 Tearing Modes

Tearing modes [22, 23] are typically the most influential plasma instability in RFPs including MST. They are primarily responsible for producing the fluctuating fields that interact to produce the dynamo, which is the mechanism by which the

RFP moves towards the relaxed state predicted by the Taylor hypothesis. Tearing modes with poloidal and toroidal mode numbers m and n are resonant at magnetic flux surfaces defined by a divergence-free condition for a Fourier decomposition of the magnetic fluctuation [5],

$$\mathbf{K} \cdot \mathbf{B} = k_\theta B_\theta + k_\phi B_\phi = \frac{m}{r} B_\theta + \frac{n}{R} B_\phi = 0 \tag{1.28}$$

Also, the safety factor, which is the number of toroidal transits per poloidal transit of a field line, is defined as

$$q(r) = \frac{rB_\phi(r)}{RB_\theta(r)} \tag{1.29}$$

Comparing Eq. 1.28 and Eq. 1.29, it is seen that $q = -m/n$ on a mode-resonant surface.

In the RFP sustained by a DC inductive toroidal electric field, the component of the electric field parallel to the mean magnetic field is large in the core, which tends to create a peaked λ profile, providing free energy to make the core tearing modes linearly unstable. The currents and electromagnetic fields associated with these modes produce a dynamo EMF. They also nonlinearly couple with linearly stable m=0 tearing modes resonant at the plasma reversal surface, causing them to grow and to produce dynamo as well, especially at the sawtooth crash. The toroidal electric field forces the plasma out of the RFP relaxed state because the component parallel to the mean magnetic field leads to a current profile, and therefore a λ profile, that grows more peaked at the center of the plasma. However, the gradient in the λ profile produced by E_ϕ is simultaneously the source of energy for growth of the tearing modes, which produce the dynamo that works to restore and maintain the RFP relaxed state.

1.2 The Madison Symmetric Torus

The Madison Symmetric Torus (MST), seen in Fig. 1.2, is a toroidal magnetic confinement plasma device [24]. It is designed to make reversed field pinches (RFP), which are magnetically confined plasmas where the plasma current produces most of the magnetic field. The term "pinch" refers to how the $\mathbf{J} \times \mathbf{B}$ force from the large current in the plasma squeezes the plasma together, while "reversed field" refers to the toroidal magnetic field B_ϕ reversing direction in the edge of the plasma due to the plasma current.

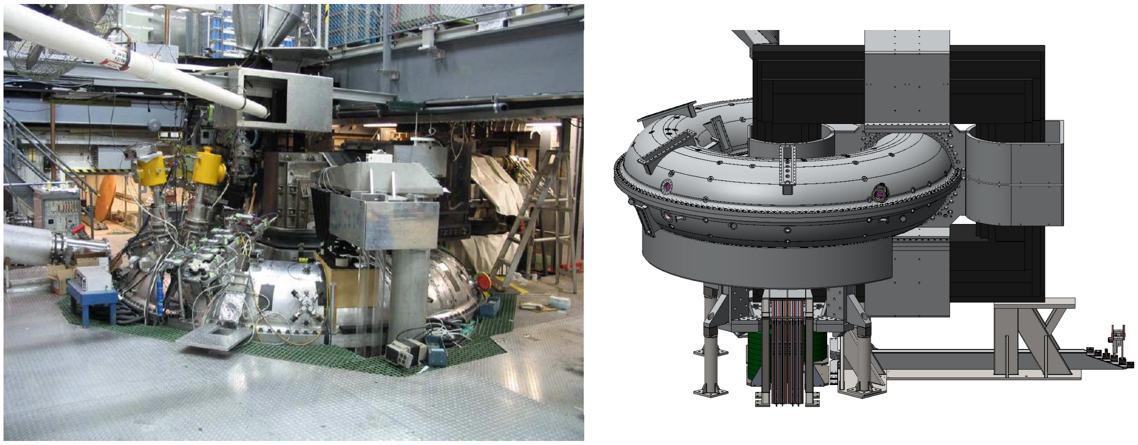

Figure 1.2: (left) Picture of MST with some of the experiments and diagnostics removed. The top half of the aluminum vacuum vessel is sticking out of the floor. (right) CAD drawing of MST vacuum vessel with poloidal and toroidal magnetic-field transformer cores. (Courtesy S. Oliva)

The MST RFP plasma is formed by first creating a toroidal magnetic guide field in the vacuum vessel. A small amount of deuterium gas is added to the vacuum vessel. The gas is pre-ionized by small filaments, and then an inductive toroidal electric field is created by the B_θ tranformer to create a plasma with a large toroidal current. The current creates a poloidal magnetic field in the edge. To first approximation, the plasma current follows the magnetic field everywhere in the plasma so poloidal current

Table 1.1: MST Parameters

Major Radius	1.5 m
Minor Radius	0.52 m
Wall Thickness	0.05 m
Plasma Current	150-600 kA
Electron Density	0.2-2.0$\times 10^{19}/m^3$

is produced as well. As the plasma current increases, the magnetic field at the edge becomes increasingly poloidal as its toroidal component goes towards zero.

Magnetic relaxation is required for the vanishing toroidal field at the edge to reverse direction. Once this occurs, typically by a discrete sawtooth event, the reversal of the edge magnetic field is enhanced by the MST Bt crowbar circuit, which applies a reversed B_ϕ magnetic field once the B_ϕ field at the edge goes through zero on its own. The applied B_ϕ field helps the plasma to maintain reversal of B_ϕ but the dynamo is still needed to maintain the edge current.

Once the MST RFP is formed, the current profile peaks in the core over the course of a few milliseconds, causing the tearing modes to grow, overlap and non-linearly couple to produce an enhanced dynamo at discrete relaxation events called sawteeth. The sawtooth, which is $\sim 100\mu s$ in duration, flattens the current profile and moves the RFP towards its relaxed state. The relaxed state magnetic field profile was shown in Fig. 1.1.

In MST under normal operating conditions, $m = 1$, $n = -6, -7, -8, \ldots, -\infty$ modes and sometimes the $m = 1$, $n = -5$ mode are resonant inside the reversal surface and $m = 0$, $n = 1, 2, 3, \ldots, \infty$ modes at the reversal surface. Outside of the reversal surface, $m = 1$ modes of opposite helicity to those in the core are resonant, but their n numbers are much larger since q is so small (see Fig. 1.3). During OFCD experiments, the usual MST tearing modes are resonant at and inside the reversal surface. However, $q(a)$ oscillates over the range $-0.2 < q(a) < 0$ over the course of the OFCD cycle so $m = 1$ tearing modes are periodically resonant outside the reversal surface with $n \geq 6$, depending on the instantaneous value of $q(a)$.

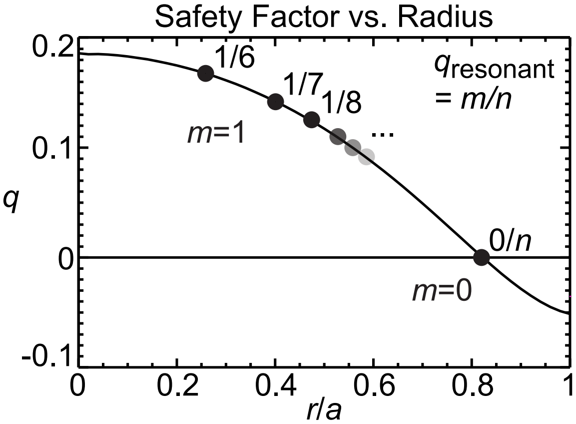

Figure 1.3: The typical q profile during standard plasmas for MST. (Courtesy K. McCollam).

MST's poloidal magnetic field windings surround the large iron core, represented by a black square loop in Fig. 1.2. These act as the primary of a transformer to produce the inductive toroidal electric field in the plasma, which acts as the tranformer secondary. MST's vacuum vessel has an insulated poloidal cut, called the poloidal gap, at the toroidal location of the iron core and aluminum continuity windings that branch out from the poloidal gap in four directions and wrap around the iron core, which allow the primary to be inside the MST vacuum vessel from an electrical perspective while being outside of it physically. MST's toroidal magnetic field is produced by using the vacuum vessel, which also has an insulated toroidal cut, as a single-turn magnetic field winding that is connected to an iron core transformer (visible directly below the vacuum vessel in Fig. 1.2). These poloidal and toroidal magnetic field windings will be used to apply the OFCD AC electromagnetic fields during partial OFCD experiments as well as the electromagnetic fields that usually create and sustain the MST RFP.

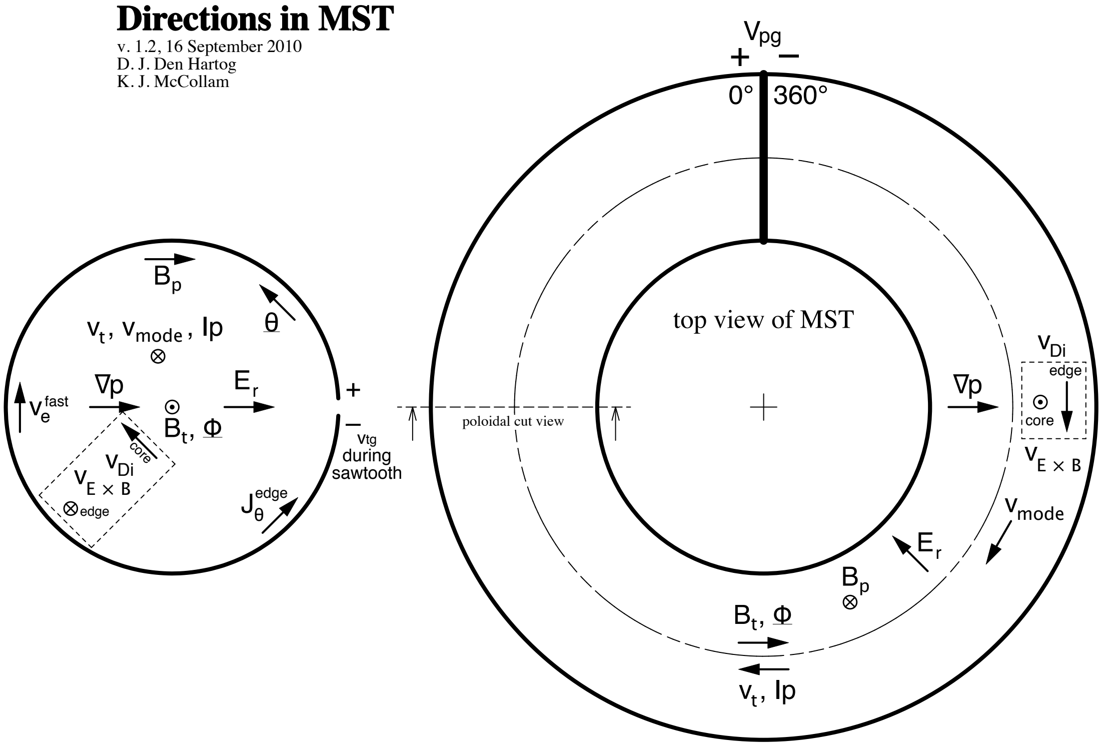

Figure 1.4: Directions used in this thesis ($\hat{\mathbf{r}}$ is outward)

Historically, multiple coordinate systems have been used on MST. In this thesis, the right-handed coordinate system shown in Fig. 1.4 will be used. Also note that the plasma current is antiparallel to the mean magnetic field, $\mathbf{B_0}$. For the currents and electric fields measured in this thesis, it will be important to discuss the component of the measurements tangent to $\mathbf{B_0}$ (parallel or antiparallel). When discussing parallel quantities the average parallel current will always be negative. Any electric field or electromotive force supporting the current will also be negative while electric fields and electromotive forces opposing the current will be positive.

1.3 Oscillating Field Current Drive

OFCD is a proposed method to completely sustain the plasma current in a reversed field pinch. It was proposed by Bevir and Grey [1], who referred to it as F-Θ pumping because OFCD produces a characteristic trajectory in F-Θ space. They posited that if Taylor's hypothesis is correct, then the RFP current could be sustained against resistive dissipation by adding magnetic helicity to the RFP using solely AC magnetic fields.

The time derivative of magnetic helicity in a torus (Eq. 1.22) can be rewritten by substituting Ohm's law (Eq. 1.1) for **E**

$$\frac{\partial K}{\partial t} = 2V_\phi\Phi - 2\int \eta\mathbf{J}\cdot\mathbf{B}dv - 2\int \chi\mathbf{B}\cdot d\mathbf{s} \tag{1.30}$$

where V_ϕ is the toroidal loop voltage, Φ is the toroidal magnetic flux, η is the resistivity, $\mathbf{J} = \nabla\times\mathbf{B}/\mu_0$ is the current density, and χ is the electrostatic potential. The first and third terms of Eq. 1.30 are inductive and electrostatic helicity injection terms and the second is a resistive decay term. In OFCD, magnetic helicity is added through the inductive injection term using an oscillating poloidal loop voltage $V_\theta = \hat{V}_\theta sin(\omega t)$, where $V_\theta = -d\Phi/dt$, and an oscillating toroidal loop voltage $V_\phi = \hat{V}_\phi sin(\omega t + \delta)$. This results in an average helicity injection rate over the OFCD cycle of

$$2\overline{V_\phi\Phi} = (\hat{V}_\phi\hat{V}_\theta/\omega)sin(\delta) \tag{1.31}$$

where the over-bar indicates the OFCD cycle average. Thus, a net amount of helicity can be added to the RFP to counter resistive decay using solely AC electromagnetic fields.

The net amount of helicity added depends on $sin(\delta)$, where δ is the phase between the two oscillating loop voltages. δ can be adjusted in OFCD experiments on MST. The experimental dependence of magnetic relaxation on δ will be examined in this thesis.

Note that Eq. 1.30 also can be used to describe other methods of plasma sustainment. Traditional inductive sustainment of the RFP adds helicity via a single flux swing of toroidal loop voltage applied along toroidal magnetic flux to counter resistive dissipation of the plasma current through the first term on the right. This term can also describe another type of helicity injection involving sinusoidal fields similar to those in OFCD, called steady inductive helicity injection, which has been used to form and sustain spheromak plasmas [25]. The last term on the right of Eq. 1.30 describes the sustainment of a plasma by electrostatic helicity injection. This has been the typical sustainment method for spheromaks, where it is called coaxial helicity injection [26, 27]. It has been used to form [28, 29] and sustain tokamak plasmas [30].

OFCD relies on magnetic relaxation to sustain the RFP current profile in a comparable way to the RFP that is sustained by an inductive toroidal electric field. In order for this to happen, it is expected that OFCD will need to provide energy to tearing modes, which would produce a dynamo everywhere to maintain the RFP relaxed state. This also sets a requirement on the OFCD oscillation period. The tearing mode growth time is in between the Alfven time, $\tau_A = a/V_a = a\sqrt{\rho\mu_0/B^2}$, where ρ is the mass density, and the resistive diffusion time, $\tau_R = \mu_0 a^2/\eta$, where η is the resistivity and a is the plasma minor radius. The OFCD period should be long relative to the hybrid tearing time scale $\tau_H \sim \sqrt{\tau_A \tau_R}$ so that the plasma has time to relax.

In addition, simulations show that the OFCD period should be short relative to the resistive diffusion time τ_R. If the OFCD frequency is too slow then the OFCD fields will be able to penetrate to the core of the RFP and cause the toroidal plasma current to change directions with the OFCD oscillation [31]. Therefore, the OFCD period is constrained to be $\tau_R > \tau_{OFCD} > \tau_H$. Within those limits, a lower OFCD frequency might be preferable to a higher frequency since the OFCD magnetic helicity injection rate is $(\hat{V}_\phi \hat{V}_\theta / \omega) sin(\delta)$.

Helicity balance and DEBS simulations suggest the viability of a reactor-scale RFP sustained solely with OFCD. According to helicity balance and relaxed state modeling, the size of the toroidal current oscillations are shown to be proportional to $\sim S^{-1/4}$ and the poloidal current oscillations also decrease substantially with S, where $S = \tau_R/\tau_A$ is the Lundquist number. The oscillations in current theoretically required for a fusion reactor scale RFP are only a few percent of the average current. According to DEBS simulations, the MHD activity in the full OFCD sustainment case would be the same scale as an RFP sustained by a DC (i.e. steady) inductive toroidal electric field [2].

Complete OFCD sustainment of an RFP has not been attempted to date due to the the large oscillator power required. Also, the size of the equilibrium oscillations would be too large on current RFPs (MST, RFX [32]) due to the Lundquist number scaling. However, partial OFCD experiments, in which OFCD is applied in conjunction with the usual DC inductive toroidal electric field, have been performed on ZT-40M and MST. On ZT-40M, OFCD drove $\sim$ 5% additional plasma current in low current (I_p=50-70 kA) partial OFCD experiments, while high current (I_p=180-200 kA) produced no discernable increase in plasma current, which was attributed to increased plasma resistivity due to plasma-wall interactions [33]. Up to 10% additional plasma current is added during partial OFCD experiments on MST [34]. Results of partial OFCD experiments will be presented in greater detail in Ch. 2. Partial OFCD experiments have also been performed on tokamaks but no increase in current was observed, presumably because magnetic relaxation in tokamaks is minimal [35].

Plasma confinement is the primary concern for OFCD sustainment of an RFP fusion reactor. OFCD on the RFP is seen to require tearing modes in order for the RFP to relax. These tearing modes could also produce stochastic magnetic fields, which could substantially degrade confinement. However, equilibrium reconstruction of partial OFCD experiments on MST demonstrated confinement that was as good or better than the standard MST RFP [36]. DEBS simulations also showed that partial OFCD might suppress magnetic fluctuations in the RFP [37].

OFCD is considered by many to be the best option for heating and sustaining the current in an RFP fusion reactor, due to the efficiency and simplicity of inductively applying AC toroidal and poloidal electromagnetic fields. The theoretical TITAN study proposed an RFP fusion reactor sustained by OFCD. The technology to produce the magnetic fields required for OFCD already exists and is scalable to meet the needs of a projected RFP fusion power plant where the plasma is sustained by OFCD, and the projected cost of electricity would be competitive with that for tokamaks [38].

What is not well understood is if the RFP plasma will react as expected to OFCD. It is uncertain if magnetic relaxation will maintain the RFP current profile when current is driven by OFCD or whether the dynamo will behave in the same manner as in the standard RFP. It is also uncertain whether the plasma's reaction to OFCD will have effects that are detrimental for a fusion plasma such as decreased confinement. This thesis will primarily address the question of dynamo behavior in the edge of MST during partial OFCD experiments.

Chapter 2

Oscillating Field Current Drive on MST

Partial OFCD sustainment experiments on MST are a method of exploring the physics of OFCD on a medium size experiment (compared to a fusion reactor) with relatively minimal invested time and resources. Full sustainment OFCD experiments are impossible on MST due to prohibitively large required oscillations in $\mathbf{B}_0$ since $S < 10^7$ in MST and the oscillation amplitude scales with $\sim S^{(-1/4)}$ [2]. Instead, partial OFCD sustainment experiments are performed. OFCD is applied at 275 Hz (period = 3.65 ms) in addition to the DC (i.e. constant) inductive toroidal electric field during the MST current flattop (15-40 ms). We are able to investigate the physics of magnetic relaxation during OFCD because the MST current flattop is very long compared to the hybrid relaxation time ($\tau_H \sim 100\mu s$).

OFCD is tested on MST with two tank (LC) circuits driven by two pulse forming networks (PFN). The PFN current in each circuit is directed by a novel ignitron switching method in order to maintain a constant tank circuit oscillation amplitude. This approach is cheap relative to other options such as programmable power supplies with solid state switches like the one recently developed for the MST B_ϕ circuit and proposed for the MST B_θ circuit, but the driven tank circuits don't offer as much control of the OFCD waveforms. In addition, the circuits suffer from moderately frequent ignitron commutation (switching) failures. The oscillator circuits were adequate but not ideal for the experiments in this thesis, which required large data sets of reproducible OFCD plasmas.

2.1 Hardware

OFCD uses MST's toroidal magnetic field and poloidal magnetic field windings, discussed in Sec. 1.2, to apply the AC magnetic fields to the plasma. The two tank circuits use aircore tranformers to connect to the transmission lines that go between MST's capacitor banks and its poloidal and toroidal field circuits.

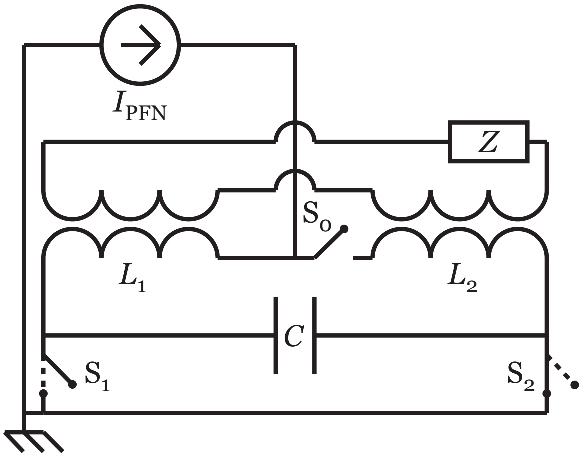

Figure 2.1: [39] OFCD driven oscillator circuit conceptual schematic. The tank (LC) circuit is composed of L_1, L_2, and C while S_0, S_1, and S_2 are ignitron switches, I_{PFN} is the PFN current, and Z is the plasma load.

The conceptual schematic of the OFCD driven oscillator circuit is seen in Fig. 2.1. The tank circuit, which is composed of L_1, L_2, and C, is pre-charged for immediate full-amplitude oscillation. The connection ignitron, S_0, initiates the oscillation while the PFN current, I_{PFN}, is directed by S_1 and S_2, the commutating ignitrons. S_1/S_2 simultaneously open/close and then close/open once every OFCD cycle to direct the PFN current to drive the tank circuit oscillation. One oscillator tank circuit inductively couples via an air-core transformer to the transmission line for the MST B_θ windings, and likewise for the other oscillator circuit to the B_ϕ windings, which apply the AC OFCD electromagnetic fields to the plasma load Z, as shown in the schematic for one of the tank circuits.

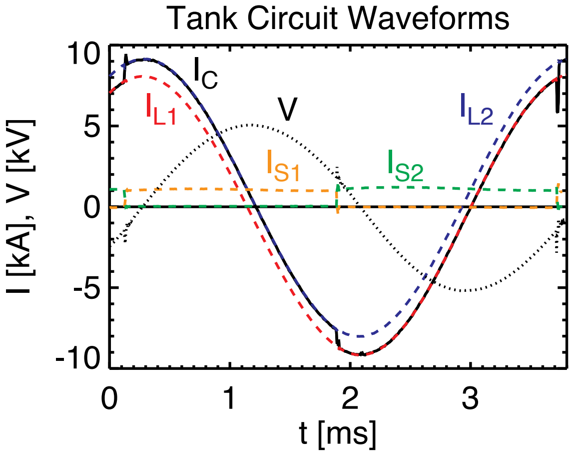

Figure 2.2: [39] Voltages and currents on the OFCD tank circuit. The subscripts C, L1, L2, S1, and S2 correspond to the circuit components in 2.1 and $V = V_C$

The currents in a tank circuit during one OFCD cycle can be seen in Fig. 2.2. The entire PFN current passes through S_1 for the first half of the cycle. Then S_1 switches off while S_2 switches on and carries I_{PFN} for the second half of the cycle. The inductors L_1 and L_2 each carry the capacitor current I_C and their corresponding commutating ignitron currents S_1 and S_2 i.e. $I_{L1} = I_C - I_{S1}$ and $I_{L2} = I_C + I_{S2}$. When the PFN current is directed by the commutating ignitrons in this manner, it keeps the amplitude of the LC oscillation in the tank circuit constant.

The most important factor governing the success or failure of these oscillator circuits on a given plasma shot is whether or not the commutating ignitrons turn on and off correctly. Each commutating ignitron is switched on by its own dedicated feedback trigger circuitry, which measures the tank current using a Rowgowski coil and sends a voltage pulse to the ignitron's ignitor at the appropriate time to turn it on. Ideally, the feedback circuitry would be set to turn the commutating ignitrons on and off when the voltage V on the capacitor was zero. Instead, the feedback circuitry is set to switch S_1 and S_2 slightly before $V = 0$ because a substantial voltage is required to achieve reliable commutation.

When a commutating ignitron is turned on, the voltage on its anode drops to zero virtually instantaneously. This voltage drop is used to turn the other commutating ignitron off via a small coupling capacitor. Ignitrons are not designed to turn off when conducting, but the sudden voltage change communicated by the coupling capacitor briefly applies a reverse bias to the conducting ignitron that turns it off. It is hypothesized that this reverse bias clears the space inside the ignitron of electrons long enough for the ignitron's conducting arc to cease.

A less common source of OFCD circuit failure is the connection ignitron, S_0. This ignitron is intended to be turned on to start OFCD and remain on. It only conducts the tank circuit current for half the cycle so it is installed in parallel with a diode stack, which conducts the tank current for the other half of the cycle. To keep the connection ignitron conducting (i.e. turned on), one RC circuit continuously drives current through the connection ignitron while another RC circuit provides current through its holding anode. The connection ignitron will occasionally turn off prematurely, even with these two redundant methods for keeping it conducting. For more details on the circuit, see appendix A for the complete circuit schematic or [39] for a more extensive discussion.

These features and others in the OFCD circuit substantially improved the reliability of OFCD performance and reduce the frequency of various failure modes, which was important for obtaining the large ensembles of OFCD data presented in this thesis. Without these features, the time necessary for data collection would have been prohibitively long.

Even with these features, the primary failure mode of these oscillator circuits is commutating ignitrons switching on and off at the wrong times. Two examples of the voltages across the commutating ignitrons for one circuit are shown in Fig. 2.3. One plasma shot with good commutation is shown in green and a shot with bad commutation is shown in red. At ∼ 16 ms, the bottom red signal shows the ignitron spontaneously turning on early. At the same time, the top red signal shows the coupling capacitor turning the other ignitron off as designed.

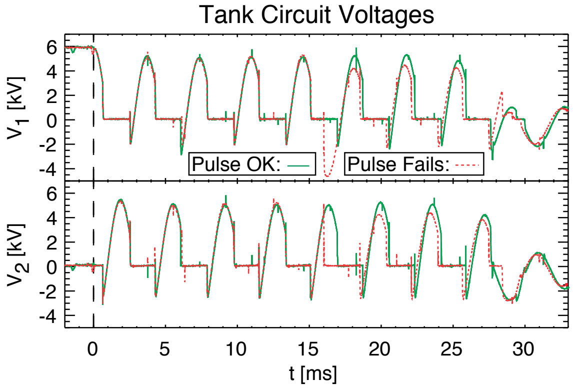

Figure 2.3: [39] Examples of good and bad OFCD circuit ignitron commutation during plasma shots.

The red shot shows a substantial decrease in oscillation amplitude and a phase shift after ∼ 16 ms because of the commutation failure. This is a consistent feature of a commutation failure, which is due to the PFN incorrectly driving the tank circuit for part of that cycle. Therefore, if the two shots in 2.3 were part of an ensemble in this thesis, then the first seven cycles of the green shot would be included in the data ensembles while only the first four cycles would be included from the red shot because the commutation failure at ∼ 16 ms affects the OFCD phase and amplitude for the rest of the shot. One result of this selection criteria is that the OFCD ensembles in this thesis have more events from the begin of the plasma flat top than from the end.

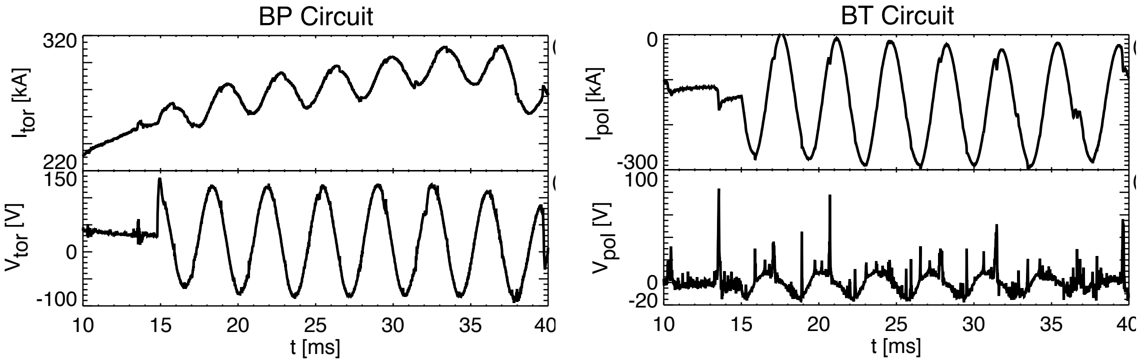

Figure 2.4: [39] Current and voltage oscillations produced by the OFCD circuits on the MST RFP at typical experimental settings and conditions.

Figure 2.4 shows an example of the currents and voltages produced by the two OFCD oscillator circuits in the MST RFP under typical experimental settings. The B_θ circuit produces an AC B_θ and corresponding inductive V_ϕ and I_ϕ. Likewise, the B_ϕ circuit produces an AC B_ϕ, V_θ, and I_θ. OFCD turns on at 15 ms so comparing $10 < t < 15ms$ to $15 < t < 40ms$ shows that the size of the applied OFCD oscillations is large compared to the background fields in MST. These large oscillations are not ideal for the RFP but are necessary for substantial current drive. They are predicted to scale with $S^{-1/4}$ so they'd be smaller relative to the background fields in an RFP fusion reactor [2].

2.2 Current Drive Results

In partial OFCD experiments on MST, the plasma is established and OFCD is applied in conjunction with the MST DC E_ϕ beginning at 15 ms. Figure 2.5 compares the resulting plasma current from OFCD with $\delta = +\pi/2$, $+\pi/4$, 0, and $-\pi/2$ to the resulting plasma current if OFCD is off. In the four OFCD cases, the current oscillates at the OFCD frequency but the cycle-averaged current increases for $\delta \geq 0$ and decreases for $\delta = -\pi/2$ relative to the standard RFP. The length of OFCD is limited by the size of the two PFNs for the OFCD circuit to 25 ms (t = 40 ms). If this weren't the case and the MST pulse weren't also limited by the volt-seconds of the transformer then the current would asymptotically reach a steady state on the L/R $\sim$ 30 ms timescale.

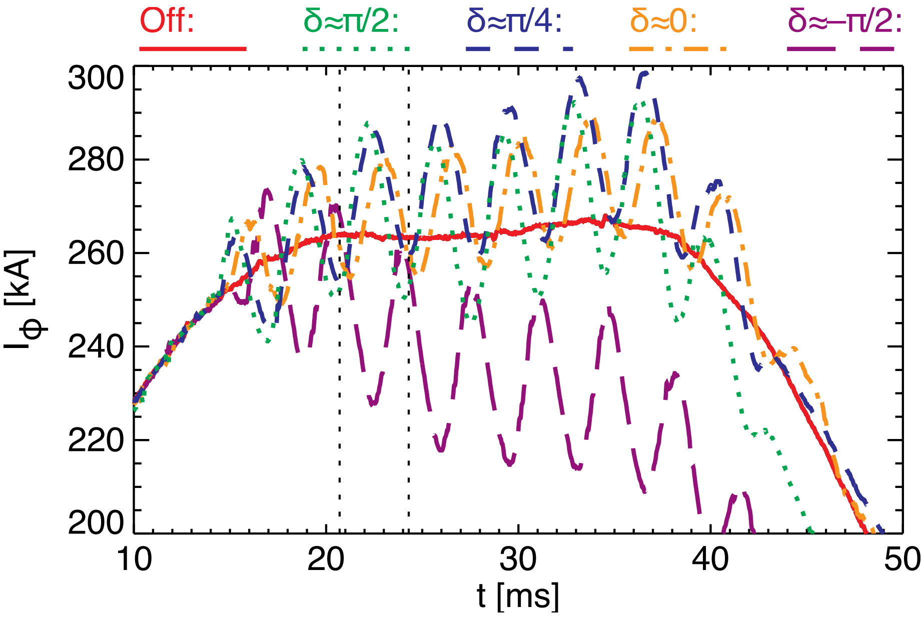

Figure 2.5: [36] The toroidal plasma current from partial OFCD experiments with phases $\delta = +\pi/2$, $+\pi/4$, 0, and $-\pi/2$ is compared to the RFP without OFCD. $\Delta I(\delta)$ is unexpected based on the dependence of helicity injection on OFCD phase.

An enigma of OFCD experiments on MST is the phase dependence of the current added to the plasma. The OFCD cycle-averaged helicity injection rate is $2\overline{V_\phi \phi} = (\hat{V}_\phi \hat{V}_\theta/\omega) sin(\delta)$, so the phase of maximal helicity injection is $\delta = +\pi/2$ while $\delta \approx +\pi/8$ produces the largest increase in current ($\Delta < I_\phi > \sim$ 10% additional, where $<>$ indicates the OFCD cycle average). Figure 2.5 shows that $\delta = +\pi/4$ and even $\delta = 0$ result in a larger increase in current than $\delta = +\pi/2$. This is particularly surprising for

$\delta = 0$, since this phase produces no average helicity injection over a cycle. However, OFCD $\delta = 0$ does add helicity for half of the OFCD cycle and eject it for the other half so helicity injection could play a complicated role in the current increase for $\delta = 0$. In any case, partial OFCD isn't as simple as adding more helicity with OFCD to produce more plasma current. The dependence of $\Delta < I_\phi >$ on the OFCD phase, δ, is one of the primary questions regarding partial OFCD experiments on MST.

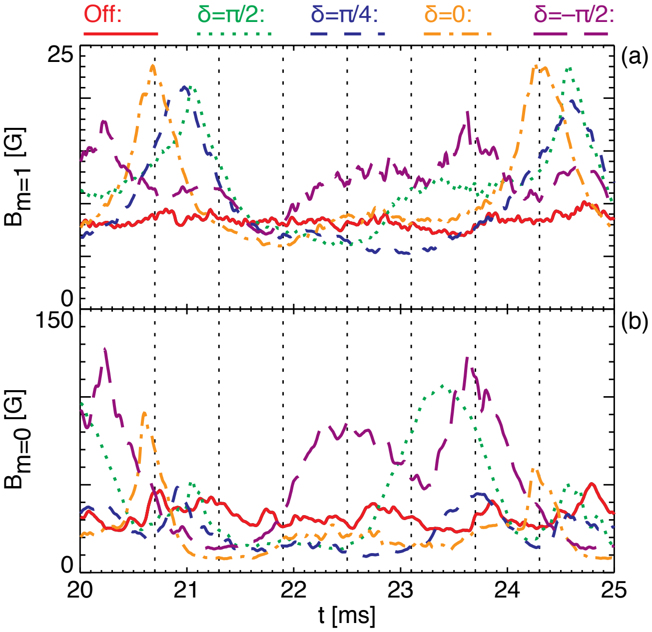

Figure 2.6: [36] The sums of the m=0 ($1 \leq n \leq 4$) and m=1 ($5 \leq n \leq 15$) mode amplitudes of OFCD $\delta = +\pi/2$, $+\pi/4$, 0, and $-\pi/4$ are compared to the case without OFCD. The amplitudes of the m=0 modes are inversely correlated with $\Delta < I_\phi > (\delta)$ (Fig. 2.5)

The amplitudes of the m=0 tearing modes in MST have a dependence on the OFCD phase (Fig. 2.6) that's inversely correlated with $\Delta < I_\phi > (\delta)$ (Fig. 2.5). The m=0 mode amplitudes are smallest and the increase in current is largest for OFCD $\delta = +\pi/4$ while $\delta = +\pi/2$ is the current drive case with the largest m=0 amplitudes and the second smallest $\Delta < I_\phi > (\delta)$. The best OFCD current drive result on MST, achieved with $\delta \approx +\pi/8$ (not shown), has the smallest m=0 amplitudes and adds up to $\sim$ 10% additional plasma current. The anti-current drive case, $\delta = -\pi/2$, has large m=0 modes in addition to injecting magnetic helicity with the opposite sign as the helicity in MST, which is correlated with a substantial decrease in plasma current (the magnetic helicity in MST is negative while $\delta = -\pi/2$ injects positive helicity). Therefore, the current drive does depend on magnetic helicity but is also correlated to the m=0 mode amplitudes. The m=1 mode amplitudes are slightly larger during partial OFCD experiments than in experiments without OFCD. However, the OFCD $\Delta < I_\phi > (\delta)$ is inversely correlated with the m=1 amplitudes as well.

DEBS simulations of MST partial OFCD experiments with $\delta = +\pi/2$, $+\pi/8$, 0, and $-\pi/2$ show a nearly identical $\Delta < I_\phi > (\delta)$ to the OFCD experiments [36], shown in Fig. 2.7. The simulations also showed a minimization of m=1 mode amplitudes for $\delta = +\pi/8$ but didn't agree on the phase dependence of m=0 mode amplitudes, likely because of the simulation boundary conditions. The simulations indicated that OFCD $\delta = +\pi/2$ has increased cycle-averaged helicity dissipation $2\int < \eta \mathbf{J}\cdot\mathbf{B} > dv$ (Eq. 1.27) that almost completely cancelled the helicity injected by OFCD. DEBS is a nonlinear 3D resistive-MHD code so this result suggests that although MST OFCD $\Delta < I_\phi > (\delta)$ is not consistent with the simple helicity injection argument, it is described by resistive magnetohydrodynamics. These DEBS results also increase confidence in the DEBS simulations that demonstrate the feasibility of full OFCD sustainment in an RFP fusion reactor [2].

2.3 The Sawtooth Crash During OFCD

One robust feature of partial OFCD experiments on MST is that the sawtooth crash preferentially occurs at specific points during the OFCD cycle. This sawtooth entrainment is demonstrated by the fraction of OFCD cycles that have a sawtooth in

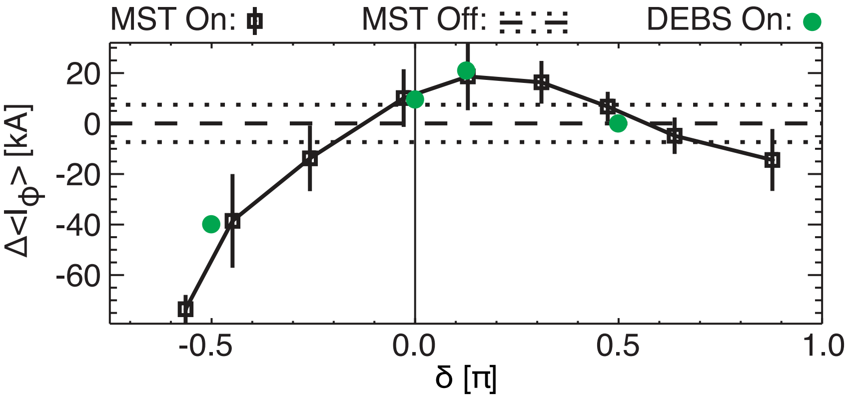

Figure 2.7: [36] Comparison of the current added by partial OFCD, $\Delta < I_\phi > (\delta)$, during partial OFCD experiments on MST and in 3D resistive-MHD DEBS simulations of MST experiments.

each 100 μs time window, shown in Fig. 2.8 (the sawtooth width is $\sim 100\mu s$). At the sawtooth crash, there is a large spike on virtually every plasma measurement. The sawteeth in the plot are selected based on spikes on the voltage across MST's toroidal gap (VTG). Every VTG spike greater than 5 volts that also has a corresponding spike in the reversal parameter F is included. Note that the OFCD cycle is $\sim$ 3.65 ms long so the 0.35 ms periods at the beginning and end of each plot are the same part of the OFCD cycle.

The VTG spike size distribution (not shown) was examined for these OFCD ensembles. In all four OFCD ensembles there was clearly two separate quasi-Maxwellian distributions of VTG spike sizes with a minimum between the two at $\sim$ 15 volts. Therefore, the subset of the sawtooth crashes with a VTG spike greater than 15 volts is plotted in red to give an indication of relative strengths of the crash at different points during the OFCD cycle.

This sawtooth entrainment is another indicator that OFCD has a large influence on the tearing modes (Fig. 2.6) and magnetic relaxation. For an RFP at the same MST

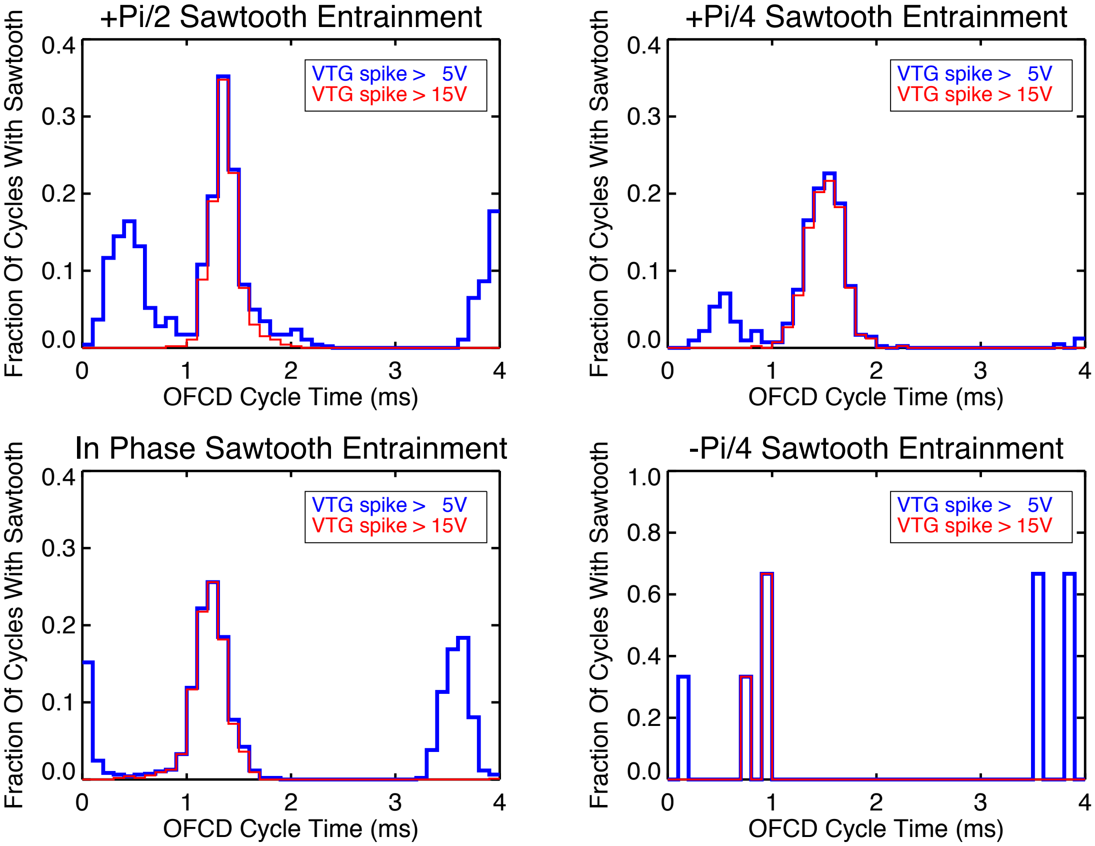

Figure 2.8: Fraction of OFCD cycles that have a sawtooth in each 100μs time window. Blue includes the sawteeth with VTG spikes greater than 5V and red is the subset of blue with VTG spikes greater than 15V. Note that the OFCD $\delta = -\pi/4$ y-axis has a larger range. Data is from the same ensembles of shots used in subsequent chapters.

settings, the sawtooth period would be 4-5 ms whereas in these OFCD experiments it is forced to approximately match the OFCD period of 3.65 ms. Detailed observations of the effect of OFCD on the tearing modes will be presented in Ch. 3.

2.4 Magnetic Relaxation During OFCD

In the RFP, OFCD attempts to force the current profile away from the relaxed state and magnetic relaxation is expected to oppose OFCD and flatten the current profile. In full OFCD sustainment, OFCD would attempt to increase the current principally at the edge of the RFP, which would lead to a hollow current profile unless the OFCD cycle-averaged $E_{\|}$ is opposed by the dynamo. Similarly, in partial OFCD experiments such as those performed on MST, the DC (i.e. steady) inductive E_{ϕ} attempts to peak the current profile in the core and the OFCD cycle-averaged contribution attempts to peak the current profile at the edge, which would lead to insufficient current at the mid-radius unless the dynamo EMF opposes the current where it is over-driven and supports the current at the mid-radius where it is under-driven.

In partial OFCD experiments on MST, the parallel electric field contributions from the MST DC inductive electric field and from OFCD have been determined from equilibrium reconstructions [36]. The effective OFCD electric field should be $< E >_{OFCD} = < \mathbf{E} \cdot \mathbf{B} > / < B > - < \mathbf{E} > \cdot < \mathbf{B} > / < B >$, where $<>$ denotes a cycle average, not a flux-surface average as in the previous chapter, while the MST DC electric field is $< E_{\|} > = < \mathbf{E} > \cdot < \mathbf{B} > / < B >$. Radial profiles of both electric fields are shown in Fig. 2.9 on the left. The $< E >_{OFCD}$ is localized to the edge while the DC $< E >_{\|}$ extends across the entire radius. MST's applied $< E >_{\|}$ is the same for all cases, as can be observed at the edge (r/a = 1.0). The variation of $< E >_{\|}$ in the core is due to variations in plasma resistivity, which is lower for OFCD $\delta = +\pi/4$ and 0 than the case with OFCD off and is higher for OFCD $\delta = -\pi/2$.

The total cycle-averaged parallel electric field, $< E_{\|} > = < E >_{\|} + < E >_{OFCD}$, is shown in Fig. 2.9 on the right along with $< \eta \mathbf{J}_{\|} >$ for partial OFCD experiments and for the MST RFP with OFCD off. In all cases, $< E_{\|} > = < \eta \mathbf{J}_{\|} >$ at only one location, $r/a \approx 0.6$. If the two-fluid resistive MHD model holds true for these cases, then parallel Ohm's law (Eq. 1.2) implies that there is a dynamo, $< \varepsilon_{\|} > = < \eta \mathbf{J}_{\|} > - < E_{\|} >$,

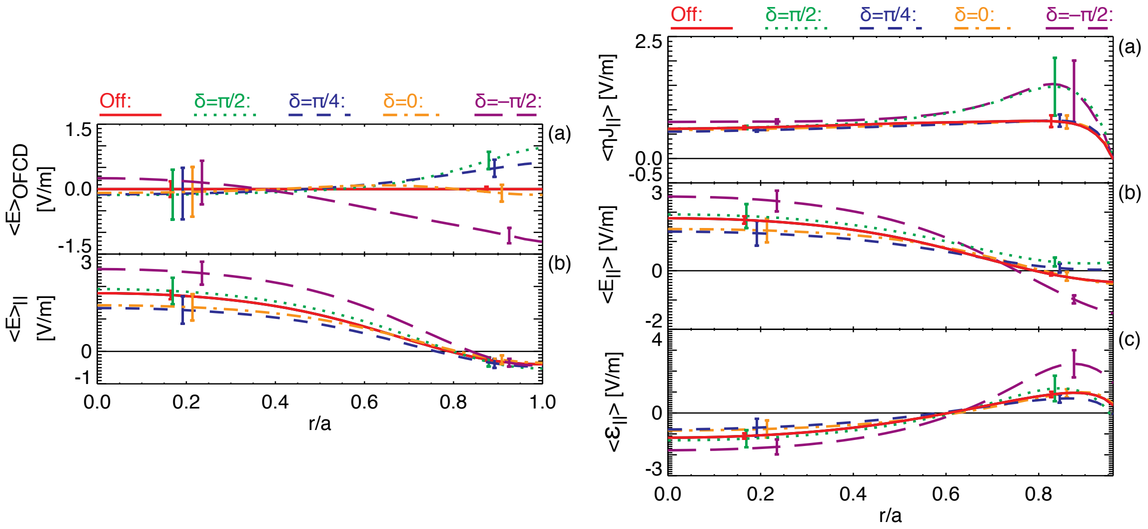

Figure 2.9: [36] Radial profiles of the average electric field and its components, $< E \cdot B > / < B > = < E >_{\parallel} + < E >_{OFCD}$, along with $< \eta \mathbf{J}_{\parallel} >$, $< \mathbf{E}_{\parallel} >$, and $< \varepsilon_{\parallel} > = < \eta \mathbf{J}_{\parallel} > - < E_{\parallel} >$ for OFCD phases $\delta = +\pi/2$, $+\pi/8$, 0, and $-\pi/2$ and the RFP with OFCD off. $< \varepsilon_{\parallel} >$ is the dynamo EMF that would balance Ohm's law. Uncertainty estimates are shown at two radii.

plotted in the bottom right graph of Fig. 2.9, where $< \varepsilon_{\parallel} > \approx < \tilde{\mathbf{v}}_e \times \tilde{\mathbf{B}} >$.

In the OFCD $\delta = +\pi/4$ and 0 cases and in the RFP with OFCD off, the plot of $\eta \mathbf{J}$ suggests that the dynamo maintains a fairly flat current profile despite the large radial variation in $< E >_{\parallel}$. In the OFCD $\delta = +\pi/2$ case, the bump in $\eta \mathbf{J}$ at $r/a \approx 0.85$ suggests that the dynamo is not as successful at keeping the current profile flat, although the resistivity could also be higher. The bump in the edge during OFCD $\delta = -\pi/2$ is certainly due to a large resistivity caused by anti-current drive and the resulting poor confinement.

The time dependence of the radial profiles of $E_{\parallel}$, $\eta \mathbf{J}_{\parallel}$, and $\varepsilon_{\parallel}$ are shown in Fig. 2.10 over a single OFCD cycle for the same cases as above. A bump in $\eta \mathbf{J}_{\parallel}$ develops in the edge at $t = 23.7$ ms in the $\delta = +\pi/2$ case and at $t = 21.9$ ms in the $\delta = -\pi/2$ case, but otherwise the dynamo does an excellent job keeping $\eta \mathbf{J}_{\parallel}$ constant. This constant

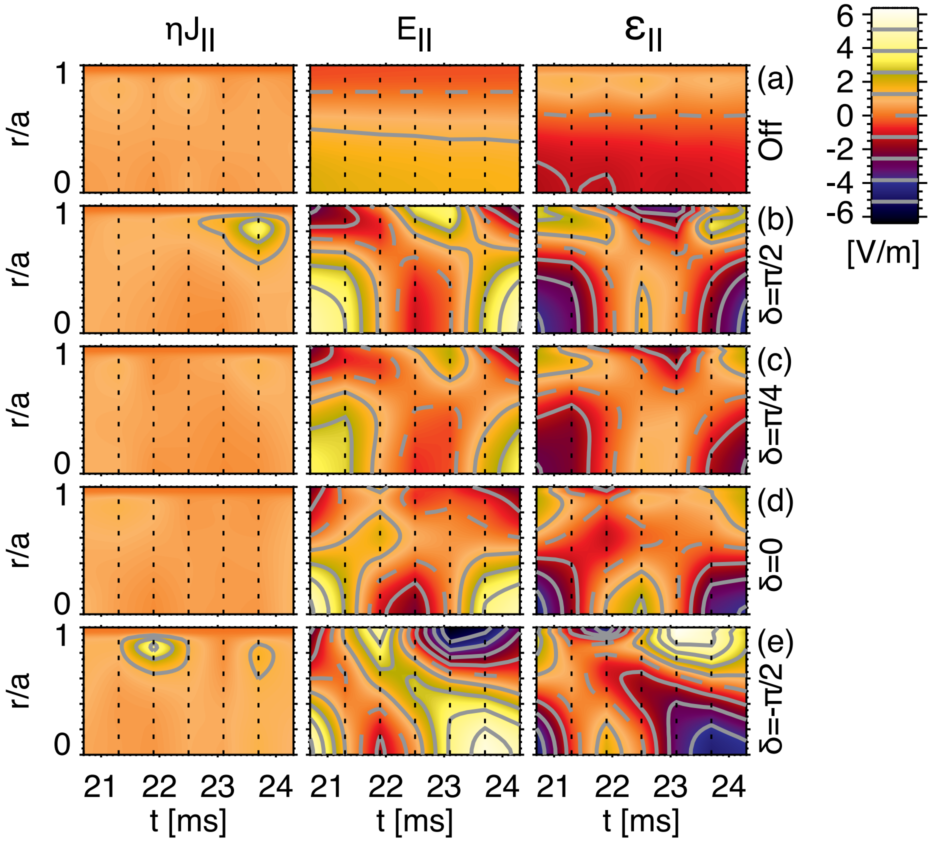

Figure 2.10: [36] The electric field $\mathbf{E}_{\parallel}$, $\eta\mathbf{J}_{\parallel}$, and $\boldsymbol{\varepsilon}_{\parallel} = \eta\mathbf{J}_{\parallel} - \mathbf{E}_{\parallel}$ plotted versus minor radius and time over an OFCD cycle. $\boldsymbol{\varepsilon}_{\parallel}$ is presumably equal to the dynamo.

$\eta\mathbf{J}_{\parallel}$ profile is produced by the interplay of $E_{\parallel}$ and $\varepsilon_{\parallel}$ despite the large variations in $\mathbf{E}_{\parallel}$ compared to $\eta\mathbf{J}_{\parallel}$ or to $\mathbf{E}_{\parallel}$ during the OFCD off case, which requires similar large oscillations in the dynamo. The dynamo, $\boldsymbol{\varepsilon}_{\parallel}$, is also required to change direction relative to $\mathbf{B}_0$ over the course of the OFCD cycle in both the core and the edge, which is unusual for an RFP. This is most obvious for OFCD $\delta = +\pi/2$ and $-\pi/2$.

For the results presented in this section, it has been assumed that two-fluid resistive MHD is a good model for the plasma during partial OFCD experiments since it has been previously shown to be a good model for the RFP without OFCD. The dynamo, $\boldsymbol{\varepsilon}_{\parallel} \approx < \tilde{\mathbf{v}}_e \times \tilde{\mathbf{B}} >_{\parallel}$, has not been measured but rather has been inferred under the assumption that parallel Ohm's law (Eq. 1.2) describes the plasma well. The $\boldsymbol{\varepsilon}_{\|}$ implied by Ohm's law and shown in Fig. 2.10 has magnitude and sign changes due to OFCD that are not present in the standard RFP and have never before been directly measured. In subsequent chapters, direct measurements of dynamo terms in the edge will be presented in order to examine whether Ohm's law accurately describes the plasma during partial OFCD experiments and to examine various contributions to the dynamo.

Chapter 3

Tearing Modes on MST

Tearing modes (Sec. 1.1.5) are primarily responsible for magnetic self-organization in the RFP. OFCD drives current in the edge, which appears to destabilize edge-resonant tearing modes (for more information on mode stability in MST, see [40]). The tearing mode electromagnetic fields interact to create a dynamo that effectively redistributes the current throughout the rest of the RFP. Therefore, examining the mode behavior during partial OFCD sustainment experiments on MST may yield insight into OFCD results and its feasibility for full current sustainment on an RFP. Examining the tearing modes is also beneficial for understanding the physics of magnetic self-organization.

In addition, the validity of the analysis method for calculating dynamo terms using the Dynamo Probe is dependent upon mode behavior (Sec. 4.3). The analysis method assumes that the ensemble of events completely and evenly sample the mode structures in the plasma. Usually the plasma rotates toroidally with a rate greater than 1 kHz and the tearing mode phases are fairly randomly distributed so this condition is easily satisfied. In this chapter, the tearing mode amplitudes, phases, and velocities will be examined in detail in plasmas with and without OFCD using the same ensembles of shots as those used to calculate the dynamo and other Ohm's law terms in Ch. 5 and Ch. 6.

3.1 Mode Measurements Using the Toroidal Array

The magnetic fields from the tearing modes extend throughout the plasma so the modes can be measured using an array of Mirnov coils on the inner surface of the MST vacuum vessel. There is one array spaced toroidally around the vacuum vessel to resolve the toroidal mode structure (i.e. the mode n numbers) and another array spaced poloidally that would resolve the poloidal mode structure (i.e. the mode m numbers). They are called the toroidal array and the poloidal array, respectively. Unfortunately, the poloidal array has been difficult to calibrate properly, so the poloidal mode structure cannot be well resolved. The inability to measure the poloidal mode structure is not a severe detriment for the majority of MST experiments but is problematic for partial OFCD experiments, as will be discussed later in this chapter.

The toroidal array consists of 64 magnetic triplets evenly spaced toroidally around the inner wall of MST at $\theta = 241$ degrees. They can measure modes up to a toroidal mode number n=32, since 32 is the Nyquist wavelength for the array. The amplitude and phase of each mode are calculated using the toroidal array data, Eq. 3.1, and least squares fitting. Only a_{32} or b_{32} can be calculated since a_0 needs to be calculated as well [41].

The structure of the magnetic field as seen by the toroidal array can be expressed as

$$X(\phi) = \sum_{n=0}^{32} [a_n sin(n\phi) + b_n cos(n\phi)] \tag{3.1}$$

assuming contributions from modes with $n > 32$ are negligible. An equivalent expression for Eq. 3.1 is

$$X(\phi) = \sum_{n=0}^{32} [c_n cos(n\phi - \delta_n)] \tag{3.2}$$

$$a_n = c_n sin(\delta_n) \tag{3.3}$$

$$b_n = c_n cos(\delta_n) \tag{3.4}$$

$$c_n = \sqrt{a_n^2 + b_n^2} \tag{3.5}$$

$$\delta_n = arctan\left(\frac{a_n}{b_n}\right) \tag{3.6}$$

The mode velocity is determined by taking the derivative of δ_n (Eq. 3.6) with respect to time

$$2\pi f_n = \frac{b_n \frac{da_n}{dt} - a_n \frac{db_n}{dt}}{a_n^2 + b_n^2} \tag{3.7}$$

$$v_{\phi n} = \frac{2\pi R f_n}{n} \tag{3.8}$$

Using the toroidal array alone, toroidal mode structures can be measured for a given n value that are a superposition of all resonant modes with that n value. In the standard MST RFP, the modes with $n = 1, 2, 3, 4$ are dominantly $m = 0$ since they are resonant at the reversal surface while $m = 1$ modes with $n = \pm 1, \pm 2, \pm 3, \pm 4$ do not have resonant surfaces inside the plasma. Modes $m = 1$, $n = -6, -7, \ldots, -\infty$ and sometimes $m = 1$, $n = -5$ are resonant inside the plasma reversal surface. Outside of the reversal surface, $m = 1$ modes with $n \sim 20$ are resonant, depending on $q(a)$.

It has been experimentally observed on MST during typical RFPs without OFCD for $n = 5 - \infty$ that the m=1 modes are larger than the m=0 modes. In addition, m=0 mode amplitudes decrease with increasing n. Therefore, it is acceptable to ignore the m=0, $n \geq 5$ modes. This is accomplished by measuring the modes $m = 1$, $n = -5, -6, \ldots, -32$ using the toroidal array B_θ coils, which will only resolve the m=1 modes [5]. In MST, the wall is approximately a perfect conductor with a 1 cm vacuum region between the wall and the plasma. Consequently, $\tilde{B}_r(a) = 0$ and $\tilde{J}_r(a) = 0$, which can be combined with Ampere's law to derive

$$\frac{b_\theta}{b_\phi} = \frac{mR}{na} \tag{3.9}$$

Therefore, b_θ from m=0 modes will be zero at the MST wall so m=0 modes are invisible to the toroidal array b_θ coils. This approach to toroidal array mode measurements is the reason why a working poloidal array is not a critical detriment for most MST research.

3.2 Tearing Mode Amplitudes and Velocities

The ensemble averages of the amplitudes and velocities of the modes over the course of the sawtooth cycle are presented in Fig. 3.1 for the 210 kA MST RFP with normal reversal ($F \approx -0.18$). The $m = 1$ modes grow slowly until the sawtooth crash at $t = 0$, where they increase sharply and the $m = 0$ modes suddenly increase to many times their previous amplitude due to nonlinear coupling with the $m = 1$ modes. The velocities of the $m = 1$ modes and the $m = 0$ modes have opposite signs, as the plasma rotates in the opposite toroidal direction in the core to that in the edge, which is a robust feature of the MST RFP. Measurements of the dynamo and other Ohm's law

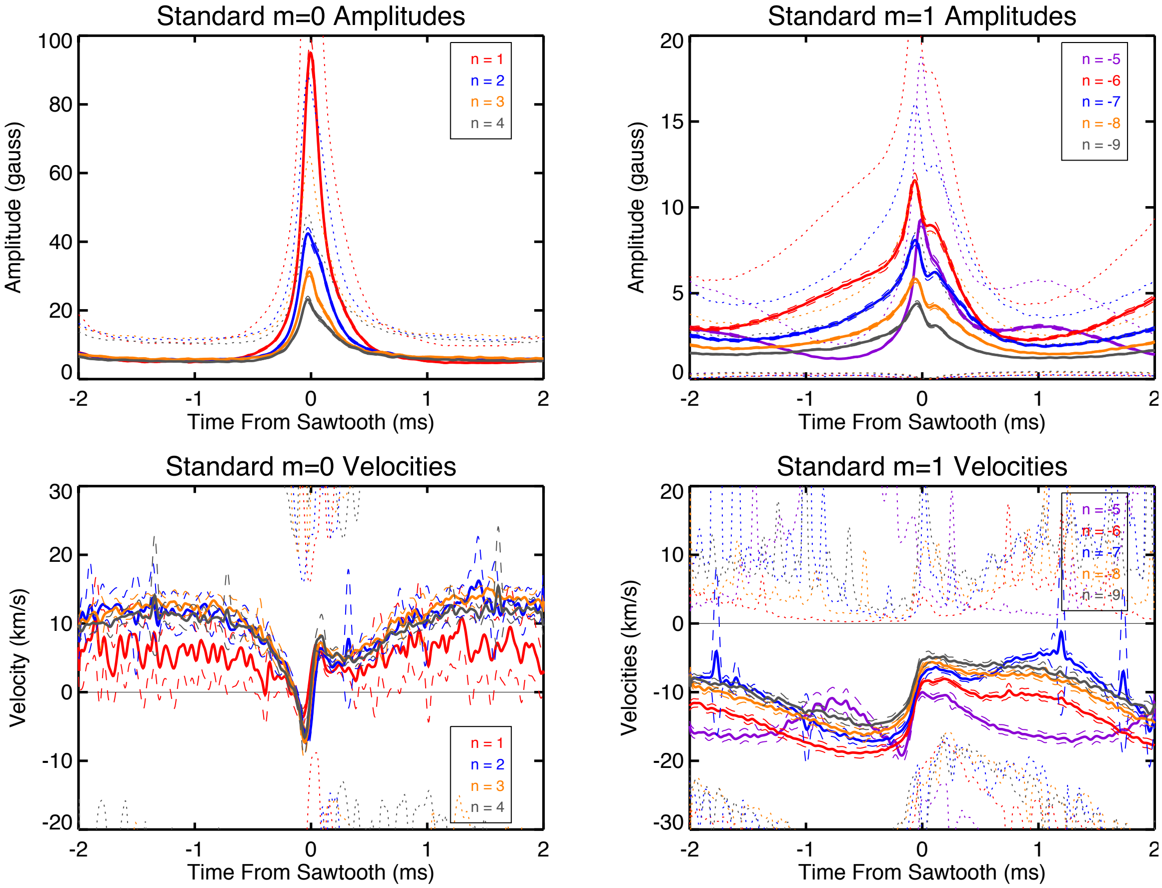

Figure 3.1: Amplitudes and velocities of tearing modes over the course of a sawtooth cycle for the standard 210 kA RFP. The dotted lines show the standard deviations, σ, while the dashed lines show $\sigma/\sqrt{N}$.

terms for this ensemble will be presented in Sec. 5.1 and Sec. 5.2.

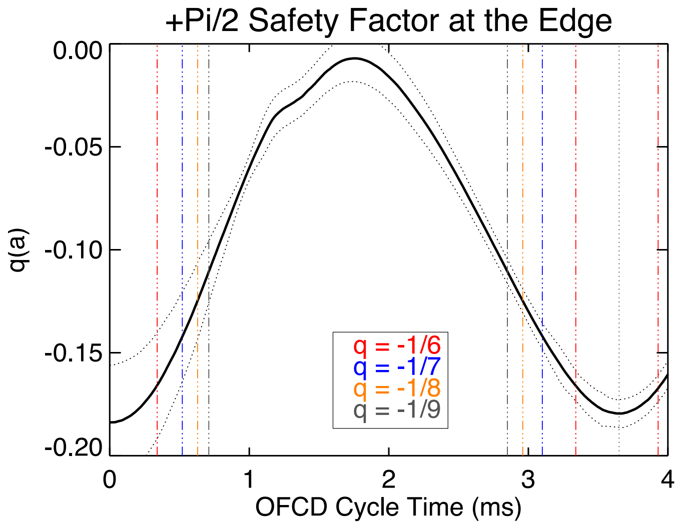

Figure 3.2: The value of q(a), the safety factor at the edge, during the 250 kA OFCD case of $\delta = +\pi/2$. The vertical lines show when the edge +n modes become resonant.

During partial OFCD experiments on MST, the oscillations of B_θ and B_ϕ result in large oscillations in the safety factor at the edge, $q(a)$, shown in Fig. 3.2. At the most negative value of $q(a)$, $m = 1$, $n \geq +6$ modes are resonant outside of the reversal surface. If the standard analysis is performed under the assumption that there is only one dominant mode for each value of n, as shown in Fig. 3.3, then the signals of each pair of m=1, $\pm n$ modes will be mixed.

This can be observed in the $m = 1$ velocity graphs because the modes resonant outside the reversal surface have the opposite toroidal velocity of the modes resonant in the core. When the amplitude of a given edge $m = 1$ mode becomes larger than the core mode with the same magnitude of n, the phase velocity given by the resulting analysis changes sign because it is actually the combination of the phase velocities of the +n and -n modes. The m=1, $|n| > 5$ amplitudes measured by the toroidal array when the +n modes are resonant are also the combined amplitude from the two

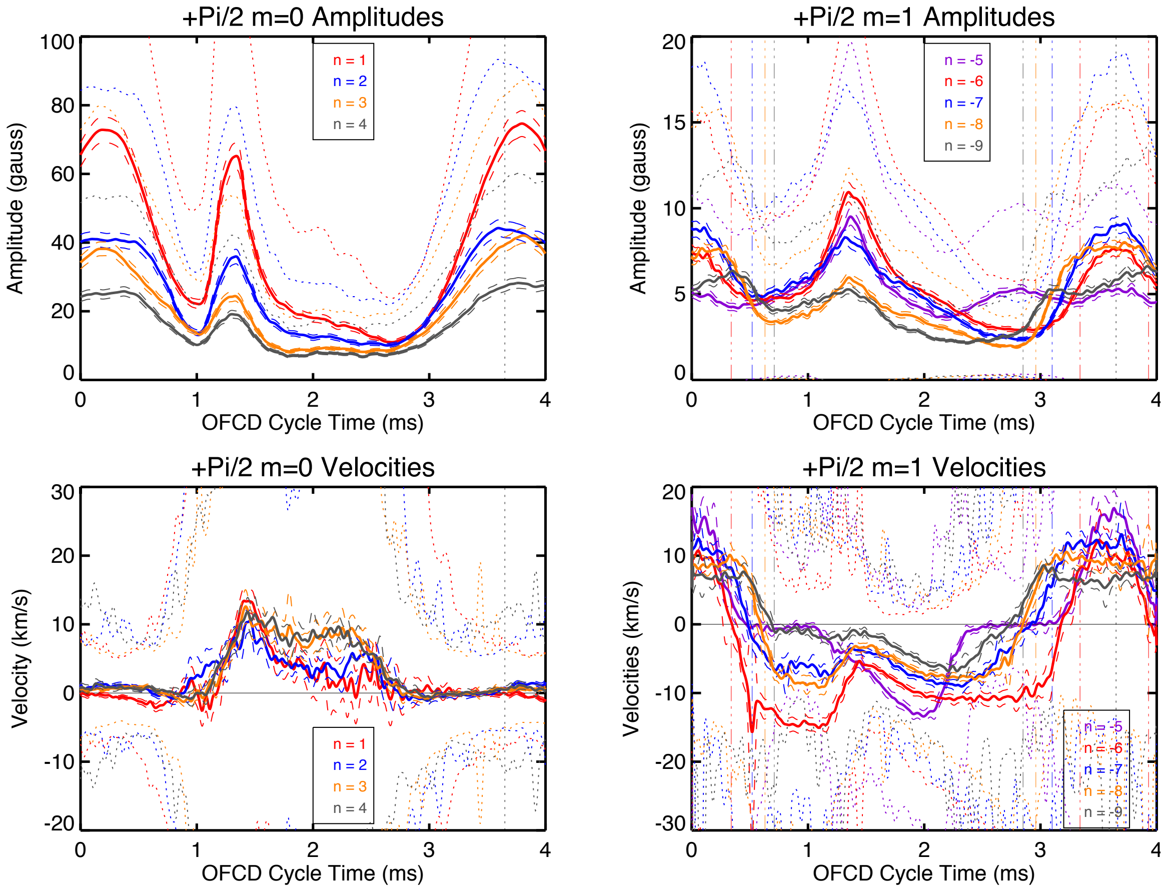

Figure 3.3: The mode amplitudes and velocities for the m=0 and m=1 tearing modes for the 250 kA OFCD case of $\delta = +\pi/2$. The m=1 mode signals shown here are a mix of +n and -n modes. The vertical lines show when the edge +n modes become resonant. The dotted lines show the standard deviations, σ, while the dashed lines show $\sigma/\sqrt{N}$.

modes with the same magnitude of n. Therefore, the toroidal array data needs to be carefully considered in order to develop a clear picture of the tearing mode activity during OFCD. For $m = 1$, $|n| > 6$ the +n and -n modes are simultaneously resonant during part of the OFCD cycle and the standard analysis of toroidal array data cannot distinguish between +n and -n.

Fortunately, the m=1, $n = +6 \ldots + \infty$ modes resonant outside of the reversal surface and the m=1, $n = -6 \ldots - \infty$ modes resonant inside the reversal surface often have phase velocities in the opposite directions. This is due to the plasma flowing in opposite toroidal directions in the core and the edge. It is not well understood why the plasma flows in opposite directions. Conceivably, it might be related to the relatively large ion gyroradii in the extreme edge of the plasma resulting in extra ion losses that oppose the radial electric field direction caused by electron transport losses, giving rise to a change in the $E_r \times B_0$ drift direction between the core and the edge.

Since the core and edge modes counter-propgate, they can be distinguished by taking the FFT of each mode $c_n e^{i\delta_n}$, where c_n and δ_n are taken from the standard toroidal array mode analysis. The positive frequencies are due to the mode with a positive phase velocity (typically +n in MST) so that mode can be extracted by zeroing the negative frequencies and taking the reverse FFT. Likewise, the negative frequencies are due to a mode with a negative phase velocity (typically -n in MST) so they can be resolved by zeroing the positive frequencies and taking the reverse FFT.

The amplitude, phase, phase velocity, and frequency of the extracted positively and negatively rotating signals can be calculated in the usual way using Eq. 3.5, Eq. 3.6, Eq. 3.7, and Eq. 3.8. The resulting amplitudes and velocities for OFCD $\delta = +\pi/2$ are shown in Fig. 3.4. As expected, the -n modes resonant in the core behave similarly during OFCD and during the standard RFP. They peak at the sawtooth crash between 1 ms and 2 ms and are similar amplitude to the standard case away from the crash. Although they slow down at the crash, they rotate the same direction throughout the OFCD cycle.

The +n modes resonant outside of the reversal surface are small like the standard RFP except when they are resonant at $\sim 3-4$ ms and $\sim 0-0.5$ ms. The colored vertical lines indicate when the resonant surfaces for the +n modes enter and leave the plasma based on the value of q(a) as shown in Fig. 3.2. The +n modes grow and

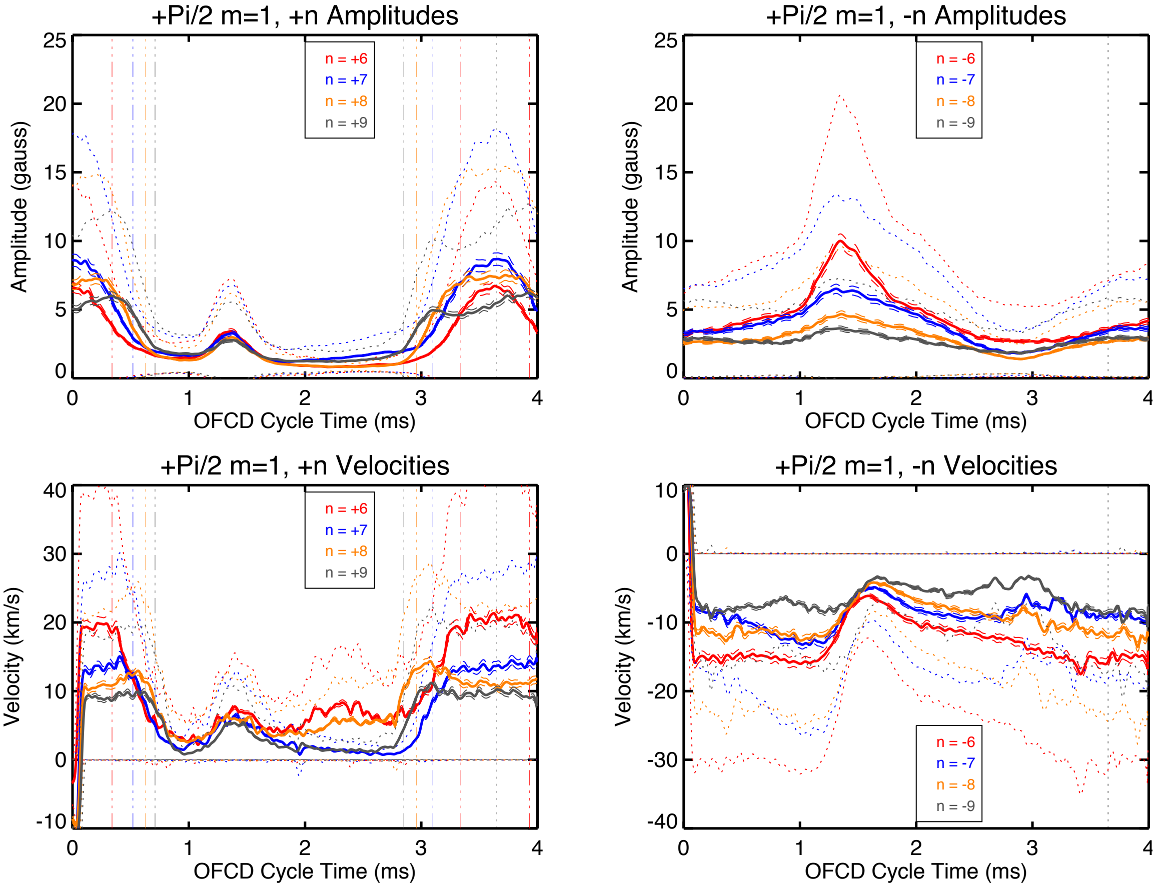

Figure 3.4: The mode amplitudes and velocities for the m=1, +n and -n tearing modes for the 250 kA OFCD case of $\delta = +\pi/2$. The vertical lines show when the edge +n modes become resonant and nonresonant. The dotted lines show the standard deviations, σ, while the dashed lines show $\sigma/\sqrt{N}$.

decay as their resonant surfaces enter and leave the plasma.

When the +n modes are resonant, they move in the same toroidal direction as the typical direction for the m=0 modes and opposite the direction of the -n modes in the core. The +n modes are resonant during the same period that the m=0 modes slow down and possibly lock (Fig. 3.3). Interestingly, the velocities of the +n modes are smaller for those resonant closer to the reversal surface and larger for those resonant closer to the edge. Together, the mode velocities present a picture of how the plasma's toroidal velocity varies with radius to the degree the frozen flux theorem is assumed to hold. These mode velocity measurements demonstrate that when the edge modes are resonant, there is a fairly constant radial gradient in plasma rotation from the core to the edge with zero velocity at the reversal surface.

The +n and -n mode amplitudes and velocities for the standard RFP are shown in Fig. 3.5 as a check on the method of separating the m=1 modes based on phase velocity. As expected, the amplitude of the +n modes is insignificant since they aren't resonant in the plasma while the +n velocities are not physically significant since the +n modes do not have substantial amplitudes. The amplitudes and velocities of the -n modes match the amplitudes and velocities before separating the modes into +n and -n (Fig. 3.1).

The mode amplitudes and velocities during the OFCD phases $\delta = +\pi/4$, 0, and $-\pi/4$ have similar behavior, although slightly less pronounced. Data for these OFCD phases can be found in Appendix D. The m=0 mode velocities significantly decrease during $\sim 3 - 4$ ms and $\sim 0 - 0.5$ ms. However, the amplitudes of the m=0 modes only increase slightly during this period. The +n modes become resonant during this period for all phases, although their amplitudes for these other phases are $\sim 30 - 50\%$ smaller than the $\delta = +\pi/2$ case as well. Amplitudes are likely smaller for other phases because the cycle averaged parallel electric field from OFCD is smaller for these other cases. It is thought that the large $E_{\|}$ field results in an edge current profile unstable to m=0 modes, which are otherwise stable in MST. In addition, the period where the combined OFCD and MST $E_{\|}$ is the same direction as the edge current shifts forward relative to the OFCD cycle time while the period where the +n modes are resonant remains centered at ~ 0 ms and ~ 3.65 ms (Ch. 6). Therefore, it is not surprising that the m=1, +n modes do not grow as large when they are resonant in other OFCD phases.

3.3 Tearing Mode Phases

The phases of the tearing modes during standard plasmas and partial OFCD experiments are fundamentally interesting. They are also important for the data analysis of fluctuations presented in the second half of this thesis since a fairly flat distribution of mode phases is required at every point in time if a probe at a single location is to sample the entire flux surface. The phase distribution of the 210 kA standard plasma ensemble is binned with respect to phase at each time point and plotted in greyscale in Fig. 3.6. The phases are not perfectly evenly distributed, but the counts do not drop to zero for any substantial phase region.

The phase distributions of some of the modes in the standard ensemble are surprisingly uneven (e.g. $n = 1, 7, 11, 12$) away from the sawtooth crash at t=0. The measured mode velocities (Fig. 3.1) indicate that all the modes are rotating but the phase measurements are more meaningful for the analysis than the velocity measurements (Sec. 4.3.2). The phase measurements are more accurate when the mode amplitudes are large, which occurs at the crash when the phases also appear to be more evenly distributed. The apparent phase locking when the mode amplitudes are small away from the crash is probably not believable due to problems with the measurement for small mode amplitudes. Even if the phase locking is believable, the mode amplitudes are small enough that mode locking isn't a major concern.

The phase distributions for the OFCD $\delta = \pi/2$ ensemble are plotted in a similar manner in Fig. 3.7. In the OFCD case, there are periods where many of the modes have strong preferential phases that correspond to when the modes are large. Compared to the standard RFP phase distribution, the OFCD $\delta = +\pi/2$ phases are much less evenly distributed. The phase distributions of the $\delta = +\pi/4$, 0, and $-\pi/4$ ensembles (see Appendix D) exhibit similar behavior to the $\delta = +\pi/2$ phase distribution shown here.

The periods $\sim 0 - 1$ ms and $\sim 3 - 4$ ms, when the m=0 modes are large and their velocities are small or zero (Fig. 3.3), are also when the m=0 modes are observed to have the strongest preferential phase. The m=0 modes appear to lock (i.e. stop rotating) with a preferential phase during this period for most of the shots. This mode locking will be problematic for the data analysis of fluctuations in subsequent chapters.

The cause of the m=0 mode locking during OFCD experiments is not completely understood. It is possible that the large amplitude of the m=0 modes during this period are locking them to the MST vacuum vessel wall. During this period, the wall might not stabilize the m=0 modes as effectively because the reversal surface is farther away from the wall.

In summary, the tearing modes behave quite differently during partial OFCD experiments on MST as compared to standard RFP experiments. This could be good for the feasibility of OFCD. In OFCD, the modes can create an EMF that opposes the current in the edge and supports it in the core during part of the OFCD cycle, which is opposite the RFP sustained by a DC (i.e. constant) inductive E_ϕ, so the modes might behave differently in order to produce the required EMF. However, the mode behavior (particularly the m=0 locking) will be problematic for the analysis of fluctuations measured by an insertable probe in this thesis.

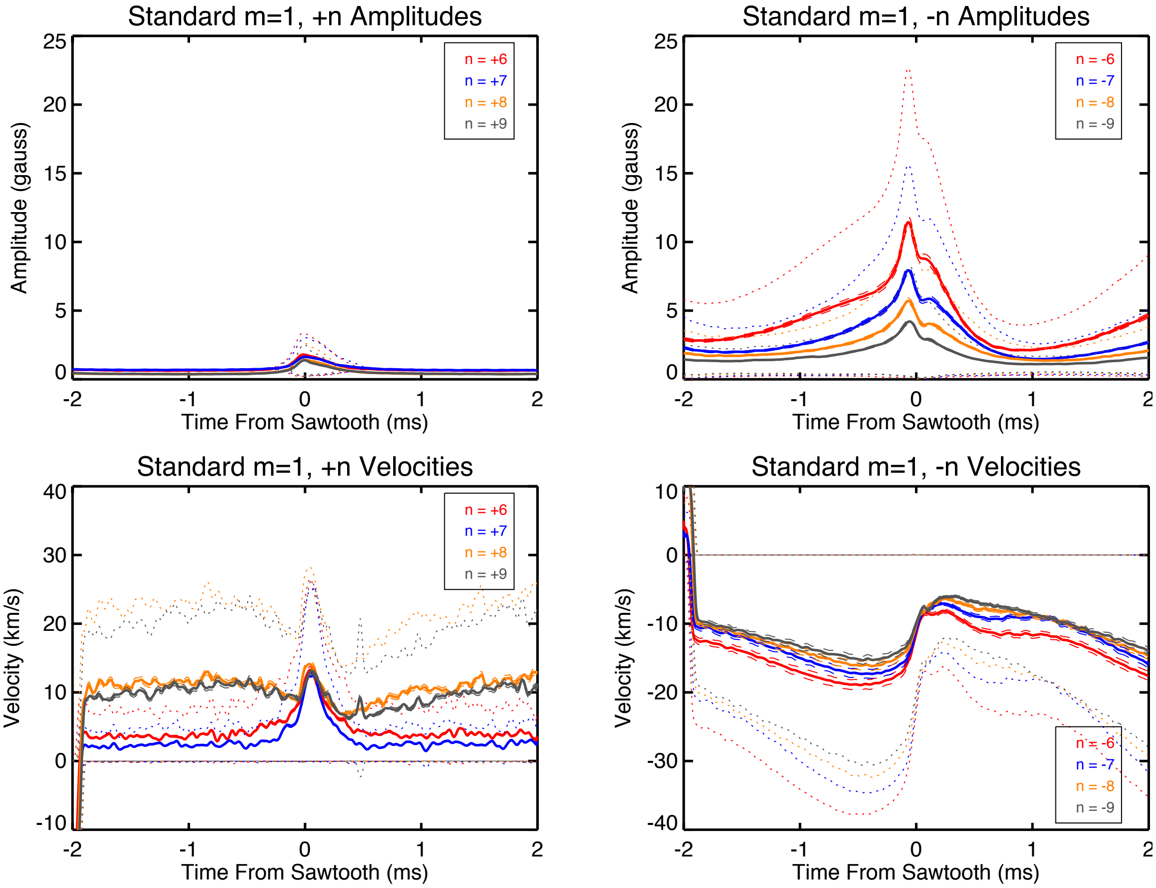

Figure 3.5: The mode amplitudes and velocities for the m=1, +n and -n tearing modes during the 210 kA RFP without OFCD. The amplitudes of the +n modes are small since they're not resonant in the plasma. Velocities are not well-defined when the corresponding amplitudes are small so the +n velocities are not physically significant. The dotted lines show the standard deviations, σ, while the dashed lines show $\sigma/\sqrt{N}$.

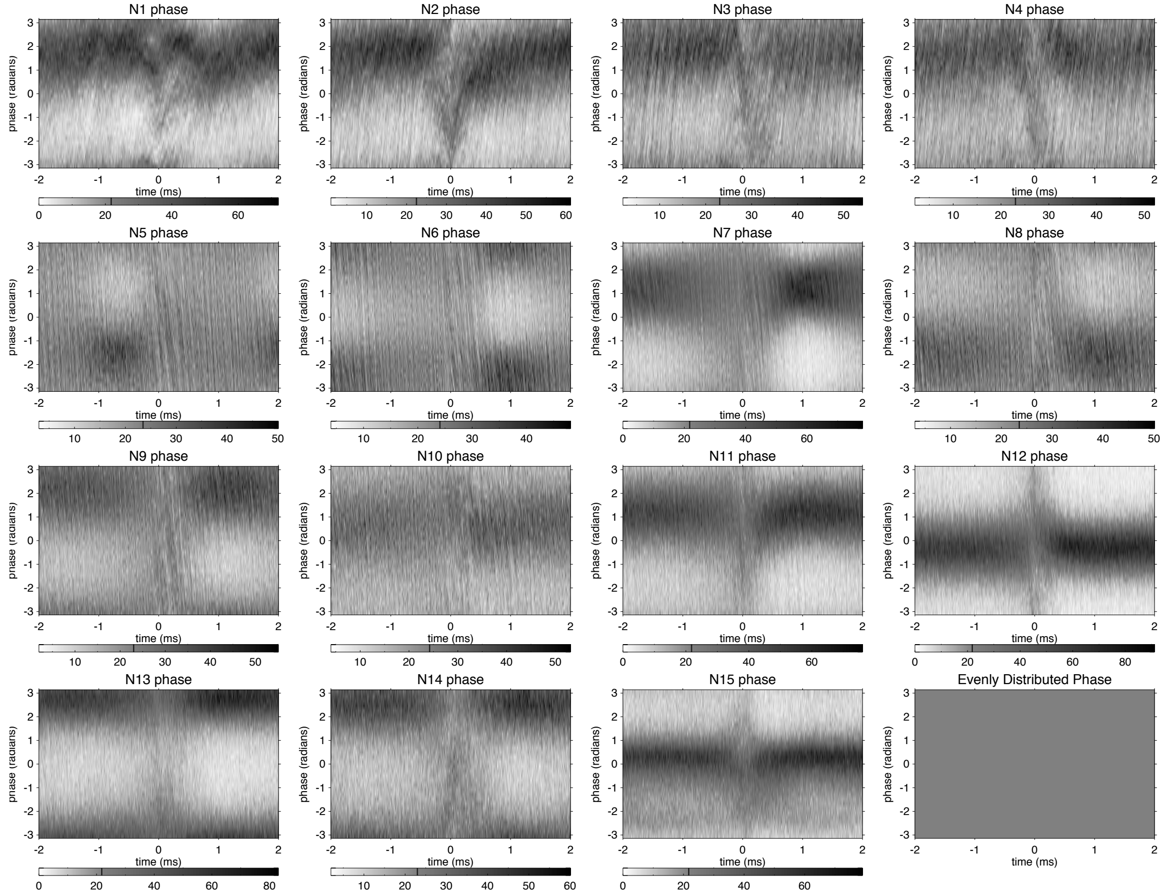

Figure 3.6: Phase distribution of the tearing modes for the standard RFP ensemble. Note that the scale of each graph is shown in the bar below each graph and is adjusted according to the data so the range of each bar is a good indicator of the flatness of each phase distribution. The line through the bar indicates the color corresponding to the average number of events with that phase at each time point. The bottom right graph is the color of an even phase distribution at every time point.

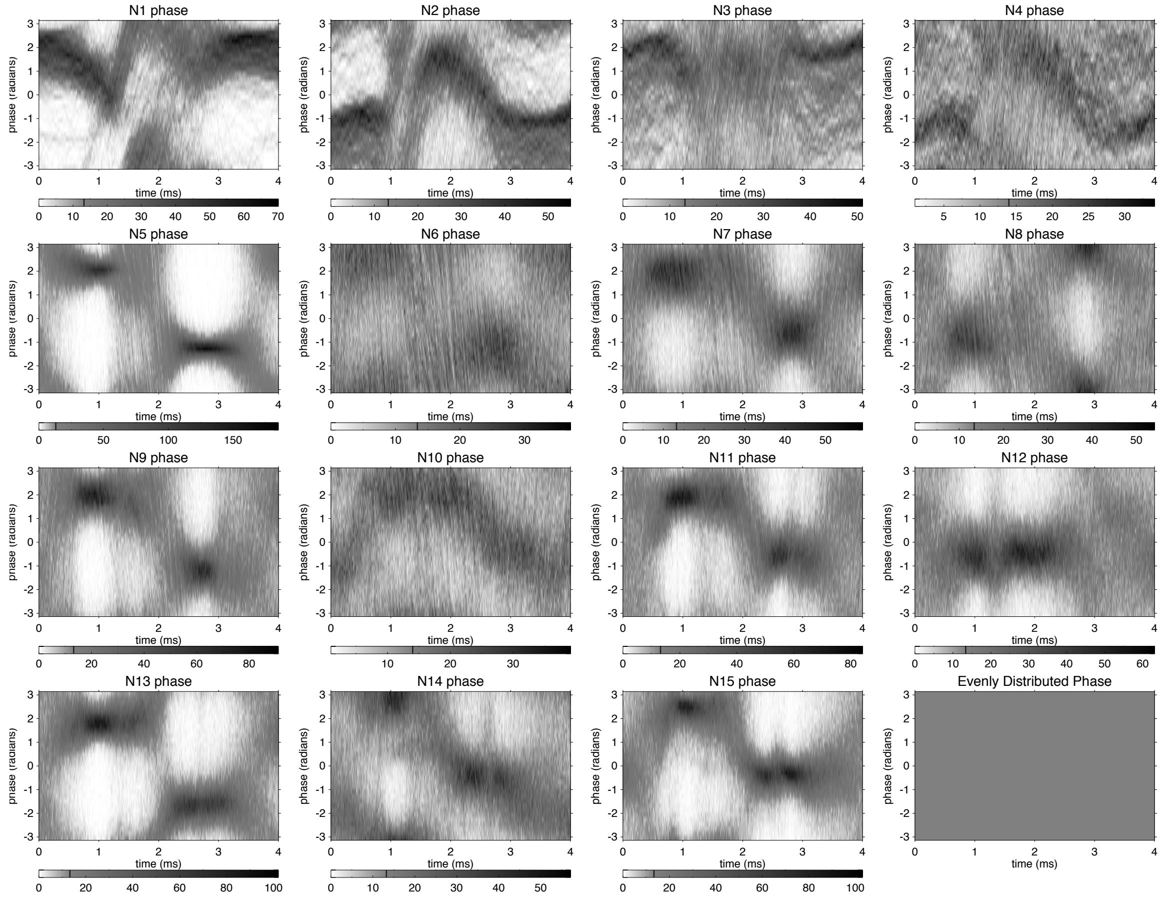

Figure 3.7: Phase distribution of the tearing modes for the OFCD $\delta = +\pi/2$ ensemble. Note that the scale of each graph is shown in the bar below each graph and is adjusted according to the data so the range of each bar is a good indicator of the flatness of each phase distribution. The line through the bar indicates the color corresponding to the average number of events with that phase at each time point. The bottom right graph is the color of an even phase distribution at every time point.

Chapter 4

Probes

Three insertable probes are used for the experiments in this thesis; the Dynamo Probe, the Helicity Probe, and the Electrostatic Probe. The Dynamo Probe uses passive secondary emission capacitive probes to measure plasma potential and electric field as well as Mirnov coils to measure magnetic field and plasma current density. All of the edge dynamo measurements in this thesis are conducted with the Dynamo Probe.

The Helicity Probe uses a triple Langmuir probe (TLP) to measure plasma potential and electron temperature and Mirnov coils to measure magnetic field, while the Electrostatic Probe uses floating Langmuir probes to measure electric field and Mirnov coils to measure magnetic field. The Helicity Probe and Electrostatic Probe are used in this thesis for benchmarking secondary-emission capacitive probe measurements of the plasma potential and electric field, which have never before been measured on MST. The Helicity Probe is also used to measure the electron temperature, T_e, the electron density, n_e, and as a secondary measurement of the helicity flux $\dot{\mathbf{K}}$.

In this chapter, I will first introduce the Mirnov coil, triple Langmuir probe, and secondary emission capacitive probe measurement techniques and the probe designs. Then I will review probe data analysis techniques used on MST. Finally, I will compare measurements of the three probes in standard plasmas.

4.1 Measurement Techniques

4.1.1 Mirnov Coils

The first measurement technique is that of Mirnov coils, also known as magnetic pickup coils or Bdot coils. The coils consist of boron nitride bobbins designed to be wound in three directions with HML 36 wire, creating three Mirnov coils that measure all three components of the magnetic field at a specific location. The wires are protected with a paste made from Sauereisen Cement and boron nitride powder. The bobbin and paste are then covered with a thin layer of silver paint to prevent electrostatic pickup by the coils.

Mirnov coils measure a voltage $V = -\frac{\partial \phi}{\partial t} = -N\mathbf{A} \cdot \frac{\partial \mathbf{B}}{\partial t}$, where N is the number of turns in the coil and A is the area of a single turn. This voltage is sent to an analogue integrator circuit before being sent to a digitizer, which produces a more accurate integrated signal than digitizing the Mirnov coil voltage and then integrating numerically. Also, the fluctuations we are interested in are all less than a few hundred kHz, which is well within the digitizers' capabilities.

It is important to have radial coils centered in the probe body since a probe inserted in the plasma causes the plasma current to divert around the probe body. This perturbs the radial magnetic field inside the probe. However, the perturbation averages to zero when the radial magnetic field coil is centered in the probe body [42].

4.1.2 Langmuir Probes

A Langmiur probe is essentially a piece of metal that is connected to ground via an impedance and inserted into a plasma. By measuring the current to the probe as a function of applied voltage, called the probe characteristic, it can be used to measure plasma potential, electron temperature, electron density, and many other quantities of interest. Many of these measurements require assumptions about the character of the plasma and about how the probe is or isn't perturbing the plasma, which can lead to systematic errors in the measurements. In this work Langmuir probes are used to measure floating potential, plasma potential, electric field, and electron temperature.

Plasma potential, the voltage at a particular point in the plasma, is difficult to measure accurately with probes since the presence of a probe creates a sheath around the probe that alters the voltage at the probe relative to the surrounding plasma. A crude model of the sheath is to imagine a plasma surrounding the probe where the electron and ion populations have the same Maxwellian energy distribution. Since $V_e \gg V_i$, the probe will absorb many more electrons than ions, charging the probe negatively relative to the surrounding plasma. This creates an electric field pointing towards the probe in the sheath region, which repels the less energetic electrons. The probe voltage decreases until its charge repels enough electrons so that the number of electrons capable of overcoming the electric field per second equals the number of ions incident on the probe per second. The probe's altered voltage is called the floating potential. This process is visualized in Fig. 4.1.

Multiple methods have been devised to overcome the difficulty of measuring the plasma potential. One method is to apply a voltage to a Langmuir probe, sweep the voltage from a negative value to a positive value, and measure the current from the Langmuir probe as a function of applied voltage. The plasma potential can be determined from this graph of I(V), known as the probe characteristic. Unfortunately one measurement of the characteristic is required to measure the plasma potential once, and the voltage cannot easily be swept fast enough to measure the entire probe characteristic before plasma relaxation dynamics alter it.

Another common method for measuring plasma potential is to use three Lang-

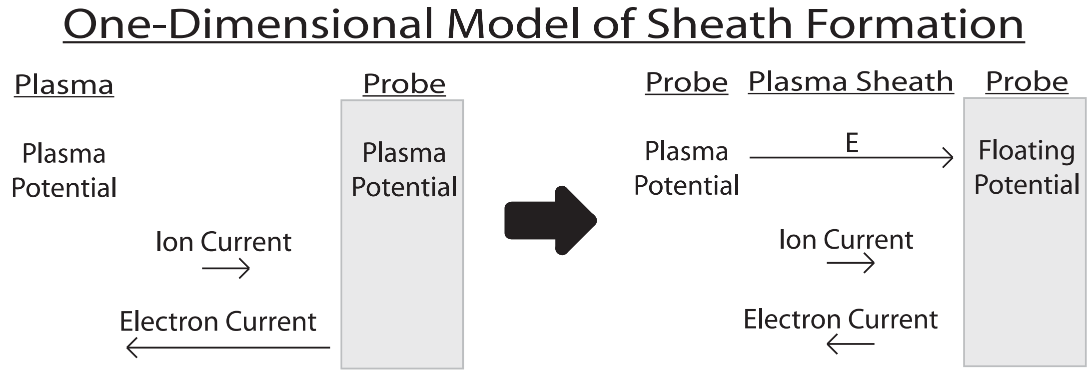

Figure 4.1: One dimensional cartoon of the formation of the sheath region around a probe. On the left is the plasma before the sheath has formed. On the right the charge of the probe is in equilibrium since the electron and ion currents to the probe cancel. Note that the electron current direction is opposite the direction of the electron flow.

muir probes together. This is known as a triple Langmuir probe (TLP). One probe is isolated from ground to measure the floating potential. A bias voltage several times larger than the plasma electron temperature is applied between the other two probes, which causes the negative probe to draw ion saturation current, and the current between the two biased probes is measured. The three probes provide three unique points of the probe characteristic, allowing the entire characteristic to be fit assuming the electron temperature is Maxwellian. The plasma electron temperature is calculated based on the current between the biased probes, which is related to the slope of the probe characteristic. The floating potential and the electron temperature are used to calculate the plasma potential

$$V_p = V_f + \alpha * T_e \tag{4.1}$$

$$\alpha = ln\left(\sqrt{\frac{2\pi m_e}{m_i}}\right) - \frac{1}{2} \tag{4.2}$$

where α is a constant that depends on the probes geometry with respect to plasma properties such as magnetic field direction and partical gyroradii [43]. This calculation assumes that $\rho_i \gg a \gg \rho_e$, where a is the size of the Langmuir probe tip and ρ_i and ρ_e are the gyroradii. For the experiments in this thesis, $\rho_e \approx 10^{-4}m$ and $\rho_i \approx 10^{-2}m$ in the edge of the plasma while the Helicity Probe Langmuir probe tips are $3.175 \times 10^{-3}m$ in diameter. It also assumes that the electron temperature distribution is Maxwellian. Using the calculation with non-Maxwellian electrons will introduce a systematic error into the plasma temperature measurement.

The electron temperature in the edge of MST is non-Maxwellian due to a significant fast electron population in the tail of the temperature distribution [44]. However, this population is present only on one side of the Maxwellian. The vast majority of the fast electrons travel parallel to $\mathbf{B_0}$ but not antiparallel to it so we can physically block the fast electrons with a boron nitride shield while still sampling half of the electron population. Matthew Miller modelled how fast electrons and a boron nitride shield affect TLP measurements. He determined that fast electrons have a significant impact on TLP measurements only without the boron nitride shield and that the shield does not significantly affect TLP measurements [45].

4.1.3 Secondary Emission Capacitive Probes

The secondary emission capacitive probe is a combination of two techniques, the emitting probe and the capacitive probe. It is designed to measure the AC plasma potential accurately in sufficiently hot plasmas. The idea of an emitting probe is that the probe will emit enough electrons to balance the electron current to the probe, preventing the formation of a plasma sheath around it. The most common method of creating a sufficient electron emission current from a probe is to heat it. For example, a probe could be made of a tungsten wire with a current running through it to produce heat leading to thermal emission of electrons. The method employed in this thesis is to rely on sufficiently hot electrons from the plasma to produce secondary electron emission from the probe surface.

4.1.3.1 Secondary Electron Emission

Secondary electron emission is when primary electrons (electrons from the plasma, in this case) collide with a solid and electrons are emitted as a result. The emitted electrons are a combination of primary electrons that have scattered elastically or inelastically off of the solid and the true secondary electrons from the solid, which are emitted because they have absorbed energy from the primary electrons greater than the work function of the solid. The secondary electron emission (SEE) current yield, $\sigma(E_p)$, is defined as the ratio of secondary electrons to primary electrons, where E_p is the primary electron energy. The SEE, $\sigma(E_p)$, includes both the scattered primaries and the true secondary electons in the numerator. It is a function of the energy of the primary electrons and the physical properties of the solid. The dependence on E_p is similar in character for all solids [46].

In order to prevent a plasma sheath from forming we need hot primary electrons from the plasma and a material with high secondary electron emission. Boron nitride is a suitable candidate since it has $\sigma > 1$ for $E_p > 35eV$ [47]. It is also the material of choice for constructing probes on MST since it works well in vacuum and handles thermal shocks extremely well. It is not a suitable material for a Langmuir probe since it is an insulator but it works well as the dielectric in a capacitive probe.

An approximate solution for the floating potential of a material with substantial secondary electron emission in a plasma with a thermal electron population is [48]

$$V_{float} \simeq V_{plasma} - kT_e ln\left(\frac{1-\sigma(T_e)}{\sqrt{2\pi m_e/m_i}}\right) \tag{4.3}$$

where $\sigma(T_e)$ is the SEE total yield integrated over the electron population. This approximate solution breaks down when $\sigma(T_e)$ approaches unity (i.e. when $V_{float} \approx V_{plasma}$). Once the plasma is hot enough for $\sigma(T_e) = 1$, the boron nitride will be at the plasma potential since the net flow of electrons to the probe will be zero. When $\sigma(T_e)$ would become greater than one most of the true secondary electrons are reabsorbed by the boron nitride since true secondary electrons only have a few eV of energy [46] and are unable to escape the potential well. This serves to lock $\sigma(T_e)$ at one since the reabsorbed secondary electrons are counted again as primary electrons in $\sigma(T_e)$. Consequently, this keeps the potential of the boron nitride at the plasma potential when the primary electrons from the plasma produce excess secondary electrons.

The SEE, $\sigma(E_p)$, was measured [47] for grade HP boron nitride from Saint Gobain Corp., which is the type of boron nitride used currently for probes on MST. Fitting the measurements to a power law, it was found that $\sigma(E_p) = (E_p/E_1)^\alpha$ where $E_1 = 35$ eV and $\alpha = 0.5$. Boron nitride SEE data from Bugeat and Koppel was also fit to the same power law, giving a similar result, $E_1 = 30$ eV and $\alpha = 0.57$. Integrating this SEE current yield over a thermal electron distribution gives

$$< \sigma(T_e) > = \left(\frac{< E_p >}{2E_1}\right)^\alpha \Gamma(2+\alpha) \tag{4.4}$$

where $< E_p > = 2kT_e$ is the average primary electron energy. Using Eq. 4.3 and Eq. 4.4, we can plot $V_{float}(T_e)$ (Fig. 4.2) and see that boron nitride should be at the plasma potential for plasmas with $T_e > 18$ eV. The floating potential should not become higher than the plasma potential because true secondary electrons are low energy and would be reabsorbed if $V_{float} > V_{plasma}$.

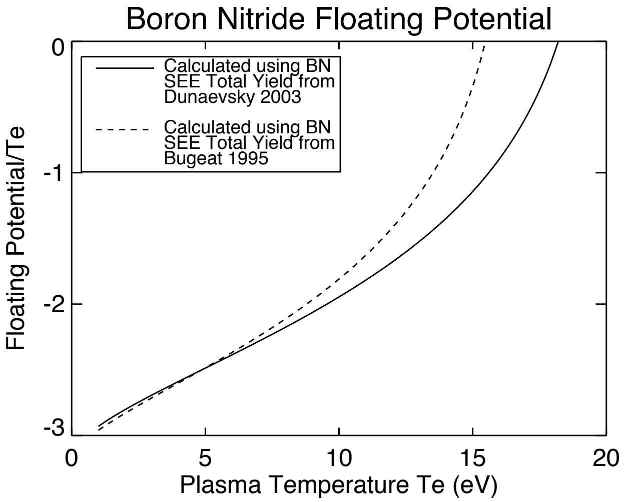

Figure 4.2: Floating potential of boron nitride relative to the plasma potential for a thermal electron distribution.

4.1.3.2 Capacitive Probes

The capacitive probe was invented by Schmidt and Kerst [49, 50]. It is composed of a conductor that capacitively couples to the plasma and is separated from the plasma by a dielectric. The capacitor connects to ground via a capacitive divider circuit (Fig. 4.3) and the voltage across the divider is sent via an op amp to a digitizer to be recorded.

The gain of this circuit is complex and a function of frequency $G(\omega)$. Above a few hundred Hz with the circuit values as specified $G(\omega)$ is real and approximately constant. When used for studying fluctuations with frequencies greater than 1 kHz, the probe signal can either be highpass filtered or divided by the complex gain in frequency space to account for the frequency dependence of the complex gain. The circuit gain is also affected by the gain of the operational amplifier circuit, which is flat at low frequencies and rolls off at high frequencies with a 3 dB point of 100 kHz.

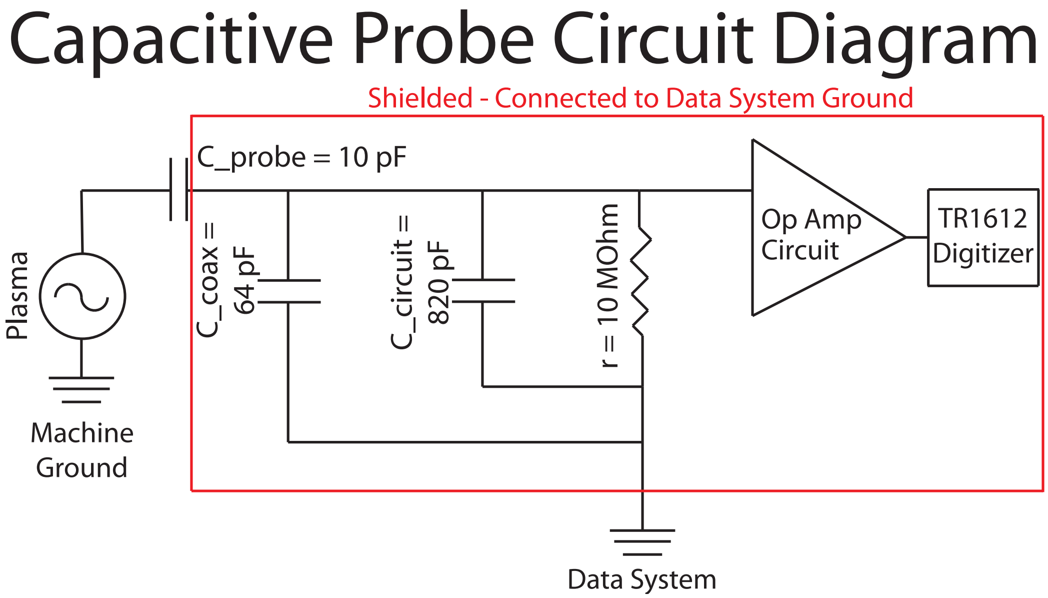

Figure 4.3: Capacitive probe circuit drawing.

For the experiments in this thesis, the capacitive probe gains were measured by surrounding the probe with liquid mercury and applying a sinusoidal voltage to the liquid. Electrically, the liquid mercury surrounds the probe like a plasma in which no sheath has formed around the probe. A lock-in amplifier was used to measure $G(\omega)$ by comparing the phase and amplitude of the capacitive probe signal and the voltage of the mercury. An automated Labview program used the lock-in to scan hundreds of frequency points from 10 Hz to 100 kHz. An example of the calibration data is shown in Fig. 4.4. The theoretical capacitive probe gains can be found in Appendix B.

The capacitors were calibrated one time with a new set of shields. After calibration this set of shields was not used in plasma in order to avoid introducing trace amounts of mercury into MST. The capacitive probes are also calibrated any time the boron nitride shields are going to be replaced since only the shields come in contact with the mercury. The shields are replaced after approximately every third run day, since it was observed that after four run days the capacitor gains had increased by

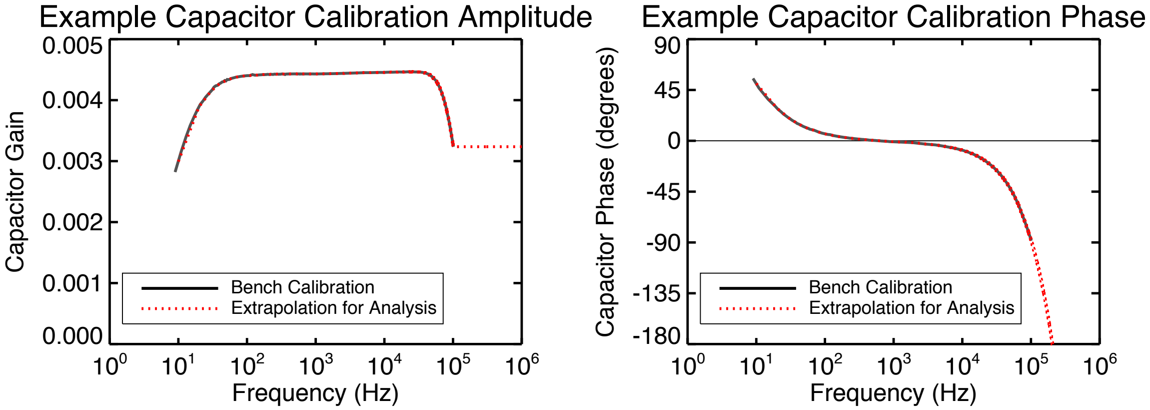

Figure 4.4: Example of a complex, frequency-dependent capacitor calibration. The phase shift above 1 kHz is due to a constant delay of $\sim 2.3\mu s$ in the capacitive probe signal. The calibration is extrapolated above 100 kHz (shown in red) by using the 100 kHz calibration amplitude for the frequency gain and the average delay from the 90-100 kHz calibration frequencies to calculate the phase delay.

slightly less than 10% from the calibration using new shields. A change in gain of $\sim$ 5% should be acceptable for these measurements.

During data analysis, the capacitor signals are divided by $G^*(\omega)$ in frequency space to account for the complex, frequency-dependent gain of the capacitors using the following method. First, a Hamming window (chosen to minimize frequency sidebands) with a 100 ms width is applied to the capacitive probe signals before performing the FFT. The Hamming window is approximately centered on the 30 ms MST current flat top. An FFT is also applied to the output signal of the capacitor probe on the bench for a cosine wave with an amplitude of 1 corresponding to each frequency of the capacitive probe frequency axis (i.e. 10 Hz, 20 Hz, 30 Hz,...,1 MHz since a 100 ms window digitized at 2 MHz is used). Once in frequency space, each point on the frequency axis is divided by the complex conjugate of the corresponding cosine wave. Then the reverse FFT is performed on the signal and it is divided by the Hamming window to recover the original amplitude.

The frequency-dependent calibration method was checked with artificial data. It was also checked by using a complex, freqency dependent gain to apply a uniform time delay to a probe signal in frequency space and then using the reverse FFT to return it to time space. The resulting signal was identical to shifting the signal in time space without use of the FFT. The time delay for the integrators used with the Bdot coils is accounted for in this manner. The Bdot integrators have a $\sim 0.67 \mu s$ time delay since to a good approximation each one is an ideal integrator followed by a single pole filter with a pole frequency of 240 kHz.

In MST, standard plasmas with a plasma current of 200 kA have an electron temperature of around 30 eV at a depth of 5 cm into the edge ($r/a = 0.9$), according to TLP measurements. Therefore, the boron nitride shield of the capacitive probe should produce enough secondary electron emission to prevent formation of the plasma sheath for standard plasmas in these conditions. However, it is well-known that the edge electron energy distribution is not Maxwellian. In particular, there is a fast electron component in the tail of the temperature distribution that will stimulate extra emission of fast electrons and decreasing the required electron temperature to prevent sheath formation so that a capacitive probe can measure the plasma potential directly. Therefore, it is thought that fast electrons will not significantly degrade the measurements of plasma potential or electric field made by the Dynamo Probe. All of the measurements in this thesis will have had hot enough plasmas that capacitive probes would measure the plasma potential since all measurements were of plasmas with plasma currents greater than 200 kA.

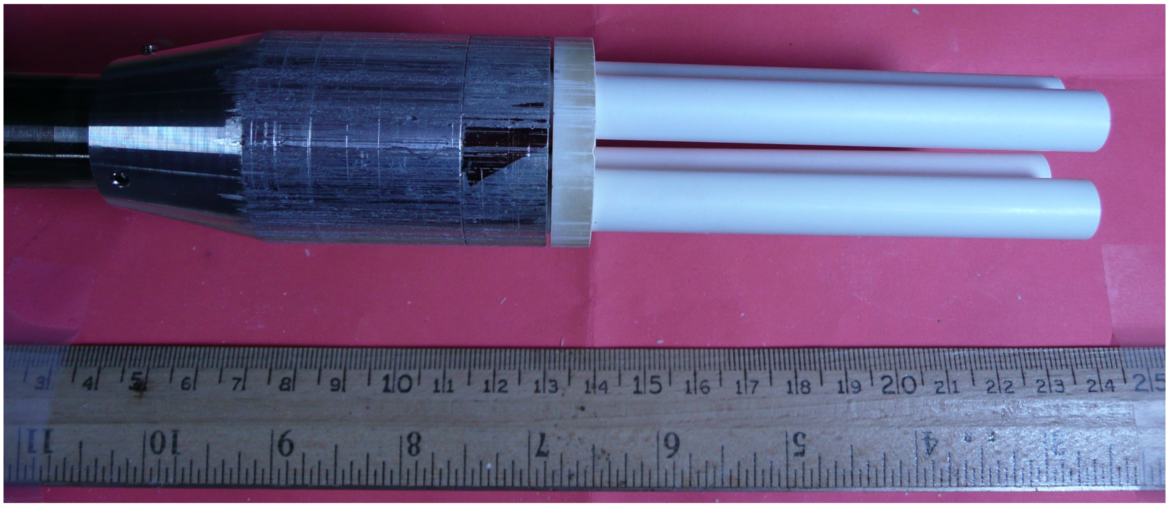

Figure 4.5: Photograph of the Dynamo Probe. Each stalk contains a capacitive probe and a Bdot triplet.

4.2 Probe Designs

4.2.1 Dynamo Probe

The Dynamo Probe, photographed in Fig. 4.5, is capable of measuring the plasma voltage fluctuations, electric field fluctuations, magnetic field, and current density at a single location in the plasma. It accomplishes this with four stalks, each of which contains a capacitive probe and a Bdot triplet, as shown in Fig. 4.6. The center of all four measurements is in between the stalks and equidistant from all eight measurment locations. The average of the magnetic field measurements is assumed to be the magnetic field at the central point. The same is true for the voltage measurements. The electric field fluctuations and current density are calculated using the spatial derivatives of the measured voltage fluctuations and magnetic fields. To the author's knowledge, this is the first time capacitive probes have been used to measure electric field fluctuations. The combination of these measurements allows the simultaneous local measurement of many fluctuations of interest for the study of

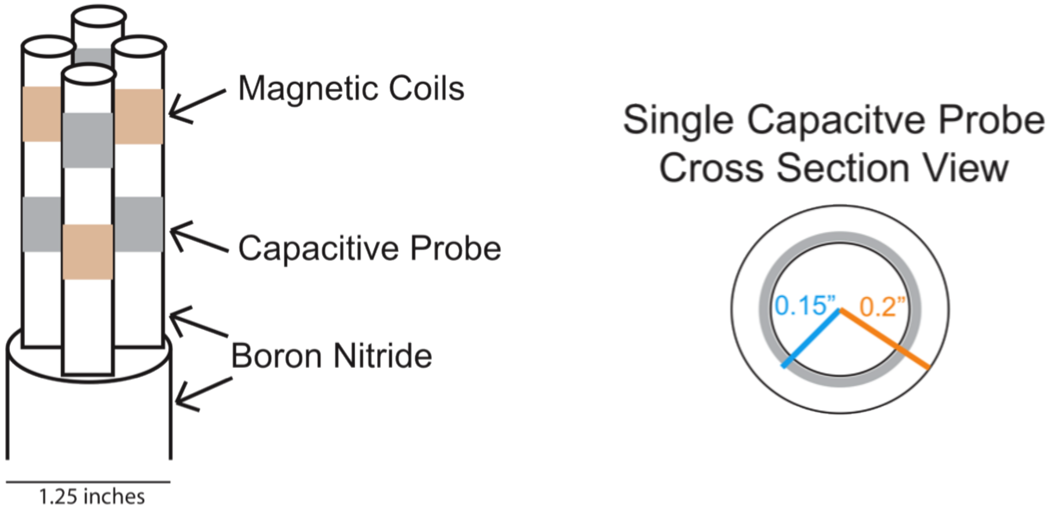

Figure 4.6: (left) Cartoon of the Dynamo Probe Bdot coil and capacitor locations. The top four measurements are centered 1.5 cm from the end of each stalk. The second set is centered 2 cm below the top set. (right) Cross section view of a capacitive probe in one of the stalks of the Dynamo Probe. The grey circle shows the capacitor electrode surrounded by the boron nitride dielectric shield.

magnetic relaxation.

In MST, probe outer boron nitride shields show substantially more ablation and wear on the side on which the fast electrons are incident. During experiments on MST, the Dynamo Probe is rotated 90 degrees every $\sim$ 20 shots in order to evenly distribute this wear between the four stalks of the probe and extend the life of the four boron nitride shields. It is also good to distribute this wear because the gains of the capacitor measurements increase as the thickness of the boron nitride shields wear away.

4.2.2 Helicity Probe

The Helicity Probe contains a Bdot triplet as well as a triple Langmuir probe (TLP). The Langmuir probes are molybdenum with a boron nitride shield on one side to block half of the electron and ion parallel temperature distribution, including the

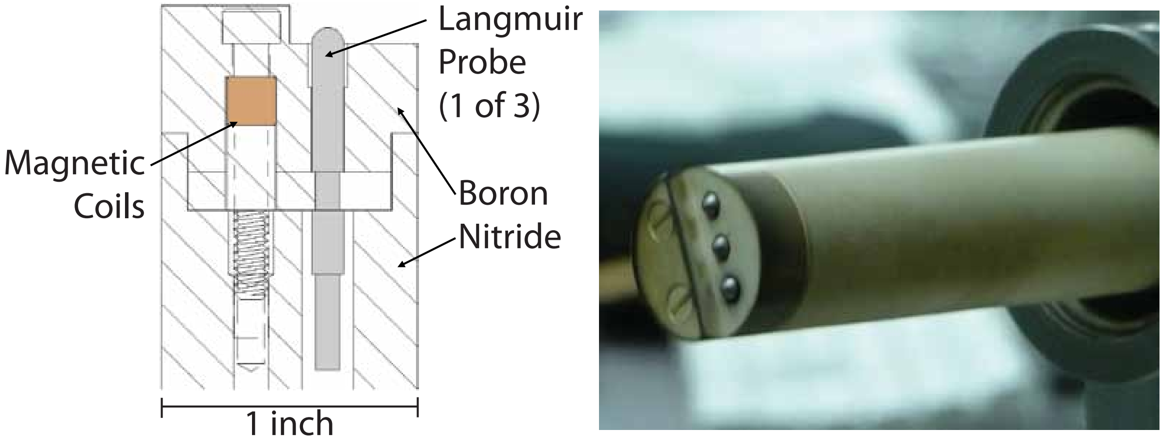

Figure 4.7: The Helicity Probe contains a triple Langmuir probe, which is shielded from the plasma in one direction to block fast electrons, and a magnetic coil triplet.

fast electrons. This probe is called the Helicity Probe because it is designed to measure the magnetic helicity flux, $2 < \tilde{V}_{plasma}\tilde{B}_r >$. It should be noted that the Bdot triplet is slightly off-center in this probe, which will produce a slight low-frequency systematic error in the Br measurement proportional to the plasma current, as explained in Sec. 4.1.

Measurements of the plasma potential by the Helicity Probe and the Dynamo Probe produce similar results in the 210 kA MST RFP. For example, the two probes measure similar shapes and amplitudes for the negative spike in plasma potential at the sawtooth crash, although the spike is slightly larger for the capacitive probe. Both probes were used to measure the helicity flux, $2 < \tilde{V}_p\tilde{B}_r >$, and they both gave the same result as previous TLP measurements on MST [13]. This increases our confidence in both methods of measuring the plasma potential.

4.2.3 Electrostatic Probe

The Electostatic Probe, shown in Fig. 4.8, contains six Bdot triplets and two sets of four Langmuir probes. Each set of Langmuir probes is arranged in a square. One is

Figure 4.8: Photograph of the Electrostatic Probe. Four electrode in a square measure Er and either Ep or Et depending on probe orientation. A magnetic coil triplet is inside the probe just to the left of the electrodes in this picture.

located at the end of the probe and the other is located on its side. In this thesis, the four Langmuir probes on the side where set up as floating probes to measure electric field fluctuations. E_θ and E_r are measured simultaneously in one orientation and the probe is rotated 90 degrees to measure E_ϕ and E_r. Both orientations are chosen such that the probe body shields these Langmuir probes from the fast electrons.

Using the difference in floating potentials instead of plasma potentials to measure the electric field in the plasma can introduce a systematic error in the measurement since the true value of the electric field is $E = -\partial V_{plasma}/\partial \mathbf{x}$. However, there are several factors which are likely to make this error small. First, TLP measurements suggest that $\nabla T_e \ll \nabla V_p$ in MST. Using this assumption and (4.1) to calculate the true electric field gives:

$$E = V_{p2} - V_{p1} = V_{f2} - V_{f1} + \alpha * (T_{e2} - T_{e1}) \cong V_{f2} - V_{f1} \tag{4.5}$$

Also, when measuring fluctuations in plasma potential or electric field, using the floating potential measured by single Langmuir probes should be fairly accurate if $\widetilde{T_e} \ll \widetilde{V_f}$, which is a fairly good assumption based on TLP measurements in these plasmas. Although when measuring $\widetilde{V_p}$ or $\tilde{\mathbf{E}}$ it is most accurate to use TLP's or secondary emission capacitive probes, using floating Langmuir probe measurements is thought to be accurate enough when either $\nabla T_e \ll \nabla V_p$ or $\widetilde{T_e} \ll \widetilde{V_f}$.

Separate measurements of the dynamo term, $< \tilde{\mathbf{E}} \cdot \tilde{\mathbf{B}} > /B_0$, in the 210 kA MST RFP with the Dynamo Probe and the Electrostatic Probe both produce similar results to previous measurements on MST where the electric field fluctuations were measured using pairs of TLPs [12]. Demonstrating that this dynamo term can be measured using the electric field fluctuations from pairs of capacitive probes, Langmuir probes, or triple Langmuir probes increases our confidence in the individual measurement techniques and in the result.

4.3 Data Analysis Technique

This thesis is primarily concerned with measurements of the average spatial quantities $\bar{X}$ and correlations of spatial fluctuations $\tilde{X} = X - \bar{X}$ on a flux surface in MST, where X represents a single probe measurement and $\bar{X}$ represents the instantaneous flux surface average of X. In theory, many probes spaced toroidally and poloidally around MST and all inserted to the same depth could measure the averages and fluctuations. In practice, this is impossible due to limited port hole access to MST and because many probes would substantially perturb the plasma and degrade plasma quality to the point where it would be impossible to make an RFP.

4.3.1 Random Phase Approximation

Intead of using many probes, we can measure flux surface averages $< X >$ and fluctuations $\tilde{X} = X- < X >$ using a single probe, many similar plasmas, and the random phase approximation. MST plasmas generally rotate toroidally so one probe at a single port hole location is actually scanning the plasma flux surface as it moves past. If we make many otherwise identical plasmas and the location of the mode structure in the plasma relative to the probe at a particular shot time is random from shot to shot, then the probe samples many points on the flux surface at every time point. In the case where the probe ensemble of shots samples the flux surface evenly and the shots are identical, an ensemble of shots with a probe measurement at a single location is equivalent to a single shot with many probes spaced toroidally around MST.

The data analysis method used to measure fluctuations in the MST RFP relies on three assumptions. The validity and accuracy of the method depends on how well these assumptions hold. First, it assumes that all the events in the ensemble are identical. This is approximately true since only shots that have similar density and plasma current are included in the ensemble. In addition, the probe data can also be highpass filtered to decrease the difference between $\bar{X}$ and $< X >$ caused by shot to shot variation. This removes low-frequency differences between the events in the ensemble.

Highpass filtering is valid since the toroidal plasma velocity in standard plasmas is large enough that spatial variations in flux surface quantities will have frequencies greater than 1 kHz in the probe measurements (assuming the plasma is not locked). The averages and standard deviations of the mode frequencies for the standard 210 kA ensemble (Eq. 3.7) are shown in Fig. 4.9. In this case, the mode frequencies are generally large enough that a highpass filter with a 1 kHz cutoff frequency will not remove the spatial variation of the signal over the flux surface from the measurements but will remove the low frequency and DC shot to shot variation in $\bar{X}$. Variations in the sawtooth shape cannot be removed this way since the frequency range of the

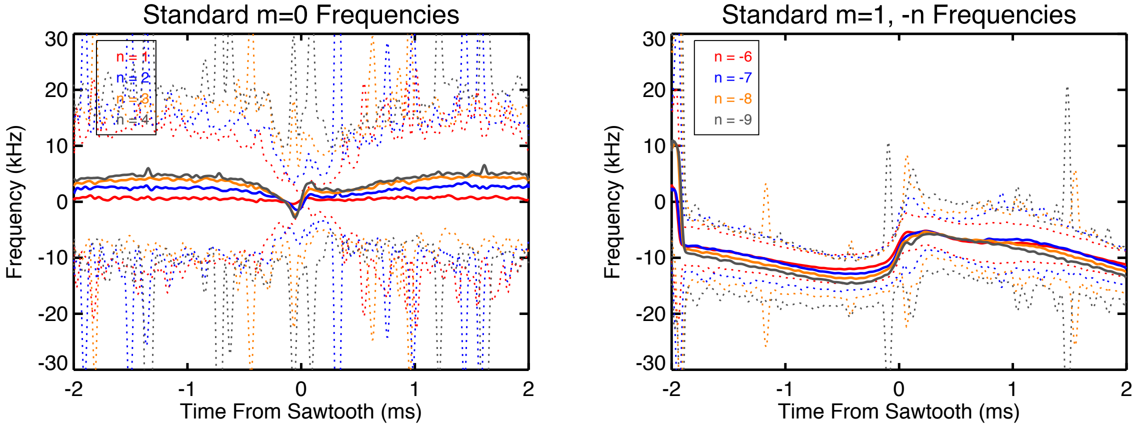

Figure 4.9: The tearing mode frequencies during the standard 210 kA RFP as observed by a stationary observer. The dotted lines show the standard deviation, σ.

$\sim 100\mu s$ wide sawtooth overlaps with the tearing mode frequencies measured in the lab frame.

The second assumption required for the data analysis is that the location of the probe relative to the plasma from shot to shot evenly samples the plasma toroidally (the random phase approximation). The tearing modes are the primary source of spatial asymmetries and their locations are measured with the toroidal array so toroidal array data is used to confirm an even toroidal distribution, as discussed in Sec. 3.3. The third assumption is that the poloidal and toroidal variation of the plasma are interdependent such that either sampling the plasma toroidally or poloidally will be equivalent to sampling the entire flux surface. This is true for the tearing modes, which are the primary source of spatial variation. However, there could also be poloidal variation due to the toroidal geometry and the Shafranov shift, which is ignored.

4.3.2 The OFCD Cycle and Fluctuation Analysis in MST

It is extremely challenging to use the analysis method presented in this chapter to measure fluctuations during OFCD with an insertable probe. During $\sim 1/3$ of the cycle the first assumption that the events in the ensemble are identical isn't well satisfied due to the timing of sawtooth magnetic relaxation events (Sec. 2.3). During $\sim 1/2$ of the cycle the second assumption that the probe evenly samples the flux surface at every time point over the ensemble doesn't hold because many of the modes lock with a preferential phase relative to the vacuum vessel and probe (Ch. 3). In addition, contributions to the dynamo from the locked and slowly rotating modes during half of the OFCD cycle will be rejected by highpass filtering the probe signals, which rules out highpass filtering for part of the OFCD cycle. These problems can be partially mitigated with variations to the analysis method but there is currently no established method that eliminates all these problems.

In the RFP without OFCD, the time dependence of the plasma dynamics during the current flat top is governed by the sawtooth cycle. The sawteeth in an ensemble are similar to one another while the periods before and after the sawteeth also match each other fairly well. Therefore, selecting periods of the plasma flat top based on the occurrence of sawteeth (i.e. setting the sawtooth time as t=0) works to select an ensemble that satisfies the requirement that all events are approximately identical.

During OFCD, the time dependence of the plasma dynamics is governed both by the OFCD cycle and by sawteeth and other magnetic relaxation events. It is necessary to choose time windows for events in the ensemble either based on OFCD or on magnetic relaxation events. Ideally there would be identical relaxation events at the same time during every OFCD cycle, in which case one could choose the time window based on either the OFCD cycle or magnetic relaxation events. This would satisfy the random phase approximation and would give the same answer whether one used the OFCD cycle or the magnetic relaxation events to choose the time windows for events to include in the ensemble. In reality, the sawteeth are entrained by the OFCD cycle (see Sec. 2.3), but since they have a duration of $\sim 100\mu s$ and the sawtooth timing varies by $\sim 1ms$, the entrainment is not good enough to perfectly satisfy the requirement that all the plasmas are identical at every time point with respect to the ensembling time window.

During the part of the OFCD cycle where sawteeth and other magnetic relaxation events are common, one can choose ensemble windows based on the OFCD cycle. However, systematic errors will be introduced to the magnetic relaxation event region due to cycle-to-cycle variation in the location of magnetic relaxation events. Alternately, one can choose ensemble windows based on the occurence of sawtooth crashes. This approach should be fairly accurate at the crash since the flux surface average fields at the crash are larger than the fields away from the crash. However, the crash has a duration of $\sim 100\mu s$ and the flux surface average fields everywhere but the crash are dominated by OFCD. Therefore, the sawtooth crash ensemble is fairly accurate only at the crash itself and has a systematic error before and after the crash again due to cycle-to-cycle variation in the location of magnetic relaxation events relative to the OFCD cycle.

Usually in the MST RFP, the plasma rotates toroidally at a frequency greater than 1 kHz while the plasma equilibrium changes relatively slowly except during the sawtooth crash. This separation of frequency scales is extremely useful for separating spatial fluctuations measured at a single point from variations in the equilibrium using a highpass filter. In OFCD, some of the plasma flux surfaces regularly slow down or stop rotating toroidally during the OFCD cycle, as shown by the averages and standard deviations of the m=0 mode frequencies in Fig. 4.10. The frequencies of the m=0 modes are regularly small from $\sim 0-1$ ms and $\sim 3-4$ ms so using a highpass filter on the probe data in the same way as the standard ensemble would also reject

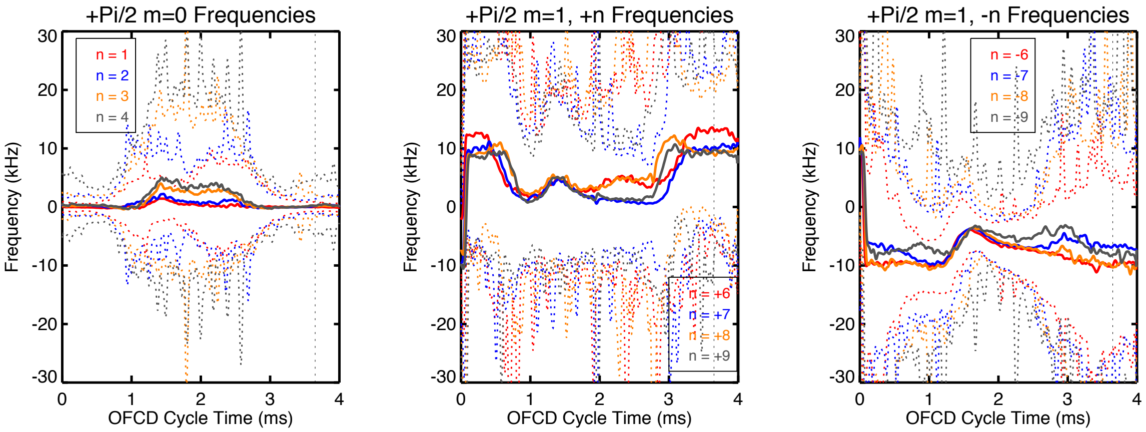

Figure 4.10: The tearing mode frequencies during OFCD $\delta = +\pi/2$ as observed by a stationary observer. The dotted lines show the standard deviation, σ.

contributions to probe signals due to the m=0 modes at the times when the plasma isn't rotating. This is the same time period when the m=0 amplitudes are large and therefore likely to make a substantial contribution to the dynamo.Therefore, highpass filtering to reduce the difference between $\bar{X}$ and $< X >$ caused by cycle-to-cycle variation is not an option during the half of the OFCD cycle where the m=0 tearing modes are locked. The modes exhibit similar behavior during the other OFCD phases as well, which can be seen in Appendix D.

In conclusion, spatial fluctuations on a flux surface can be measured using a single probe to collect data over an ensemble of shots. However, most of the assumptions made by the analysis method that hold true in the standard RFP are not completely satisfied during various parts of the OFCD cycle. Different variations of the analysis method will be used in the following chapters during different parts of the OFCD cycle in an attempt to extract the electric and magnetic field fluctuations from the mean electric and magnetic fields in order to calculate dynamo terms.

Chapter 5

Magnetic Relaxation During the Standard RFP

Magnetic relaxation is the means by which a plasma alters its magnetic fields in order to approach a minimum energy state. In the RFP, the dynamo typically opposes the inductive toroidal electric field (i.e. opposes the current in the core and drives current in the edge) such that the plasma stays near the minimum energy Taylor state. Measuring Ohm's law in the edge is a method of examining the details of the interaction of the dynamo and externally applied electric field that sustains the MST RFP against resistive dissipation of the plasma current.

This chapter presents measurements of Ohm's law during RFPs without partial OFCD, which will serve a few different purposes. First, it will demonstrate the ability of the capacitive probe to measure dynamo terms through comparison to results from Langmuir probes. Secondly, it will present the best probe measurements to date of Ohm's law in the edge of MST, which is an important result in its own right. Finally, it will provide standard results to compare to the results during partial OFCD sustainment presented in Ch. 6.

An ensemble of 210 kA plasmas with normal reversal will be presented in this chapter, which matches previous studies [12, 9] of magnetic relaxation in the MST

Table 5.1: RFP Parameters For Thesis

	No OFCD	No OFCD	OFCD (Cycle Average)
Plasma Current	210 ± 10 kA	250 ± 10 kA	250 ± 15 kA
Reversal Parameter	-0.18 ± 0.02	-0.5 ± 0.5	-0.6 ± 0.5
Electron Density	$1.0 \pm 0.15E13/cm^3$	$1.0 \pm 0.15E13/cm^3$	$1.0 \pm 0.15E13/cm^3$

plasma edge. An ensemble of 250 kA plasmas with deep reversal, which is a more appropriate plasma current and perhaps a more appropriate reversal for comparing to the OFCD cases in Ch. 6, can be found in Appendix D. Plasma conditions for all ensembles in this thesis can be found in Table 5.1.

5.1 Measurement of $\mathbf{E} - \eta\mathbf{J}$

The parallel electric field $\mathbf{E}_{\parallel} = \mathbf{E_0} \cdot \mathbf{B_0}/B_0$ is measured using a combination of measurements from the Dynamo Probe and measurements at the MST inner wall. Although the Dynamo Probe measures electric fields directly, its capacitive design prevents it from measuring steady inductive electric fields. Instead, the average electric field at the radius of the probe measurements can be determined by measuring the inductive electric and magnetic fields at the inner wall of the vacuum vessel as well as the magnetic fields at the Dynamo Probe.

The average electric field at the edge of the plasma is measured using MST's poloidal and toroidal flux loops. The voltages measured by these loops are called the VTG (toroidal gap voltage) and the VPG (poloidal gap voltage). Both the poloidal and toroidal magnetic fields at the wall are effectively measured by Rogowski coils.

The change in the magnetic field between the wall and the probe measurement location at $r/a = 0.9$ should be approximately linear. Therefore, Faraday's law can be used to derive the difference between the electric field at the wall and the electric field at the probe by integrating $\partial\mathbf{B}/\partial t$ from the wall to the probe measurement location. The resulting electric fields at the probe measurement location are

$$\begin{aligned} E_\theta(r=r_{probe}) = {} & E_\theta(r=a) + (a/r_{probe}-1)E_\theta(r=a) \\ & - \frac{\partial B_\phi(r=r_{probe})}{\partial t}\frac{(r_{probe}-a)(2r_{probe}+a)}{6r_{probe}} \\ & - \frac{\partial B_\phi(r=a)}{\partial t}\frac{(r_{probe}-a)(r_{probe}+2a)}{6r_{probe}} \end{aligned} \tag{5.1}$$

$$E_\phi(r=r_{probe}) = E_\phi(r=a) - \frac{(a-r_{probe})}{2}\left(\frac{\partial B_{\theta wall}}{\partial t} + \frac{\partial B_{\theta probe}}{\partial t}\right) \tag{5.2}$$

where $E_\theta(r=a)$ and $E_\phi(r=a)$ are the electric field measured at the inner wall and everything else on the right hand side of the equations are the corrections. The full derivation of these equations can be found in appendix C. These equations are used to calculate the parallel electric field at the probe, $\mathbf{E}_{||} = \mathbf{E_0}(r_{probe}) \cdot \hat{\mathbf{b}}_\mathbf{0}(r_{probe})$.

Figure 5.1 shows sawtooth ensemble averages of the signals that go into this calculation and the resulting parallel electric field. The correction to $\mathbf{E}_{||}$ plotted in the bottom left is the difference between $\mathbf{E}(a) \cdot \hat{\mathbf{b}}(r_{probe})$ at the MST vacuum vessel and $\mathbf{E}(r_{probe}) \cdot \hat{\mathbf{b}}(r_{probe})$ at the probe calculated using Eq. 5.1 and Eq. 5.2. This correction to $\mathbf{E}_{||}$ is negligible except at the sawtooth crash.

The parallel electric field is nearly identical in magnitude to the poloidal electric field but the opposite sign since the probe ($r/a = 0.9$) is close to the reversal surface ($r/a \approx 0.8$) but the edge magnetic field is in the negative poloidal and negative toroidal directions. At the crash, the electric field is positive, which means that it opposes the current since the current is anti-parallel to the mean magnetic field. In Ch. 5 and Ch. 6, the ensemble averages will be plotted using thick solid lines, the ensemble standard deviation of the mean, $\sigma/\sqrt{N}$, will be plotted using thin solid lines, and the

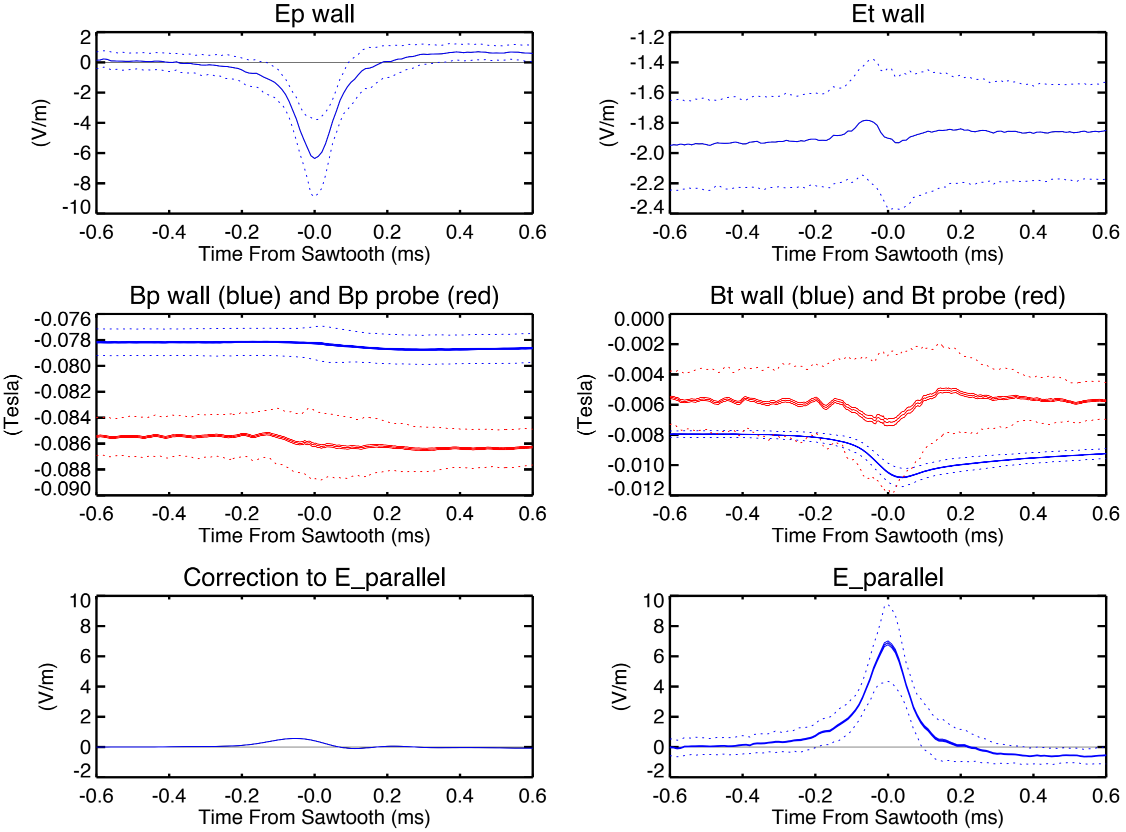

Figure 5.1: Ensemble averages of measurements that are combined to calculate the parallel electric field during the standard 210 kA RFP at the probe measurement location. Dotted lines are $\pm\sigma$.

standard deviations, σ, will be plotted with dotted lines. $\sigma/\sqrt{N}$ is often too small for the thin lines representing $\pm\sigma$ to be distinguishable from the thick lines representing the ensemble averages.

Next we will consider the resistivity and current density $\eta\mathbf{J}$. The current $\mathbf{J}$ is measured using the four magnetic coil triplets in the Dynamo Probe as outlined in Sec. 4.2. The resistivity is estimated using electron temperature measurements and estimates of the other factors in the parallel Spitzer resistivity [51]

$$\eta_\parallel = \frac{\eta_\perp}{2} = \frac{1.03\times10^{-4}}{2} Z_{eff} \ln\Lambda T^{-3/2}\Omega m \qquad (5.3)$$

The electron temperature (in eV) is measured in a separate ensemble of MST plasmas with the same conditions using the Helicity Probe (triple Langmuir probe). The Coulomb Logarithm, $\ln \Lambda$, is estimated to be 13.7.

The average effective ionization, Z_{eff}, is not well-known in MST. It has been inferred using using a combination of hard xray measurements and modeling with CQL3D to be approximately 5 during 400 kA MST PPCD discharges [52] but it is not well-known in the edge of the low-current standard RFP. In this thesis Z_{eff} will be estimated to be 3 ± 1 in the edge of 200-250 kA plasmas. This is the dominant uncertainty in our estimate of $\eta \mathbf{J}$.

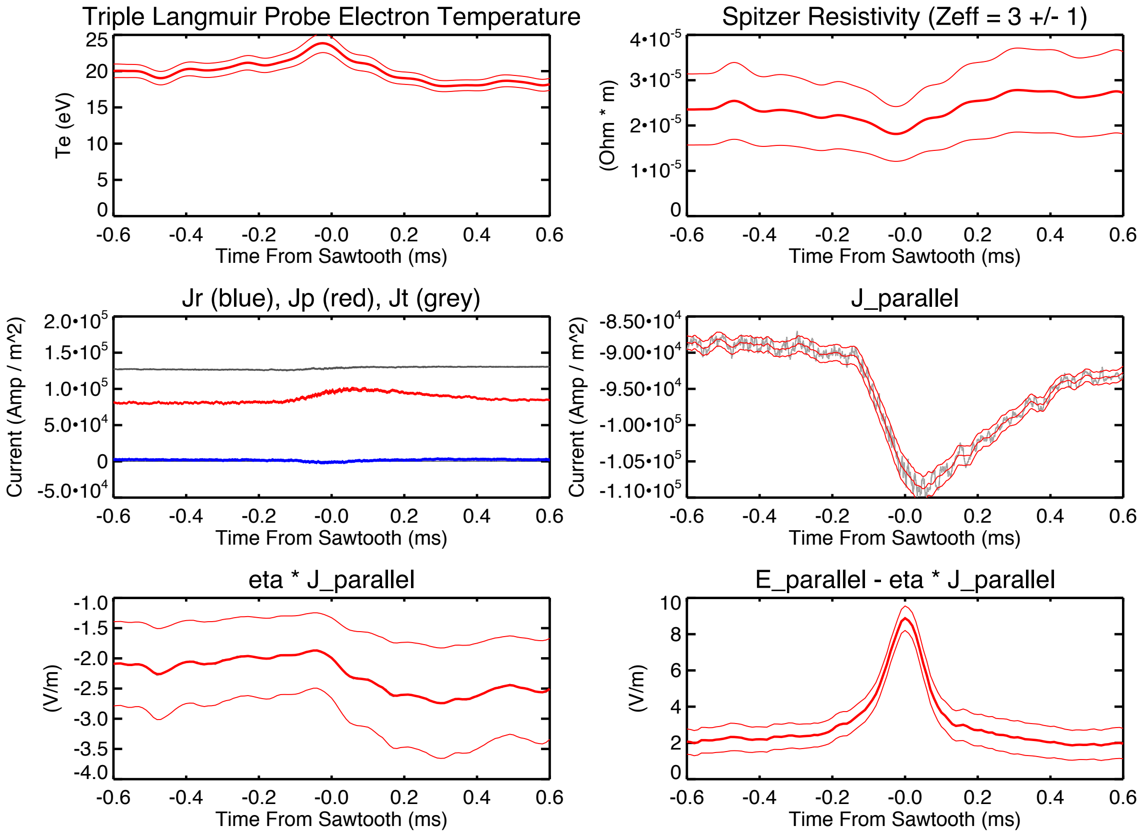

Figure 5.2: Ensembles of measurements that are combined to calculate $\eta \mathbf{J}$ at the probe minor radius. The measurements are shown in grey with smoothed data and standard deviations of the mean shown in red.

The electric field is not equal to $\eta\mathbf{J}$, as seen in the bottom right graph of Fig. 5.2. The difference is due to non-axisymmetric fields and currents, primarily from tearing modes, interacting to produce a dynamo EMF. The dynamo EMF allows the plasma to remain close to the relaxed state even though the applied electric field is not the appropriate direction or magnitude to maintain the relaxed state on its own.

5.2 The Dynamo and Ohm's Law Balance

Dynamo terms are required to be included in Ohm's law to demonstrate an Ohm's law balance in the RFP. The significant dynamo terms in Ohm's law have been previously measured to be the MHD Dynamo and the Hall Dynamo. These terms are equivalent to $< \tilde{\mathbf{E}} \cdot \tilde{\mathbf{B}} > /B \approx < \tilde{\mathbf{v}}_\mathbf{e} \times \tilde{\mathbf{B}} >$, as discussed in Sec. 1.1. This section will examine the signals measured by the dynamo probe in this ensemble, the resulting dynamo calculated from them, and the interplay of the dynamo and $\mathbf{E} - \eta\mathbf{J}$.

The ensemble averages of the probe electric and magnetic fields are plotted in Fig. 5.3 in grey with smoothed ensemble averages and the smoothed standard deviation of the mean overplotted in red. The smoothing window is 200 data points, which corresponds to 100 μs at the probe digitization frequency of 2 MHz. The standard deviation of the mean is calculated solely from the ensemble statistics. It is expected that shot to shot variation of the plasma is the dominant uncertainty in the ensemble averages so this should be a good estimate of the standard deviation of the signals.

The average toroidal and poloidal electric fields measured by the probe are two orders of magnitude larger than the inductive electric fields measured at the wall using the VTG and VPG. The average toroidal and poloidal electric fields are expected to be close to zero because the electrons should be capable of moving to cancel out any electric fields parallel to a flux surface that are due to a lack of local charge neutrality. One possible explanation is that the Dynamo probe is not able to correctly measure

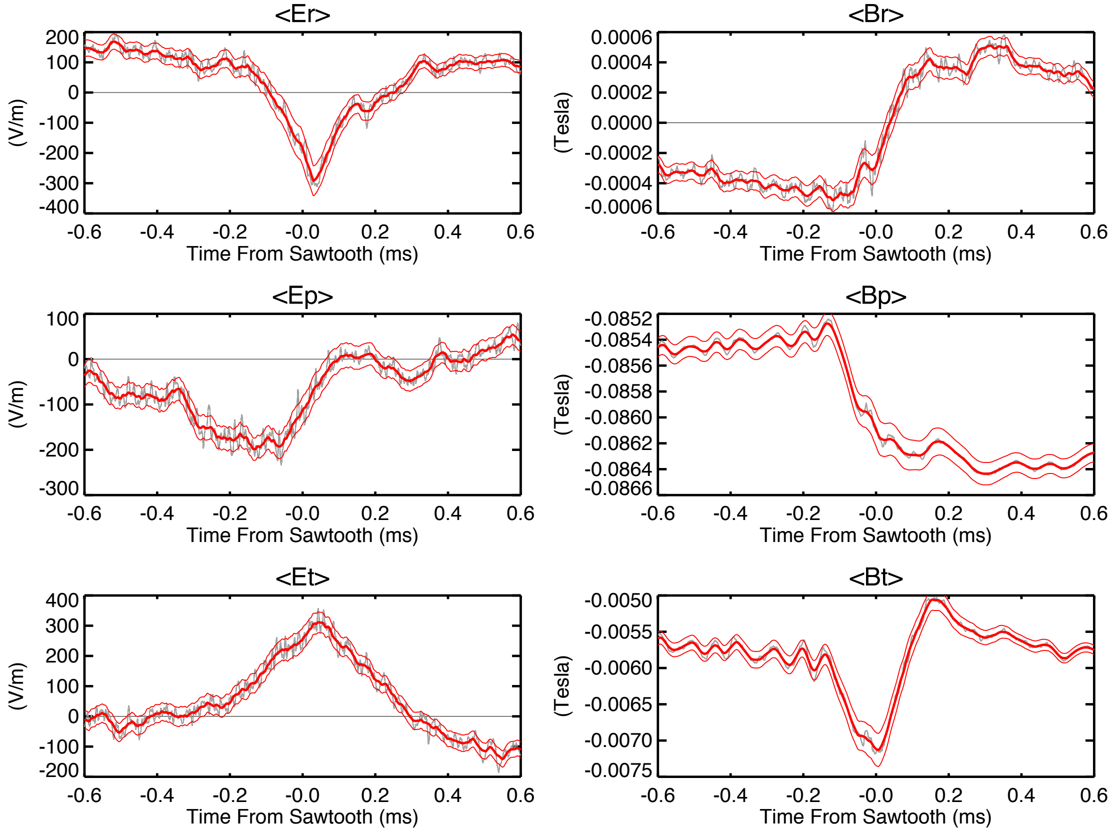

Figure 5.3: Ensemble average Dynamo Probe signals for the standard ensemble with normal reversal. The measurements are shown in grey with smoothed data and standard deviations of the mean shown in red.

quasi-DC electric fields because the complex gain $G(f)$ of the capacitive probes is strongly frequency dependent below 100 Hz and goes to zero as the frequency goes to zero. The capacitive probes are calibrated using the complex gain down to 10 Hz (Sec. 4.1.3) but that might not be low enough to get the DC level of the electric fields correct.

In addition, the uncertainty in capacitor gains could be compounded by the gain being much smaller at low frequencies. This could result in large uncertainties in the low frequency electric field measurements, especially since the electric field is calculated from differences in capacitive probe measurements. The pairs of capacitive probes measuring E_θ and E_ϕ are 2.1 cm apart, which means that an electric field measurement of $200V/m$ corresponds to a voltage difference of $4.2V$. This is only a $\sim$ 10% error considering that the voltage measured by the capacitive probes is approximately -25 V away from the sawtooth and spikes to approximately -40 V at the crash.

The fluctuations of a probe signal X are calculated from $X_{highpass}$, the probe signal highpass filtered at 1 kHz, as $\tilde{X} = X_{highpass} - < X_{highpass} >$, as described in Sec. 4.3. This is reasonable as long as the plasma is rotating fast enough that the contributions to the probe signals due to spatial variation on the flux surface have measured frequencies greater than the 1 kHz cutoff frequency, which is usually the case for the tearing modes in MST in a standard plasma. Highpass filtering should fix any issues with low frequency shot-to-shot variation as well as the unphysical average parallel electric fields measured in Fig. 5.3.

It is illustrative to look at the RMS fluctations $\sqrt{< \tilde{X}\tilde{X} >}$, as shown in Fig. 5.4, to get an idea of the relative amplitudes of the quantities going into the dynamo measurement. The relative amplitudes of the components of $\tilde{\mathbf{B}}$ roughly match the expected scaling for tearing mode magnetic fluctuations near the edge of the plasma. In particular, $\tilde{\mathbf{B}}_\phi \sim 2 \times \tilde{\mathbf{B}}_\theta$, which is reasonable since $\mathbf{k} \times \tilde{\mathbf{B}}$ should be zero at the conducting wall ([5], see Eq. 3.9). Of course, $< \tilde{X}(t)\tilde{Y}(t) > \neq \sqrt{< \tilde{X}(t)\tilde{X}(t) >}\sqrt{< \tilde{Y}(t)\tilde{Y}(t) >}$ but rather $< \tilde{X}(t)\tilde{Y}(t) > = \sqrt{< \tilde{X}(t)\tilde{X}(t) >}\sqrt{< \tilde{Y}(t)\tilde{Y}(t) >} \cos\delta(t)$ where $\delta(t)$ is the average instantaneous phase between the two signals. Note also that the electric field fluctuation amplitudes in Fig. 5.4 are large compared to the ensemble averages in Fig. 5.3, which is expected.

The dynamo, $< \tilde{\mathbf{E}} \cdot \tilde{\mathbf{B}} > /B$, is plotted in Fig. 5.5 with the smoothed dynamo and the standard deviation overplotted in blue. This is the dynamo parallel to $\mathbf{B}$. The

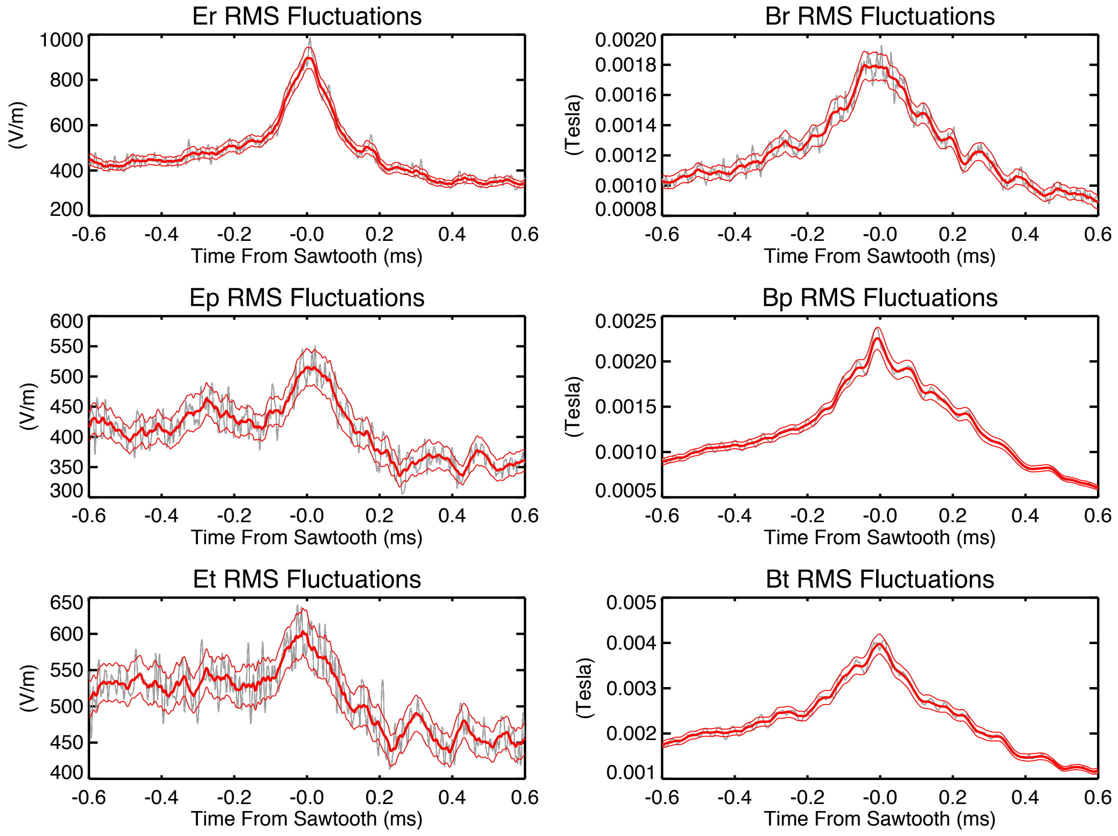

Figure 5.4: Probe fluctuation RMS amplitudes. Smoothed versions of the signals and standard deviations of the mean are overplotted in red.

parallel current in MST is the opposite direction of the magnetic field, so this measured negative EMF supports the current. It is reasonable for the unsmoothed measurement to have points outside one standard deviation of the smoothed measurement since each time point is an independent calculation. The smoothed measurement is believed to be a more accurate representation of the actual dynamo, since each time point is an independent calculation.

The individual contributions to the parallel dynamo from the radial, poloidal, and toroidal electromagnetic field fluctuations are also plotted in separate graphs in Fig. 5.5. All three are contributions to the parallel dynamo. The physical meaning of the individual contributions to the dynamo is which component of $\tilde{\mathbf{E}}$ and $\tilde{\mathbf{B}}$ creates

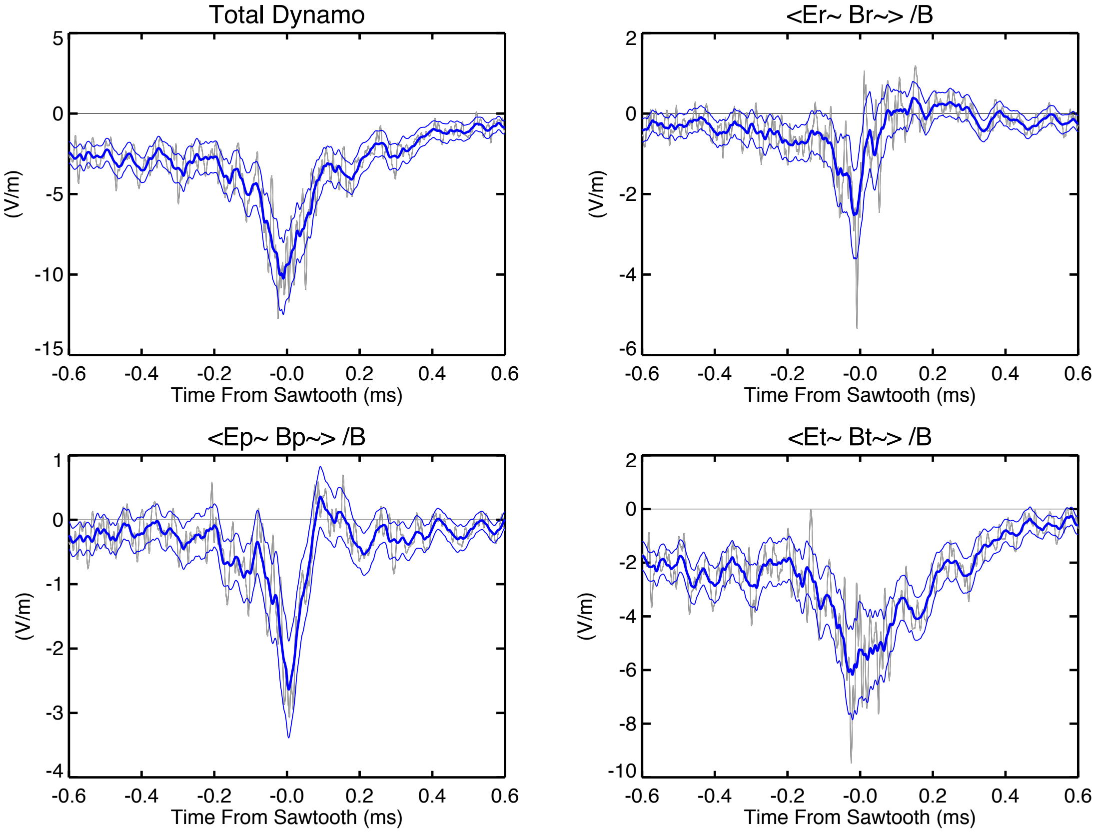

Figure 5.5: The dynamo and the contributions from the separate components of **E** and **B**. Smoothed versions of the signals and standard deviations of the mean are overplotted in blue. All plots are contributions to the parallel dynamo regardless of the directions of the fluctuations.

each contribution. It is useful to look at the individual components from a diagnostic standpoint. The probe has a corresponding geometry so each component came from a subset of the signals from the probe.

The contribution to $< \tilde{\mathbf{E}} \cdot \tilde{\mathbf{B}} > /B$ from parallel electromagnetic field fluctuations is expected to be small (Sec. 1.1.1) and has been ignored in previous measurements on MST [12]. The parallel and perpendicular contributions to the dynamo can be calculated as

$$\begin{aligned}
\frac{<\tilde{\mathbf{E}}_\parallel \cdot \tilde{\mathbf{B}}_\parallel>}{B_0} &= \frac{<(\tilde{\mathbf{E}}\cdot\hat{\mathbf{b}}_\mathbf{0})(\tilde{\mathbf{B}}\cdot\hat{\mathbf{b}}_\mathbf{0})>}{B_0} \\
&= \frac{<\tilde{\mathbf{E}}_\theta\tilde{\mathbf{B}}_\theta> B_{\theta 0}^2 + <\tilde{\mathbf{E}}_\phi\tilde{\mathbf{B}}_\phi> B_{\phi 0}^2}{B_0^3} \\
&\quad + \frac{(<\tilde{\mathbf{E}}_\theta\tilde{\mathbf{B}}_\phi> + <\tilde{\mathbf{E}}_\phi\tilde{\mathbf{B}}_\theta>)B_{\theta 0}B_{\phi 0}}{B_0^3} \\
\frac{<\tilde{\mathbf{E}}_\perp \cdot \tilde{\mathbf{B}}_\perp>}{B_0} &= \frac{<\tilde{\mathbf{E}}\cdot\tilde{\mathbf{B}}>}{B_0} - \frac{<\tilde{\mathbf{E}}_\parallel \cdot \tilde{\mathbf{B}}_\parallel>}{B_0}
\end{aligned} \tag{5.4}$$

and are shown in Fig. 5.6 for this ensemble ($\hat{\mathbf{b}}_0 \approx \hat{\theta}$ for the standard RFP with $F \approx -0.18$). The contribution from the parallel electromagnetic fluctuations is small but not negligible compared to the contribution from perpendicular fields, which suggests that there is a substantial contribution to the dynamo from $<\tilde{\mathbf{U}}_\perp \times \tilde{\mathbf{B}}_\parallel \cdot \tilde{\mathbf{B}}_\perp>$ (Eq. 1.16 and Eq. 1.20).

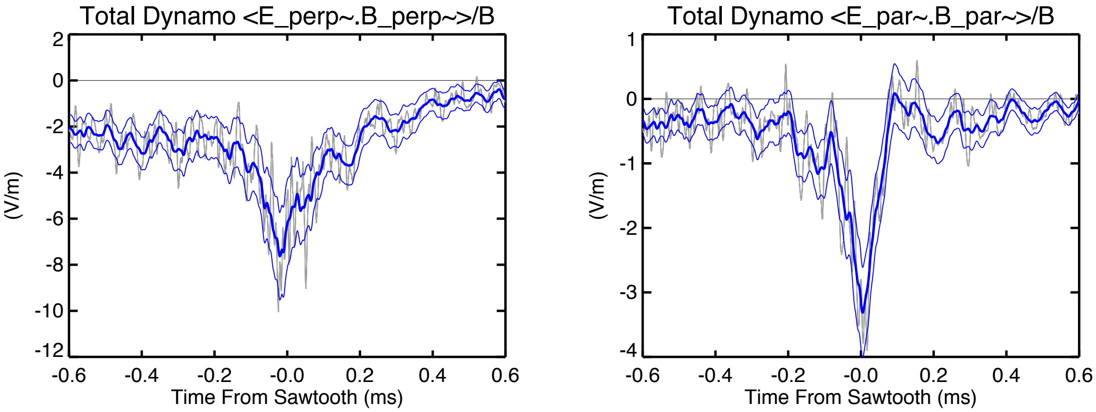

Figure 5.6: The dynamo contributions from the perpendicular and parallel components of **E** and **B**. Smoothed versions of the signals and standard deviations of the mean are overplotted in blue. All plots are contributions to the parallel dynamo regardless of the directions of the fluctuations.

The dynamo, **E**, and $\eta\mathbf{J}$ can be compared to confirm that parallel Ohm's law is a good model for the edge of the RFP, assuming the other terms in Ohm's law are negligible. The dynamo is multiplied by -1 and plotted with $\mathbf{E} - \eta\mathbf{J}$ in Fig. 5.7. A balance in Ohm's law is observed to within a standard deviation whenever the error bars of the two measurements overlap. Therefore, it is observed that Ohm's law balances to within one standard deviation over the entire sawtooth cycle. The sawtooth cycle is $\sim 3ms$ long but only $1.2ms$ is plotted to focus on the sawtooth itself. The dynamo and $E_{\|} - \eta_{\|}\mathbf{J}_{\|}$ far from the sawtooth are similar to the periods $-0.6ms < t < -0.3ms$ and $0.2ms < t < 0.6ms$.

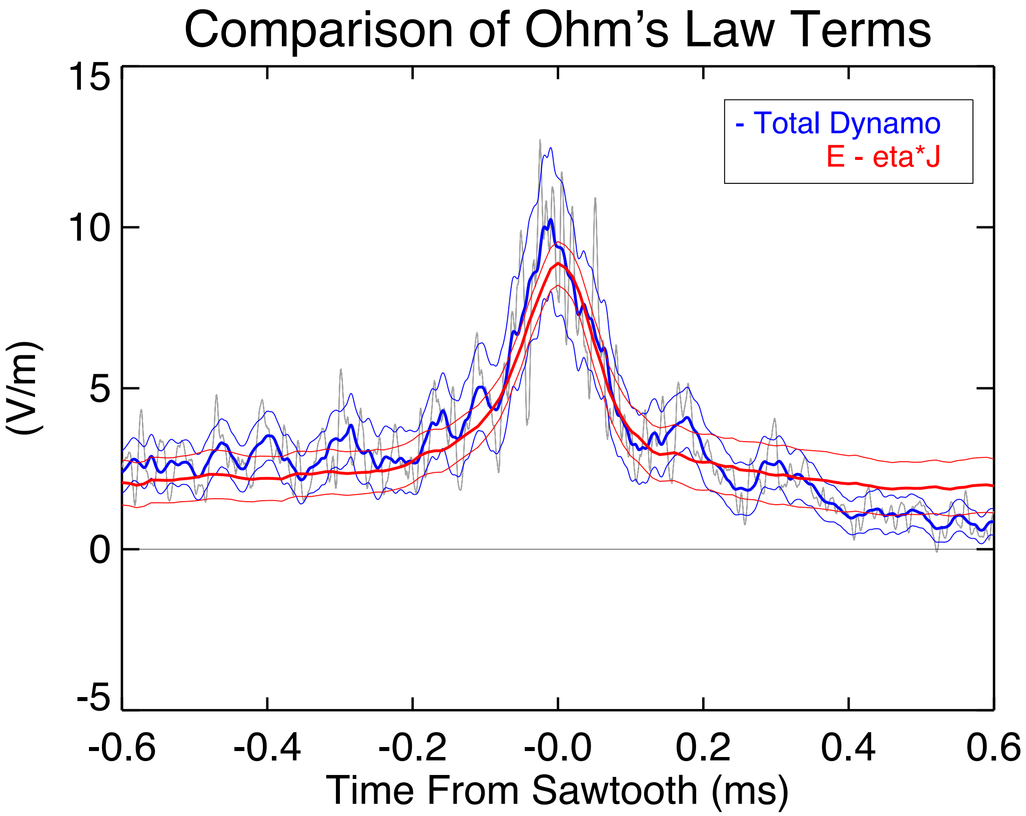

Figure 5.7: The dynamo, $\mathbf{E}$, and $\eta\mathbf{J}$ are compared to see if parallel Ohm's law is a good model for the edge of the plasma (neglecting other Ohm's law terms). The sign of the dynamo $< \tilde{\mathbf{E}} \cdot \tilde{\mathbf{B}} > /B$ has been reversed so that Ohm's law balance is illustrated by $\mathbf{E} - \eta\mathbf{J}$ overlaying $- < \tilde{\mathbf{E}} \cdot \tilde{\mathbf{B}} > /B$.

This result is the best measurement of parallel Ohm's law in the edge of the MST

RFP. The measurement of these Ohm's law in the edge of the MST standard RFP is consistent with a previous measurement of Ohm's law in MST in similar plasmas using triple Langmuir probes instead of capacitive probes for the electric field [12]. The noise on the Dynamo Probe measurement is roughly half as large as the previous measurement. This is likely due to a combination of factors but the biggest one is the size of the ensemble. The Dynamo Probe ensemble contains 400 sawtooth crashes ($\sqrt{N} = 20$) compared to 150 events in the previous ensemble ($\sqrt{N} \approx 12$).

Ignoring the contribution of fluctuations parallel to the mean magnetic field ($< \tilde{\mathbf{E}}_\perp \cdot \tilde{\mathbf{B}}_\perp > /B$) still results in a fairly well-balanced Ohm's law, as seen in Fig. 5.8. The calculated dynamo is slightly smaller at the crash compared to the correct calculation, $< \tilde{\mathbf{E}} \cdot \tilde{\mathbf{B}} > /B$, and doesn't quite match to within one standard deviation. This confirms that the parallel contribution, which is likely due to $< \tilde{\mathbf{U}}_\perp \times \tilde{\mathbf{B}}_\parallel \cdot \tilde{\mathbf{B}}_\perp >$, is fairly small everywhere but not negligible at the crash.

This result provides additional confidence in the ability of the Dynamo Probe to measure the dynamo. In addition, reproducing the dynamo result using a different method increases confidence in the result itself. Probe electric field measurements are much more problematic than magnetic field measurements. Using capacitive probes on four separate stalks to produce the same result as TLPs on one stalk increases confidence in the measurement of $\tilde{\mathbf{E}}$ by TLPs or capacitive probes, which is the most challenging component of the dynamo measurement.

5.3 Hall Dynamo and MHD Dynamo

The dynamo, $< \tilde{\mathbf{E}} \cdot \tilde{\mathbf{B}} > /B \approx < \tilde{\mathbf{v}}_\mathbf{e} \times \tilde{\mathbf{B}} >_\parallel$, is equal to the sum of the parallel MHD dynamo, $- < \tilde{\mathbf{v}} \times \tilde{\mathbf{B}} >_\parallel$, and the parallel Hall dynamo, $< \tilde{\mathbf{J}} \times \tilde{\mathbf{B}} >_\parallel /(n_e e)$. The dynamo, along with the mean electric field, is what causes the current in the plasma and therefore is of primary concern. However, historically on MST and elsewhere

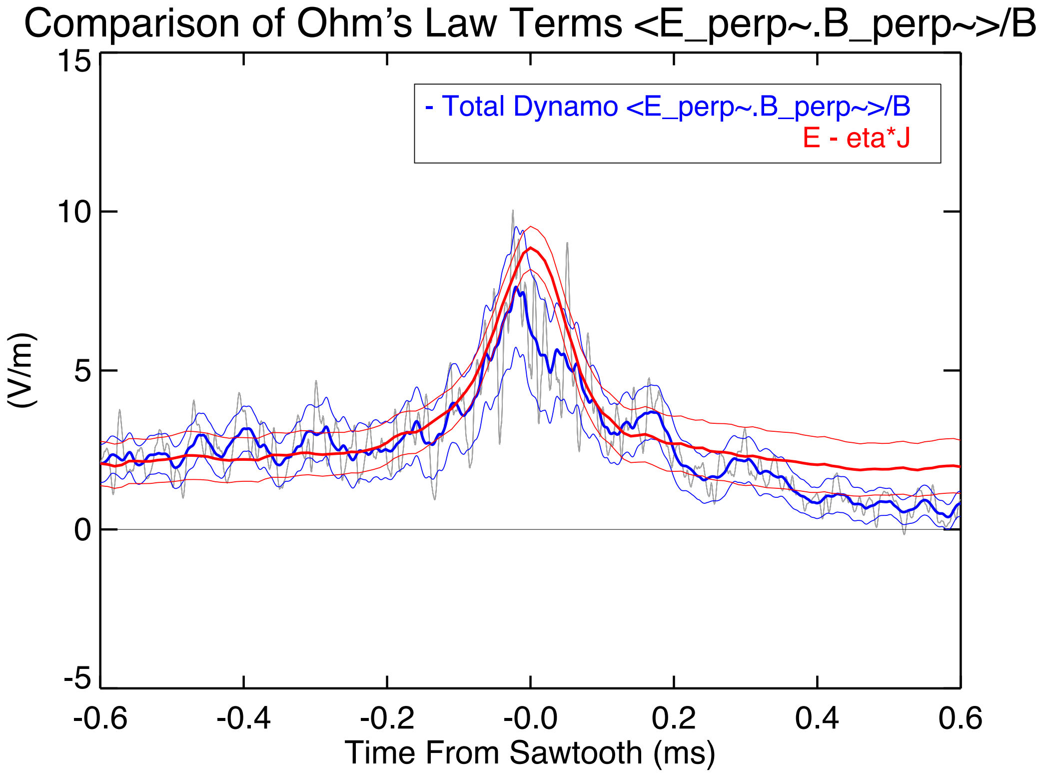

Figure 5.8: The dynamo from $\tilde{\mathbf{E}}_\perp$ and $\tilde{\mathbf{B}}_\perp$ are compared to $\mathbf{E}$, and $\eta\mathbf{J}$ to see if parallel Ohm's law is a good model for the edge of the plasma (neglecting other Ohm's law terms). The sign of the dynamo $< \tilde{\mathbf{E}}_\perp \cdot \tilde{\mathbf{B}}_\perp > /B$ has been reversed so that Ohm's Law balance is illustrated by $\mathbf{E} - \eta\mathbf{J}$ overlaying $- < \tilde{\mathbf{E}}_\perp \cdot \tilde{\mathbf{B}}_\perp > /B$.

the Hall Dynamo and the MHD Dynamo have been measured separately so it is of interest to consider them. In addition, the Hall dynamo couples to momentum transport through the Maxwell stress, $< \tilde{\mathbf{J}} \times \tilde{\mathbf{B}} >_{\|}$ [53]. In principle, electron density fluctuations, $\tilde{n}_e$, could also contribute to the Hall Dynamo, but these contributions have not been systematically measured in the edge of MST with probes.

The Hall dynamo is measured using the four Mirnov coil triplets in the Dynamo Probe to measure correlated fluctuations in magnetic field and current and using the TLP in the Helicity Probe for the electron density. $\mathbf{B}$ at the center of the probe measurement region is calculated as the average of the four Dynamo Probe Bdot coils while spatial derivatives of $\mathbf{B}$ are used to determine $\mathbf{J} = \nabla \times \mathbf{B}/\mu_0$. The electron density, n_e, was measured during a separate ensemble with almost identical plasma conditions.

The MHD dynamo is not measured. Rather, it assumed to be the difference between the dynamo and the Hall Dynamo as was derived in Eq. 1.10 under the assumption that the $< \eta\tilde{\mathbf{J}} \cdot \tilde{\mathbf{B}} >$ and $< \nabla\widetilde{p_e/(n_e}e) \cdot \tilde{\mathbf{B}} >$ terms are small (note that the wide tilde applies in principle to the entirety of $\nabla p_e/(n_e e)$, although contributions from $\tilde{n}_e$ to the diamagnetic dynamo have historically been ignored on MST as well). Measurements of $< \tilde{\mathbf{J}} \cdot \tilde{\mathbf{B}} >$ by the Dynamo Probe combined with η calculated using T_e from the Helicity Probe demonstrate that $< \eta\tilde{\mathbf{J}} \cdot \tilde{\mathbf{B}} >$ is orders of magnitude smaller than the other Ohm's law terms for every ensemble in this thesis. On the other hand, $< \nabla\widetilde{p_e/(n_e}e) \cdot \tilde{\mathbf{B}} >$ is not measured. If $< \nabla\widetilde{p_e/(n_e}e) \cdot \tilde{\mathbf{B}} >$ were not small, then the combined MHD and Hall dynamo contributions would be equal to $< \tilde{\mathbf{E}} \cdot \tilde{\mathbf{B}} > /B + < \nabla\widetilde{p_e/(n_e}e) \cdot \tilde{\mathbf{B}} >$ (Eq. 1.9) and the dynamo measurements presented in this thesis would be flawed.

The RMS values for $\tilde{\mathbf{J}}$ and $\tilde{\mathbf{B}}$ that are used to calculate the Hall dynamo are plotted in Fig. 5.9. The parallel Hall dynamo is primarily due to the $\hat{\mathbf{r}}$ and $\hat{\phi}$ components because $\hat{\mathbf{b}}_0 \approx \hat{\theta}$ at the measurement location at $r/a = 0.9$, as can be seen in Fig. 5.3. The Hall dynamo cannot be determined simply by multiplying these signals together since the phase between signals is important just as it was in the dynamo measurement.

The parallel Hall dynamo, $< \tilde{\mathbf{J}} \times \tilde{\mathbf{B}} >_{\parallel} /(n_e e)$, is shown to be positive in Fig. 5.10, which means that it opposes the parallel current and is the same direction as $\mathbf{E}_{\mathbf{0}\parallel}$. The direction is consistent with previous probe measurements of the Hall dynamo in

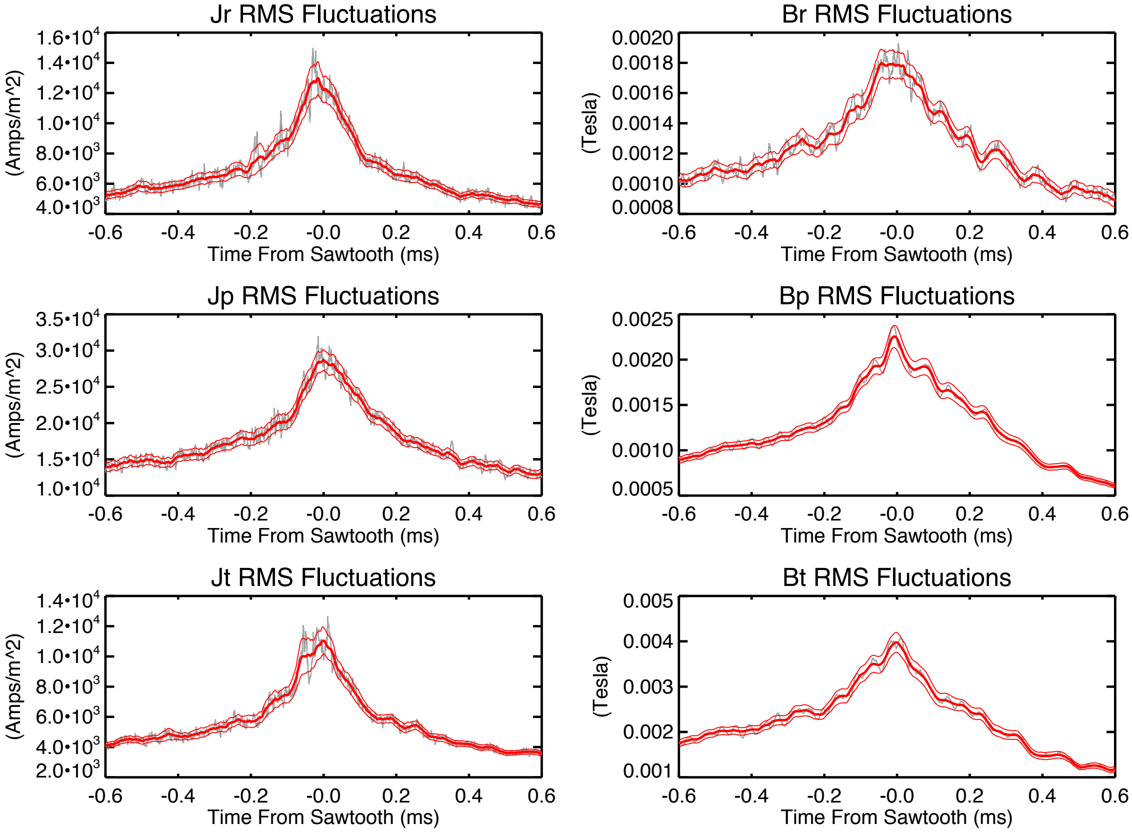

Figure 5.9: RMS values of **J** and **B** from the Dynamo Probe used for calculating the Hall Dynamo. The measurements are shown in grey with smoothed data and standard deviations of the mean ($\sigma/\sqrt{N}$) shown in red.

the edge of MST and the amplitudes of the two measurements are similar [10]. The previous result shows a well-defined positive spike in the Hall dynamo at the sawtooth and $\sim 0V/m$ before and after at the reversal surface ($r/a = 0.84$). The previous paper only presents the average Hall electromotive field at the location of the measurement in this thesis ($r/a = 0.91 \approx 0.90$) during the $100\mu s$ sawtooth. During this period, the paper claims that the Hall dynamo is $3.5 \pm 3V/m$, which is consistent with the measurement presented here.

The MHD dynamo is not measured directly. Rather, the implied parallel MHD dynamo, $< \tilde{\mathbf{v}} \times \tilde{\mathbf{B}} >_{\parallel}$, is calculated by plugging direct measurements of the dynamo

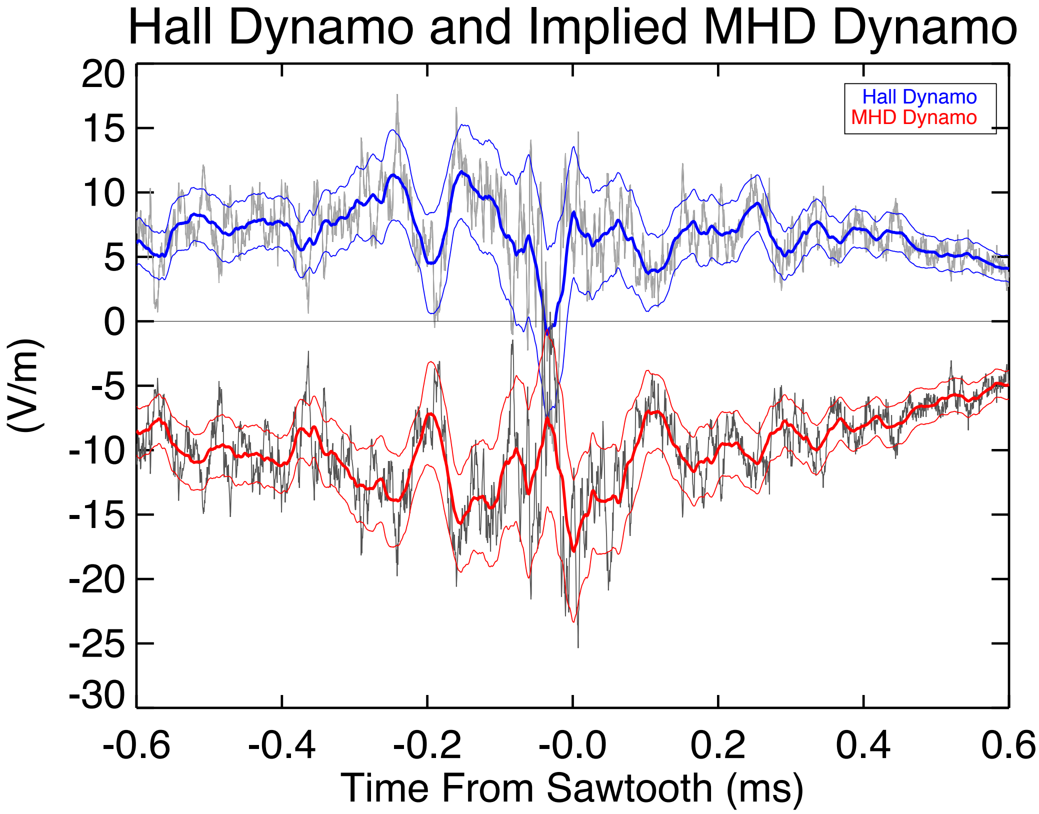

Figure 5.10: The Hall Dynamo and the assumed MHD Dynamo ($=<\tilde{\mathbf{E}}\cdot\tilde{\mathbf{B}}>/B_0+<\tilde{\mathbf{J}}\times\tilde{\mathbf{B}}>_{\parallel}/(n_e e)$). The measurements are shown in grey with smoothed data and standard deviations of the mean ($\sigma/\sqrt{N}$) shown in red and blue.

and the Hall dynamo into Eq. 1.10. The result is plotted in Fig. 5.10 along with the Hall dynamo. The high frequency fluctuations on the Hall dynamo are believed to be measurement errors rather than actual variations in the Hall dynamo so the signal is lowpass filtered and plotted over the unfiltered signal with error bars. It is expected that high frequency fluctuations in the Hall dynamo will be mirrored in the implied MHD dynamo due to the method of calculating it, as can be observed in the plot. The fact that the fluctuations are observable in both is not a reason to believe that they are real. The implied MHD dynamo is also lowpass filtered and plotted over the unfiltered signal with error bars.

The MHD dynamo is slightly larger than measured previously in similar plasmas ($I_p \approx 210kA$, $n_e = 1.0 \times 10^{19}/m^3$, measurement $r/a = 0.92$) where $\tilde{v}$ was measured spectroscopically [9], particularly before and after the crash. In the previous direct measurement, the MHD dynamo was shown to balance $\mathbf{E} - \eta\mathbf{J}$ by itself. However, the deuterium plasma was doped with a small amount of helium and the local velocity of the plasma (ions and electrons) was assumed to be equivalent to the velocity of the helium atoms. Also, only $\tilde{v}_r$ and $\tilde{v}_\phi$ were measured and it was assumed that $\tilde{\mathbf{v}}_\perp = \tilde{v}_r\hat{r} + \tilde{v}_\phi\hat{\phi}$. These assumptions may have lead to systematic errors in the previous measurement.

The dynamo ($\approx < \tilde{v}_e \times \tilde{B} >_\parallel$) is of primary importance for plasma dynamics. It is interesting that the Hall dynamo and implied MHD dynamo presented here oppose one another and that their amplitudes are equal or greater than the dynamo. This opposition between the Hall dynamo and MHD dynamo and their large amplitudes compared to the amplitude of the total dynamo has been observed previously in the core of MST as well as the edge. It has also been observed in two-fluid MHD simulations [54].

5.4 Magnetic Helicity Flux

The magnetic helicity flux, $2 < \tilde{V}_{plasma}\tilde{B}_r >$ (Sec. 1.1.4), is measured by the Dynamo Probe and plotted in Fig. 5.11. The direction of the flux is defined as radially outward from the flux surface. Recall that the current in MST is antiparallel to the magnetic field, which means that the total magnetic helicity in the plasma is negative. Therefore, in this case a negative helicity flux is an outward flux of negative helicity.

The helicity flux over the sawtooth cycle measured by the dynamo probe matches

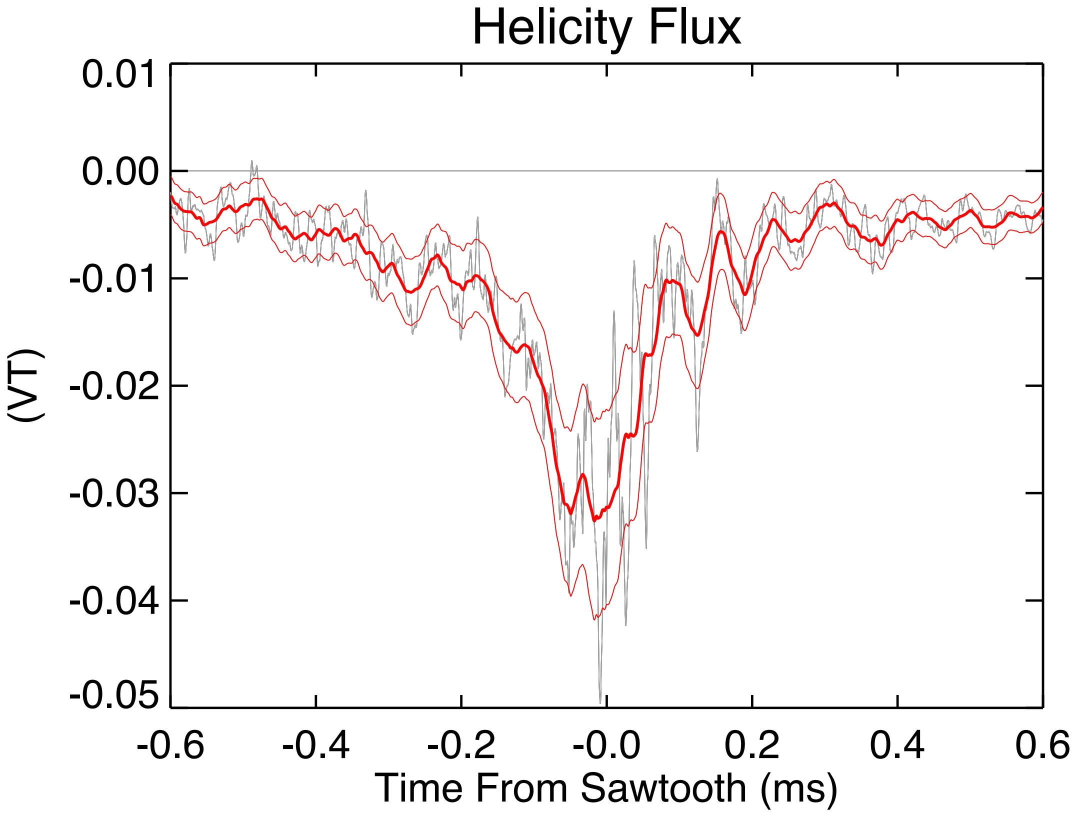

Figure 5.11: The magnetic helicity flux, $2 < \tilde{V}_{plasma}\tilde{B}_r >$, during the standard RFP. The measurements are shown in grey with smoothed data and standard deviations of the mean ($\sigma/\sqrt{N}$) shown in red.

previous results in MST [13]. It also matches helicity flux measurements using the Helicity Probe, which are not shown. The helicity flux is expected to be outward (i.e. negative for MST) in the edge when the dynamo supports the current in the edge, and inward (i.e. positive) when the dynamo opposes the current [14]. Therefore, in partial OFCD experiments we expect that the magnetic helicity flux will change sign when the dynamo changes sign.

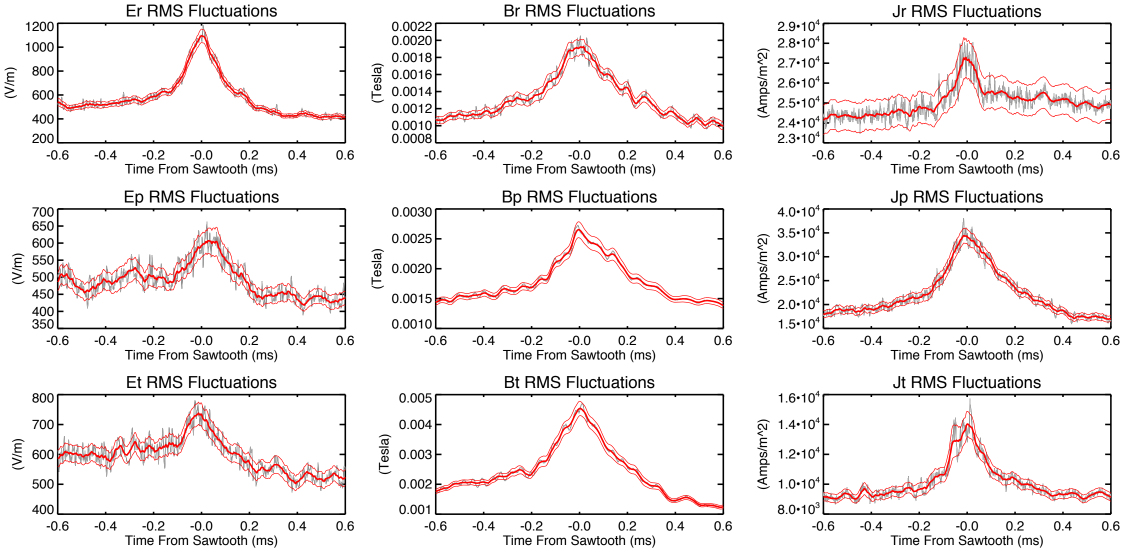

Figure 5.12: Probe fluctuation RMS amplitudes when the fluctuations are calculated using probe signals that are not highpass filtered. Smoothed versions of the signals and standard deviations of the mean are plotted in red.

5.5 Analysis Variation: Unfiltered Signals

One option for calculating fluctuations $\tilde{X}$ from probe signals is not to highpass filter each signal X before calculating $\tilde{X} = X - < X >$ even though highpass filtering removes some of the undesired event-to-event variation from the probe signals (Sec. 4.3). Using unfiltered signals will be necessary for the portion of the OFCD cycle when the m=0 modes are locked or slowly rotating (Fig. 3.3), leading to important m=0 contributions to the probe measurements at low frequencies (Fig. 4.10). In this section, it is demonstrated that calculating dynamo terms using fluctuations from unfiltered Dynamo Probe signals produces results that match the preferred analysis method using highpass filtering to within about one standard deviation.

The RMS values of most of the probe fluctuations calculated from unfiltered signals are slightly larger than the probe fluctuations calculated using filtered signals, as can be seen by comparing Fig. 5.12 to Fig. 5.4 and Fig. 5.9. The increase in the

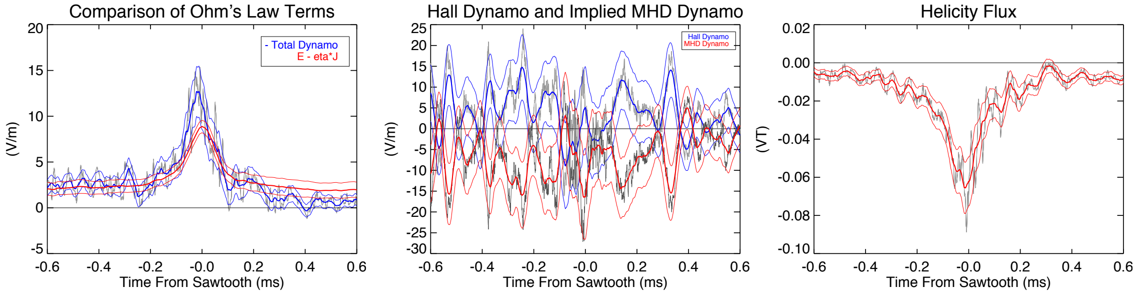

Figure 5.13: The dynamo, Hall dynamo, implied MHD dynamo, and magnetic helicity flux from the same standard RFP ensemble as the data in the previous sections but with the fluctuations calculated using probe signals that have not been highpass filtered with a 1 kHz cutoff.

fluctuation RMS amplitude of **B** is almost entirely due to keeping the low-frequency differences between the ensemble averages of the signals, $< X >$, and the instantaneous averages of the signals over the flux surface, $\bar{X}$, since the plasma is rotating around MST at a rate faster than 1 kHz for this ensemble. For example, two signals during an individual event are $X = cos(t) + 1$ and $Y = cos(t) + 1$ while the cycle averages are $< X >= 0$ and $< Y >= 0$. Highpass filtering would yield $\tilde{X}\tilde{Y} = cos(t)cos(t)$ whereas not filtering would yield $\tilde{X}\tilde{Y} = cos(t)cos(t) + 2cos(t) + 1$, where $2cos(t) + 1$ is additional undesired signal due to the DC offset of X and Y relative to the ensemble average.

The electric field and current density fluctuations, $\tilde{\mathbf{E}}$ and $\tilde{\mathbf{J}}$, increase partially due to the random phase approximation $\bar{X} =< X >$ not being as accurate for low frequencies. Another reason for the increase in these signals, particularly $\tilde{J}_r$ and $\tilde{J}_\phi$, is that the highpass filter was applied to the measurements of **B** and **V** before calculating **J** and **E** from the spatial derivatives of **B** and **V**. Therefore, uncertainties in the calibration of the probe magnetic coils and capacitors that are amplified by subtracting large fields to find a relatively small differences between them are largely negated by highpass filtering the signals before calculating $\mathbf{J} = \nabla \times \mathbf{B}/\mu_0$ and $\mathbf{E} = -\nabla V$.

Figure 5.13 shows the dynamo, Hall dynamo, implied MHD dynamo, and helicity flux when the probe signals are not highpass filtered with a 1 kHz cutoff before calculating the fluctuations. The result for the dynamo and helicity flux are largely unaffected but the Hall dynamo and consequently the implied MHD dynamo have a substantially smaller signal-to-noise ratio. Unfortunately, it will not be valid to highpass filter the magnetic signals during part of the OFCD cycle when calculating the Hall dynamo.

Not highpass filtering the capacitive probe signals means that the unphysical $< E >_{\|}$ (Fig. 5.3) could affect calculations of the electric field fluctuations. For the measurements of the dynamo, accurately measuring $< \mathbf{E} >$ is only an issue insofar as it affects our ability to accurately measure $\tilde{\mathbf{E}}$. Note that $\tilde{\mathbf{E}}_{RMS}$ is several times larger than $< \mathbf{E} >$ so the effect of errors in $< \mathbf{E} >$ on $\tilde{\mathbf{E}}$ should be somewhat small. This is confirmed by obtaining similar results for the dynamo without highpass filtering.

As an additional check that unphysical average electric fields do not strongly impact calculations of electric field fluctuations, the dynamo was calculated two other times, once with $\tilde{\mathbf{E}}_{\theta,\phi} = \mathbf{E}_{\theta,\phi}$ (less accurate) and once with $\tilde{\mathbf{E}}_{\theta,\phi} = \mathbf{E}_{\theta,\phi} - smooth(\mathbf{E}_{\theta,\phi})$ (possibly more accurate), and it was observed that the effect on the dynamo calculated was less than the standard deviation of the measurement. This suggests that incorrectly or correctly subtracting off $< \mathbf{E} >$ does not substantially affect the calculation of $\tilde{\mathbf{E}}$, presumably because $\tilde{\mathbf{E}}$ is substantially larger than $< \mathbf{E} >$.

Highpass filtering probe signals before calculating the fluctuations is a better approach if the entire plasma is rotating quickly. The results in this subsection demonstrate that not highpass filtering the Dynamo Probe data before calculating the fluctuations, which will be necessary for part of the OFCD cycle, yields approximately the same result for the dynamo and magnetic helicity flux as highpass filtering when the plasma is rotating at a rate greater than 1 kHz. However, the Hall dynamo result suggests that the Hall dynamo will be noisier in other ensembles in this thesis when **B** from the Dynamo Probe is not highpass filtered before calculating **J**.

Chapter 6

Magnetic Relaxation During OFCD

Understanding how the terms in Ohm's law balance one another during partial OFCD sustainment broadens our understanding of magnetic relaxation. In addition, it can provide insight into the feasibility of an RFP sustained solely by OFCD. In partial OFCD experiments, the OFCD electromagnetic fields support the current in the edge during part of the OFCD cycle and oppose the edge current during the rest of the cycle while the constant inductive toroidal electric field applied by MST sustains the current inside the reversal surface and opposes the current outside of it. In the standard MST plasma, the dynamo opposes the electric field almost everywhere in order to relax toward the minimum energy Taylor state.

In the standard MST plasma the edge dynamo is generated by linearly unstable core m=1 modes which nonlinearly couple to the m=0 modes at the reversal surface to support the edge plasma current. During partial OFCD experiments the edge parallel inductive electric field adds too much current during part of the OFCD cycle, tending to move the plasma out of its relaxed state. Also, the edge m=0 modes are thought to be linearly destabilized during this period. In this chapter, it will be shown that the edge dynamo resulting from these modes is capable of opposing the edge current, which has never before been observed in an RFP.

	Region I	Region II	Region III
Cycle Time	0.0 - 1.0 ms	1.0 - 2.6 ms	2.6 - 3.65 ms
Analysis Challenges	m=0 Modes Locked Small Sawteeth	Large Sawteeth	m=0 Modes Locked
$\mathbf{E}_{\parallel}$	$-1 \rightarrow +4V/m$	$+4 \rightarrow -1V/m$	$-1 \rightarrow -2 \rightarrow -1V/m$

Table 6.1: The three regions of the OFCD cycle are roughly defined with respect to the cycle time used for the X axis of OFCD graphs. The fluctuation analysis challenges and approximate values of notable global parameters are listed. Recall that $-\mathbf{E}_{\parallel}$ supports the parallel current.

This chapter will also show that the significant Ohm's law terms during the standard RFP, namely the electric field, the MHD dynamo, the Hall dynamo, and $\eta\mathbf{J}$, are generally the only significant terms during the partial OFCD case. This will be demonstrated by showing that these terms result in a balanced Ohm's law for the majority of the OFCD cycle, which supports the theory that this parallel Ohm's law is a good model for the RFP. It will also be shown that Ohm's law does not balance during the part of the cycle immediately preceding the large sawtooth crash region when all of the Ohm's law terms that are usually significant in MST are considered. Possible explanations such as significant systematic errors or an unmeasured, non-negligible diamagnetic dynamo will be discussed.

Unfortunately, m=0 mode locking and the imperfect entrainment of sawtooth crashes by the OFCD cycle means that a single ideal data analysis method does not exist for the entire OFCD cycle (Sec. 4.3.2). Throughout this chapter, three distinct periods of the OFCD cycle will be discussed. Important features and analysis challenges of the three regions are outlined in table 6.1. Global parameters for the OFCD $\delta = +\pi/2$ case are plotted in Fig. 6.1.

The X axis of the plots of the OFCD cycle in this chapter have a domain of 0-4

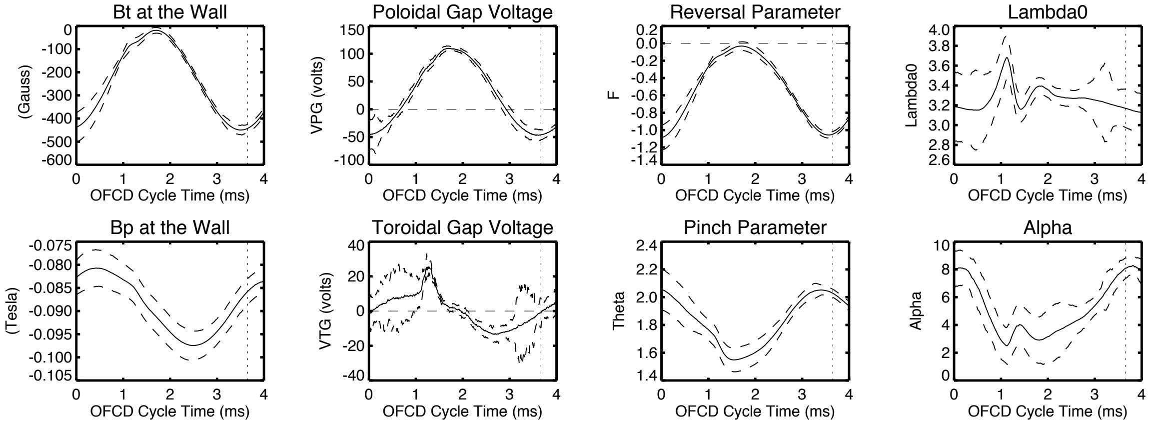

Figure 6.1: Global parameters during the OFCD $\delta = +\pi/2$ ensemble and their standard deviations, σ. α and λ_0 describe the radial current profile (Eq. 1.25 and Eq. 1.26). Dotted lines show $\pm\sigma$.

ms while the OFCD period is $\sim$3.65 ms so the signals begin to repeat at $t = 3.65$ ms in these graphs. $T = 0$ is determined from the point at which the voltage on the capacitors in the OFCD Bt circuit crosses zero. The zero times are quite reproducible from shot to shot so choosing $t = 0$ in this way should not produce a significant error in the measurements.

Section 6.1 will examine one OFCD phase, $\delta = \pi/2$ in detail in the same manner that Ch. 5 examined the RFP with normal reversal and no OFCD. The dynamo will be measured using fluctuations calculated from unfiltered probe signals since the m=0 modes lock in regions I and III of the OFCD cycle. Section 6.2 will summarize data for the OFCD phases $\delta = \pi/4$, $\delta = 0$, and $\delta = -\pi/4$. Additional plots for the other OFCD phases can be found in appendix D. Section 6.3 will address analysis issues and possible solutions during the three regions of the OFCD cycle. Finally, Sec. 6.4 will further the discussion of a possible significant diamagnetic dynamo contribution to Ohm's law during OFCD on MST.

6.1 OFCD $\delta = \pi/2$

6.1.1 Measurement of $\mathbf{E} - \eta\mathbf{J}$

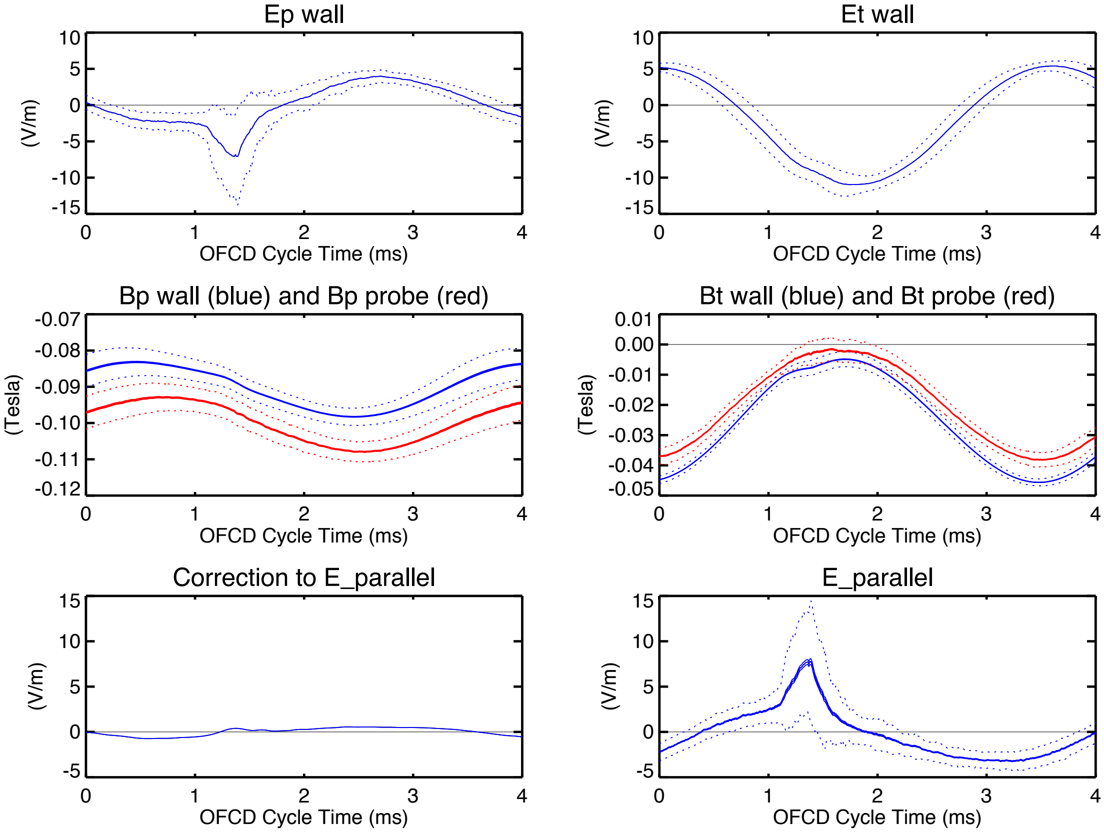

Figure 6.2: Ensembles of measurements that are combined to calculate the parallel electric field at the probe minor radius for the OFCD $\delta = +\pi/2$ ensemble. Dotted lines are $\pm\sigma$.

First the axisymmetric electric field will be examined for the flux surface located at the probe measurement location ($r/a = 0.9$). This electric field is determined using the poloidal and toroidal electric and magetic fields at the wall, the magnetic field measured at the probe, and Eq. 5.1 and Eq. 5.2, which assume that dB_θ/dr and dB_ϕ/dr are constant from the wall to the probe measurement location. This electric field and the signals used to calculate it are shown in Fig. 6.2.

The OFCD contributions to the magnetic and electric fields can be easily observed in the electric fields measured at the wall as well as the magnetic fields measured by the probe and at the wall. B_θ oscillates around -0.1 tesla, which is a typical value for this plasma current. B_ϕ has a much more negative average value than is typical for this current in order to keep $B_\phi < 0$ with the large amplitude oscillations from OFCD. E_θ oscillates around 0 V/m, discounting the sawtooth spike, while E_ϕ oscillates around the DC E_ϕ contribution of 4 V/m from the normal MST circuits. $E_\parallel$ is a combination of MST's inductive toroidal electric field and the AC fields $\hat{E}_\theta$ and $\hat{E}_\phi$ from OFCD.

In an RFP produced by the same setting on the normal MST power supplies but without OFCD, $E_\parallel = 0 \pm 1$ V/m and spikes to 12 V/m at the sawtooth, as can be seen in Appendix D. In Fig. 6.2, the sawtooth region is also evident in the measurements of $E_{\theta wall}$ and $E_\parallel$ from t=1-1.5 ms. The electric field at the sawtooth during OFCD appears wider with a smaller amplitude in these cycle ensembles because the sawtooth is not perfectly entrained by OFCD.

The OFCD contribution to $E_\parallel$ oscillates from approximately -3.5 V/m to +3 V/m over the course of the cycle. It is expected that the average $E_\parallel < 0$ V/m over an OFCD cycle with $\delta = \pi/2$, which is what we observe. The sawtooth muddies this picture slightly but one can imagine what $E_\parallel$ would look like with the spike at the sawtooth removed. Recall that parallel current in MST is anti-parallel so $E_\parallel < 0$ V/m supports the current.

$E_\parallel$ away from the sawtooth becomes both more positive and more negative in this OFCD ensemble than in an RFP ensemble with the same MST settings but no OFCD. This does not cause the toroidal current to change direction twice every OFCD cycle, but instead the dynamo EMF maintains the plasma nearer to a relaxed state with unidirectional toroidal current. This means that the dynamo is required to support the plasma current during part of the OFCD cycle and oppose it during the other part.

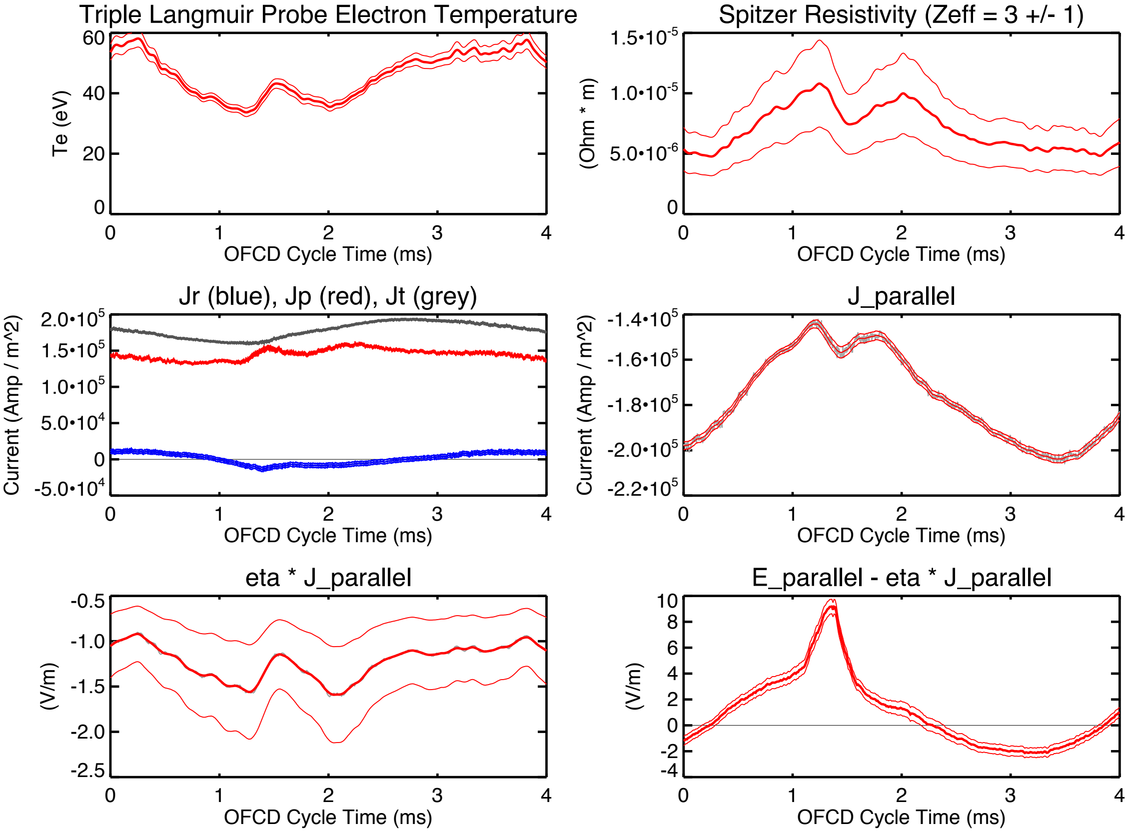

Figure 6.3: Ensembles of measurements that are combined to calculate $\eta\mathbf{J}$ at the probe minor radius for the OFCD $\delta = +\pi/2$ ensemble. The measurements are shown in black with smoothed data and standard deviations of the mean $(\sigma/\sqrt{N})$ shown in red.

The parallel Spitzer resistivity (Eq. 5.3) and the current from the probe are used to calculate $\eta\mathbf{J}$, as shown in Fig. 6.3. The Coulomb logarithm and Z_{eff} are estimated and assumed constant to calculate η and the electron temperature is measured in a separate OFCD $\delta = \pi/2$ ensemble using the Helicity Probe TLP. The uncertainty in $\eta\mathbf{J}$ is dominated by Z_{eff} since Z_{eff} is not well-known. Also, Z_{eff} probably has some variation on the OFCD timescale since OFCD probably significantly affects heating, transport, and confinement. The dominant features in T_e and $\mathbf{J}$ are an oscillation due to OFCD with an OFCD period of 3.65 ms and the sawtooth region and subsequent plasma recovery in the region t=1-2 ms.

The bottom right graph of Fig. 6.3 illustrates that $E_{\|}$ is not matched by $\eta\mathbf{J}$. Despite the large variation in $E_{\|}$, $J_{\|}$ only varies by about 40%, $\eta\mathbf{J}$ varies by about 90%, and $J_{\|}$ doesn't come close to changing direction. In the next section, direct measurements of dynamo terms are presented to examine the details of the dynamo EMF.

6.1.2 The Dynamo and Ohm's Law Balance

The dynamo, $< \tilde{\mathbf{E}} \cdot \tilde{\mathbf{B}} > /B$, is measured in the edge to determine whether it accounts for the difference between $\mathbf{E}$ and $\eta\mathbf{J}$ in the OFCD $\delta = \pi/2$ case. First, the individual Dynamo Probe signals from the ensemble are examined in the same manner as the standard ensemble probe signals were in Sec. 5.2. The ensemble averages of the components of $\mathbf{E}$ and $\mathbf{B}$ measured by the Dynamo Probe are shown in Fig. 6.4. There are three obvious features that are each visible in some or all of the signals. First, there is a spike on B_r and all of the components of $\mathbf{E}$ at the sawtooth region centered at 1.3 ms. Second, there is a period of smaller sawteeth immediately after the sawtooth until 2.3 ms, primarily visible in E_θ, E_ϕ, and B_r. Finally, there is the OFCD contribution to all of the signals, which is obscured by the first two effects but is visible everywhere else as a sinusoidal oscillation with a period of $\sim 3.65ms$.

The sawtooth region could be problematic for the correlation analysis technique used in this thesis (Sec. 4.3). The averages measured here, $< X >$, are treated as the average fields $\bar{X}$ on the flux surface for each event in the ensemble by the analysis and the fluctuations are computed as $\tilde{X} = X - < X >$. The formula for the fluctuations

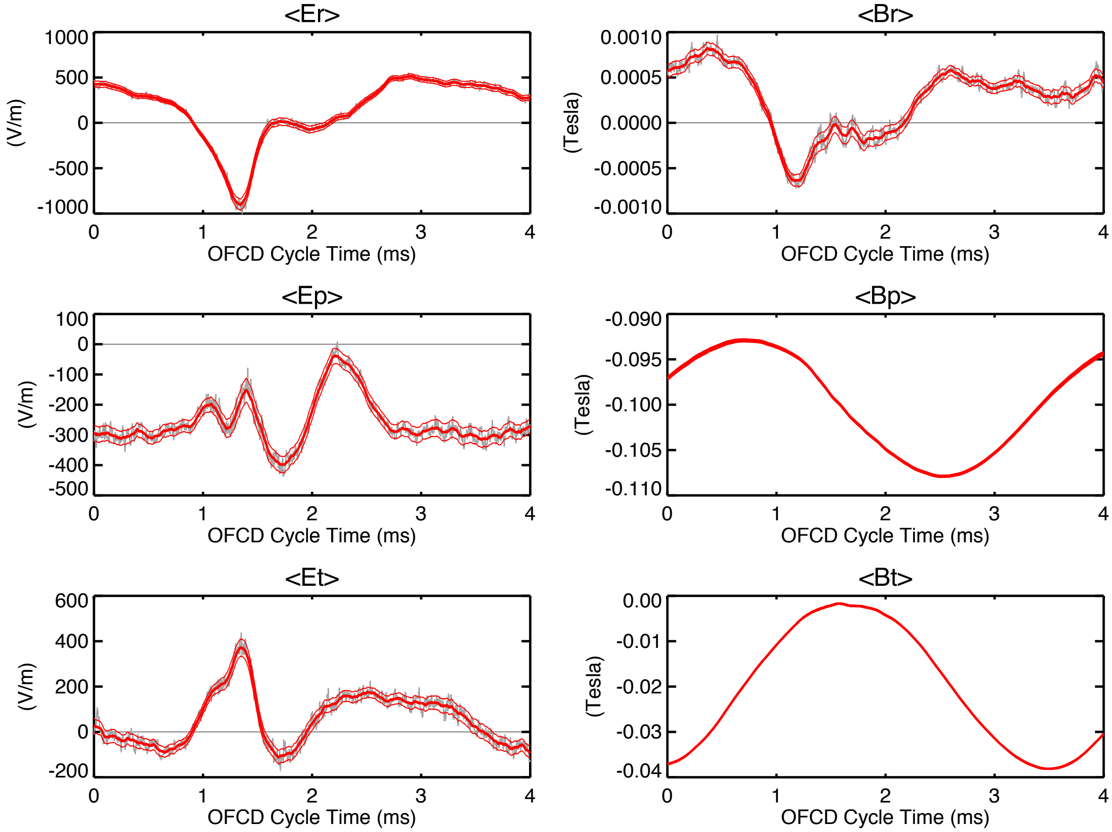

Figure 6.4: Ensemble average Dynamo Probe signals for the OFCD ensemble with $\delta = \pi/2$. The measurements are shown in black with smoothed data and standard deviations of the mean $(\sigma/\sqrt{N})$ shown in red. The standard deviations of B_θ and B_ϕ are so small compared to oscillations in the average values that the mean and error bars appear to be one red line.

will be accurate if $\bar{X} \approx < X >$ for each cycle in the ensemble. Unfortunately, the sawtooth location is not perfectly entrained by OFCD. The spike in $\bar{X}$ due to the sawtooth is $\sim 100\mu s$ wide but is spread out over $\sim 300\mu s$ and is consequently smaller amplitude in the cycle ensemble as seen in the cycle average signals, particlary $< B_r >$ and all of the electric field components. Using these ensemble averages to calculate $\tilde{X}$ introduces systematic errors in the fluctuations since differences between an individual cycle's $\bar{X}$ and $< X >$ will be treated as part of $\tilde{X}$. In other words, for a given OFCD cycle $\tilde{X}_{measured} - \tilde{X}_{actual} =< X > -\bar{X}$. Highpass filtering would partially solve this issue but it isn't an option for the entire cycle when the m=0 modes tend to lock in regions I and III.

The fluctuating probe signals for the OFCD $\delta = \pi/2$ ensemble $\tilde{X} = X - < X >$ are calculated using the ensemble averages shown in Fig. 6.4 despite the problems just mentioned (except for B_θ, discussed below). The RMS fluctuations $\sqrt{< \tilde{X}\tilde{X} >}$ are shown in Fig. 6.5. As expected, there is an increase in amplitude of all of the probe signals' RMS fluctuations at $1.1 < t < 2.3ms$ due to a combination of larger fluctuations during relaxation events as well as the systematic error due to $\bar{X} \neq < X >$.

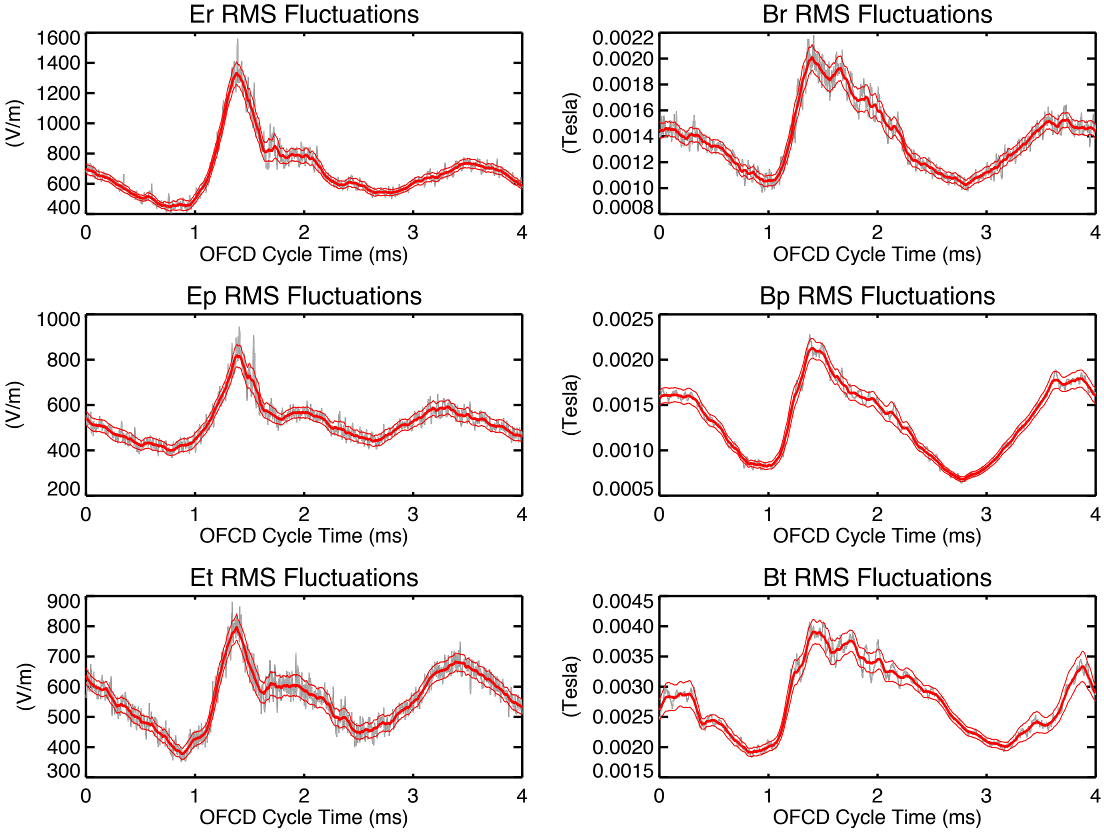

Figure 6.5: Probe fluctuation RMS amplitudes for the OFCD $\delta = +\pi/2$ ensemble. Smoothed versions of the signals and standard deviations of the mean $(\sigma/\sqrt{N})$ are overplotted in red.

There is also an increase in $\tilde{\mathbf{B}}$ at $\sim 3ms < t <\sim 0.5ms$ and a similar increase in $\tilde{\mathbf{E}}$ at $\sim 2.5ms < t <\sim 0.5ms$. Remember that the OFCD cycle has a period of $3.65ms$ so the probe signals at $3.65ms$ loop back to $0ms$. The increase in $\tilde{\mathbf{E}}$ amplitude corresponds to the period $\sim 2.2ms < t <\sim 0.2ms$ when $\mathbf{E}_{\|} - \eta\mathbf{J}_{\|} < 0$ i.e. when the dynamo must be opposing the parallel current. Unsurprisingly, the increase in $\tilde{\mathbf{B}}$ corresponds to the period $\sim 3ms < t <\sim 1ms$ when the m=0 and m=1, +n tearing modes are large.

When $\tilde{\mathbf{B}}_{\theta}$ was calculated for the OFCD ensembles using $\tilde{\mathbf{X}} = \mathbf{X} - < \mathbf{X} >$ as in the standard RFP case, it was surprisingly large. Assuming that the primary source of magnetic field fluctuations is the tearing modes and $\mathbf{k} \times \tilde{\mathbf{B}} \approx 0$ at the wall, then $\tilde{\mathbf{B}}_{\theta} \approx \tilde{\mathbf{B}}_{\phi}/2$ ([5], see Eq. 3.9). Therefore, either $\tilde{\mathbf{B}}_{\theta}$ was too big or $\tilde{\mathbf{B}}_{\phi}$ was small. It is easier to create an artificially big fluctuation using this analysis method than to create an artificially small fluctuation since errors in $\bar{X} =< X >$ lead to more power in the fluctuations. In addition, $< \tilde{\mathbf{E}}_{\|} \cdot \tilde{\mathbf{B}}_{\|} > /B_0$ was larger than expected based on the standard case. It was hypothesized that variations in $< B_{\theta} >$ were substantial compared to $\tilde{\mathbf{B}}_{\theta}$ and confirmed by demonstrating that the standard deviation of B_{θ} at the wall as determined from the measurement of the plasma current, $B_{\theta wall} = -\mu_0 I_P / 2\pi r$, which is a global measurement, is similar in size to the standard deviation of $B_{\theta probe}$. This issue was dealt with by scaling the poloidal field at the wall to the flux surface average value at the probe location and subtracting that value from the probe measurement instead of $< B_{\theta} >$ to determine $\tilde{B}_{\theta}$, which is one of the signals shown in 6.5.

The parallel dynamo from these Dynamo Probe measurements is plotted in Fig. 6.6 along with separate plots of the contributions from the radial, poloidal, and toroidal measurements. Smoothed signals and standard deviations of the mean are plotted over the unfiltered measurements in blue. As mentioned previously, the only physical

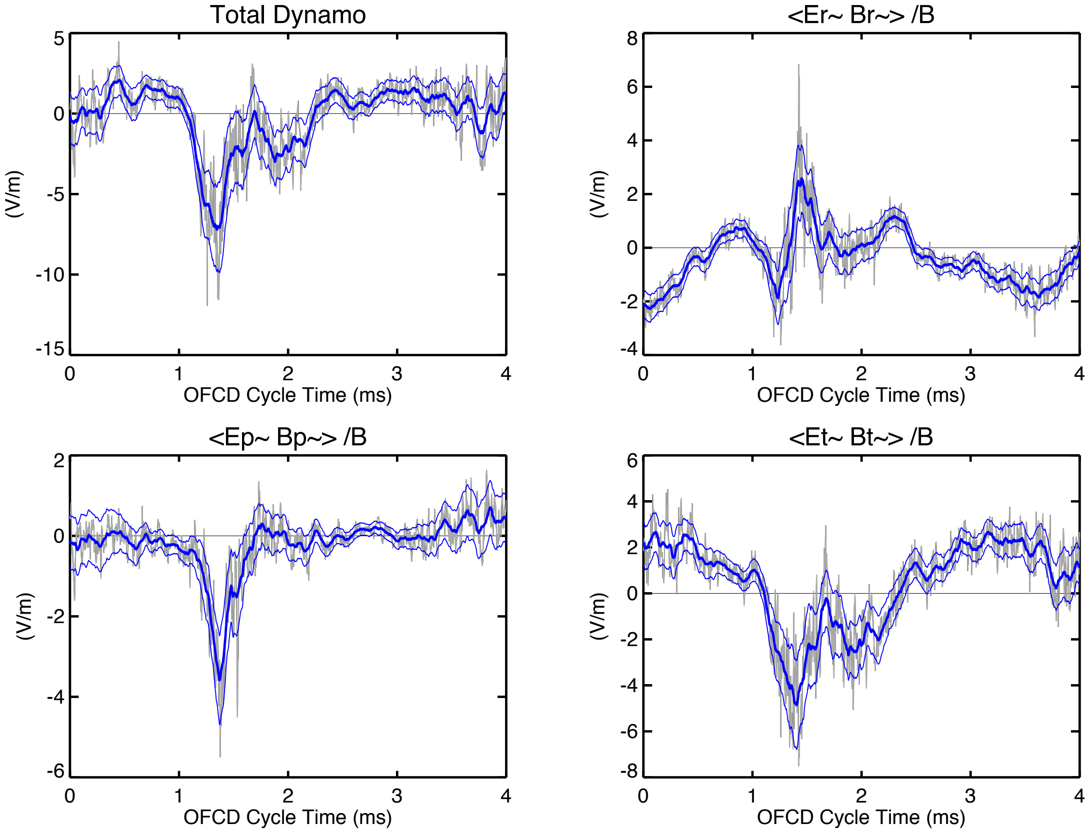

Figure 6.6: The dynamo and the contributions from the separate components of **E** and **B** for the OFCD $\delta = +\pi/2$ ensemble. Smoothed versions of the signals and standard deviations of the mean $(\sigma/\sqrt{N})$ are overplotted in blue. Looking at contributions to the dynamo this way is somewhat artificial.

meaning that can be derived from looking at the separate contributions to the parallel dynamo is approximately how much the parallel and perpendicular fluctuations each contribute to the parallel dynamo. It is not well understood why the contribution from the radial measurements appears to have the opposite sign as the contributions from the poloidal and toroidal measurements, and it does not occur to nearly the same extent in the standard RFP case (Fig. 5.5). The directions of the E_r and B_r measurements have been checked carefully.

The problems with the analysis caused by the region of discrete relaxation events

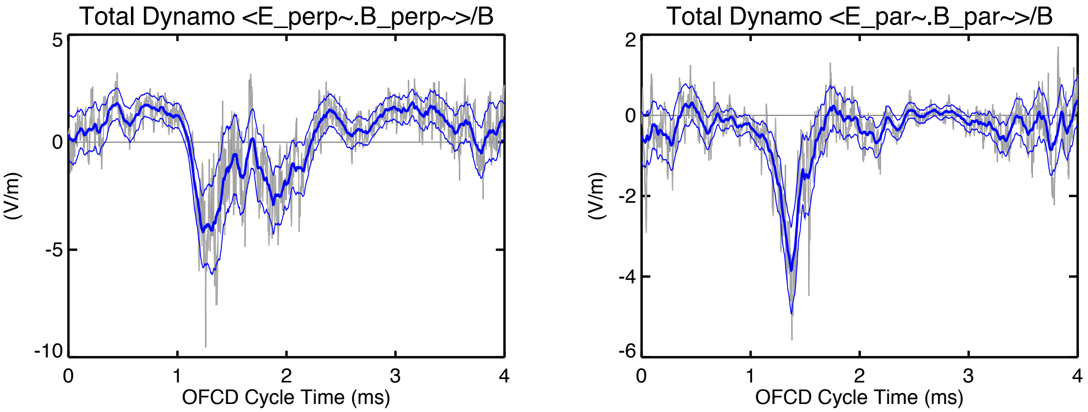

Figure 6.7: Contributions to the dynamo from the perpendicular and parallel components of $\mathbf{E}$ and $\mathbf{B}$ for the OFCD $\delta = +\pi/2$ ensemble. Smoothed versions of the signals and standard deviations of the mean $(\sigma/\sqrt{N})$ are overplotted in blue.

is clearly visible in the region $\sim 1ms < t <\sim 2.3ms$ in both the size of the fluctuations on the measurement of the dynamo and the size of the error bars. The error bars and fluctuations are $\sim 2\times$ as large during this period. Of course, this only accounts for random errors from the discrete relaxation events increasing the standard deviation of individual cycle measurements of $< \tilde{\mathbf{E}} \cdot \tilde{\mathbf{B}} > /B$. It is possible that the analysis method also has a systematic error during this period due to $< X > \neq \bar{X}$ that wouldn't be accounted for by these error bars.

The dynamo changes sign over the course of the cycle, as expected based on $\mathbf{E} - \eta \mathbf{J}$. However, there is substantial mode locking with a preferential phase at $\sim 3ms < t <\sim 4ms$ through $\sim 0ms < t <\sim 1ms$ so there could be systematic errors due to the analysis method during this period as discussed in Sec. 4.3. Systematic errors in the analysis method are thought to be small during $\sim 2.3ms < t <\sim 3ms$, and the parallel dynamo is positive, i.e. opposing the edge current. In plasmas without OFCD the dynamo in the edge always supports the edge current (Ch. 5). This is the first time the dynamo has been observed to oppose the current in the edge of the RFP.

Contributions to the dynamo from perpendicular and parallel components of $\tilde{\mathbf{E}}$ and $\tilde{\mathbf{B}}$ are shown in Fig. 6.7. The $< \tilde{\mathbf{E}}_{\parallel} \cdot \tilde{\mathbf{B}}_{\parallel} > /B_0$ contribution to the parallel dynamo is measured to be small relative to the contribution from $< \tilde{\mathbf{E}}_{\perp} \cdot \tilde{\mathbf{B}}_{\perp} > /B_0$ except near the sawtooth crash, which is similar to the standard case (Fig. 5.6). This implies that there is not a substantial contribution away from the crash from $< \tilde{\mathbf{U}}_{\perp} \times \tilde{\mathbf{B}}_{\parallel} \cdot \tilde{\mathbf{B}}_{\perp} >$.

The dynamo is compared to $\mathbf{E} - \eta\mathbf{J}$ in Fig. 6.8. $\mathbf{E} - \eta\mathbf{J}$ is negative when $\mathbf{E}$ is tending to increase the edge current and positive when it is tending to decrease the edge current since $\mathbf{J_0}$ is anti-parallel to $\mathbf{B_0}$ and the positive direction is parallel to $\hat{\mathbf{B}}_\mathbf{0}$. The sign of the dynamo has been reversed so that $\mathbf{E} - \eta\mathbf{J}$ matches the dynamo when they result in a balanced Ohm's law. Therefore, the dynamo is opposing the current when $- < \tilde{\mathbf{E}} \cdot \tilde{\mathbf{B}} > /B$ is negative on this graph and supporting the current when it is positive. The dynamo and $\mathbf{E} - \eta\mathbf{J}$ are smoothed and plotted over the unfiltered signals with error bars.

These measurements do not balance Ohm's law over the entire OFCD cycle, specifically at $\sim 0.3ms < t <\sim 1.1ms$, but that is also part of the period during the OFCD cycle where the analysis technique could have a systematic error due to mode locking with a preferential phase. Therefore, a conservative guess is that the mismatch during region I is probably due to this systematic error. The alternative is significant contributions from other unmeasured Ohm's law terms, the most likely of which is the diamagnetic dynamo. The Ohm's law terms match fairly well during the region of large sawteeth $\sim 1.1ms < t <\sim 2.3ms$. The larger error bars during this time period are probably due to the systematic error resulting from discrete relaxation events during this period.

Although $\sim 0 < t <\sim 0.3$ and the later part of $\sim 2.2ms < t <\sim 4ms$ suffer from the same mode-locking problem, a balance in Ohm's law is observed since the

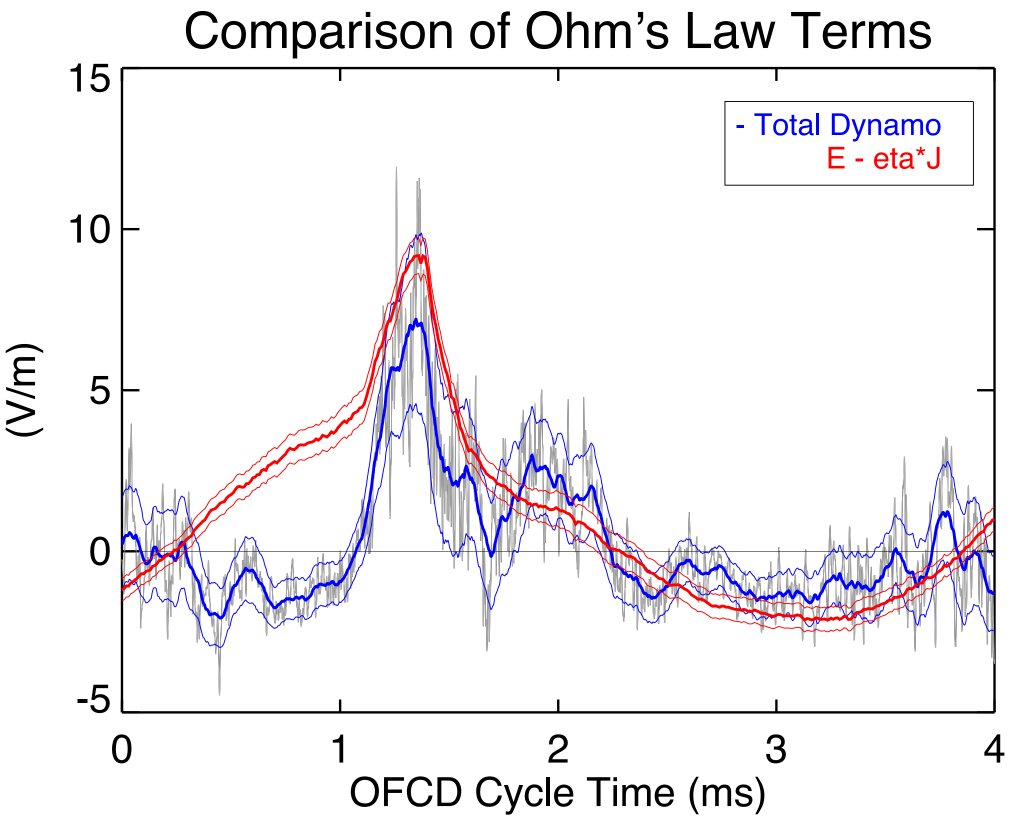

Figure 6.8: The dynamo, **E**, and $\eta\mathbf{J}$ are compared for the OFCD $\delta = +\pi/2$ ensemble to see if parallel Ohm's law is a good model for the edge of the plasma (neglecting other Ohm's law terms). The sign of the dynamo, $< \tilde{\mathbf{E}} \cdot \tilde{\mathbf{B}} > /B$, has been reversed so that Ohm's law balance is illustrated by $\mathbf{E} - \eta\mathbf{J}$ overlaying $- < \tilde{\mathbf{E}} \cdot \tilde{\mathbf{B}} > /B$. Smoothed signals and standard deviations of the mean $(\sigma/\sqrt{N})$ are overplotted in red and blue.

smoothed signals overlay during this period to within a standard deviation. The analysis technique is well trusted only at $\sim 2.3ms < t <\sim 3ms$ so it is more accurate to say that Ohm's law is observed to balance during this period. This is also a period during which the dynamo is opposing the current and the external electric field is supporting it. Therefore, at $\sim 2.3ms < t <\sim 3ms$ the dynamo, along with $\mathbf{E} - \eta\mathbf{J}$, is observed to balance parallel Ohm's law in the edge at the same time that the dynamo opposes the parallel current in the edge.

6.1.3 Hall Dynamo and MHD Dynamo

The parallel Hall dynamo, $- < \tilde{\mathbf{J}} \times \tilde{\mathbf{B}} >_\parallel /(n_e e)$, is measured using the dynamo probe while the parallel MHD dynamo, $< \tilde{\mathbf{v}} \times \tilde{\mathbf{B}} >_\parallel$, is calculated using the parallel dynamo, the parallel Hall dynamo, and Eq. 1.10 rather than being measured directly. The RMS values of $\tilde{\mathbf{J}}$ and $\tilde{\mathbf{B}}$ used in the Hall dynamo calculation are shown in Fig. 6.9. B_ϕ oscillates between $-0.04T < B_\phi < 0T$ and B_θ between $-0.11T < B_\theta < -0.09T$ over the OFCD cycle (Fig. 6.4) so the relative contribution to the parallel Hall dynamo by the different components of $\tilde{\mathbf{J}}$ and $\tilde{\mathbf{B}}$ change accordingly. The fluctuation RMS values increase during the sawtooth region $1.0ms < t < 2.3ms$ and most of the fluctuations also increase and decrease with the tearing mode growth and decay at $3.0ms < t < 4.0ms$ and $0.0ms < t < 1.0ms$. As usual, the Hall dynamo cannot be calculated simply using these signals and arithmetic since the relative phases of the signals needs to be accounted for in each event in the ensemble.

The Hall dynamo and implied MHD dynamo are plotted in Fig. 6.10. The high-frequency components of the two signals are not believed to be real. The noticeable mirroring of the high frequency components of the two signals is due to the fact that the MHD dynamo is calculated from the Hall dynamo and dynamo. The lowpass filtered signals, plotted in blue and red with error bars, more accurately represent the actual Hall dynamo and MHD dynamo. The calculation of the Hall dynamo using unfiltered signals has fairly large noise like the Hall dynamo during standard RFP when calculated with unfiltered signals.

During $0ms < t < 1ms$ and $2.8ms < t < 4ms$ the Hall dynamo and MHD dynamo have similar signs but a much larger amplitude than the RFP without OFCD. The two dynamos cross multiple times during the $1.0ms < t < 2.3ms$ sawtooth region but this is likely an artifact due to cycle to cycle variations of the sawtooth locations.

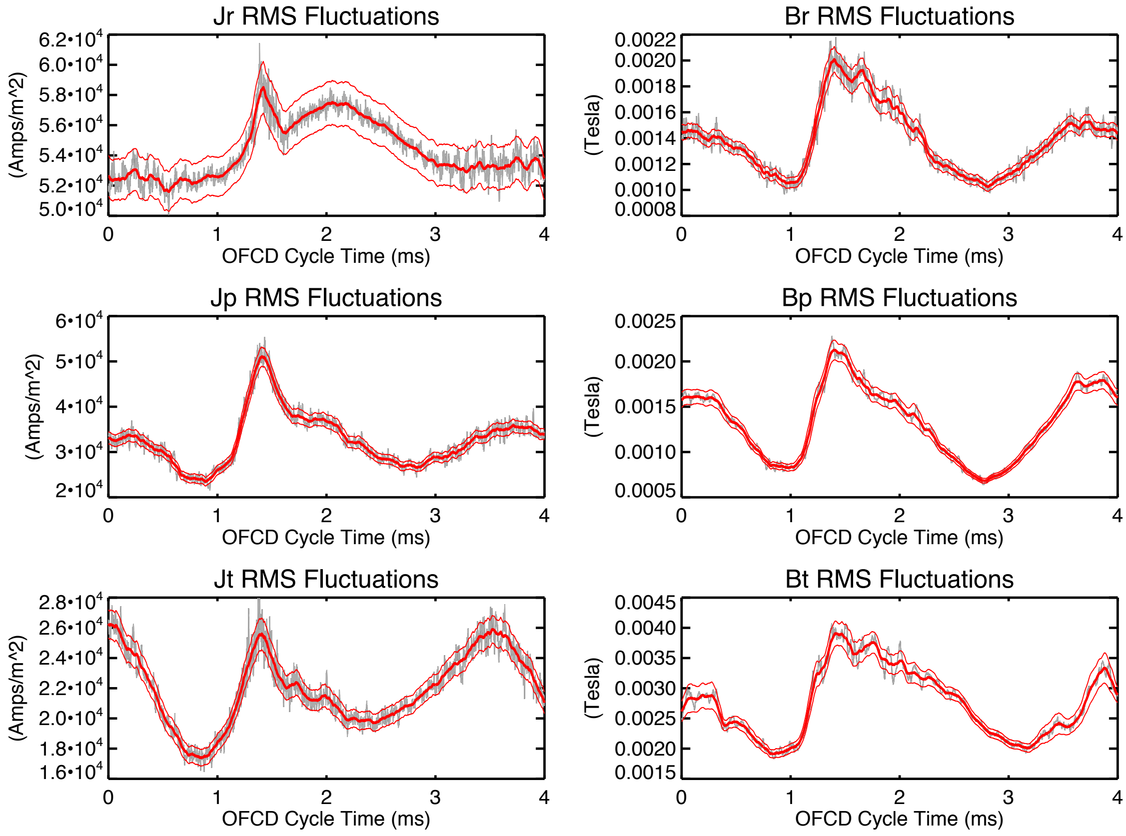

Figure 6.9: RMS amplitudes for $\tilde{\mathbf{J}}$ and $\tilde{\mathbf{B}}$ from Dynamo Probe used for Hall Dynamo calculation for the OFCD $\delta = +\pi/2$ ensemble. Smoothed signals and standard deviations of the mean $(\sigma/\sqrt{N})$ are overplotted in red.

On the other hand, after $t = 2.3ms$ there are no known problems with the analysis method so the dynamos crossing at $t \approx 2.5ms$ could be real. Similar behavior is observed in the OFCD $\delta = \pi/4$ and $\delta = 0$ ensembles presented in Sec. 6.2.

6.1.4 Helicity Flux

The magnetic helicity flux measured by the Dynamo probe during the OFCD $\delta = \pi/2$ cycle is shown in Fig. 6.11. Recall that MST's helicity is negative because the current in MST is antiparallel to the magnetic field. Therefore, in this case negative helicity flux is transporting negative helicity outward along the minor radius. It is

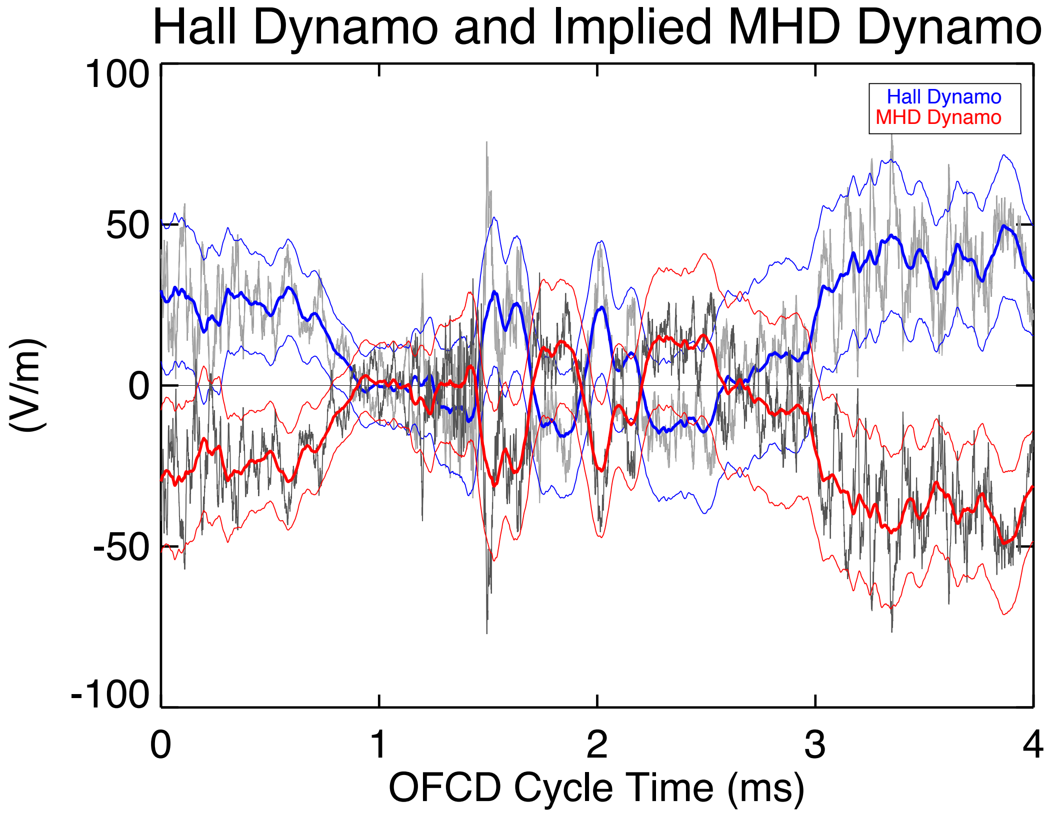

Figure 6.10: The Hall Dynamo and the assumed MHD Dynamo ($=<\tilde{\mathbf{E}}\cdot\tilde{\mathbf{B}}>/B_0+<\tilde{\mathbf{J}}\times\tilde{\mathbf{B}}>_\parallel/(n_e e)$) for the OFCD $\delta=+\pi/2$ ensemble. Smoothed signals and standard deviations of the mean ($\sigma/\sqrt{N}$) are overplotted in red and blue.

thought that the helicity flux would be positive at $\sim 2.3ms < t <\sim 3.7ms$ to correspond with the dynamo opposing the edge current. This is only observed around 3.5 ms, which is only part of when the dynamo opposes the current in the edge. However, the helicity flux has always been measured to be outward previously so this is a novel result. The positive signal at 1.5 ms could also be real and will be examined more closely in Sec. 6.3.1.

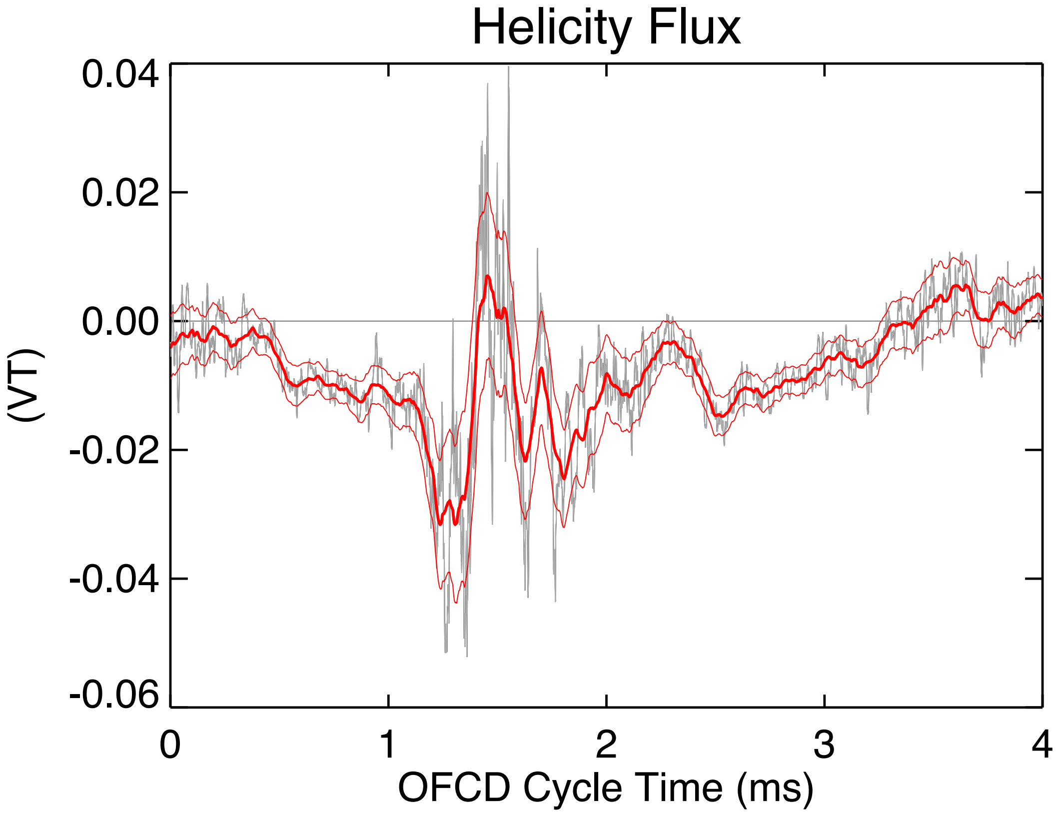

Figure 6.11: The helicity flux plotted with error bars for OFCD $\delta = +\pi/2$. The smoothed signal and standard deviations of the mean $(\sigma/\sqrt{N})$ are overplotted in red.

6.2 Other OFCD Phases

The dynamo and Ohm's law during other OFCD phases have many similarities to OFCD $\delta = \pi/2$. In this section, a summary of the dynamo and other Ohm's law terms will be presented for OFCD with $\delta = +\pi/4$, 0, and $-\pi/4$. Additional data for these ensembles corresponding to the other plots for OFCD $\delta = \pi/2$ can be found in appendix D. Comparison of Ohm's law for different phases of OFCD will demonstrate which features of the dynamo and Ohm's law are dependent on the phase. It is also interesting since $\delta = +\pi/2$ should theoretically produce the best current drive results but $\delta = +\pi/8$ has produced the best current drive results on MST (Sec. 2.2).

6.2.1 The Dynamo and Ohm's Law

Ohm's law is compared for the OFCD phases $\delta = \pi/2$, $\delta = \pi/4$, $\delta = 0$, and $\delta = -\pi/4$ in Fig. 6.12. All of the phases have similar behavior. The dynamo is observed to balance $\mathbf{E} - \eta\mathbf{J}$ from the beginning of region II, which begins around 1 ms with the large sawteeth, until sometime in region III (or region I in the case of $\delta = +\pi/2$). It is interesting that the onset of the mismatch occurs latest for $+\pi/2$ and earliest for $-\pi/4$ and 0.

The large mismatch between the dynamo in parts of regions I and III is a robust feature of all of the OFCD phases. During this period there are two potential problems with the analysis method. Mode locking with preferential mode phases relative to the probe location could create systematic errors with the measurement method. The presence of small sawteeth throughout region I could create errors due to $\bar{X} \neq < X >$. Or there could be a complex interaction between these two problems.

It is interesting that the period when Ohm's law isn't observed to balance is smallest for OFCD $\delta = +\pi/2$ even though the locked m=0 modes are largest for this phase. If the imbalance is caused by a systematic error in the analysis due to mode locking, then the phase between the $\tilde{\mathbf{E}}$ and $\tilde{\mathbf{B}}$ fluctuations must also strongly depend on the OFCD phase such that the difference between the measured dynamo and $\mathbf{E} - \eta\mathbf{J}$ is about the same amplitude for all OFCD phases and the duration of the mismatch is longer for phases with smaller amplitude m=0 modes. This scenario isn't impossible but does seem unlikely.

Another possible explanation for the consistent mismatch is that OFCD could be affecting the pressure such that $< \nabla\widetilde{p_e/(n_e e)} \cdot \tilde{\mathbf{B}} > /B_0$ is not small compared to the other terms in Ohm's law. In deriving that the dynamo, $< \tilde{\mathbf{v}} \times \tilde{\mathbf{B}} >_{\parallel} - < \tilde{\mathbf{J}} \times \tilde{\mathbf{B}} >_{\parallel}$

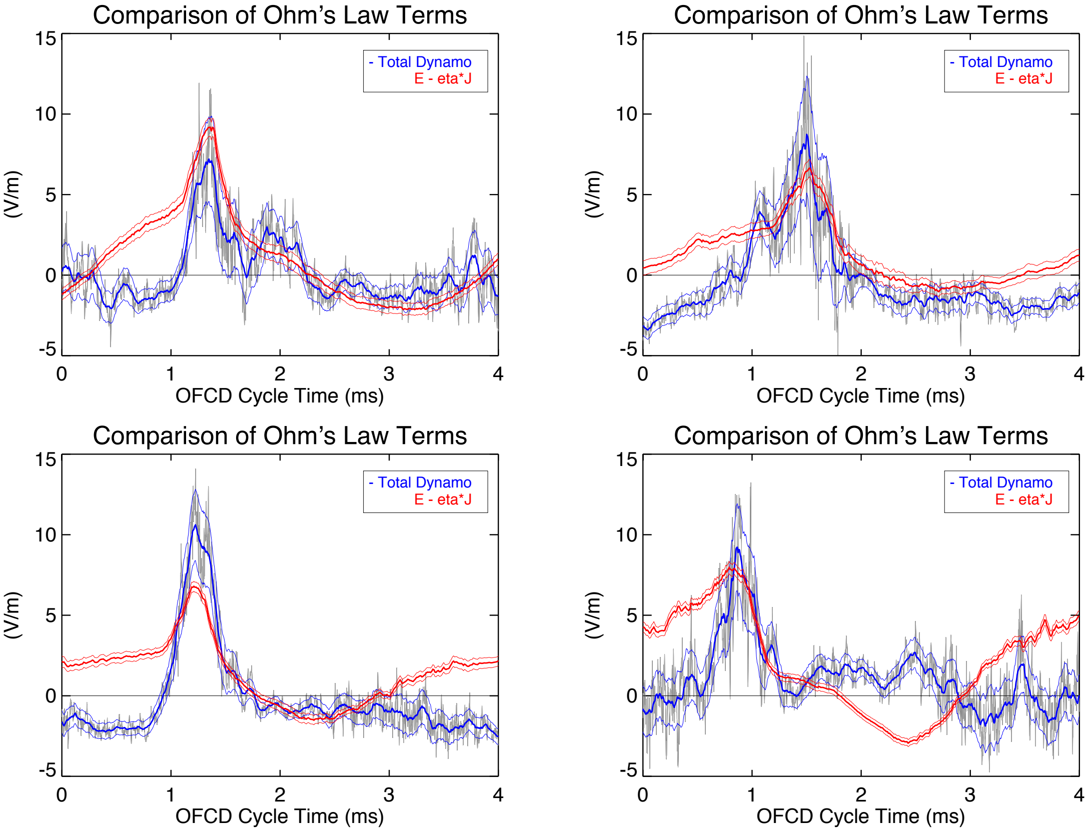

Figure 6.12: The dynamo, $\mathbf{E}$, and $\eta\mathbf{J}$ are compared for OFCD $\delta = \pi/2$ (top left), $\delta = \pi/4$ (top right), $\delta = 0$ (bottom left), and $\delta = -\pi/4$ (bottom right) to see if parallel Ohm's law is a good model for the edge of the plasma (neglecting other Ohm's law terms). The sign of the dynamo $< \tilde{\mathbf{E}} \cdot \tilde{\mathbf{B}} > /B$ has been reversed so that Ohm's law balance is illustrated by $\mathbf{E} - \eta\mathbf{J}$ overlaying $- < \tilde{\mathbf{E}} \cdot \tilde{\mathbf{B}} > /B$. Smoothed signals and standard deviations of the mean $(\sigma/\sqrt{N})$ are overplotted in red and blue.

$/(n_e e)$, is equal to $< \tilde{\mathbf{E}} \cdot \tilde{\mathbf{B}} > /B_0$ (Eq. 1.10), it was assumed that $< \eta \tilde{\mathbf{J}} \cdot \tilde{\mathbf{B}} > /B_0 \approx 0$, $< \widetilde{\nabla p_e} \cdot \tilde{\mathbf{B}} > /(n_e e B_0) \approx 0$ and that $\tilde{n}_e = 0$. The current term is measured to be small with the Dynamo Probe (with η calculated using T_e from the Helicity Probe) during the entire OFCD cycle but the pressure term is not measured. If the pressure term is not small during $\sim 0ms < t < 1ms$ in the OFCD cycle then (ignoring $\tilde{n}_e$) we have $< \tilde{\mathbf{v}} \times \tilde{\mathbf{B}} >_{\parallel} - < \tilde{\mathbf{J}} \times \tilde{\mathbf{B}} >_{\parallel} /(n_e e) =< \tilde{\mathbf{E}} \cdot \tilde{\mathbf{B}} > /B_0 + < \widetilde{\nabla p_e} \cdot \tilde{\mathbf{B}} > /(n_e e B_0)$ during that period, and both terms on the right would need to be measured in lieu of measuring both the MHD dynamo and Hall dynamo directly.

At around 2 ms, $\mathbf{E} - \eta \mathbf{J}$ reverses direction in all cases. The dynamo reverses direction to match $\mathbf{E} - \eta \mathbf{J}$ in every case except $\delta = -\pi/4$. This provides further evidence that the measured dynamo term is opposing the current in the edge of the RFP, which has never been observed outside of these OFCD experiments. This shows that the dynamo is working to flatten the current profile as expected. It suggests that other factors are responsible for the OFCD phase dependence of the experimental current drive results (Fig. 2.5), which don't have the expected dependence on the cycle-average OFCD helicity injection (Eq. 1.31).

The parallel field contribution to the dynamo, $< \tilde{\mathbf{E}}_{\parallel} \cdot \tilde{\mathbf{B}}_{\parallel} > /B_0$, is shown in Fig. 6.13 for the four OFCD ensembles. This contribution is moderately small but not negligible except at the sawtooth crash, as can be seen by comparing to the entire dynamo in Fig. 6.12. This suggests that $< \tilde{\mathbf{U}}_{\perp} \times \tilde{\mathbf{B}}_{\parallel} \cdot \tilde{\mathbf{B}}_{\perp} >$ cannot be ignored, particularly at the sawtooth crash.

6.2.2 Hall Dynamo and MHD Dynamo

The Hall dynamo and the implied MHD dynamo ($=< \tilde{\mathbf{E}} \cdot \tilde{\mathbf{B}} > /B_0 + < \tilde{\mathbf{J}} \times \tilde{\mathbf{B}} >_{\parallel} /(n_e e)$) are compared in Fig. 6.14 for the same phases. The high frequency structure in the Hall dynamo and mirrored in the implied MHD dynamo is likely due to the

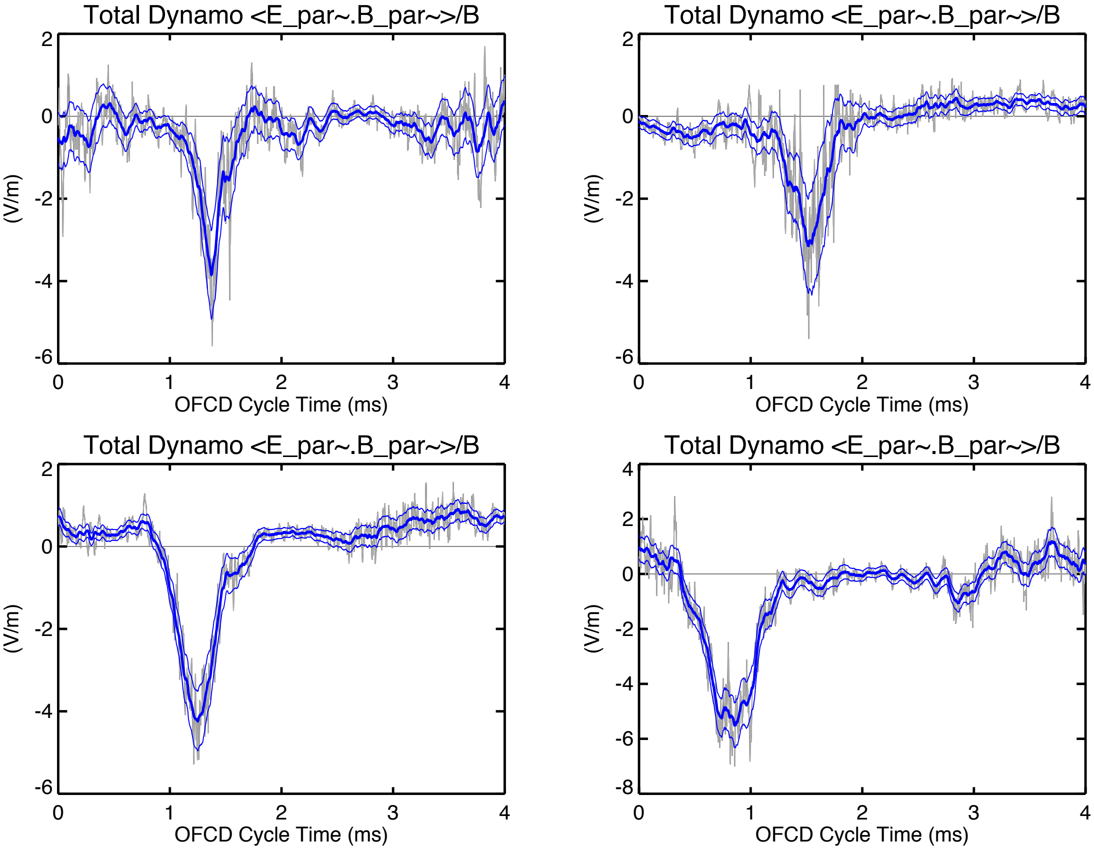

Figure 6.13: The contribution to the dynamo from parallel electromagnetic fields, $< \tilde{\mathbf{E}}_{\parallel} \cdot \tilde{\mathbf{B}}_{\parallel} > /B_0$, is shown for OFCD $\delta = \pi/2$ (top left), $\delta = \pi/4$ (top right), $\delta = 0$ (bottom left), and $\delta = -\pi/4$ (bottom right). This contribution is generally small but not negligible except at the sawtooth crash, as can be seen by comparing to the entire dynamo in Fig. 6.12. Recall that this term is thought to be equivalent to the contribution of $< \tilde{\mathbf{U}}_{\perp} \times \tilde{\mathbf{B}}_{\parallel} \cdot \tilde{\mathbf{B}}_{\perp} >$ to the dynamo EMF. Smoothed signals and standard deviations of the mean ($\sigma/\sqrt{N}$) are overplotted in blue.

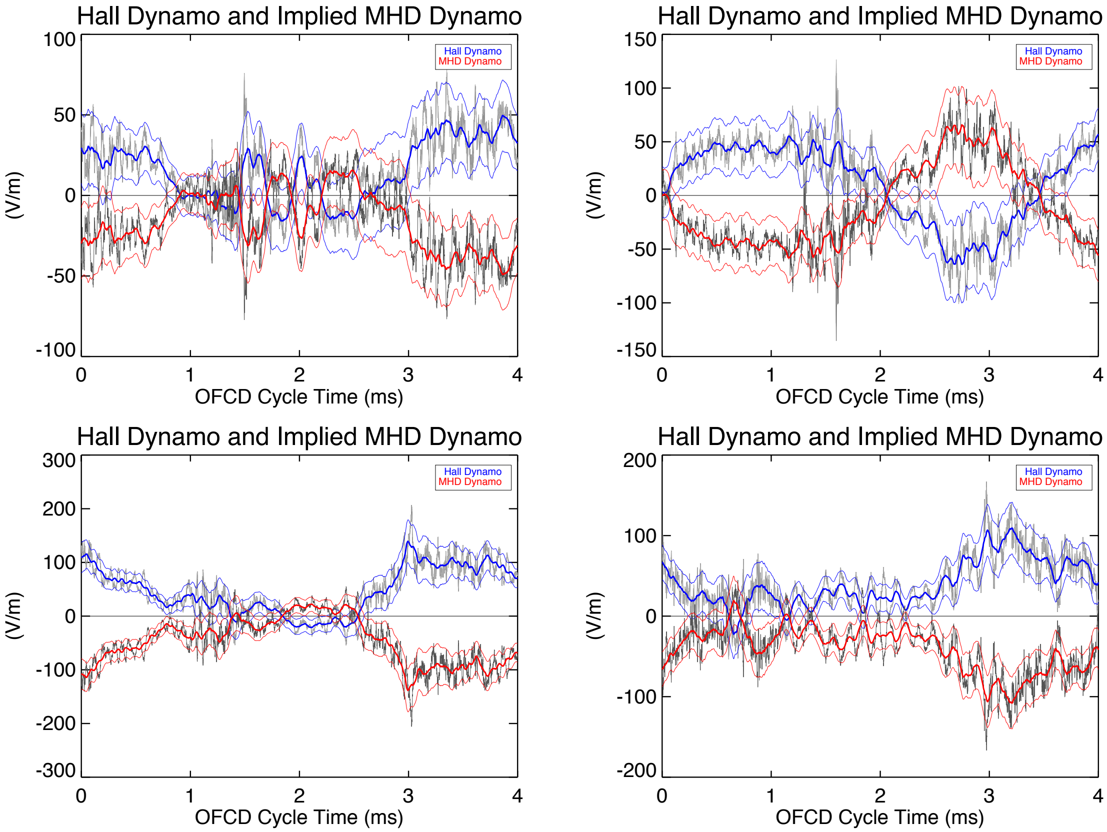

Figure 6.14: The Hall Dynamo and the assumed MHD Dynamo $(=<\tilde{\mathbf{E}}\cdot\tilde{\mathbf{B}}>/B_0+<\tilde{\mathbf{J}}\times\tilde{\mathbf{B}}>_{\|}/(n_e e))$ are compared for OFCD $\delta=\pi/2$ (top left), $\delta=\pi/4$ (top right), $\delta=0$ (bottom left), and $\delta=-\pi/4$ (bottom right). Smoothed signals and standard deviations of the mean $(\sigma/\sqrt{N})$ are overplotted in red and blue.

nature of the calculation more than the physical situation. They appear to behave in a similar way to the Hall dynamo and MHD dynamo in the MST RFP without OFCD for most of the cycle, i.e. the Hall dynamo is positive and thus opposes the current at this minor radius, the MHD dynamo is negative and supports the current, and the amplitude of the combined effect of the two dynamos generally has a smaller amplitude than either one separately.

One interesting feature of the Hall dynamo and MHD dynamo during OFCD is the period where the dynamo opposes the edge current. During part of this period

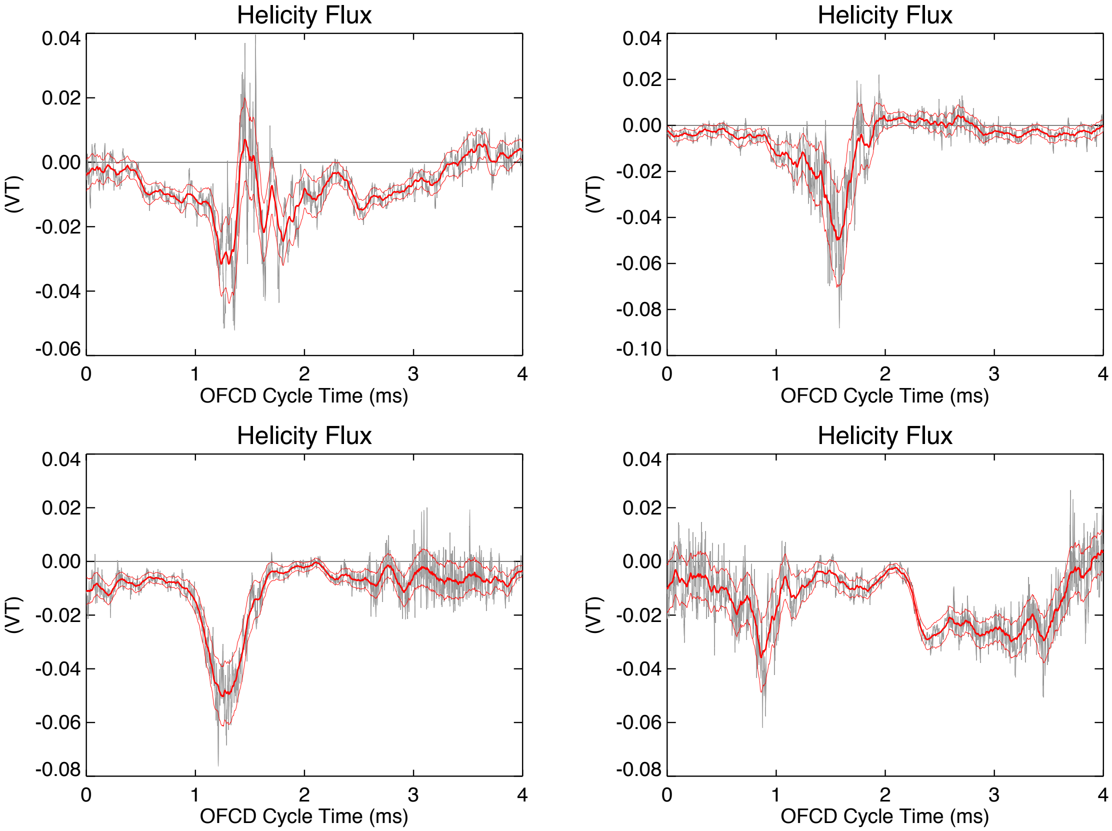

Figure 6.15: The helicity flux plotted with error bars are compared for OFCD $\delta = \pi/2$ (top left), $\delta = \pi/4$ (top right), $\delta = 0$ (bottom left), and $\delta = -\pi/4$ (bottom right). Smoothed signals and standard deviations of the mean ($\sigma/\sqrt{N}$) are overplotted in red.

in the cases of $\delta = \pi/2$, $\delta = \pi/4$, and perhaps $\delta = 0$, the Hall dynamo and MHD dynamo appear to switch signs so that briefly the Hall dynamo supports the current and the MHD dynamo opposes it. However, this behavior is not definitively observed since the error bars are large relative to the amount of separation between the two dynamos during this period. The error bars are expected to be substantially smaller when using highpass filtered signals for the calculation, as discussed in Sec. 5.5, but this is not reasonable for periods when the m=0 modes aren't rotating.

6.2.3 Helicity Flux

The helicity flux calculated from the four OFCD Dynamo Probe ensembles is shown in Fig. 6.15. A negative helicity flux indicates transport of negative helicity radially outward. The helicity flux is large and slightly noisier in the sawtooth region, as expected. It is fairly small everywhere else. In the $\delta = \pi/4$ ensemble, it becomes slightly positive as expected during $\sim 2ms < t < 3ms$, which roughy corresponds to the period when the dynamo is opposing the current in the edge. Similar behavior is observed in the $+\pi/2$ case but not in the $\delta = -\pi/4$ and $\delta = 0$ cases, which is not surprising since OFCD doesn't add net helicity to the plasma in the latter cases. The amplitude of the inward helicity flux never exceeds ~ 1 standard deviation of the measurement so, assuming no systematic errors, the likelihood that the helicity flux is inward is not more than $\sim 84\%$.

6.3 Addressing Data Analysis Issues During OFCD

In this section, variations of the data analysis will be used to explore possible issues with using the data analysis method $\tilde{\mathbf{X}} = \mathbf{X} - < \mathbf{X} >$ on the OFCD data and possible effects on the results presented in this chapter. The region of large sawteeth will be examined to confirm that the Ohm's law balance observed in region II is real. The effect of m=0 mode locking on the analysis results in regions I and III will be addressed and the error in the measurement from mode locking will be estimated.

6.3.1 OFCD Sawteeth

One approach to reduce some of the error in the analysis in the region of large sawteeth (region II) is to highpass filter the probe signals at 1 kHz before calculating the fluctuations. This is not valid in regions I and III, since then the m=0 tearing modes are not rotating, and is only relevant to region II. The dynamo calculated from highpass filtered signals is presented in Fig. 6.16 for the OFCD phases. The previous Ohm's law balance in region II ($\sim 1.1-2.5$ ms) is improved for $\delta = +\pi/2$, $+\pi/4$, and 0 and the signal-to-noise ratio is smaller, as expected. The Ohm's law balance is not as good for OFCD $\delta = -\pi/4$ as the other phases but is ok for the first half of region II. In the second half of region II for the $-\pi/4$ case, the m=0 mode frequencies are decreasing so the mismatch from 1.8-2.8 ms is expected from the highpass filtering. Figure 6.16 also shows the effect of highpass filtering on the calculation of $< \tilde{\mathbf{E}} \cdot \tilde{\mathbf{B}} > /B_0$ for the rest of the OFCD phases when the m=0 modes are locked.

It is useful to look at the Hall dynamo calculated from highpass filtered signals for the OFCD cycle since it substantially reduces the noise on this particular measurement. The Hall and MHD dynamos are calculated using probe signals that are highpass filtered at 1 kHz and are plotted in Fig. 6.17. Again, the analysis technique is only valid for $\sim 1.0 - 2.5$ ms. Compared to the unfiltered calculation (Fig. 6.14), the amplitude and noise level of the Hall dynamo and the MHD dynamo implied by Ohm's law are substantially decreased. The Hall dynamo opposes the edge current while the MHD dynamo supports the edge current in the same way as the standard case. In regions I and III it is uncertain whether the filtered or unfiltered calculation is more accurate since the filtered calculation improves the relative calibrations between Bdot coils and the calculation of $\tilde{\mathbf{J}}$ while not filtering doesn't exclude contributions from large, locked m=0 modes. Therefore, it is difficult to come to any conclusions about the Hall and MHD dynamos in regions I and III.

Another method to confirm that the calculation the flux-surface averages of Ohm's law terms during OFCD sawteeth is accurate is to cue the ensemble time axis off of the time of the sawtooth. Sawteeth are selected from the OFCD ensembles during the time period $1.1ms < t < 1.8ms$ and ensembled with the sawtooth time set

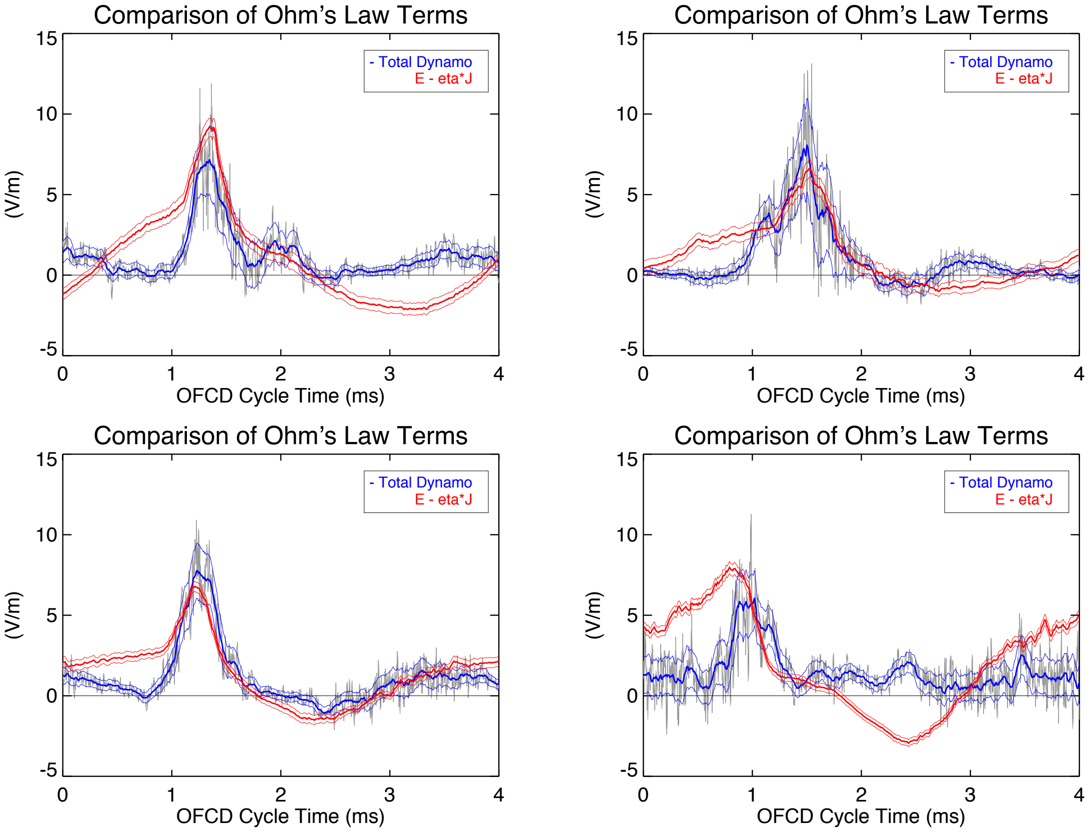

Figure 6.16: The dynamo, $\mathbf{E}$, and $\eta\mathbf{J}$ are compared for OFCD $\delta = \pi/2$ (top left), $\delta = \pi/4$ (top right), $\delta = 0$ (bottom left), and $\delta = -\pi/4$ (bottom right). The probe signals have been highpass filtered, which is only valid for $\sim$ 1-2.5 ms. The sign of the dynamo $< \tilde{\mathbf{E}} \cdot \tilde{\mathbf{B}} > /B$ has been reversed so that Ohm's law balance is illustrated by $\mathbf{E} - \eta\mathbf{J}$ overlaying $- < \tilde{\mathbf{E}} \cdot \tilde{\mathbf{B}} > /B$. Smoothed signals and standard deviations of the mean $(\sigma/\sqrt{N})$ are overplotted in red and blue.

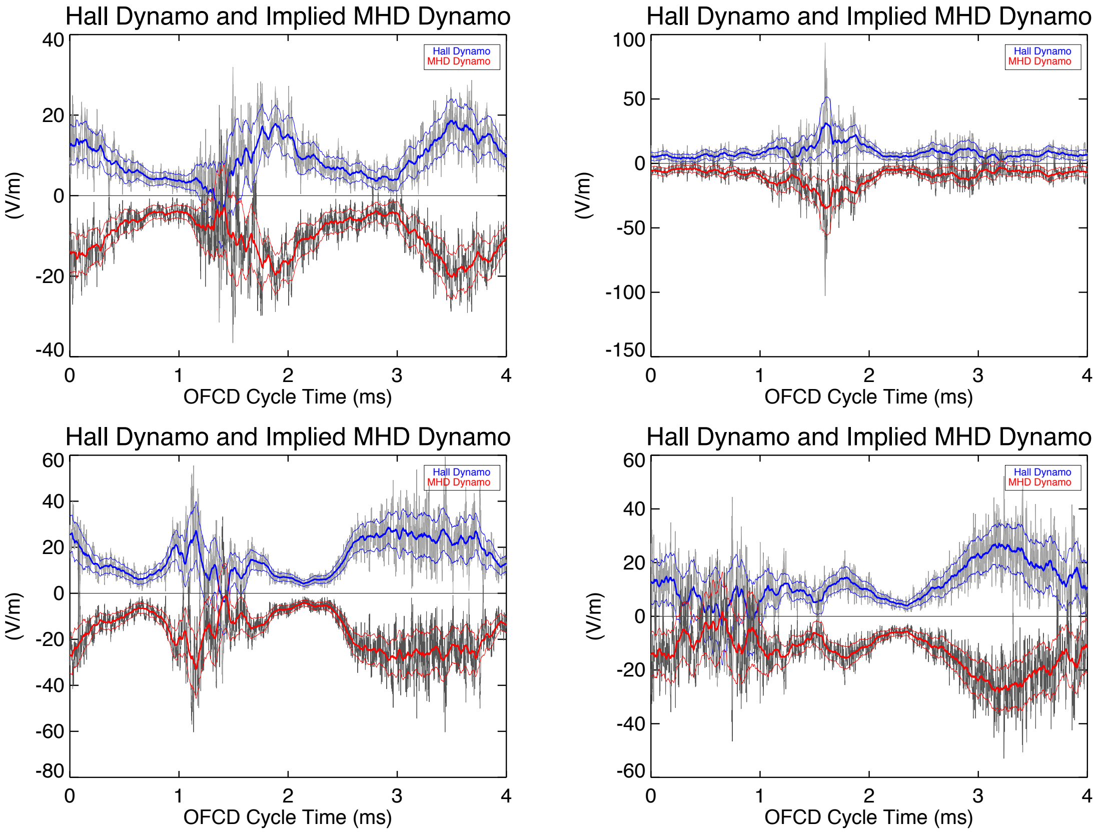

Figure 6.17: The Hall Dynamo and the assumed MHD Dynamo $(=<\tilde{\mathbf{E}}\cdot\tilde{\mathbf{B}}>/B_0+<\tilde{\mathbf{J}}\times\tilde{\mathbf{B}}>_\parallel/(n_e e))$ are compared for OFCD $\delta = \pi/2$ (top left), $\delta = \pi/4$ (top right), $\delta = 0$ (bottom left), and $\delta = -\pi/4$ (bottom right). The probe signals have been highpass filtered, which is only valid for $\sim$ 1-2.5 ms. During that period, the Hall dynamo opposes $\tilde{\mathbf{J}}_\parallel$ and the MHD dynamo supports it, as expected. Smoothed signals and standard deviations of the mean $(\sigma/\sqrt{N})$ are overplotted in red and blue.

as t=0. This is reasonable since the plasma equilibrium and fluctuations are dominated by the sawtooth during the crash so slight difference in the plasma equilibrium and fluctuations due to taking sawteeth from this time range in the cycle should be small. However, this does not hold true for the time before or after the $\sim 100\mu s$ sawtooth crash so only the period of $-0.1ms < t < 0.1ms$ is relevant. Highpass filtering the probe data will help to minimize this effect.

The dynamo and $\mathbf{E} - \eta\mathbf{J}$ are plotted in Fig. 6.18. As expected, the sawtooth spikes on all the Ohm's law terms are larger amplitude and $\sim 100\mu s$ wide compared to the $\sim 0.5ms$ wide spike in the sawtooth region of the OFCD cycle ensembles (Fig. 6.16). The spike in the measured dynamo term matches $\mathbf{E}-\eta\mathbf{J}$ to within experimental uncertainty, indicating that the Ohm's law is accurate during the sawteeth of each of the OFCD phases.

6.4 Diamagnetic Dynamo

A consistent imbalance in Ohm's law is observed during all OFCD phases in region I. This mismatch extends backward in time into region III for every phase except $+\pi/2$ (Fig. 6.12). It could be due to the diamagnetic dynamo, $< \widetilde{\nabla P_e} \cdot \tilde{\mathbf{B}} > /(n_e e)$, which comes from the turbulent electron diamagnetic drift, $\widetilde{\nabla P_e} \times \mathbf{B}_0$ [14]. The dynamo is always equal to $- < \tilde{\mathbf{v}} \times \tilde{\mathbf{B}} >_\parallel + < \tilde{\mathbf{J}} \times \tilde{\mathbf{B}} >_\parallel /(n_e e) = \mathbf{E} - \eta\mathbf{J}$. However, $< \tilde{\mathbf{E}} \cdot \tilde{\mathbf{B}} > /B \neq < \tilde{\mathbf{v}} \times \tilde{\mathbf{B}} >_\parallel - < \tilde{\mathbf{J}} \times \tilde{\mathbf{B}} >_\parallel /(n_e e)$ if OFCD influences the pressure during this time period such that $< \widetilde{\nabla P_e} \cdot \tilde{\mathbf{B}} > /(n_e e B_0)$ is large. If the potential problems with the analysis method aren't an issue, then either OFCD is altering the pressure such that this pressure term is of the same order as $< \tilde{\mathbf{E}} \cdot \tilde{\mathbf{B}} > /B_0$, or the two-fluid Ohm's law used in this thesis is not a good model for the edge plasma during this part of the OFCD cycle.

Note that contributions from $\tilde{n}_e$ to the diamagnetic dynamo and Hall dynamo

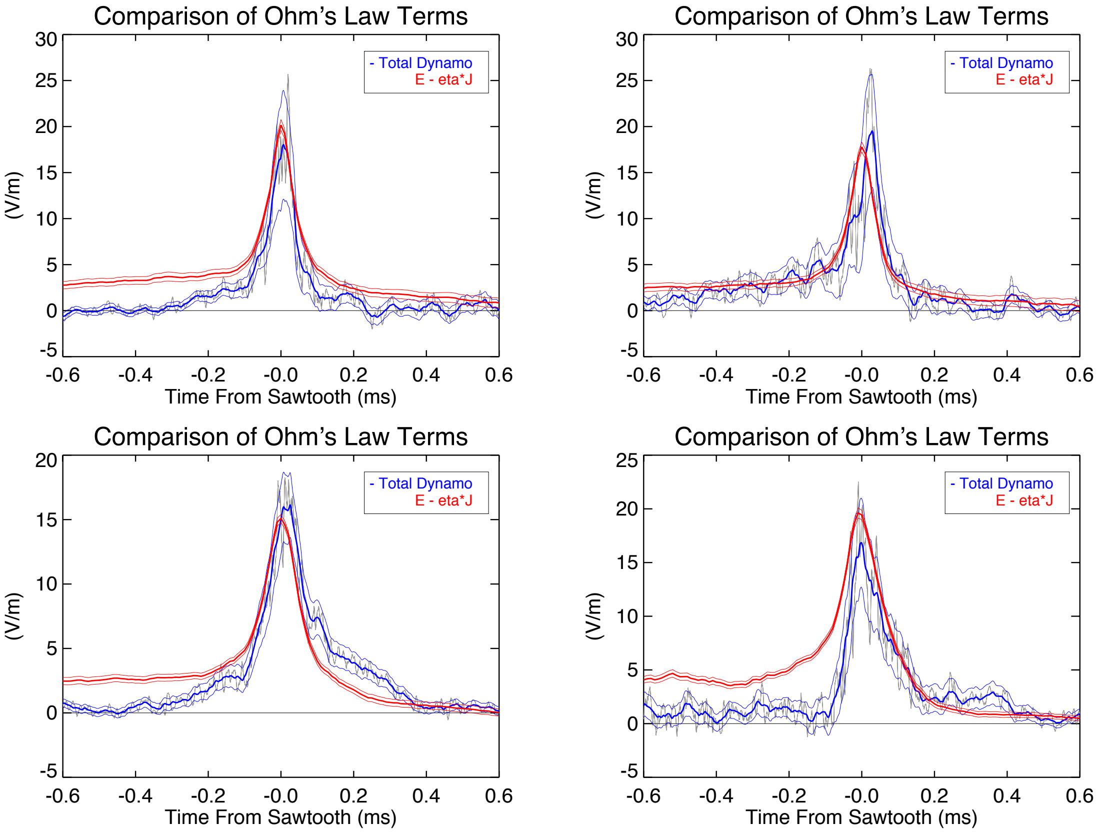

Figure 6.18: The dynamo, $\mathbf{E}$, and $\eta\mathbf{J}$ are compared for OFCD $\delta = \pi/2$ (top left), $\delta = \pi/4$ (top right), $\delta = 0$ (bottom left), and $\delta = -\pi/4$ (bottom right) sawteeth to see if parallel Ohm's law is a good model for the edge of the plasma (neglecting other Ohm's law terms). The sign of the dynamo $< \tilde{\mathbf{E}} \cdot \tilde{\mathbf{B}} > /B$ has been reversed so that Ohm's law balance is illustrated by $\mathbf{E} - \eta\mathbf{J}$ overlaying $- < \tilde{\mathbf{E}} \cdot \tilde{\mathbf{B}} > /B$. Smoothed signals and standard deviations of the mean $(\sigma/\sqrt{N})$ are overplotted in red and blue.

have been neglected in the previous paragraph. Historically, the contributions from $\tilde{n}_e$ have also been neglected when measuring these terms on MST. In principle, contributions from $\tilde{n}_e$ could be significant for the diamagnetic dynamo and the Hall dynamo but were not measured in this work.

It was noted that the strength of the diamagnetic dynamo is correlated with the electron mean free path normalized to the plasma size, or λ_e/a, by measuring the diamagnetic dynamo in three different RFPs (MST, Repute, TPE). A significant diamagnetic dynamo was observed only when $\lambda_e/a < 1$ [16] and was never observed in MST, regardless of density and temperature. Assuming that $\lambda_e/a < 1$ is a good indicator of when the diamagnetic dynamo is significantly large, the electron mean free path is calculated in cgs units as [51]

$$\lambda_{ee} = 23.5 - ln(n_e^{1/2}T_e^{-5/4}) - (10^{-5} + (ln(T_e) - 2)^2/16)^{1/2} \tag{6.1}$$

and normalized to the MST minor radius, a.

Temperature and density measurements from the Helicity Probe TLP are used to calculate λ_e during the partial OFCD experiments. The results, which are that λ_e/a is significantly greater than one (Fig. 6.19), indicate that either the diamagnetic dynamo is not significant in the partial OFCD experiments or that λ_e/a is actually not a good indicator of when the diamagnetic dynamo is large. If the diamagnetic dynamo is playing a role in Ohm's law balance during OFCD experiments, then that suggests the plasma is being altered in some way that causes the diamagnetic dynamo to become important just like it is on the smaller RFPs where it was directly observed.

It is not possible to come to a definitive conclusion about Ohm's law balance and a possible diamagnetic dynamo without measuring the diamagnetic dynamo directly. It has been shown that a diamagnetic dynamo explanation is consistent with previous

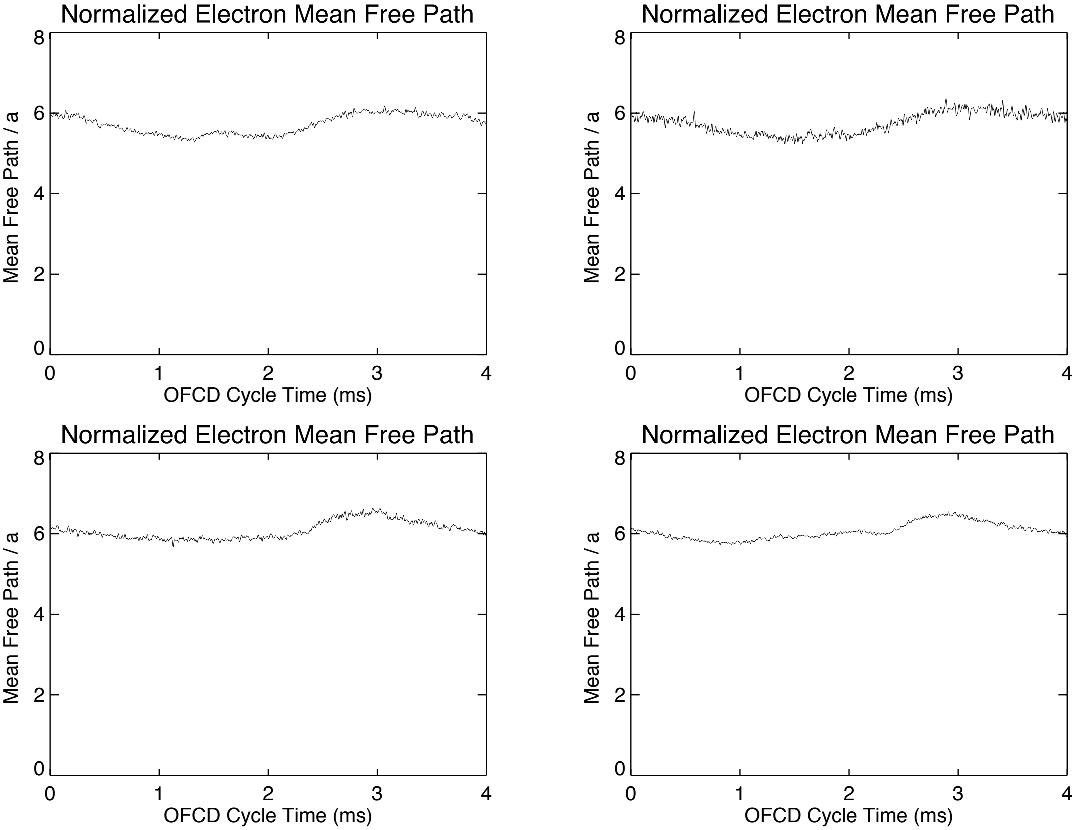

Figure 6.19: The electron mean free path normalized to the plasma size during partial OFCD experiments with $\delta = +\pi/2$, $+\pi/4$, 0, and $-\pi/4$.

observations on other RFPs [16]. Therefore, it is conceivable that the diamagnetic dynamo is contributing to the present measurements of Ohm's law during partial OFCD experiments. Another possibility is that one or multiple systematic problems with the data analysis are producing a consistent measurement error during this period of the OFCD cycle for all four OFCD phases. Further work will be required to determine if the source of the measured imbalance is due to unmeasured terms in Ohm's law or a systematic error in the data analysis.

Chapter 7

Conclusions and Future Work

Magnetic relaxation was studied in the Madison Symmetric Torus Reversed Field Pinch during partial Oscillating Field Current Drive experiments. A dynamo EMF, by which the plasma moves towards its relaxed state, was measured. It was compared to other terms in Ohm's law to better understand magnetic relaxation dynamics during partial OFCD experiments and in general.

7.1 Ohm's Law During Partial OFCD Experiments

Terms in two-fluid Ohm's law and other terms related to magnetic relaxation were measured in the edge with a novel insertable probe. Ohm's law is observed to balance with the terms considered during approximately half of the OFCD cycle for four separate OFCD phases ($\delta = +\pi/2$, $+\pi/4$, 0, and $-\pi/4$). The period of imbalance is only ~ 1 ms in duration for OFCD $\delta = +\pi/2$, ~ 2 ms in duration for $\delta = +\pi/4$ and $\delta = 0$, and the imbalance lasts for the majority of the cycle (~ 2.5 ms) for $\delta = -\pi/4$.

One possible explanation for the lack of balance between the measured Ohm's law terms is that m=0 tearing modes become large and locked for approximately half of the OFCD cycle. This might create a systematic error in the measurement. As the reversal parameter F becomes more negative, the OFCD electric field begins to support the current in the edge, the resonant surface for the m=0 modes moves away from the stabilizing conducting wall, and the m=0 modes are observed to grow to amplitudes similar to their amplitudes at the sawtooth crash. In addition, the m=0 modes are measured to have a preferential phase relative to the lab frame during this time. A roughly even phase distribution of the modes is one of the assumptions of the analysis method used to calculate the dynamo. Locking of m=0 modes with a preferential phase corresponding with large amplitudes might invalidate the dynamo measurement during this period. If this is the case then it is possible that $\mathbf{E}_\| - \eta\mathbf{J}_\| =< \tilde{\mathbf{E}} \cdot \tilde{\mathbf{B}} > /B_0$ throughout the entire OFCD cycle.

However, the observed Ohm's law imbalance is only moderately correlated with m=0 amplitude and mode locking. This is particularly evident when comparing Ohm's law for the four OFCD phases presented in this thesis. There is an observed imbalance in Ohm's law for $\delta = +\pi/4$ and 0 during approximately the same part of the OFCD cycle during which the m=0 modes are large and locked with a preferential phase. However, for $\delta = +\pi/2$ the period of observed imbalance is much shorter than the period of large, locked m=0 modes while for $\delta = -\pi/4$ the period of imbalance is significantly longer. Also, the size of the observed difference between $< \tilde{\mathbf{E}} \cdot \tilde{\mathbf{B}} > /B_0$ and $\mathbf{E}_\| - \eta\mathbf{J}_\|$ is not obviously correlated with the size of the m=0 modes for different OFCD phases while the duration of the observed imbalance is inversely correlated with the amplitude of the m=0 modes. A lack of correlation between m=0 mode behavior and Ohm's law imbalance does not necessarily imply a lack of causation. However, if m=0 mode locking with a preferential phase is causing the observed imbalance by invalidating the analysis method, then the m=0 effect on the analysis technique is more complicated than one might initially guess.

Based on these arguments, what could be a more plausible explanation for the imbalance in Ohm's law from the terms measured is that unmeasured Ohm's law terms, specifically the diamagnetic dynamo, $< \nabla \widetilde{P_e/(n_e} e) \cdot \tilde{\mathbf{B}} >$, become large enough to be significant during part of the OFCD cycle. The diamagnetic dynamo has been measured to be negligible previously in MST but has been found to be significant in smaller RFPs. It is plausible that the plasma is being altered in some way during the period of observed imbalance such that the diamagnetic dynamo becomes important, just as it is in smaller RFP plasmas. This is even more plausible since the period of imbalance is principally when the electric field is opposing the edge current and when F is increasing towards zero. Also, the imbalance has the longest duration for the anti-current drive case, $\delta = -\pi/4$.

7.2 Sawteeth During OFCD

Sawteeth are moderately well entrained by the OFCD cycle, but there is enough variation of sawtooth timing from cycle to cycle to theoretically create a systematic error in the measurement of the dynamo through $< \tilde{\mathbf{E}} \cdot \tilde{\mathbf{B}} > /B_0$. In addition, this spreads out the sawtooth over a few hundred microseconds, which increases the width and decreases the amplitude on all ensembled signals. When these issues are ignored, the dynamo is measured to balance $\mathbf{E}_{\|} - \eta \mathbf{J}_{\|}$ to within a standard deviation during the sawtooth region except for $\delta = 0$.

The issue of imperfect sawtooth entrainment is addressed in two separate ways. In one method, the ensemble time is determined by the sawtooth crash in order to better match the equilibrium from event to event during the sawtooth itself. This is reasonable since the equilibrium during an OFCD sawtooth event is dominated by the sawtooth rather than the OFCD cycle. In addition, the probe data is highpass filtered with a 1 kHz cutoff in order to remove low-frequency variations in the signals due to OFCD as well as other undesirable parts of the signals while not altering the 100 μs

sawtooth contribution to the signals. When this is done, the measured dynamo is a better match for the amplitude and shape of $\mathbf{E}_{\|} - \eta \mathbf{J}_{\|}$. In addition, the sawtooth is observed to have a larger amplitude and shorter duration than the OFCD cycle ensembles indicate.

A second method, highpass filtering the probe signals and timing the ensemble based on the OFCD cycle. This addresses the change in the equilibrium before and after the sawteeth but not during the sawteeth because there is not a separation of timescales between the sawteeth and measurements of toroidally rotating spatial variations in the plasma. This method does improve the match between the measured dynamo and $\mathbf{E}_{\|} - \eta \mathbf{J}_{\|}$, presumably because low-frequency cycle-to-cycle variation is adversely affecting the analysis when it is not removed by highpass filtering.

7.3 The Dynamo and Magnetic Relaxation

The dynamo is observed to support the plasma current in the edge during the majority of the OFCD cycle. During part of the OFCD cycle it is observed to oppose the edge current, which is the first time this has been observed in an RFP plasma. This opposition is expected since magnetic relaxation continuously attempts to move the plasma towards the relaxed state.

The contribution to the dynamo from parallel electromagnetic field fluctuations, $< \tilde{\mathbf{E}}_{\|} \cdot \tilde{\mathbf{B}}_{\|} > / B_0 \approx < \tilde{\mathbf{U}}_{\perp} \times \tilde{\mathbf{B}}_{\|} \cdot \tilde{\mathbf{B}}_{\perp} >$, was measured for the first time in the edge of MST. Unexpectedly, it was measured to produce a substantial contribution to the dynamo of a few volts per meter at the sawtooth crash. Its contribution to the dynamo in-between sawtooth crashes was minimal during standard plasmas and partial OFCD experiments.

The Hall dynamo is measured to generally oppose the current in the plasma edge during OFCD while the MHD dynamo implied by Ohm's law supports the edge current. The Hall dynamo and MHD dynamo largely cancel each other to produce a net effect that is much smaller in magnitude than the individual contribution of either one. These observations are consistent with previous measurements of the Hall dynamo and MHD dynamo during standard plasmas.

The fluctuation-induced magnetic helicity flux was measured during partial OFCD experiments. It is understood to be related to the dynamo. The measurements are consistent with this relationship since it mirrors the dynamo to some extent, and in a way that is not observed in standard plasmas. At the limit of experimental precision, it changes direction during a part of the OFCD cycle that roughly corresponds to when the dynamo is observed to oppose the edge current.

7.4 Ohm's Law During the Standard RFP

The best measurements to date of Ohm's law in the edge of the standard MST RFP were presented. The electric field, $\eta\mathbf{J}$, and dynamo measured by the Dynamo Probe demonstrate a match to within a standard deviation of the measurements throughout the sawtooth cycle. The measurements each have a standard deviation $\sigma/\sqrt{N} \approx 1$ V/m for signals that are a few volts per meter away from the crash and peak at ~ 10 V/m at the crash.

The Hall dynamo was confirmed to oppose the current in the edge while the MHD dynamo (inferred from Ohm's law and measurements of the Hall dynamo and $< \tilde{\mathbf{E}} \cdot \tilde{\mathbf{B}} > /B_0$) supported the edge current. Away from the sawtooth crash they were both 5-10 V/m and opposing one another to produce a combined effect of several volts per meter supporting the edge current. The magnetic helicity flux during the standard RFP was observed to match previous results.

7.5 Oscillating Field Current Drive

The dynamo has been directly measured to be capable of opposing the edge current in an RFP plasma. This is a requirement for an RFP plasma sustained solely by OFCD since OFCD adds current primarily to the plasma edge and relies on magnetic relaxation to flatten the current profile and sustain the current in the plasma core. The fact that the dynamo can oppose the current in the plasma edge is a promising sign for the feasibility of an RFP sustained solely by OFCD.

If the period during the OFCD cycle where Ohm's law is not measured to balance is a real effect and not due to a systematic error, it would imply that OFCD is momentarily changing the mechanism by which the plasma relaxes towards its preferential state. In particular, if the diamagnetic dynamo is significant during part of the OFCD cycle, the modification to the pressure profile that produces it could have implications for the applicability of OFCD to fusion plasmas.

7.6 Future Work

The source of the observed imbalance in Ohm's law during OFCD is uncertain. It could be due to a systematic error in the data analysis technique from the m=0 modes locking with a preferential phase. Alternately, it could be due to unmeasured dynamo terms in Ohm's law.

This issue can be addressed in two ways. First, other dynamo terms can be measured to confirm that they are insignificant. In particular, the diamagnetic dynamo should be measured during partial OFCD experiments on MST since it has been observed to be significant in smaller RFPs but measured to be small in MST during the standard RFP.

Secondly, a new analysis technique could be developed to measure fluctuations with an insertable probe that doesn't require an even distribution of m=0 mode phases. Initial attempts to develop a pseudospectral analysis method using least-squares fitting to account for the uneven mode phase distribution produced results with the right magnitude and some of the time-dependent features also observed in $\mathbf{E}_\parallel - \eta\mathbf{J}_\parallel$, but did not conclusively demonstrate a balance or imbalance in Ohm's law. More work is needed to validate the least-squares pseudospectral method.

OFCD with programmable power supplies instead of the tank circuits sustained by PFNs and ignitron switching could improve dynamo measurements during OFCD. Programmable power supplies would improve the reproducibility required by the analysis method used in this thesis and decrease the time needed to obtain the large data ensembles required for dynamo measurements. They would also greatly increase control of OFCD frequency and phase and would allow studies of OFCD with non-sinusoidal waveforms.

The Dynamo Probe is a valuable tool capable of measuring $\tilde{V}_{plasma}$ (with a sufficiently hot electron temperature distribution), $\tilde{\mathbf{E}}$, $\mathbf{B}$, and $\mathbf{J}$ at a single location in the plasma. Its capabilities are extremely valuable for measuring dynamo terms and other quantities of interest. All of the data in this thesis was collected at $r/a = 0.9$ with a plasma current of either 250 kA or 210 kA. It will be interesting to use the Dynamo Probe to measure dynamo terms at additional radii and during other plasma conditions.

The boron nitride shields protecting the capacitors and Bdot coils on the capacitive probe show significant wear after a few days of running, particularly at the tips. It is important that they be replaced approximately every three days of running since the capacitive probe gains depend on the thickness of the boron nitride shields. At higher plasma current or deeper insertion it is likely that the shields will wear out even faster. The boron nitride shields of larger diameter (>1”) single stalk probes require weeks or months of experimental runs in MST to show the same wear that the capacitive probe shields show after a few days. It is possible that surrounding the ends of all four stalks with one large piece of boron nitride (perhaps 3.5 cm diameter and 2 cm long) might substantially increase the lifetimes of the boron nitride shields, allowing measurements at deeper insertion or higher plasma current.

Bibliography

[1] Bevir, M. K., and J. W. Gray (1981) *Proceedings of the Reversed Field Pinch Theory Workshop* (LANL, Los Alamos).

[2] Ebrahimi, F., S. C. Prager, J. S. Sarff, and J. C. Wright (2003) Phys. Plasmas **10**, 999.

[3] Schnack, D. D., E. J. Caramana, and R. A. Nebel (1985) Phys. Fluids **28**, 321.

[4] Spitzer, L., Jr. (1962) *Physics of Fully Ionized Gases, 2nd Ed.* (Interscience, New York).

[5] Chapman, J. T. (1998) *Spectroscopic Measurement of the MHD Dynamo in the MST Reversed Field Pinch*, Ph.D. thesis, UW-Madison.

[6] Den Hartog, D. J., J. T. Chapman, D. Craig, G. Fiksel, P. W. Fontana, S. C. Prager, and J. S. Sarff (1999) Phys. Plasmas **6**, 1813.

[7] Ennis, D. A., D. Craig, S. Gangadhara, J. K. Anderson, D. J. Den Hartog, F. Ebrahimi, G. Fiksel, and S. C. Prager (2010) Phys. Plasmas **17** 082102.

[8] Ding, W. X., D. L. Brower, D. Craig, B. H. Deng, G. Fiksel, V. Mirnov, S. C. Prager, J. S. Sarff, and V. Svidzinski (2004) Phys. Rev. Lett. **93**, 045002.

[9] Fontana, P. W., D. J. Den Hartog, G. Fiksel, and S. C. Prager (2000) Phys. Rev. Lett. **85** 566.

[10] Kuritsyn, A., G. Fiksel, A. F. Almagri, S. C. Prager, J. S. Sarff, and T. D. Tharp (2007) *Proceedings of the 16th IEEE Pulse Power Conference* (IEEE, Alburqerque).

[11] Tharp, T. D. (2010) *Measurements of Nonlinear Hall-Driven Reconnection in the Reversed Field Pinch*, Ph.D. thesis, UW-Madison.

[12] Ji, H., A. F. Almagri, S. C. Prager, and J. S. Sarff (1994) Phys. Rev. Lett. **73**, 668.

[13] Ji, H., S. C. Prager, and J. S. Sarff (1995) Phys. Rev. Lett. **74**, 2945.

[14] Ji, H. (1999) Phys. Rev. Lett. **83**, 3198.

[15] McCollam, K. J. (2009) private communication.

[16] Ji, H., S. C. Prager, A. F. Almagri, J. S. Sarff, Y. Yagi, Y. Hirano, K. Hattori, and H. Toyama (1996) Phys. Plasmas **3**, 1935.

[17] Taylor, J. B. (1974) Phys. Rev. Lett. **33**, 1139.

[18] Jensen, T. H., and M. S. Chu (1984) Phys. Fluids **27**, 2881.

[19] Boozer, A. H. (1986) Phys. Fluids **29**, 4123.

[20] Taylor, J.B. (1986) Rev. Mod. Phys. **58**, 741.

[21] Antoni, V., D. Merlin, S. Ortolani, and R. Paccagnella (1986) Nucl. Fusion **26**, 1711.

[22] Furth, H. P., J. Killeen, and M. N. Rosenbluth (1963) Phys. Fluids **6**, 459.

[23] Coppi, B., J. M. Greene, and J. L. Johnson (1966) Nucl. Fusion. **6**, 101.

[24] Dexter, R. N., D. W. Kerst, T. W. Lovell, and S. C. Prager (1991) Fusion Technol. **19**, 131.

[25] Jarboe, T. R., W. T. Hamp, G. J. Marklin, B. A. Nelson, R. G. ONeill, A. J. Redd, P. E. Sieck, R. J. Smith, and J. S. Wrobel (2006) Phys. Rev. Lett. **97**, 115003.

[26] Jarboe, T. R. (1994) Plasma Phys. Controlled Fusion **36**

[27] McLean, H. S., S. Woodruff, R. H. Hooper, D.N. Bulmer, C. Holcomb, J. Moller, B. W. Stallard, R. D. Wood, and Z. Wang (2002) Phys. Rev. Lett. **88**, 125004.

[28] Raman, R., B. A. Nelson, M. G. Bell, T. R. Jarboe, D. Mueller, T. Bigelow, B. LeBlanc, R. Maqueda, J. Menard, M. Ono, and R. Wilson (2006) Phys. Rev. Lett. **97**, 175002.

[29] Battaglia, D. J., M. W. Bongard, R. J. Fonck, A. J. Redd, and A. C. Sontag (2009) Phys. Rev. Lett. **102**, 225003.

[30] Nelson, B. A., T. R. Jarboe, A. K. Martin, D. J. Orvis, J. Xie, C. Zhang, and L. Zhou (1995) Phys. Plasmas **2**, 2337.

[31] Harned, D. S., D. D. Schnack, H. R. Strauss, and R. A. Nebel (1988) Phys. Fluids **31**, 1979.

[32] Sonato, P., G. Chitarin, P. Zaccaria, F. Gnesotto, S. Ortolani, A. Buffa, M. Bagatin, W.R. Baker, S. Dal Bello, P. Fiorentin, L. Grando, G. Marchiori, D.

Marcuzzi, A. Masiello, S. Peruzzo, N. Pomaro, and G. Serianni (2003) Fusion Eng. Des. **66**, 161.

[33] Schoenberg, K. F., J. C. Ingraham, C. P. Munson, P. G. Weber, D. A. Baker, R. F. Gribble, R. B. Howell, G. Miller, W. A. Reass, A. E. Schofield, S. Shinohara, and G. A. Wurden (1988) Phys. Fluids **31**, 2285.

[34] McCollam, K. J., A. P. Blair, S. C. Prager, and J. S. Sarff (2006) Phys. Rev. Lett. **96**, 035003.

[35] Bellan, P. M. (1989) Nucl. Fusion **29**, 78.

[36] McCollam, K. J., J. K. Anderson, A. P. Blair, D. Craig, D. J. Den Hartog, F. Ebrahimi, R. OConnell, J. A. Reusch, J. S. Sarff, H. D. Stephens, D. R. Stone, D. L. Brower, B. H. Deng, and W. X. Ding (2010) Phys. Plasmas **17**, 082506.

[37] Ebrahimi, F., and S. C. Prager (2004) Phys. Plasmas **11**, 2014.

[38] Najmabadi, F., R. W. Conn, and R. A. Krakowski (1993) Fusion Eng. Des. **23**, 69.

[39] Nonn, P. D., A. P. Blair, K. J. McCollam, J. S. Sarff, and D. R. Stone (2011) Rev. Sci. Instrum. **82**, 064701.

[40] Choi, S., D. Craig, F. Ebrahimi, and S. C. Prager (2006) Phys. Rev. Lett. **96**, 145004.

[41] Craig, D. (2005) *Magnetic Mode Analysis in MST*, internal report.

[42] Tharp, T. D., A. F. Almagri, M. C. Miller, V. V. Mirnov, S. C. Prager, J. S. Sarff, and C. C. Kim (2010) Phys. Plasmas **17**, 120701.

[43] Hutchinson, I. H. (2002) *Principles of Plasma Diagnostics* (Cambridge)., 945.

[44] Stoneking, M. R. (1994) *Fast Electron Generation and Transport in a Turbulent, Magnetized Plasma*, Ph.D. thesis, UW-Madison.

[45] Miller, M. C. (2011) *Non-axisymmetric Flows and Transport in the Edge of MST*, Ph.D. thesis, UW-Madison.

[46] Beck, A. H., Ed. (1966) *Handbook of Vacuum Physics, Vol. 2* (Pergamon, Oxford).

[47] Dunaevsky, A., Y. Raitses, and N. J. Fisch (2003) Phys. Plasmas **10**, 2574.

[48] Hobbs, G. D., and J. A. Wesson (1967) Plasma Phys **9**, 85.

[49] Schmidt, J. A. (1968) Rev. Sci. Instrum. **39**, 1297.

[50] Schmidt, J. A., and D. W. Kerst (1971) *Capacitive-coupled Probe for Measuring Potentials in a Plasma*, United States Patent 3614606.

[51] Huba, J. D. (2009) *NRL Plasma Formulary* (Naval Research Laboratory, Washington, D.C.).

[52] Clayton, D. J. (2010) *Fast Electron Transport in Improved-Confinement RFP Plasmas*, Ph.D. thesis, UW-Madison.

[53] Kuritsyn, A., G. Fiksel, M. C. Miller, A. F. Almagri, M. Reyfman, and J. S. Sarff (2008) Rev. Sci. Instrum. **79**, 10F127.

[54] King, J. R., C. R. Sovinec, and V. V. Mirnov (2012) Phys. Plasmas **19**, 055905.

Appendix A

OFCD Complete Circuit Schematic

Here is a complete circuit schematic of one of the two OFCD powered oscillators. This circuit uses a novel ignitron switching method to sustain the tank (LC) circuit oscillation. See section 2.1 and [39] for more details.

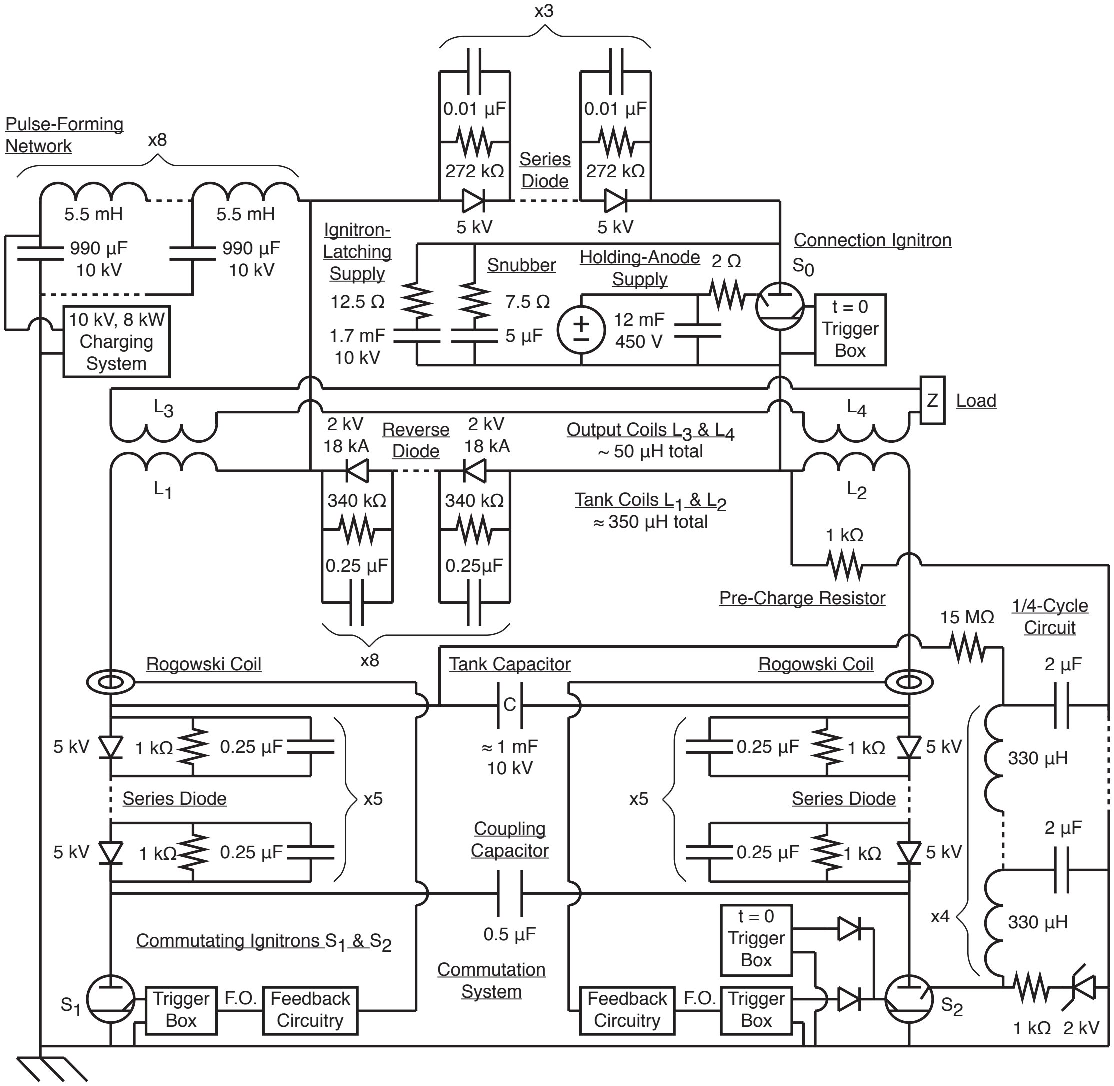

Figure A.1: ([39]) Complete OFCD circuit schematic

Appendix B

Probe Hardware

The circuit for the capacitive probe is shown below. The circuit diagram for the "Op Amp Circuit" is displayed in figure B.2. The theoretical complex, frequency-dependent gain for the capacitive probe is plotted in figures B.3 and B.4. The Helicity Probe triple Langmuir probe power supply circuit is shown in figure B.5.

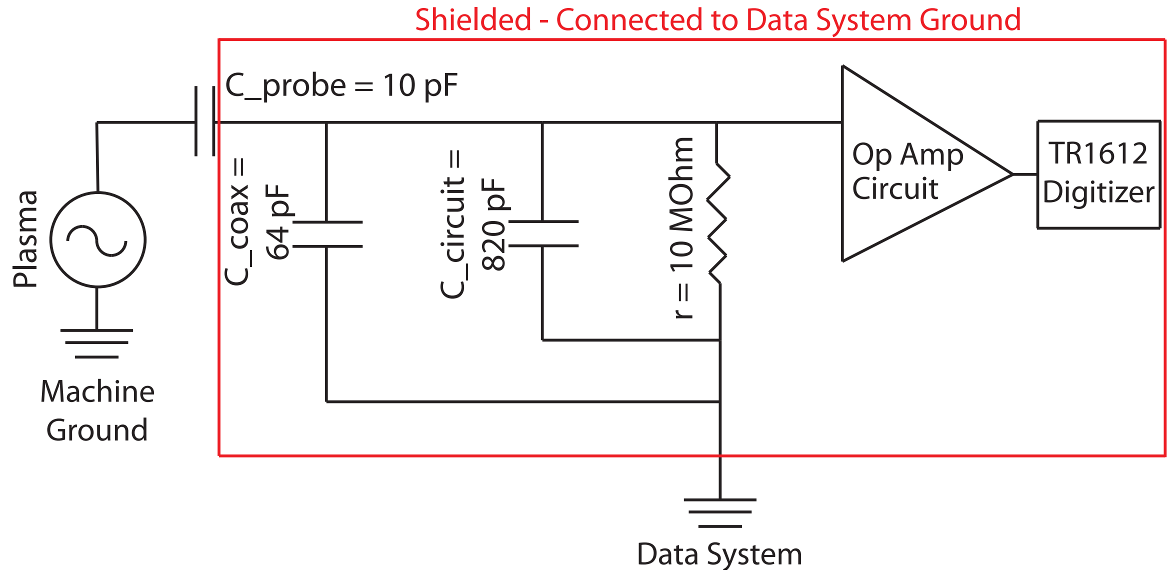

Figure B.1: Capacitive probe circuit drawing.

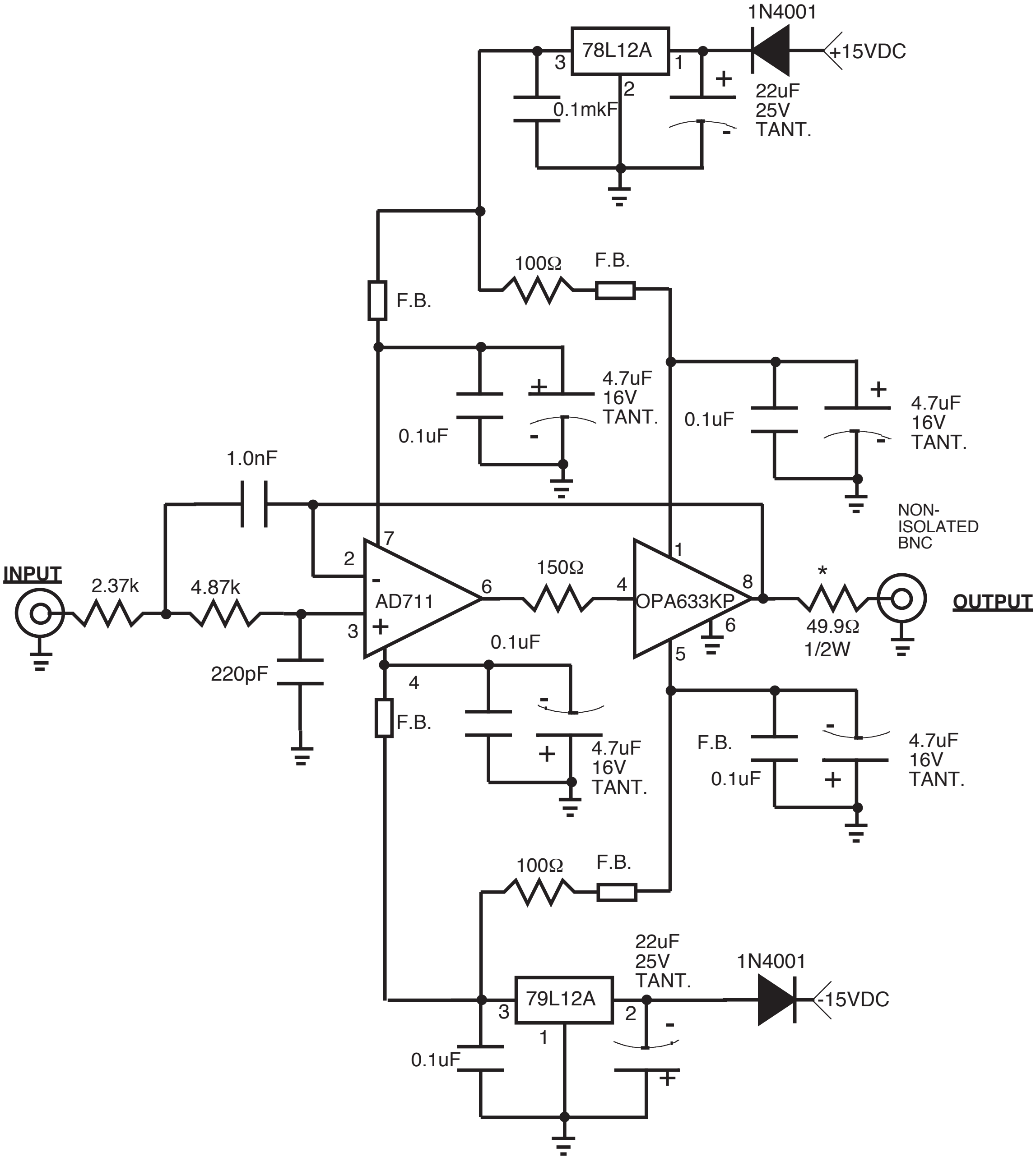

Figure B.2: Circuit diagram from the operational amplifier circuit used in the capacitive probe circuit (figure B.1). The circuit has a 3 dB point at 100 kHz.

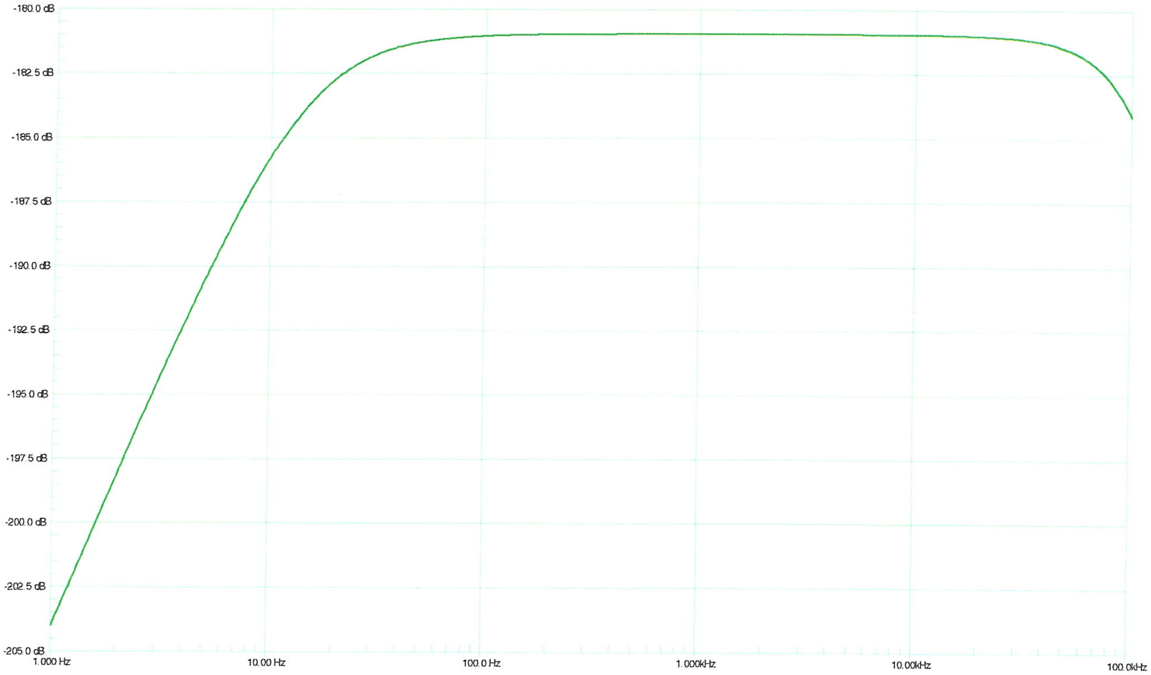

Figure B.3: Theoretical capacitive probe gain (amplitude). Axes are logarithmic. The domain is 1 Hz to 100 kHz and the range is -205 dB to -180 dB.

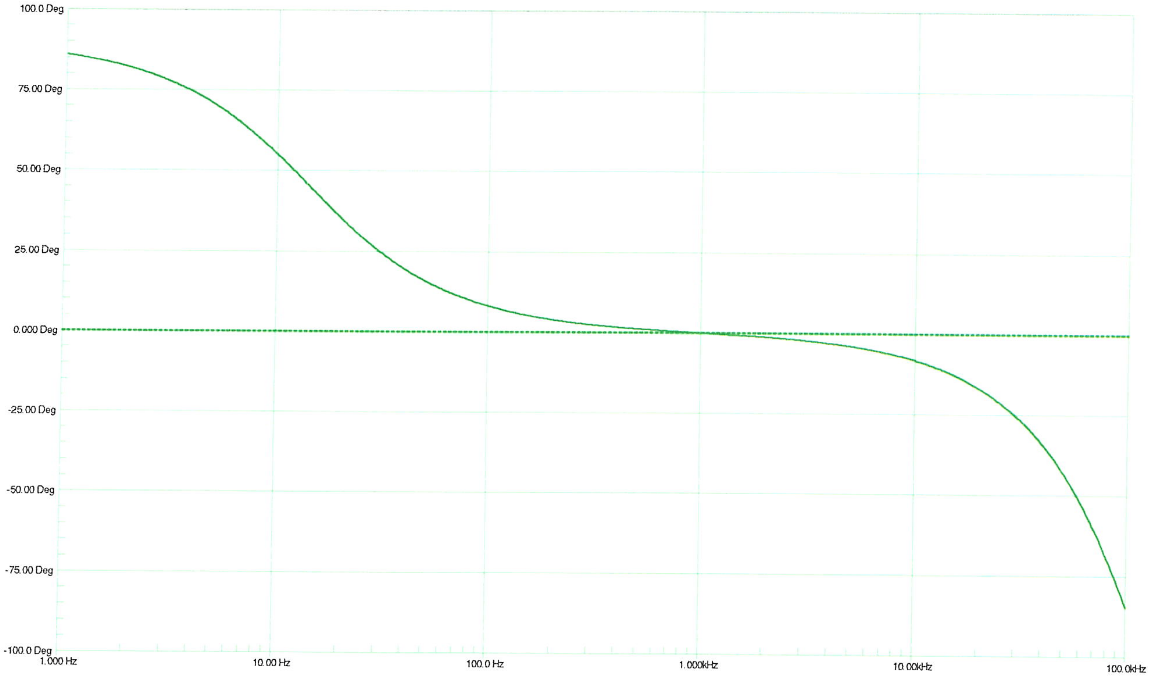

Figure B.4: Theoretical capacitive probe gain (phase). X axis is logarithmic. The domain is 1 Hz to 100 kHz and the range is -100 degrees to 100 degrees.

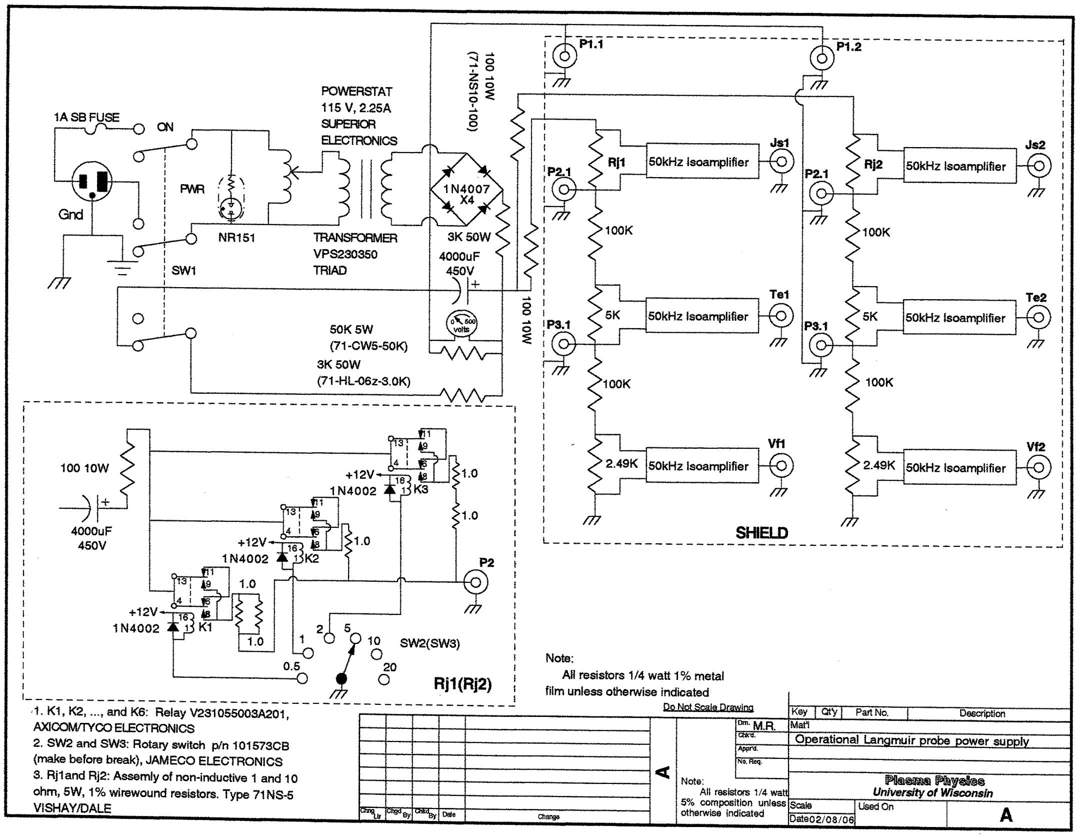

Note:
All resistors 1/4 watt 1% metal film unless otherwise indicated

Note:
All resistors 1/4 watt 5% composition unless otherwise indicated

1. K1, K2, ..., and K6: Relay V231055003A201, AXICOM/TYCO ELECTRONICS
2. SW2 and SW3: Rotary switch p/n 101573CB (make before break), JAMECO ELECTRONICS
3. Rj1and Rj2: Assemly of non-inductive 1 and 10 ohm, 5W, 1% wirewound resistors. Type 71NS-5 VISHAY/DALE

Figure B.5: Circuit diagram for circuit used with triple Langmuir probe.

Appendix C

Average Electric Field Near MST Inner Wall

The change in the magnetic field between the inner wall of the MST vacuum vessel and the probe measurement location at $r/a = 0.9$ should be approximately linear so Faraday's Law can be used to derive the electric field at the probe. A cylindrical coordinate system deformed into a torus (r, θ, ϕ) is used for this derivation.

$$\oint \mathbf{E} \cdot d\mathbf{l} = -\int \frac{\partial \mathbf{B}}{\partial t} \cdot d\mathbf{A} \tag{C.1}$$

$$\int_0^{2\pi} E_{\theta wall} a d\theta = -\int_0^a \frac{\partial B_\phi(r,t)}{\partial t}(2\pi r dr)$$

$$\int_0^{2\pi} E_{\theta wall} a d\theta = -\int_{r_{probe}}^a \frac{\partial B_\phi(r,t)}{\partial t}(2\pi r dr) - \int_0^{r_{probe}} \frac{\partial B_\phi(r,t)}{\partial t}(2\pi r dr)$$

$$\int_0^{2\pi} E_{\theta wall} a d\theta = -\int_{r_{probe}}^a \frac{\partial B_\phi(r,t)}{\partial t}(2\pi r dr) + \int_0^{2\pi} E_{\theta probe} r_{probe} d\theta$$

$$2\pi a E_{\theta wall} = -2\pi \int_{r_{probe}}^{a} \frac{\partial B_\phi(r,t)}{\partial t} r dr + 2\pi r_{probe} E_{\theta probe}$$

Assume that $d\mathbf{B}/dr = constant$ between the probe measurement location and the wall.

$$B_\phi(r,t) = B_{\phi probe}(t) + \frac{B_{\phi wall}(t) - B_{\phi probe}(t)}{a - r_{probe}}(r - r_{probe})$$

Combining (C) and (C) results in an equation for E_θ at the probe:

$$\begin{aligned} E_\theta(r = r_{probe}) = E_\theta(r = a) &+ (a/r_{probe} - 1)E_\theta(r = a) \\ &- \frac{\partial B_\phi(r = r_{probe})}{\partial t} \frac{(r_{probe} - a)(2r_{probe} + a)}{6r_{probe}} \\ &- \frac{\partial B_\phi(r = a)}{\partial t} \frac{(r_{probe} - a)(r_{probe} + 2a)}{6r_{probe}} \end{aligned} \tag{C.2}$$

We can derive $\mathbf{E}_\phi$ in a similar manner. The surface for integration in this case is slightly less intuitive. Select a rectangle in the $\mathbf{r}\phi$ plane with $d\mathbf{A}$ in the positive poloidal direction and $d\mathbf{l}$ beginning at $r = 0$ and $\phi = 0$, running in the $+\hat{\phi}$ along the axis of the torus, radially outward to $r = a$ at $\phi = 0$, running back in the $-\hat{\phi}$ direction, and finally radially inward to $r = 0$ at $\phi = 0$. Using Faraday's Law (C.1) we have:

$$\begin{aligned} -\frac{\partial}{\partial t}\int_0^a B_\theta(r) * 2\pi R_0 dr =& 2\pi R_0 * E_\phi(r = 0) + r * E_r(\phi = 0) \\ &- 2\pi R_0 * E_\phi(r = a) - r * E_r(\phi = 0) \end{aligned}$$

$$E_\phi(r = 0) - E_\phi(r = a) = -\frac{\partial}{\partial t}\int_0^{r_{probe}} B_\theta(r) dr - \frac{\partial}{\partial t}\int_{r_{probe}}^{a} B_\theta(r) dr$$

$$E_\phi(r=0) - E_\phi(r=a) = E_\phi(r=0) - E_\phi(r=r_{probe}) - \frac{\partial}{\partial t}\int_{r_{probe}}^{a} B_\theta(r)dr$$

$$B_\theta(r,t) = B_{\theta probe}(t) + \frac{B_{\theta wall}(t) - B_{\theta probe}(t)}{a - r_{probe}}(r - r_{probe})$$

$$\begin{aligned} E_\phi(r=r_{probe}) =& E_\phi(r=a) - \frac{\partial}{\partial t}\int_{r_{probe}}^{a} B_{\theta probe}(t)dr \\ & - \frac{\partial}{\partial t}\int_{r_{probe}}^{a} \frac{B_{\theta wall}(t) - B_{\theta probe}(t)}{a - r_{probe}}(r - r_{probe})dr \end{aligned}$$

Some calculus and algebra on the above equation yields E_ϕ at the probe:

$$E_\phi(r=r_{probe}) = E_\phi(r=a) - \frac{(a - r_{probe})}{2}\left(\frac{\partial B_{\theta wall}}{\partial t} + \frac{\partial B_{\theta probe}}{\partial t}\right) \qquad \text{(C.3)}$$

Appendix D

Additional Data For Probe Ensembles

Here are the additional graphs for the 250 kA deeply reversed RFP without OFCD and the OFCD $\delta = \pi/4$, 0, and $-\pi/4$ ensembles corresponding to graphs for the 200 kA standard reversal RFP without OFCD in chapter 5 and the OFCD $\delta = \pi/2$ ensembles presented in section 6.1. Probe data is highpass filtered with a 1 kHz cutoff to calculate fluctuations for sawtooth ensembles. Probe data is not highpass filtered for the OFCD cycle ensembles except to calculate the Hall dynamo and implied MHD dynamo, since this improves the calculation of $\mathbf{J} = \nabla \times \mathbf{B}/\mu_0$.

D.1 OFCD $\delta = \pi/2$

D.1.1 Sawtooth Ensemble

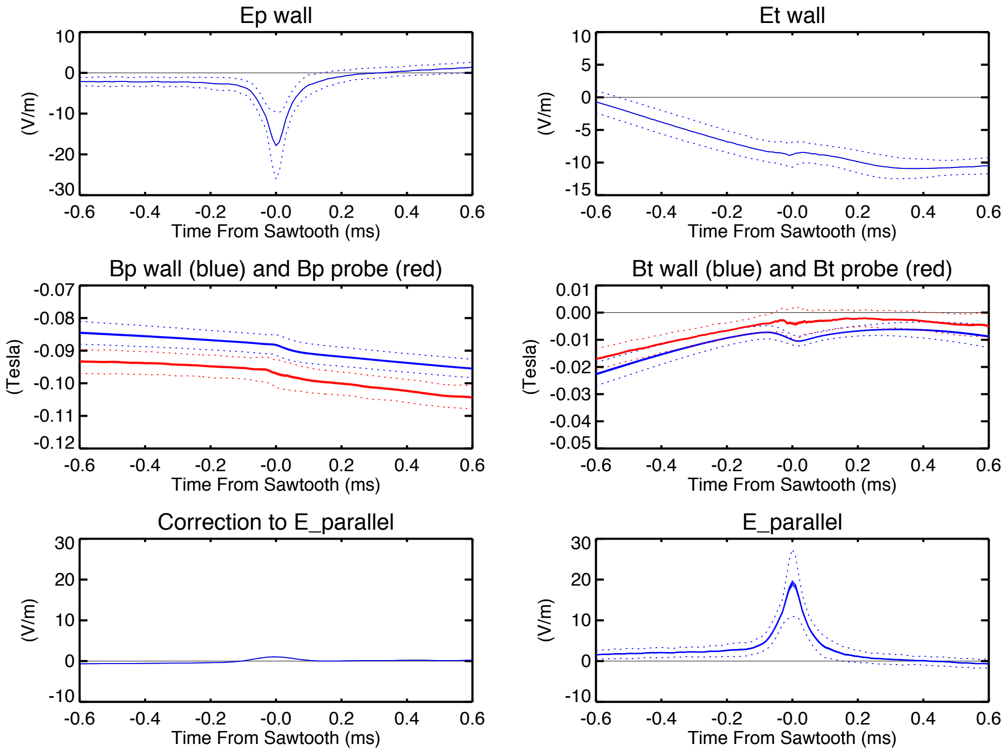

Figure D.1: Parallel electric field data, OFCD $\delta = +\pi/2$ sawtooth.

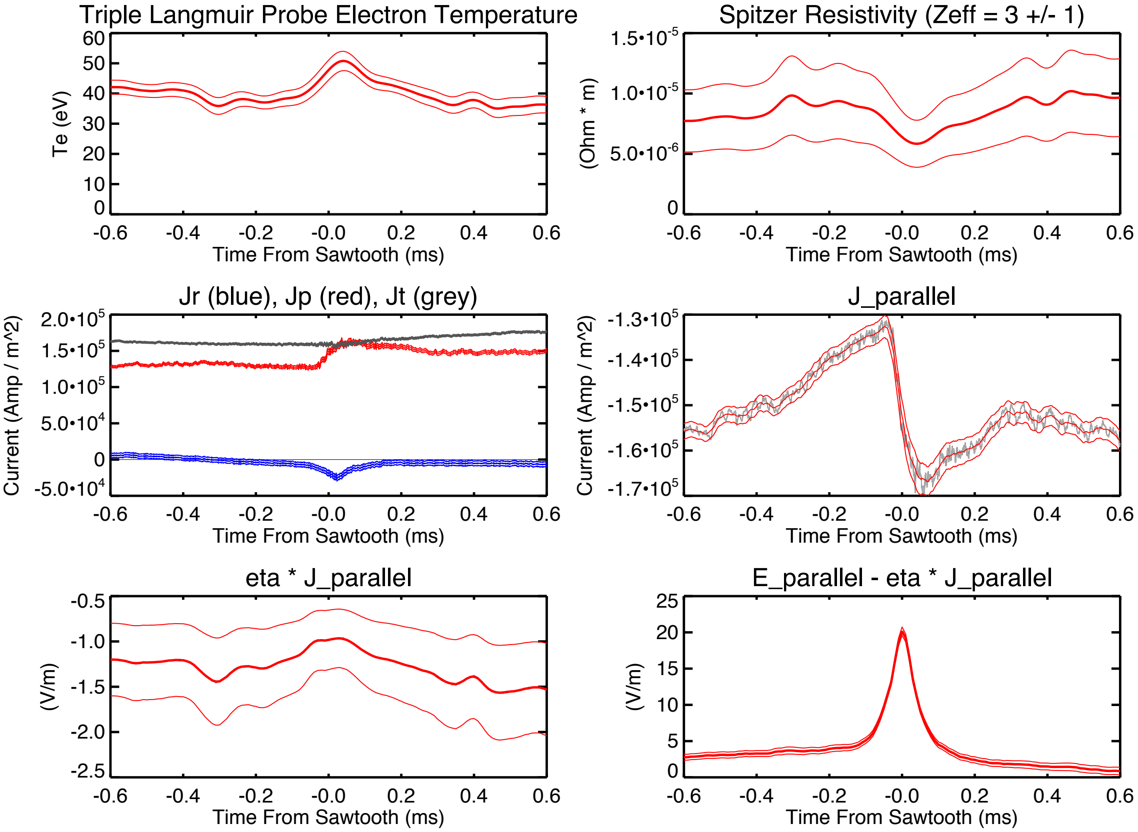

Figure D.2: Probe $\eta \mathbf{J}$ data, OFCD $\delta = +\pi/2$ sawtooth.

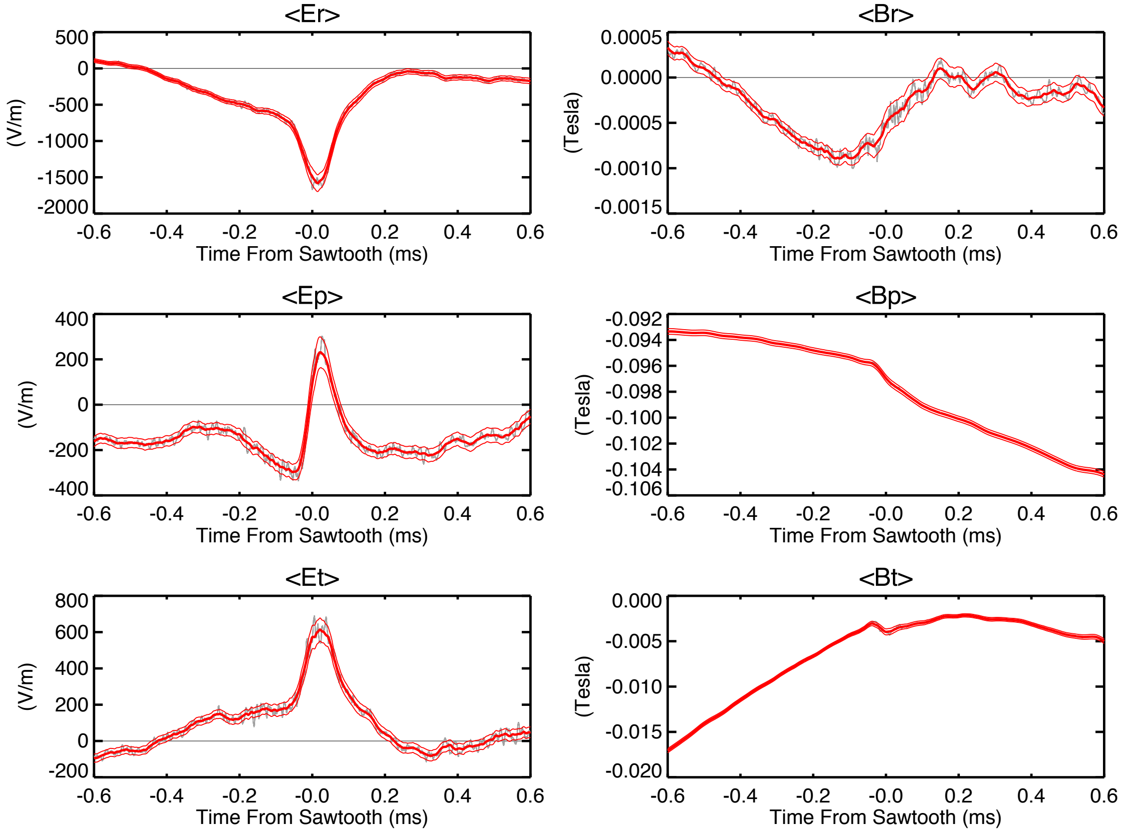

Figure D.3: Dynamo Probe $< \mathbf{E} >$ and $< \mathbf{B} >$, OFCD $\delta = +\pi/2$ sawtooth.

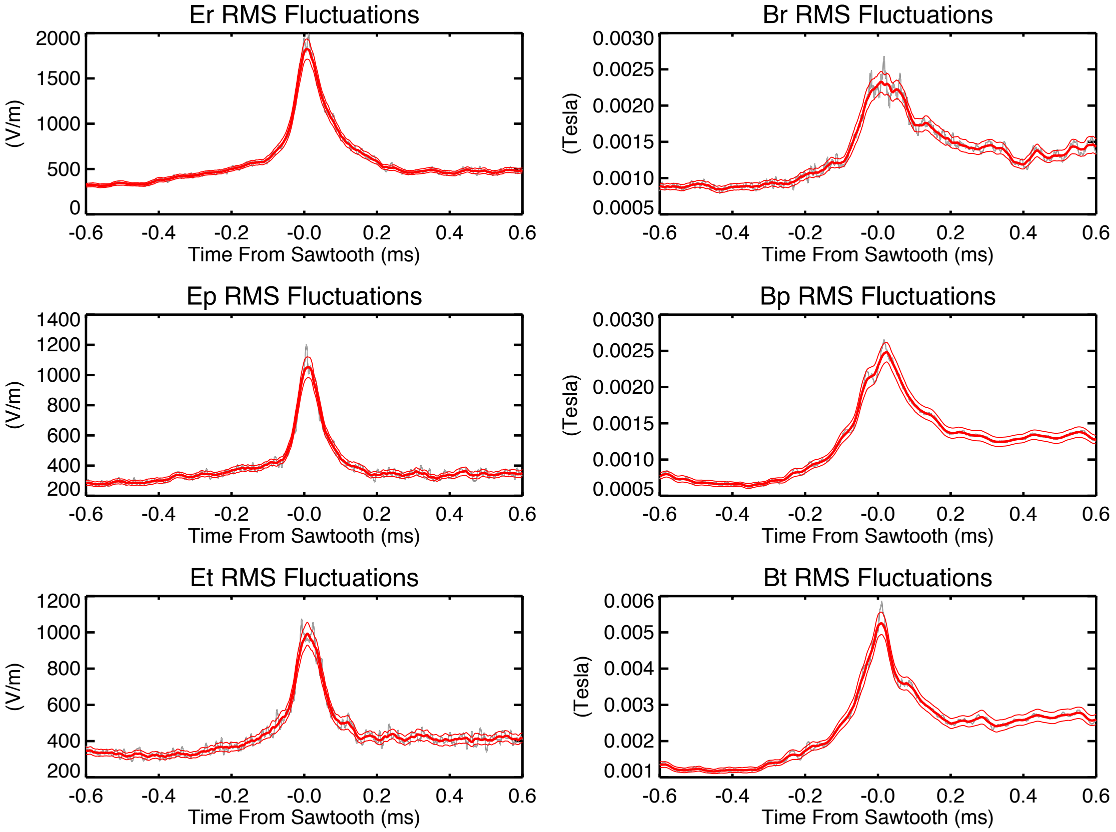

Figure D.4: Dynamo Probe $\tilde{\mathbf{E}}_{RMS}$ and $\tilde{\mathbf{B}}_{RMS}$, OFCD $\delta = +\pi/2$ sawtooth.

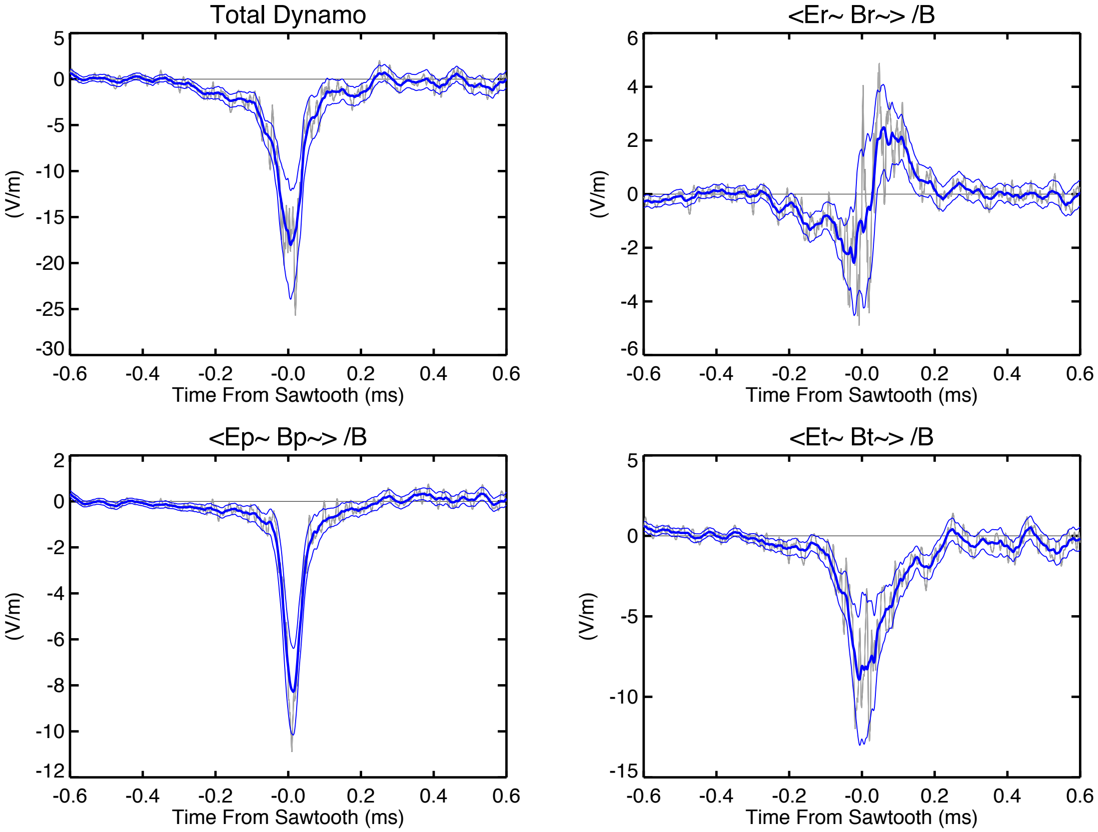

Figure D.5: Dynamo contributions from $\tilde{\mathbf{E}}$ and $\tilde{\mathbf{B}}$ components, OFCD $\delta = +\pi/2$ sawtooth.

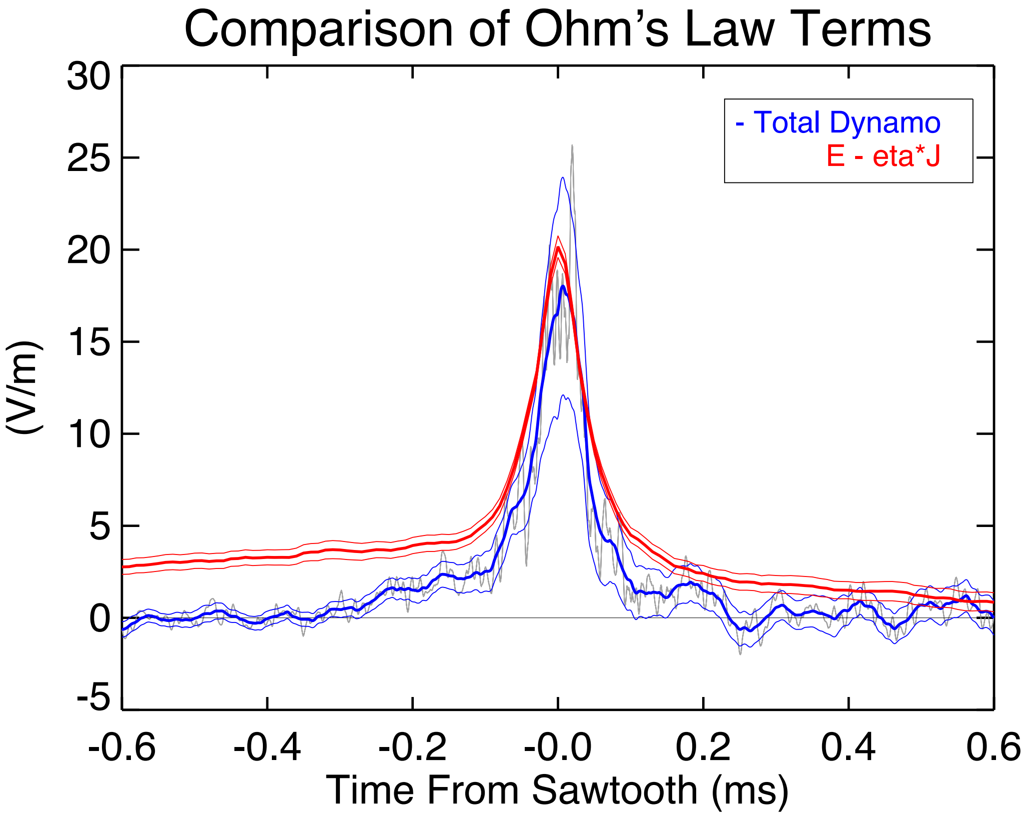

Figure D.6: Ohm's law ($\mathbf{E} - \eta\mathbf{J}$ and $- < \tilde{\mathbf{E}} \cdot \tilde{\mathbf{B}} > /B$), OFCD $\delta = +\pi/2$ sawtooth.

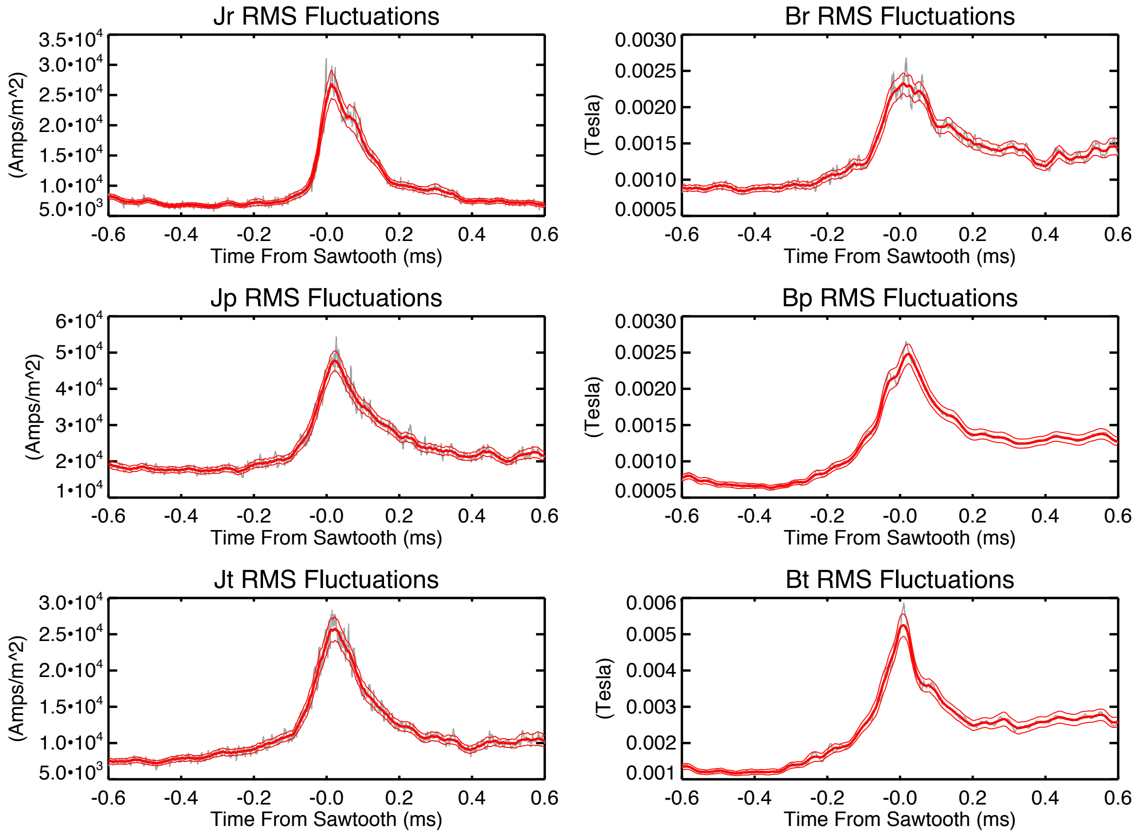
Jr RMS Fluctuations

Br RMS Fluctuations

Jp RMS Fluctuations

Bp RMS Fluctuations

Jt RMS Fluctuations

Bt RMS Fluctuations

Figure D.7: Dynamo Probe $\tilde{\mathbf{J}}_{RMS}$ and $\tilde{\mathbf{B}}_{RMS}$, OFCD $\delta = +\pi/2$ sawtooth.

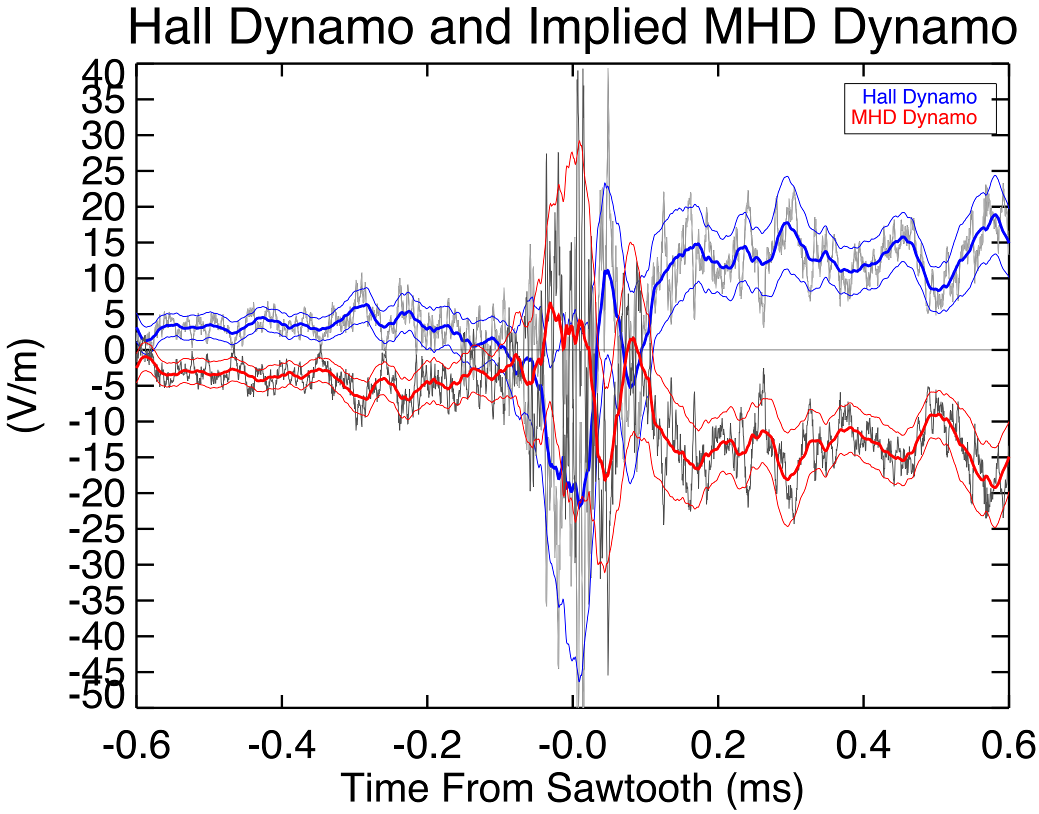

Figure D.8: Hall Dynamo and assumed MHD Dynamo (= Total Dynamo - Hall Dynamo), OFCD $\delta = +\pi/2$ sawtooth.

D.2 OFCD $\delta = +\pi/4$

D.2.1 Cycle Ensemble

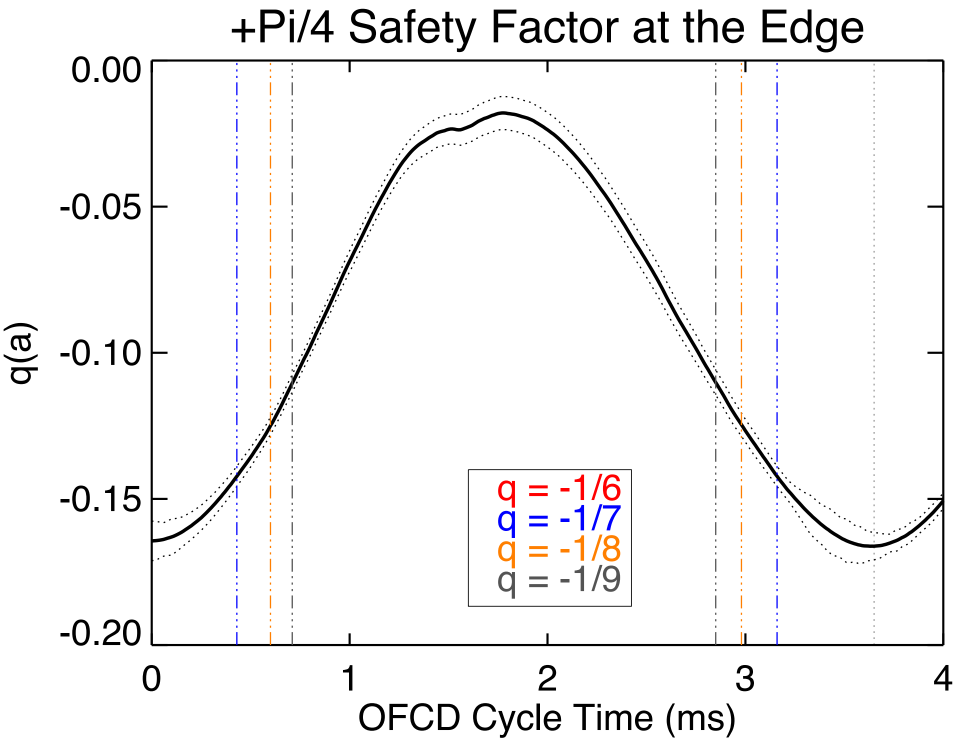

Figure D.9: Edge safety factor, OFCD $\delta = +\pi/4$ cycle.

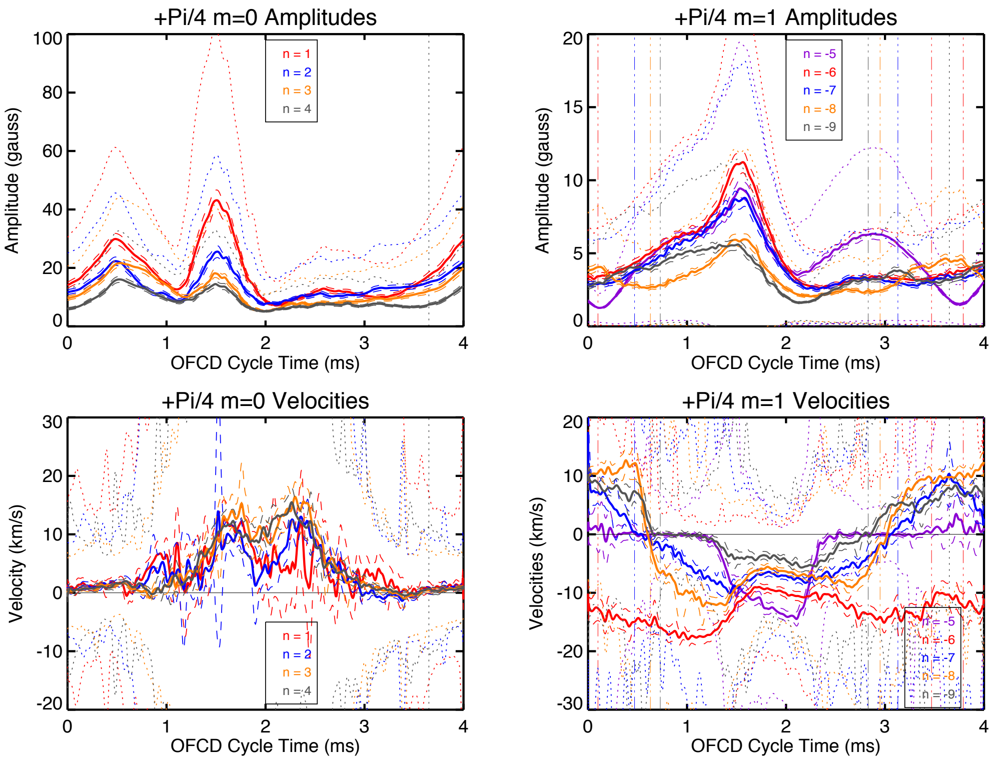

Figure D.10: Tearing mode amplitudes and velocities, OFCD $\delta = +\pi/4$ cycle.

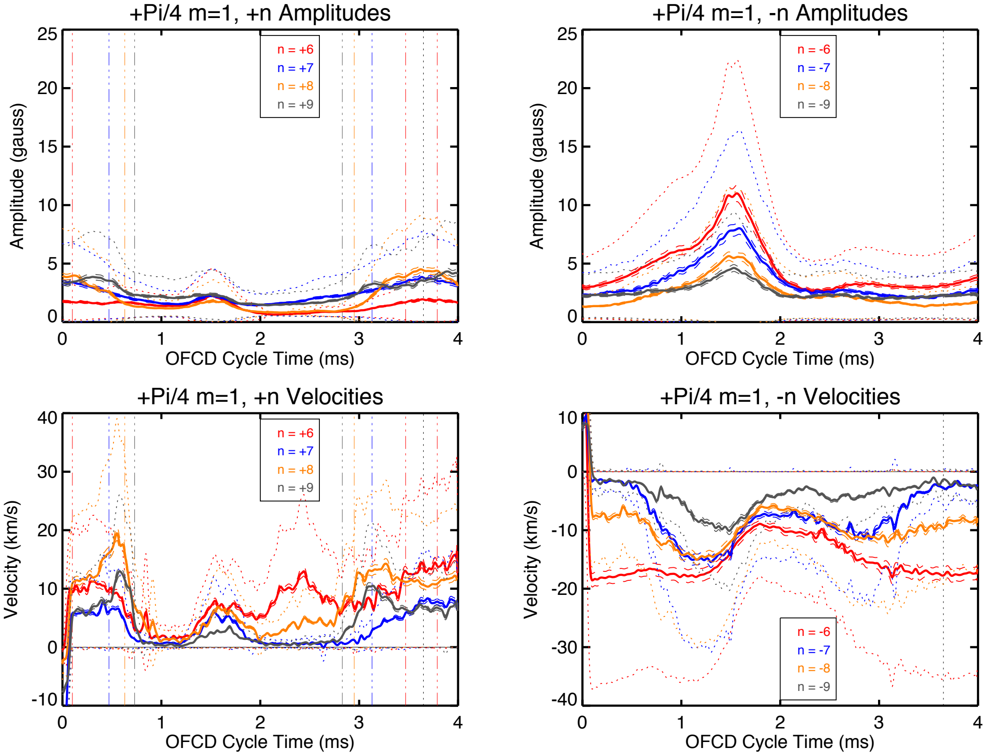

Figure D.11: Tearing mode +n and -n amplitudes and velocities, OFCD $\delta = +\pi/4$ cycle.

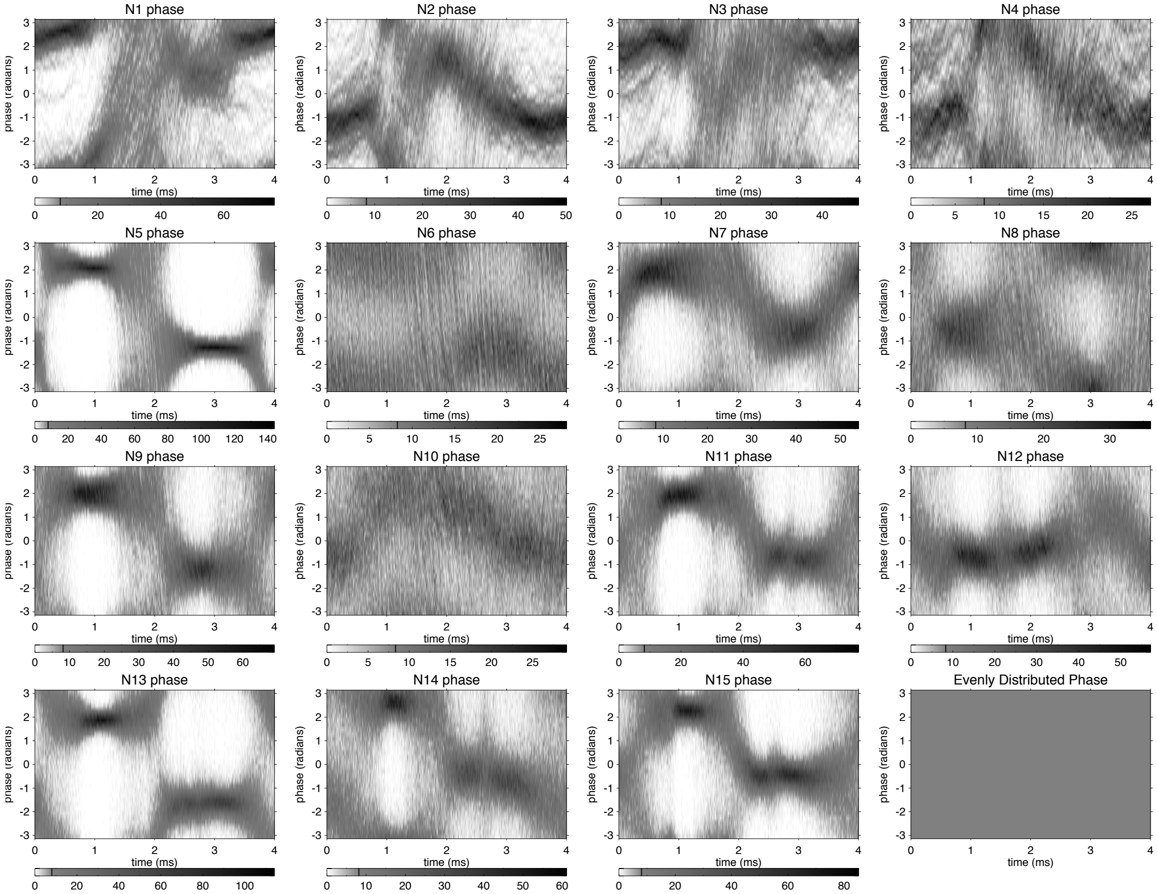

Figure D.12: Tearing mode phase distribution, OFCD $\delta = +\pi/4$ cycle.

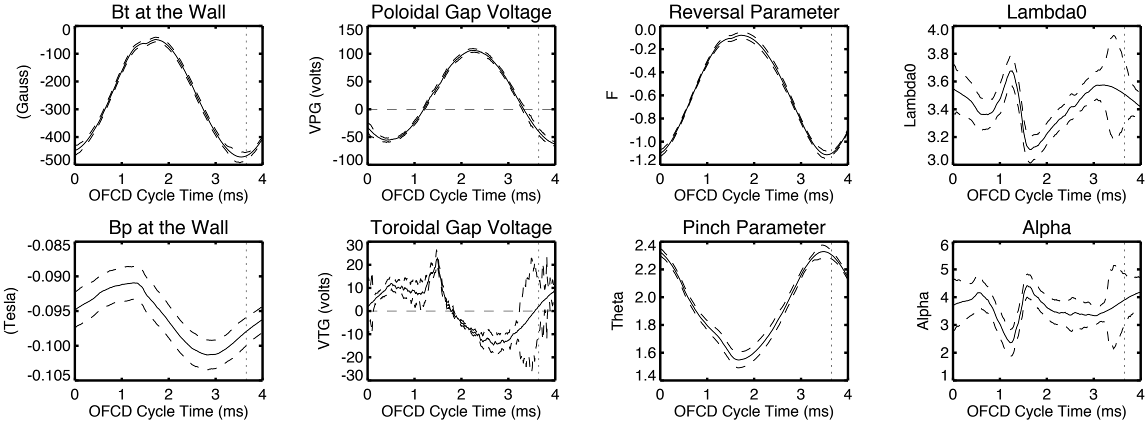

Figure D.13: Global and edge parameters, OFCD $\delta = +\pi/4$ cycle.

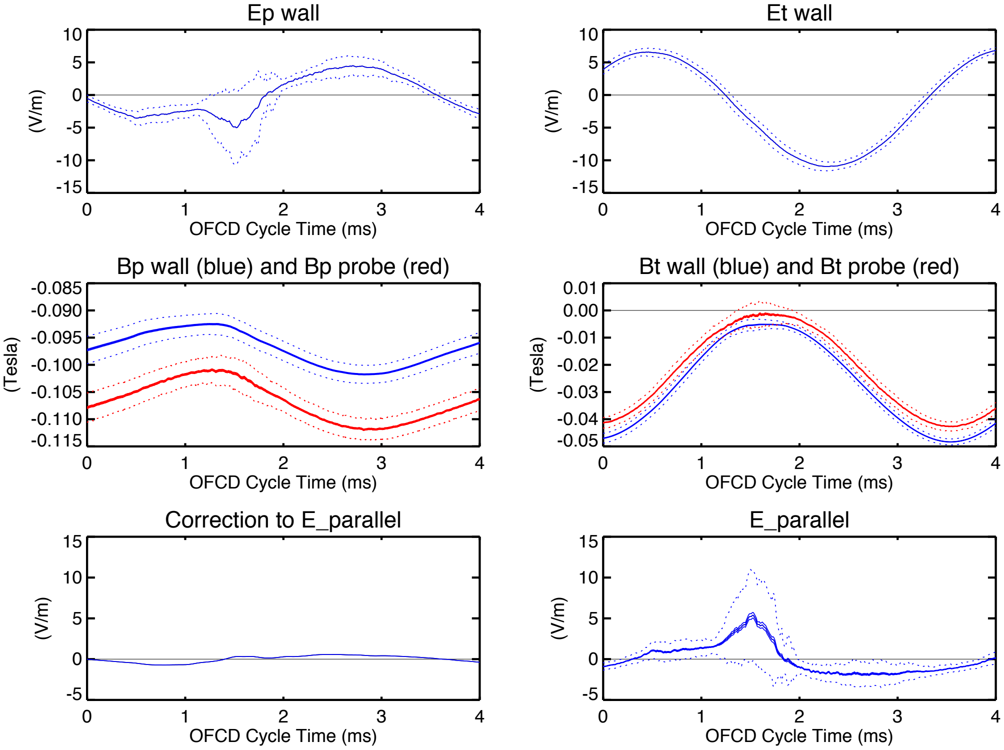

Figure D.14: Parallel electric field data, OFCD $\delta = +\pi/4$ cycle.

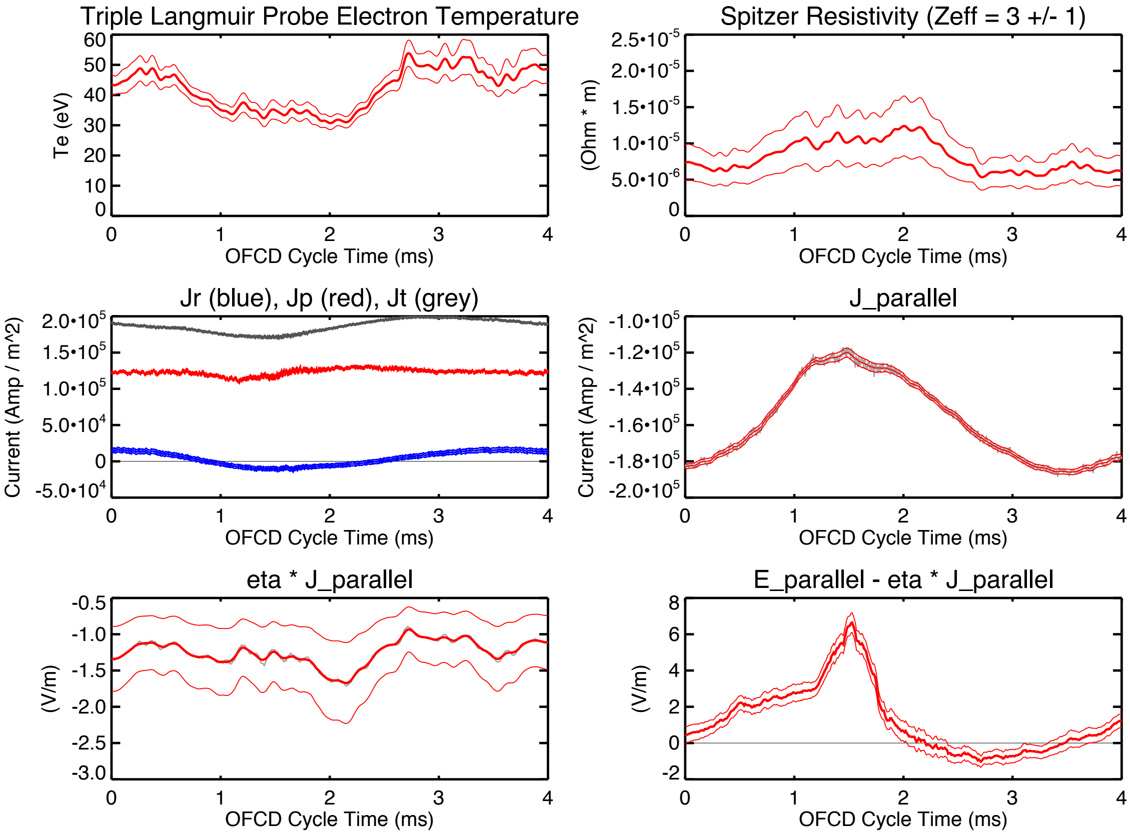

Figure D.15: Probe $\eta\mathbf{J}$ data, OFCD $\delta = +\pi/4$ cycle.

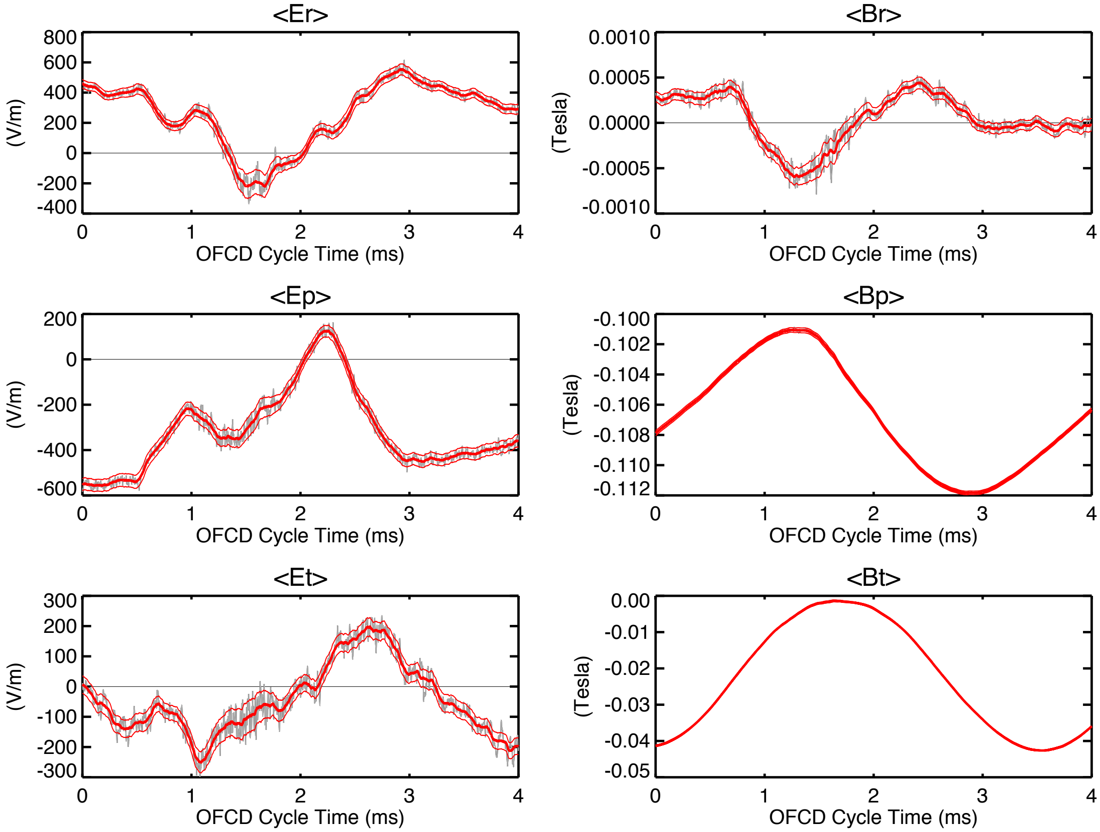

Figure D.16: Dynamo Probe $< \mathbf{E} >$ and $< \mathbf{B} >$, OFCD $\delta = +\pi/4$ cycle.

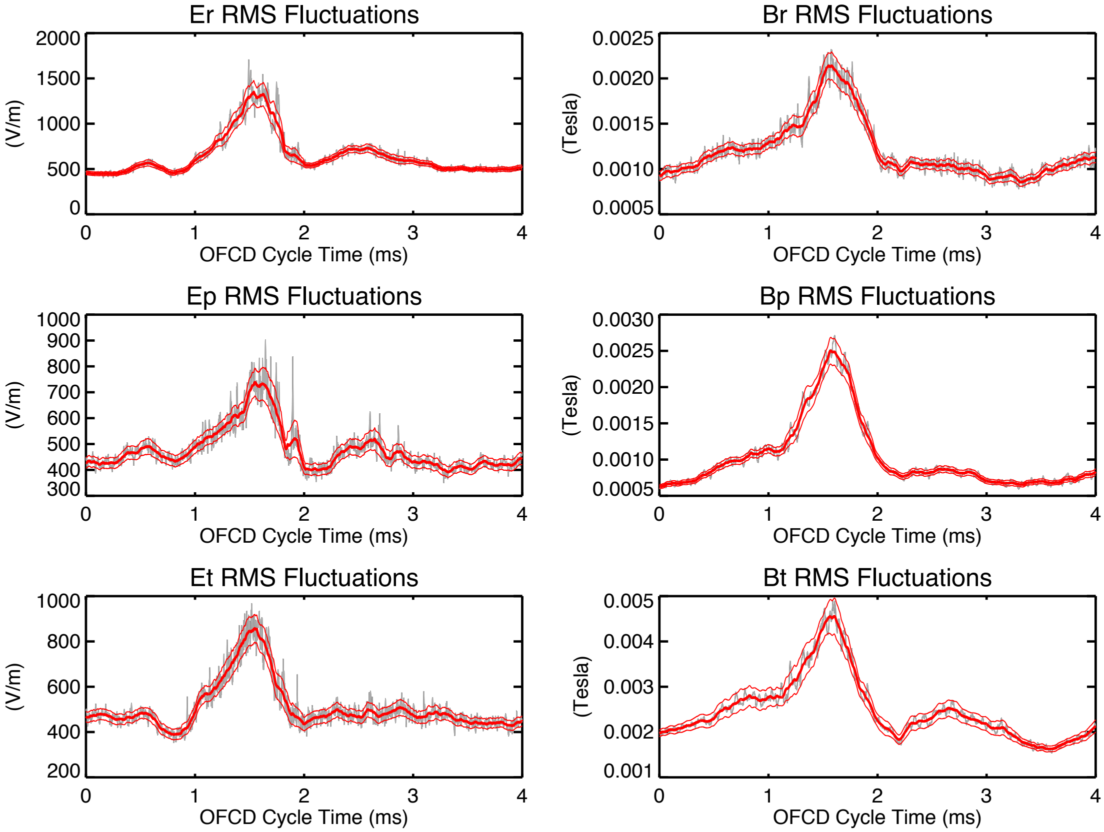

Figure D.17: Dynamo Probe $\tilde{\mathbf{E}}_{RMS}$ and $\tilde{\mathbf{B}}_{RMS}$, OFCD $\delta = +\pi/4$ cycle.

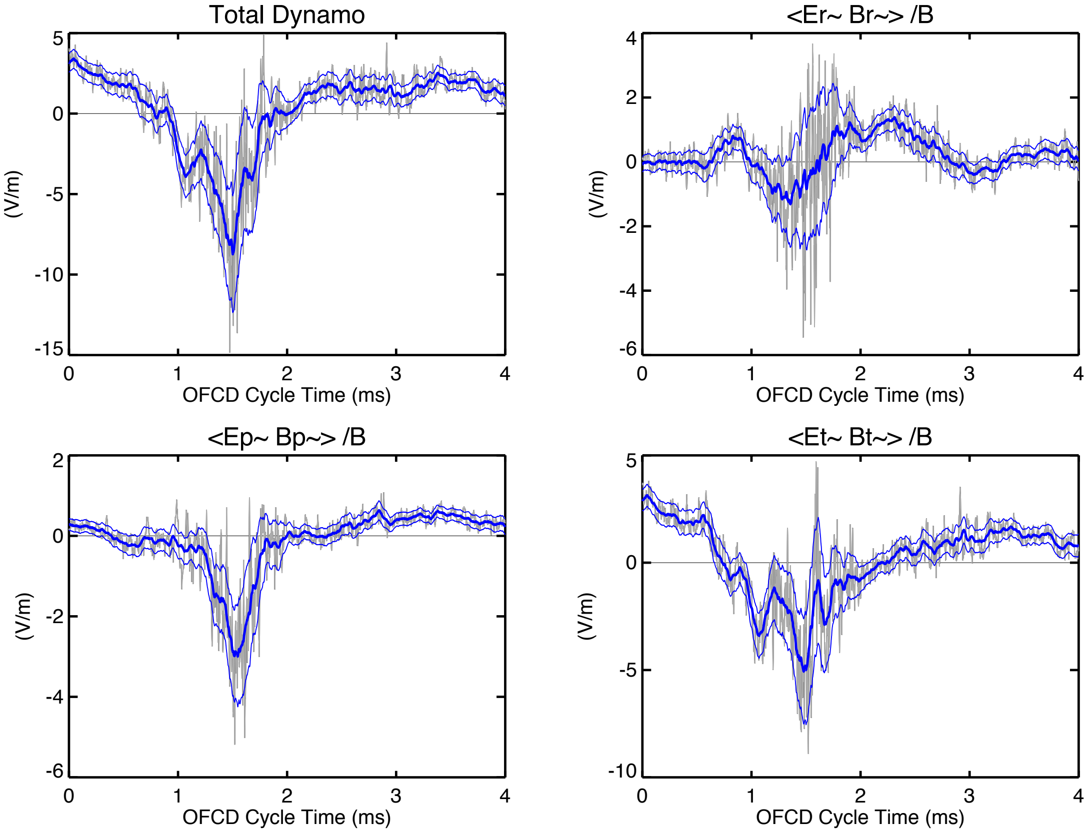

Figure D.18: Dynamo contributions from $\tilde{\mathbf{E}}$ and $\tilde{\mathbf{B}}$ components, OFCD $\delta = +\pi/4$ cycle.

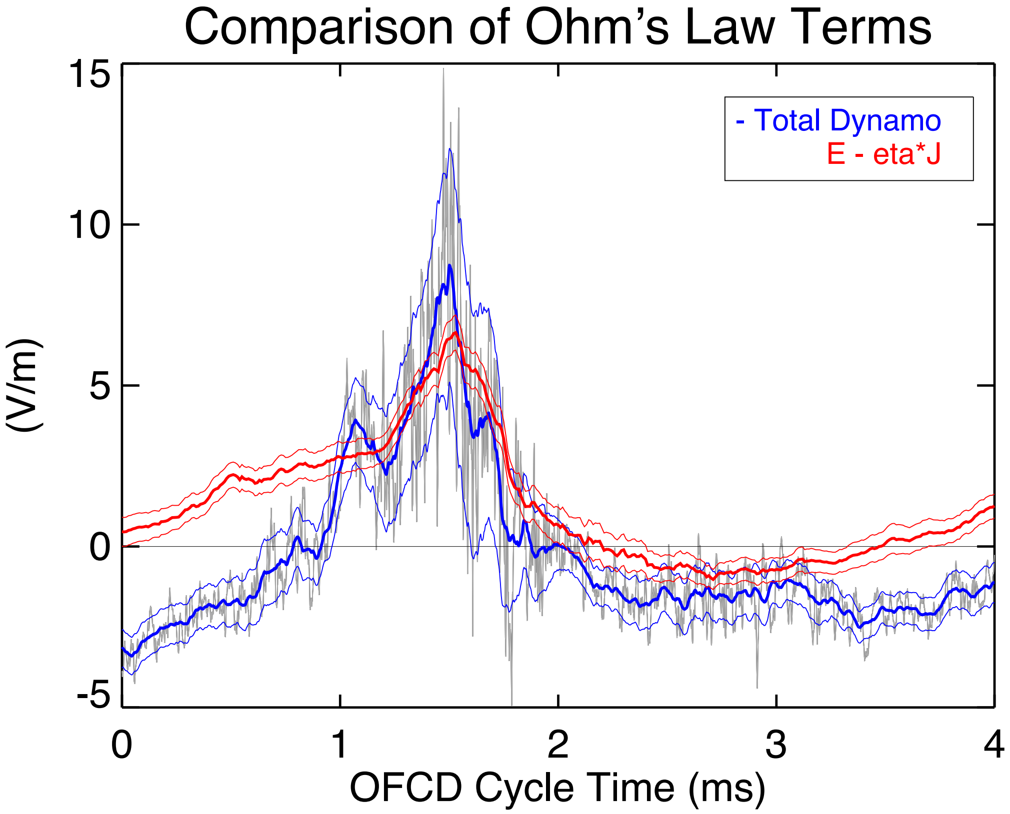

Figure D.19: Ohm's law ($\mathbf{E} - \eta\mathbf{J}$ and $- < \tilde{\mathbf{E}} \cdot \tilde{\mathbf{B}} > /B$), OFCD $\delta = +\pi/4$ cycle.

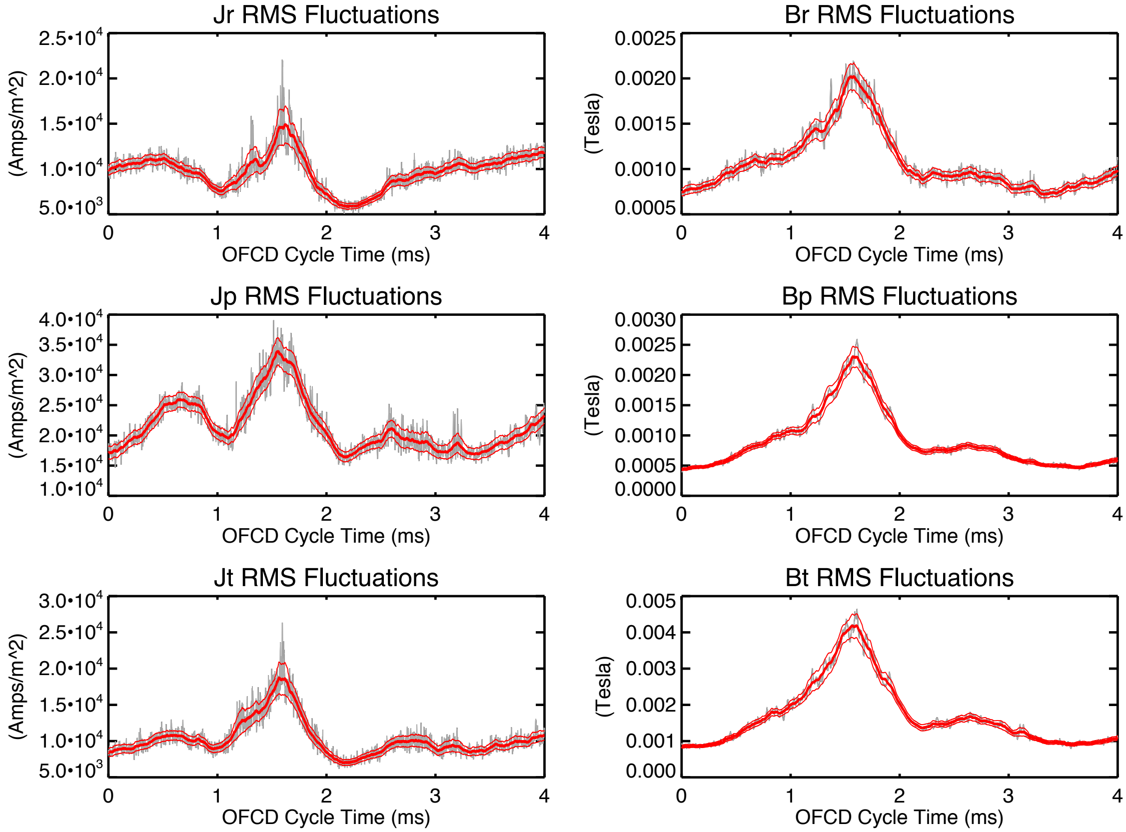

Figure D.20: Dynamo Probe $\tilde{\mathbf{J}}_{RMS}$ and $\tilde{\mathbf{B}}_{RMS}$, highpass filtered, OFCD $\delta = +\pi/4$ cycle.

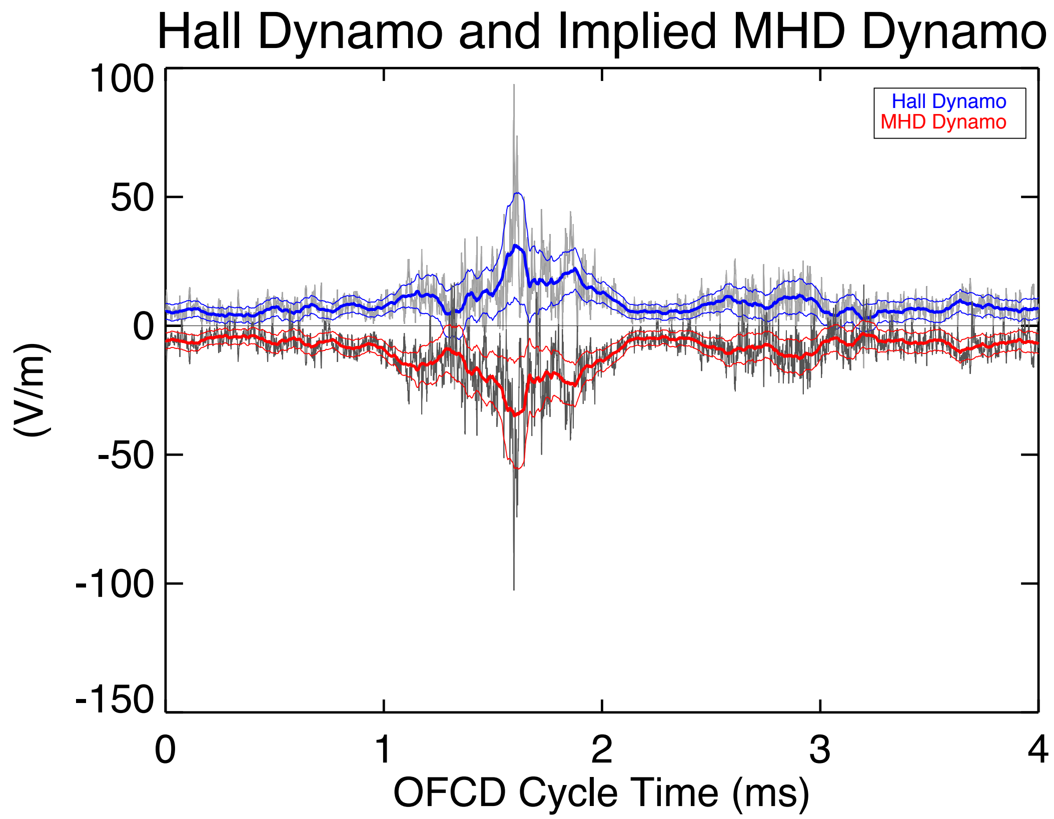

Figure D.21: Hall Dynamo and assumed MHD Dynamo (= Total Dynamo - Hall Dynamo) using highpass filtered data, OFCD $\delta = +\pi/4$ cycle..

D.2.2 Sawtooth Ensemble

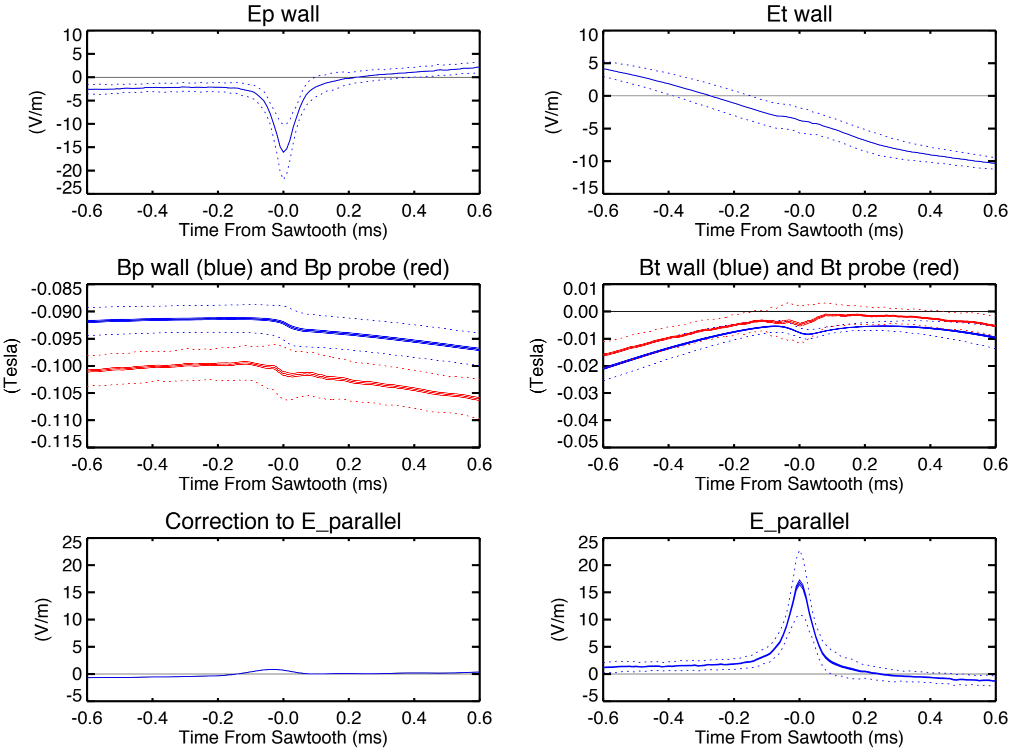

Figure D.22: Parallel electric field data, OFCD $\delta = +\pi/4$ sawtooth.

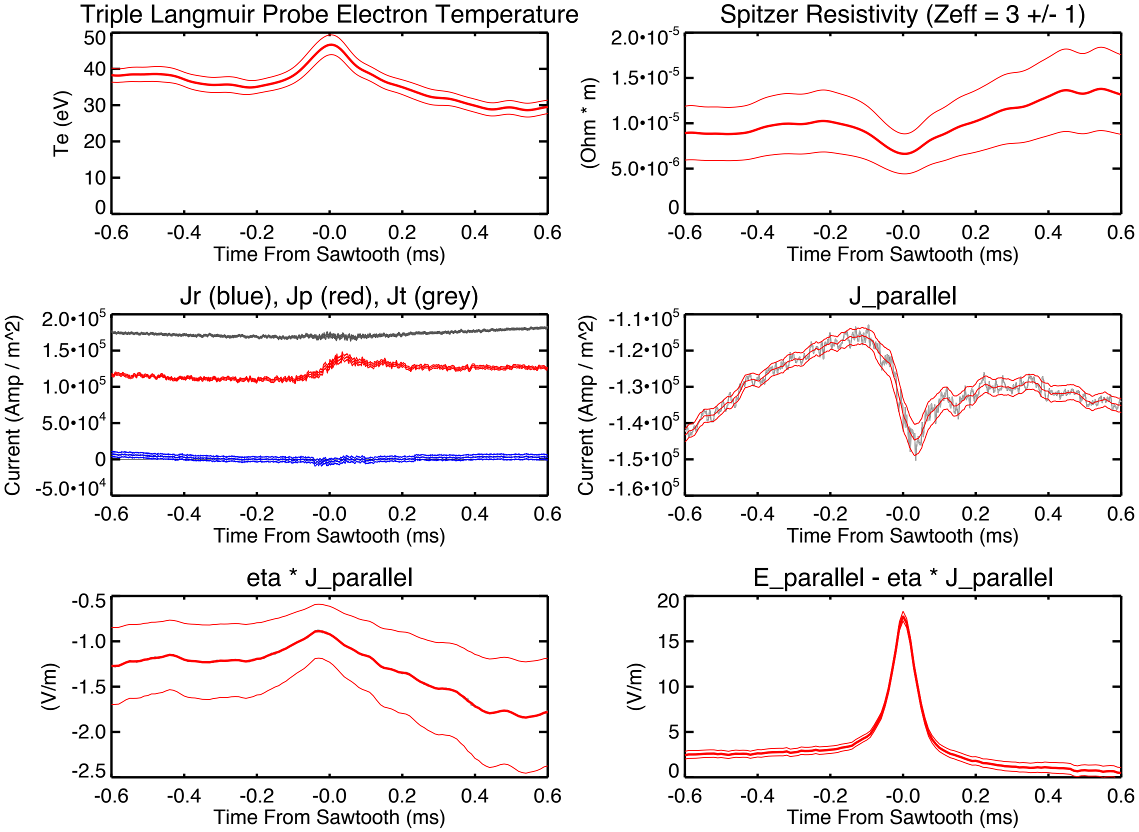

Figure D.23: Probe $\eta \mathbf{J}$ data, OFCD $\delta = +\pi/4$ sawtooth.

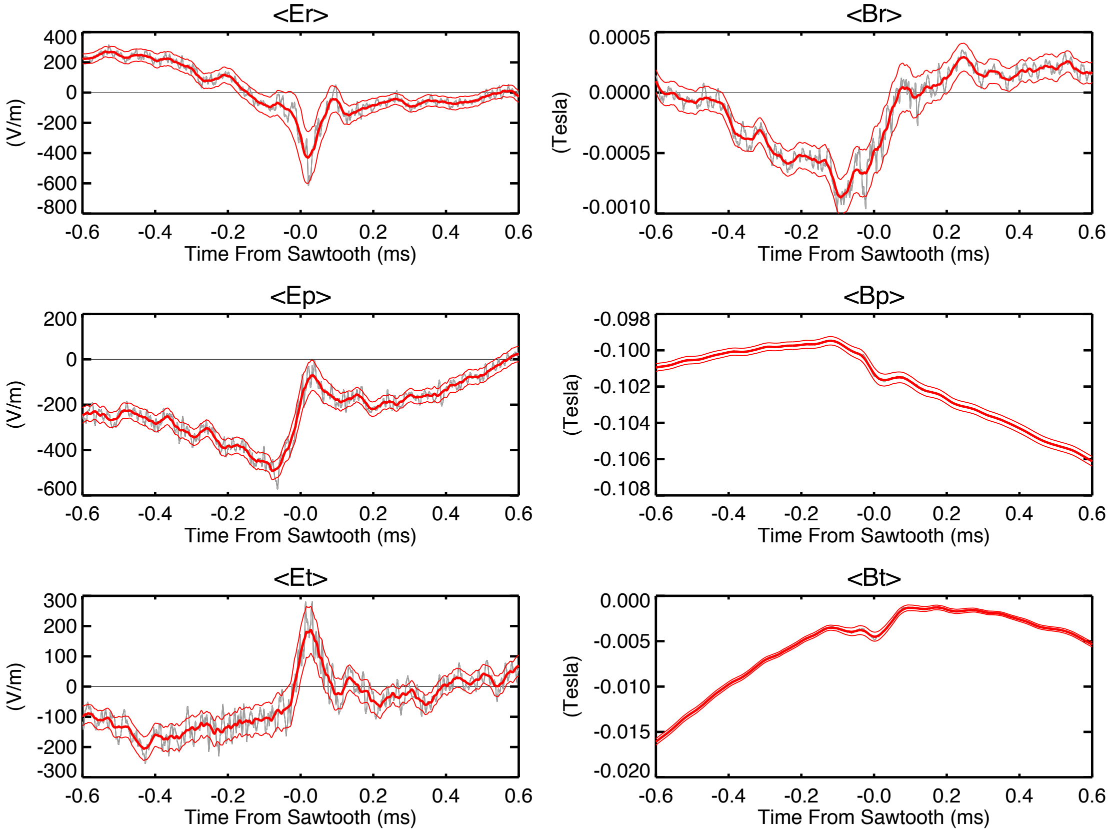

Figure D.24: Dynamo Probe $< \mathbf{E} >$ and $< \mathbf{B} >$, OFCD $\delta = +\pi/4$ sawtooth.

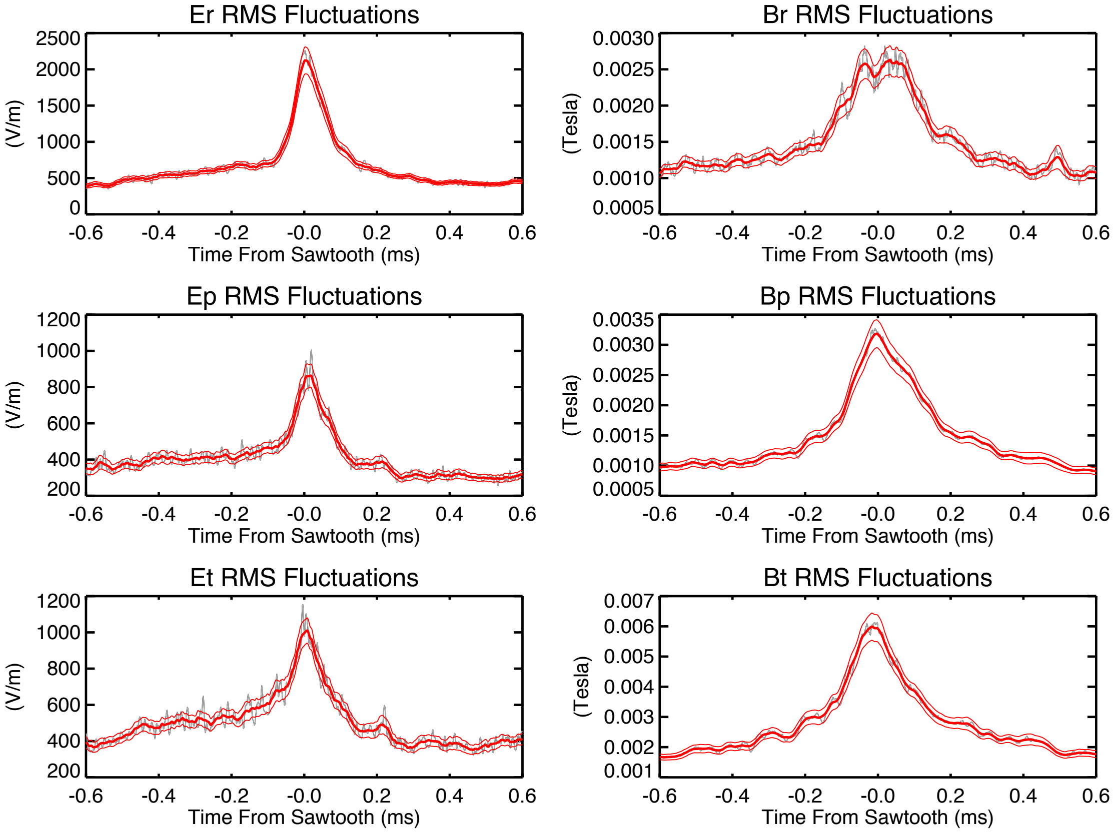

Figure D.25: Dynamo Probe $\tilde{\mathbf{E}}_{RMS}$ and $\tilde{\mathbf{B}}_{RMS}$, OFCD $\delta = +\pi/4$ sawtooth.

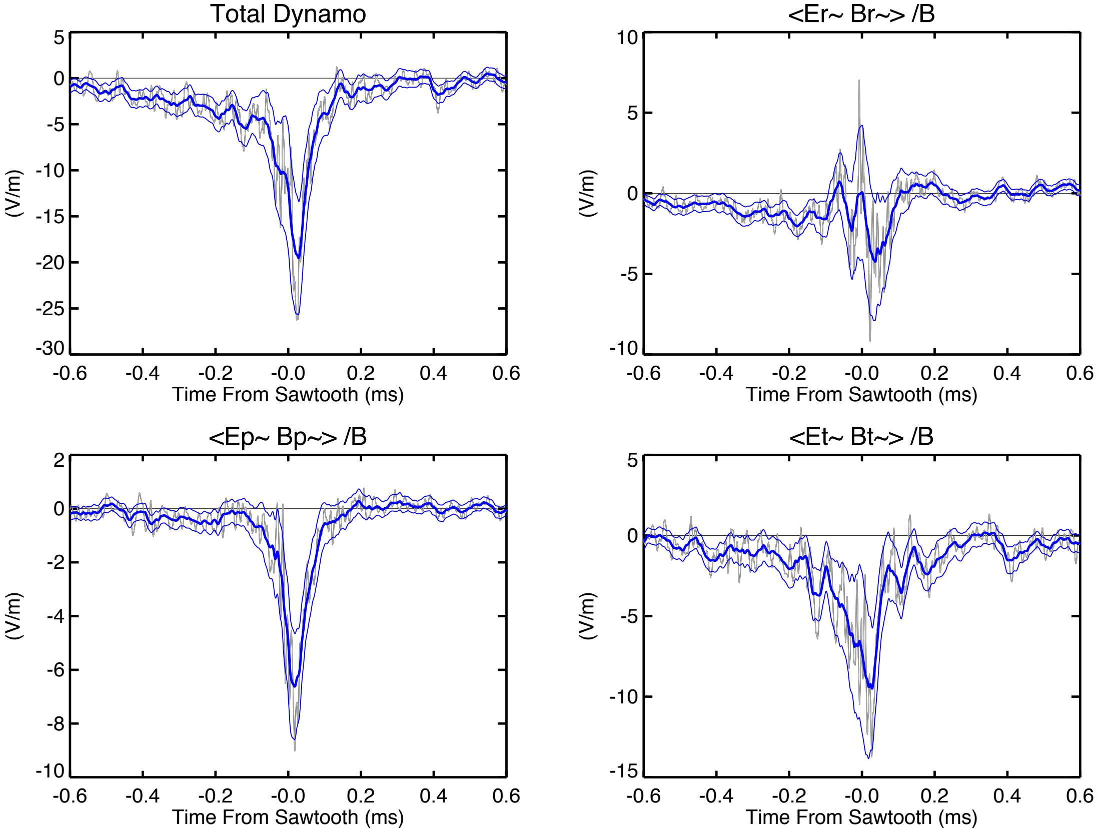

Figure D.26: Dynamo contributions from $\tilde{\mathbf{E}}$ and $\tilde{\mathbf{B}}$ components, OFCD $\delta = +\pi/4$ sawtooth.

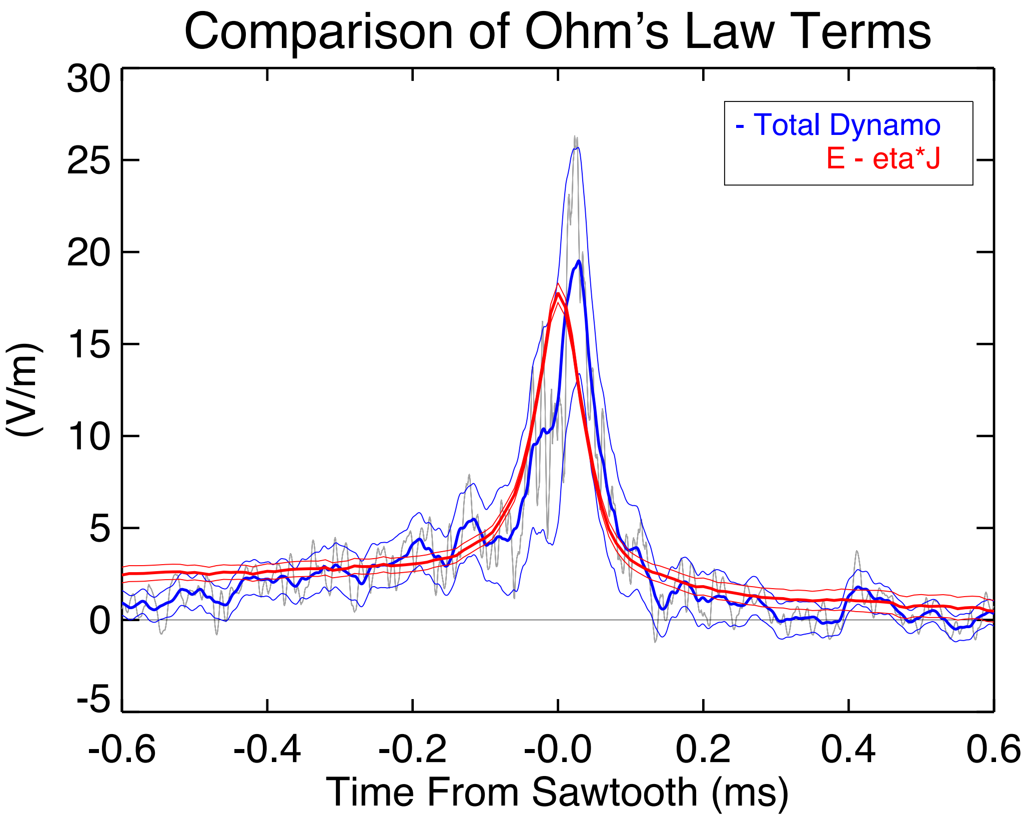

Figure D.27: Ohm's law ($\mathbf{E} - \eta\mathbf{J}$ and $- < \tilde{\mathbf{E}} \cdot \tilde{\mathbf{B}} > /B$), OFCD $\delta = +\pi/4$ sawtooth.

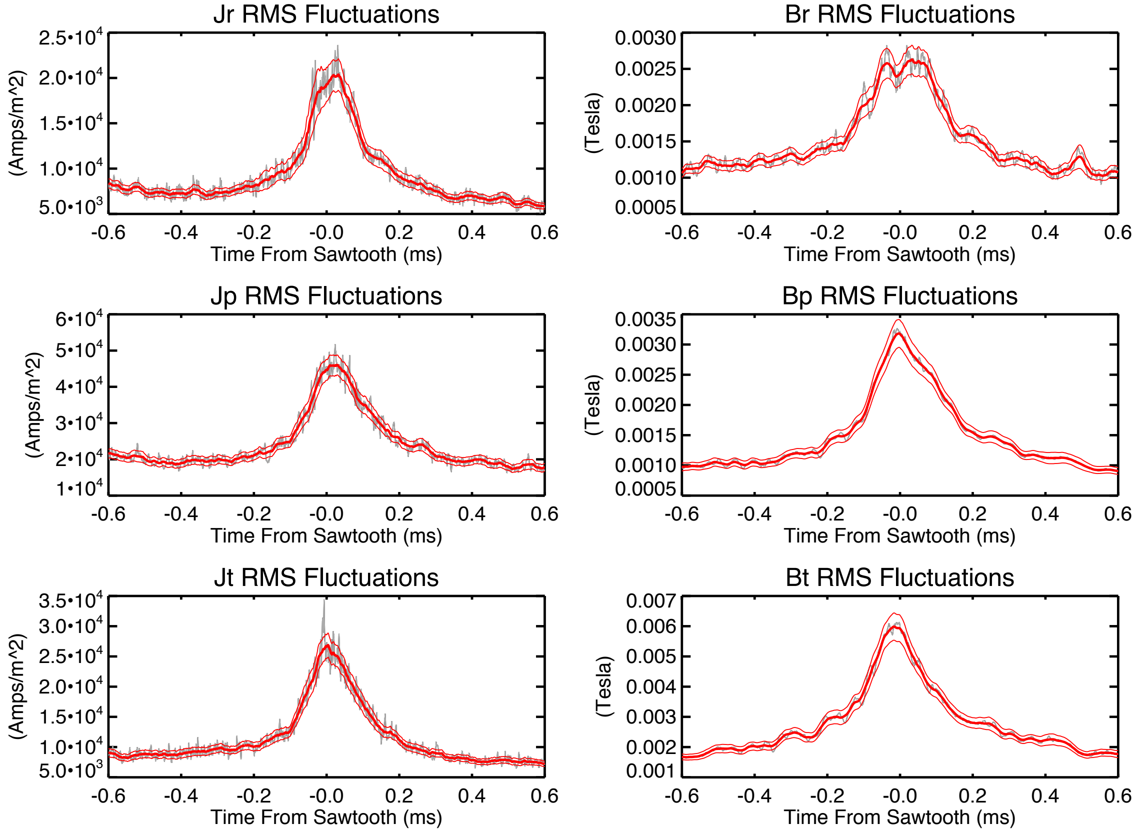

Figure D.28: Dynamo Probe $\tilde{\mathbf{J}}_{RMS}$ and $\tilde{\mathbf{B}}_{RMS}$, OFCD $\delta = +\pi/4$ sawtooth.

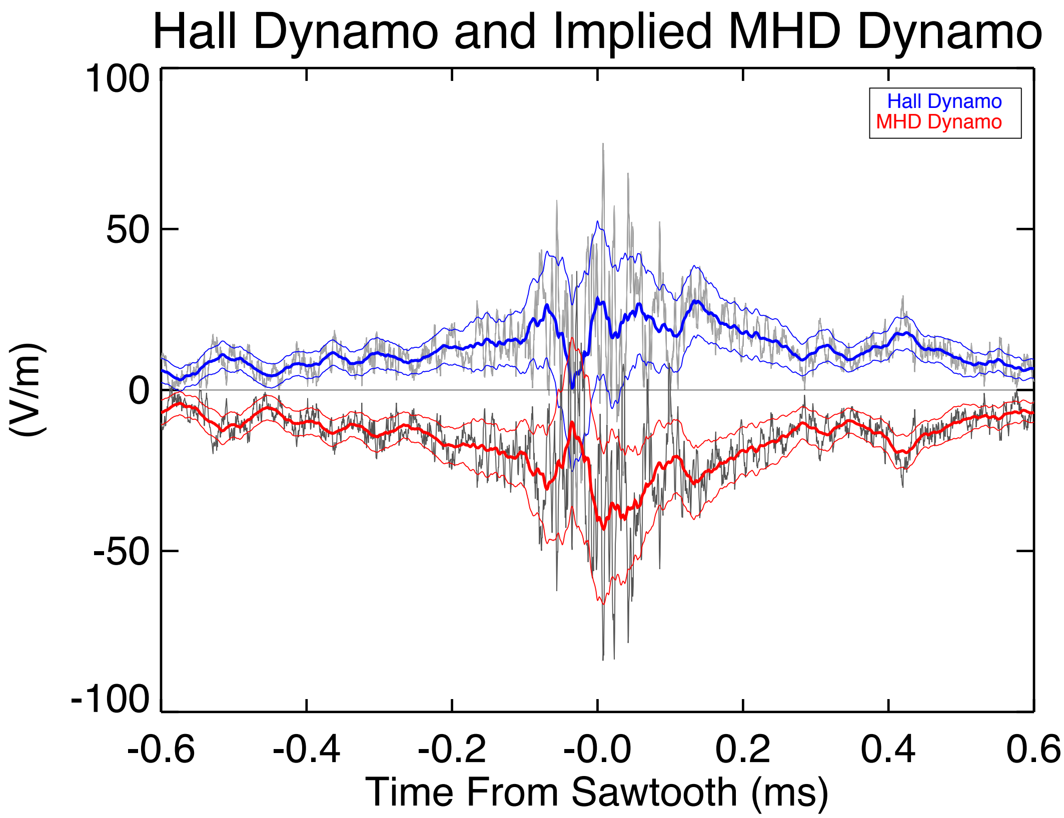

Figure D.29: Hall Dynamo and assumed MHD Dynamo (= Total Dynamo - Hall Dynamo), OFCD $\delta = +\pi/4$ sawtooth.

D.3 OFCD $\delta = 0$

D.3.1 Cycle Ensemble

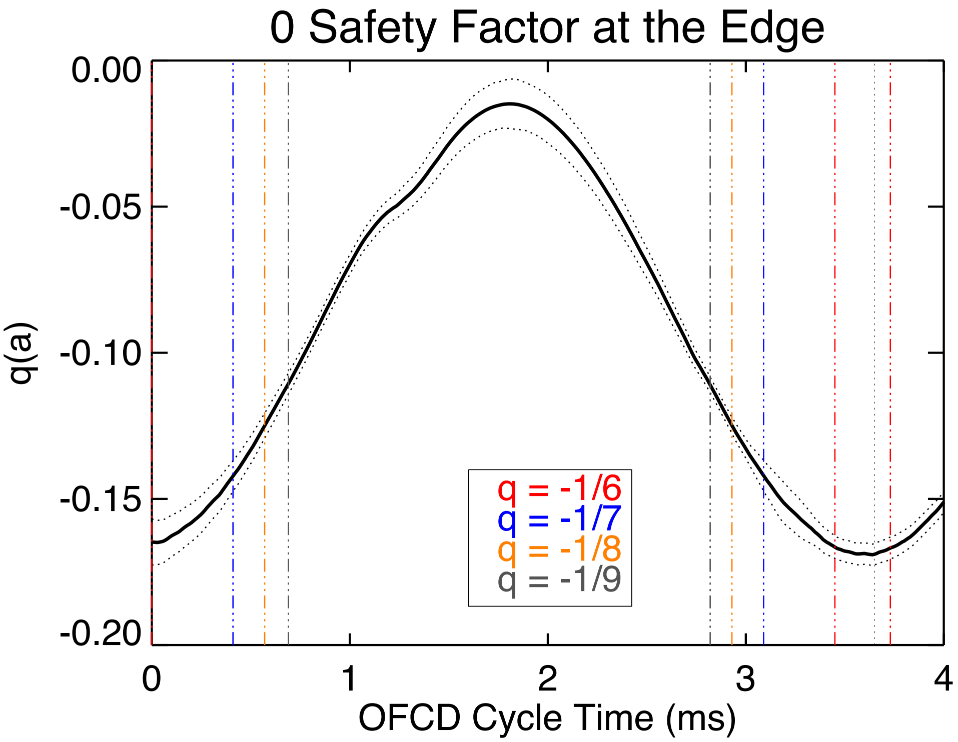

Figure D.30: Edge safety factor, OFCD $\delta = 0$ cycle.

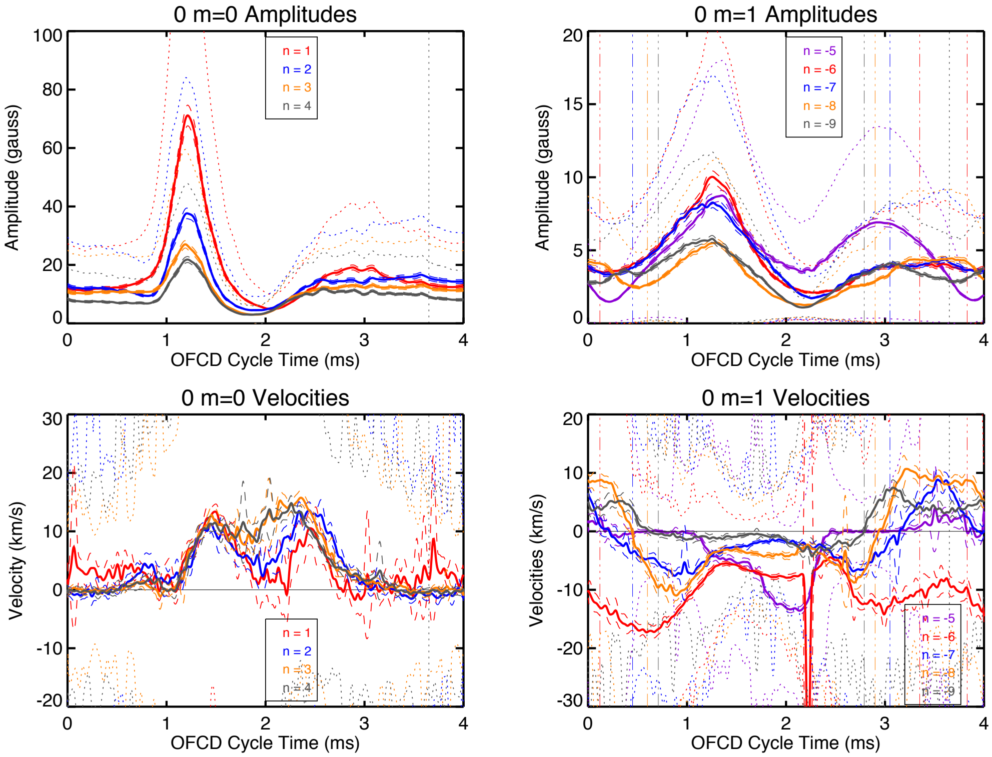

Figure D.31: Tearing mode amplitudes and velocities, OFCD $\delta = 0$ cycle.

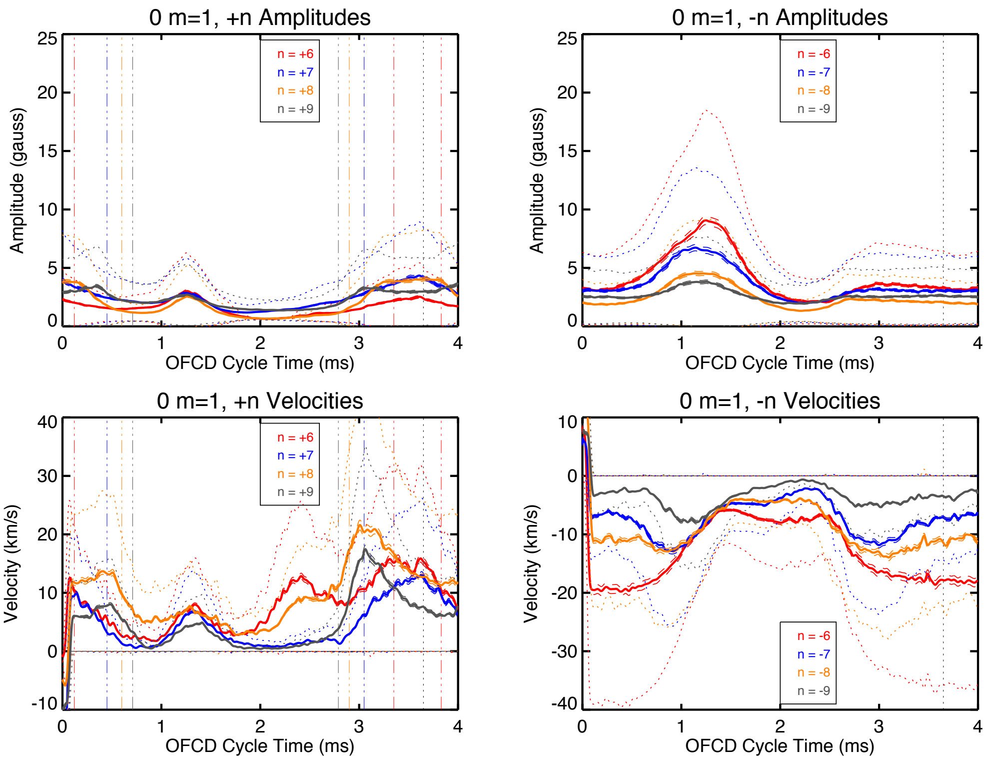

Figure D.32: Tearing mode +n and -n amplitudes and velocities, OFCD $\delta = 0$ cycle.

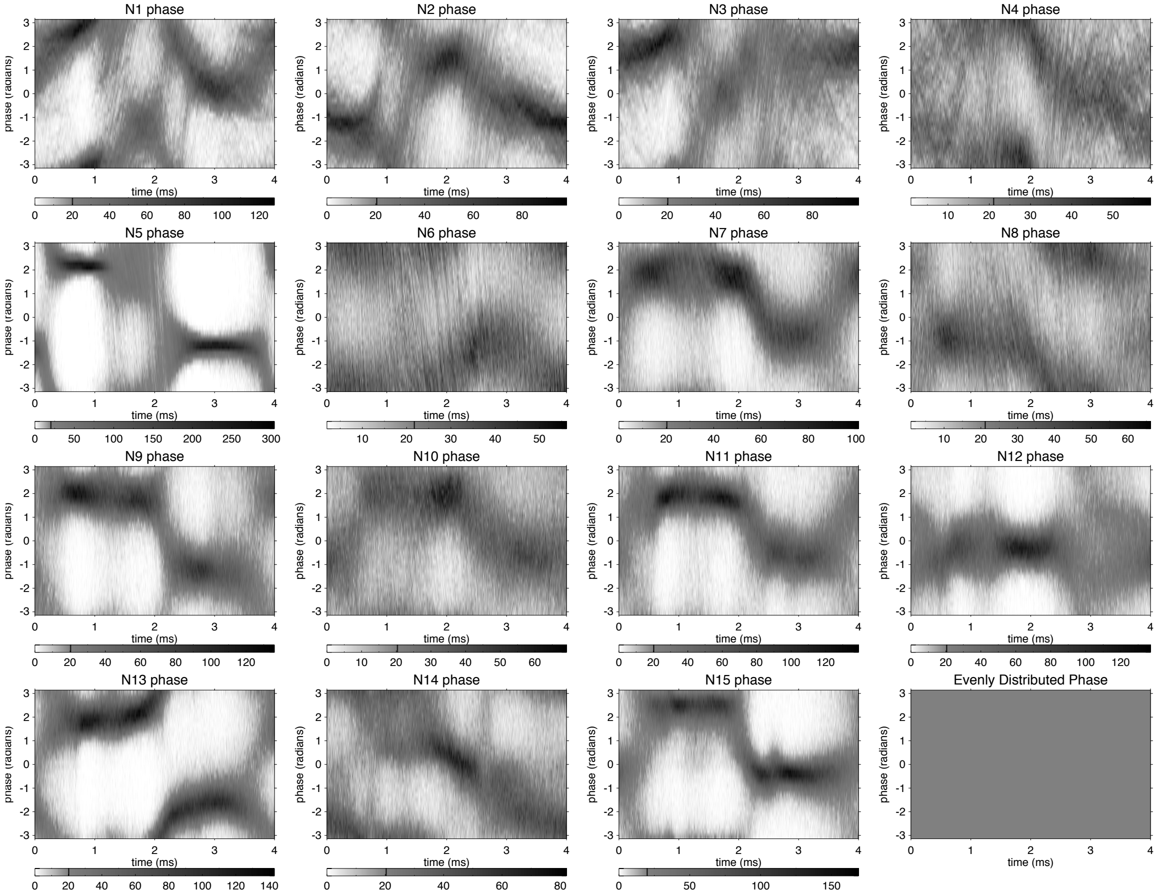

Figure D.33: Tearing mode phase distribution, OFCD $\delta = 0$ cycle.

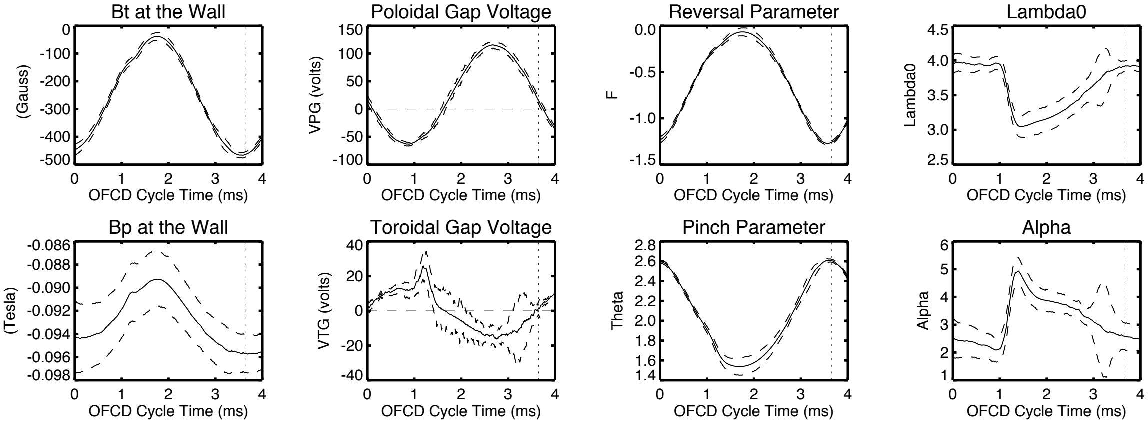

Figure D.34: Global and edge parameters, OFCD $\delta = 0$ cycle.

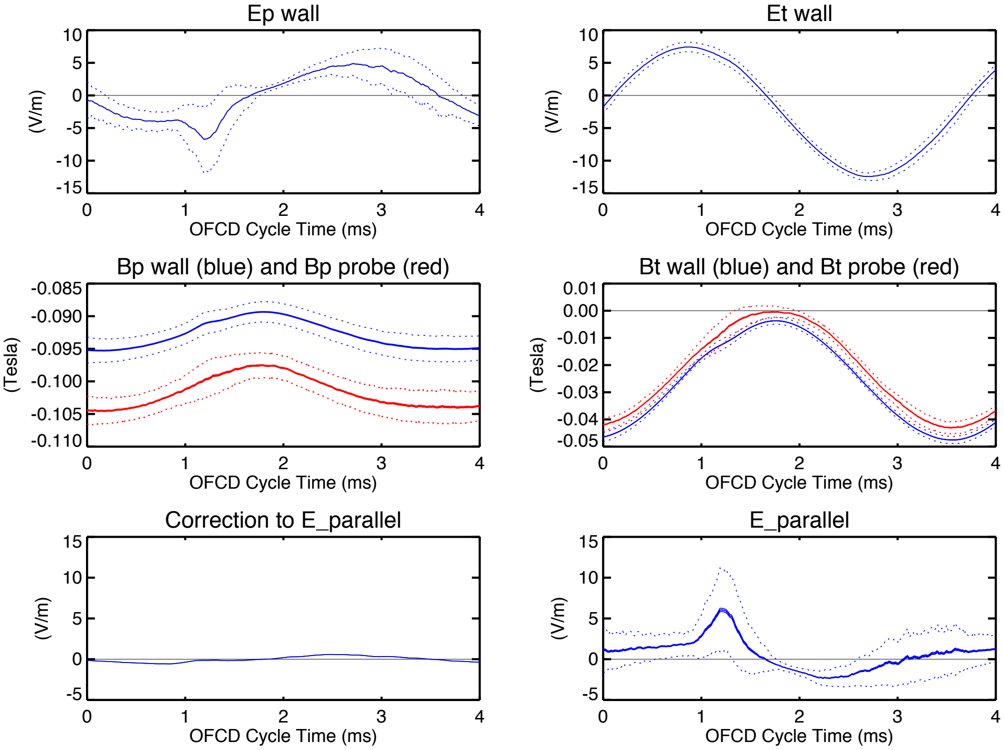

Figure D.35: Parallel electric field data, OFCD $\delta = 0$ cycle.

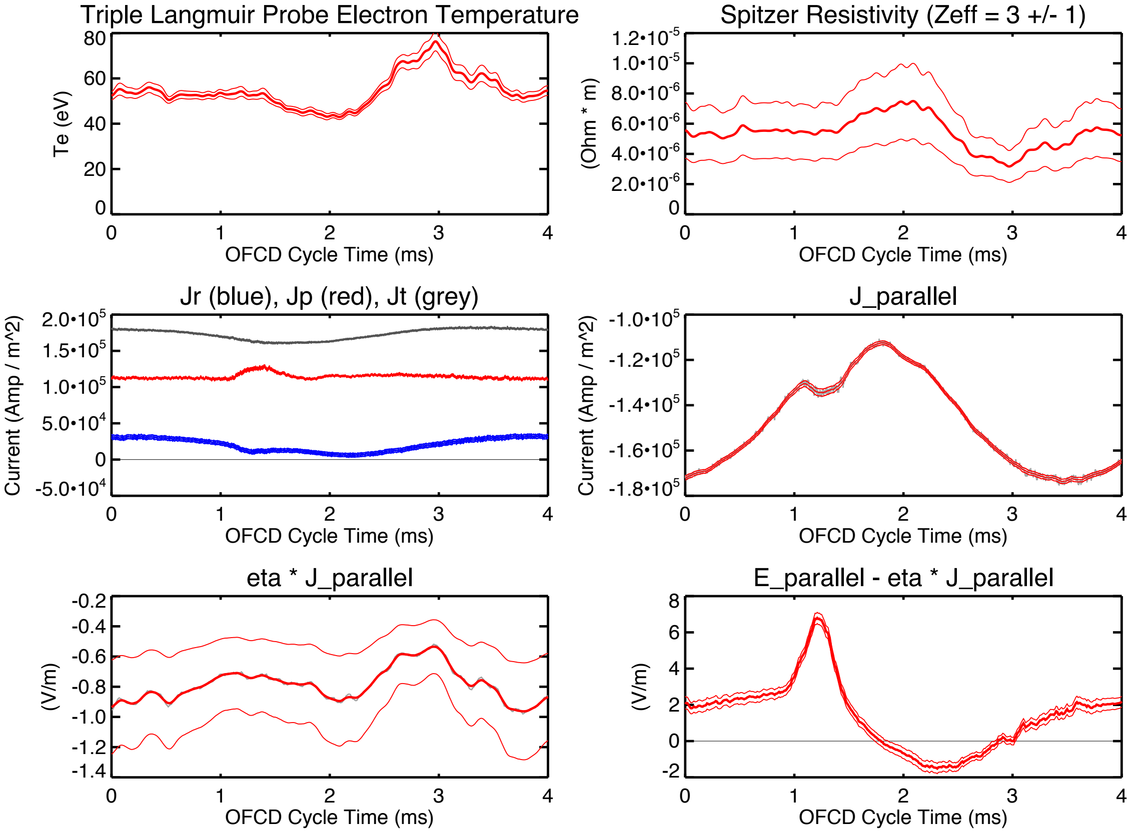

Figure D.36: Probe $\eta\mathbf{J}$ data, OFCD $\delta = 0$ cycle.

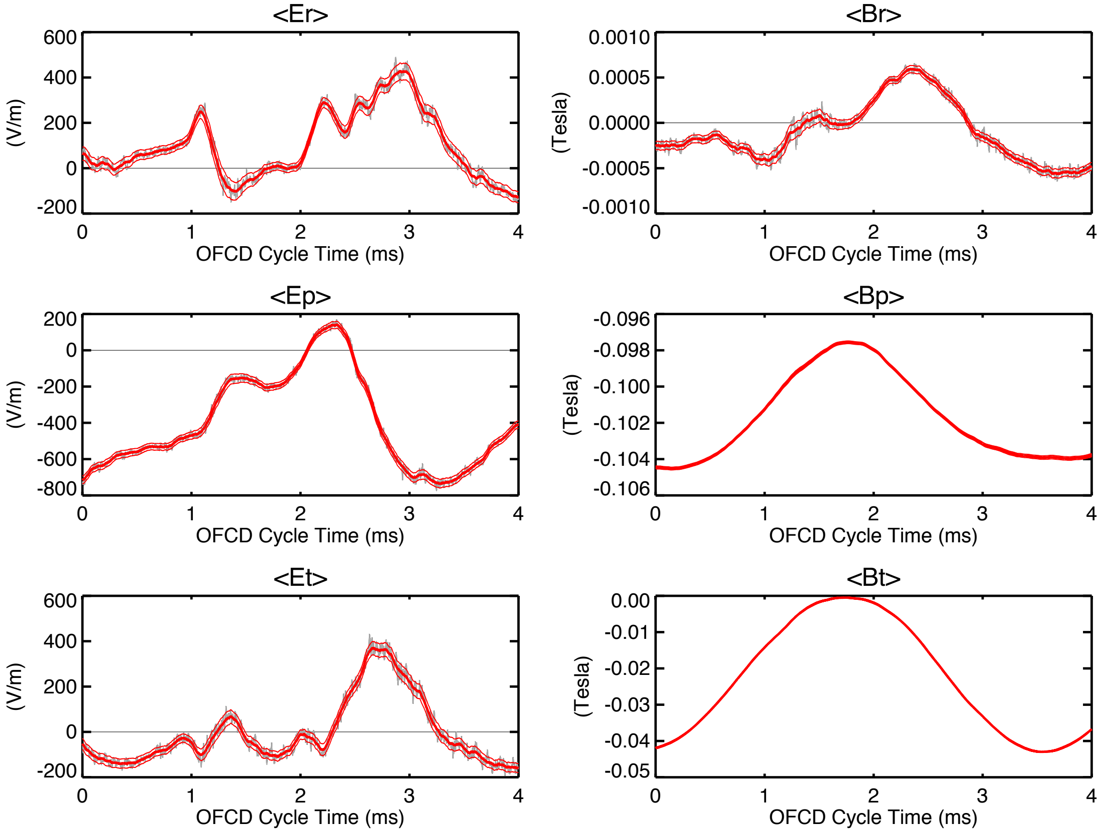

Figure D.37: Dynamo Probe $< \mathbf{E} >$ and $< \mathbf{B} >$, OFCD $\delta = 0$ cycle.

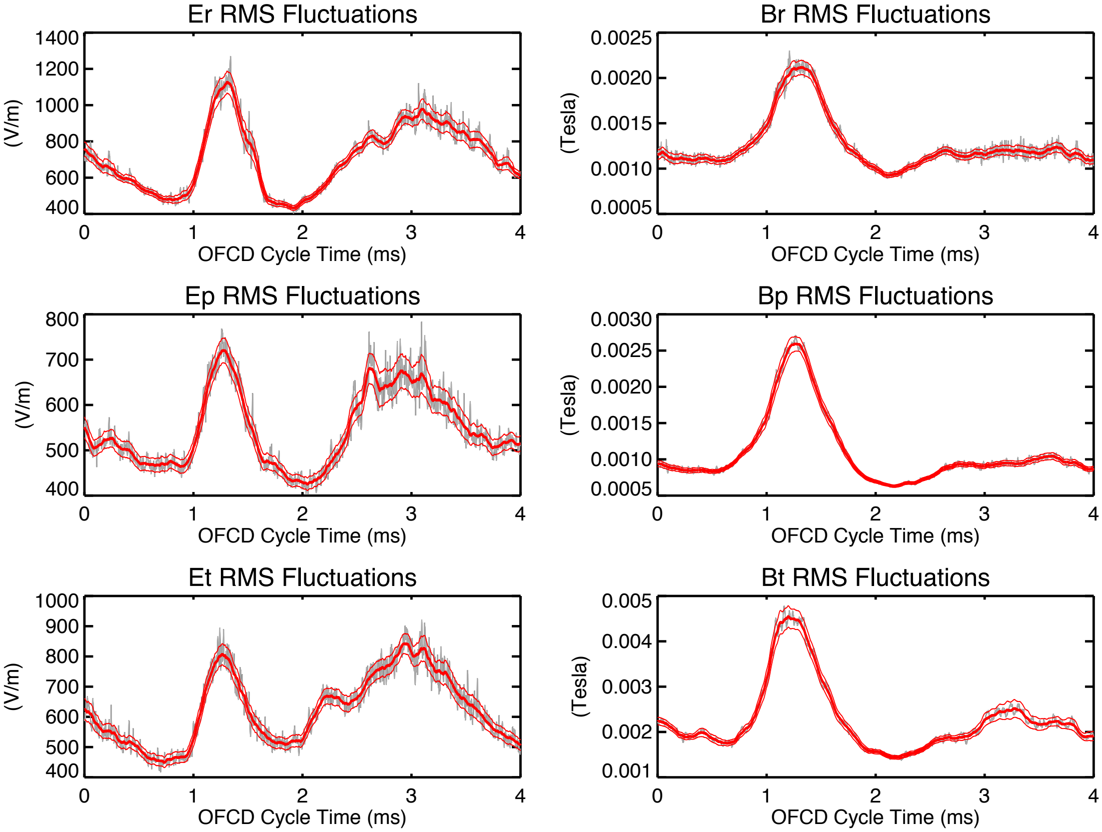

Figure D.38: Dynamo Probe $\tilde{\mathbf{E}}_{RMS}$ and $\tilde{\mathbf{B}}_{RMS}$, OFCD $\delta = 0$ cycle.

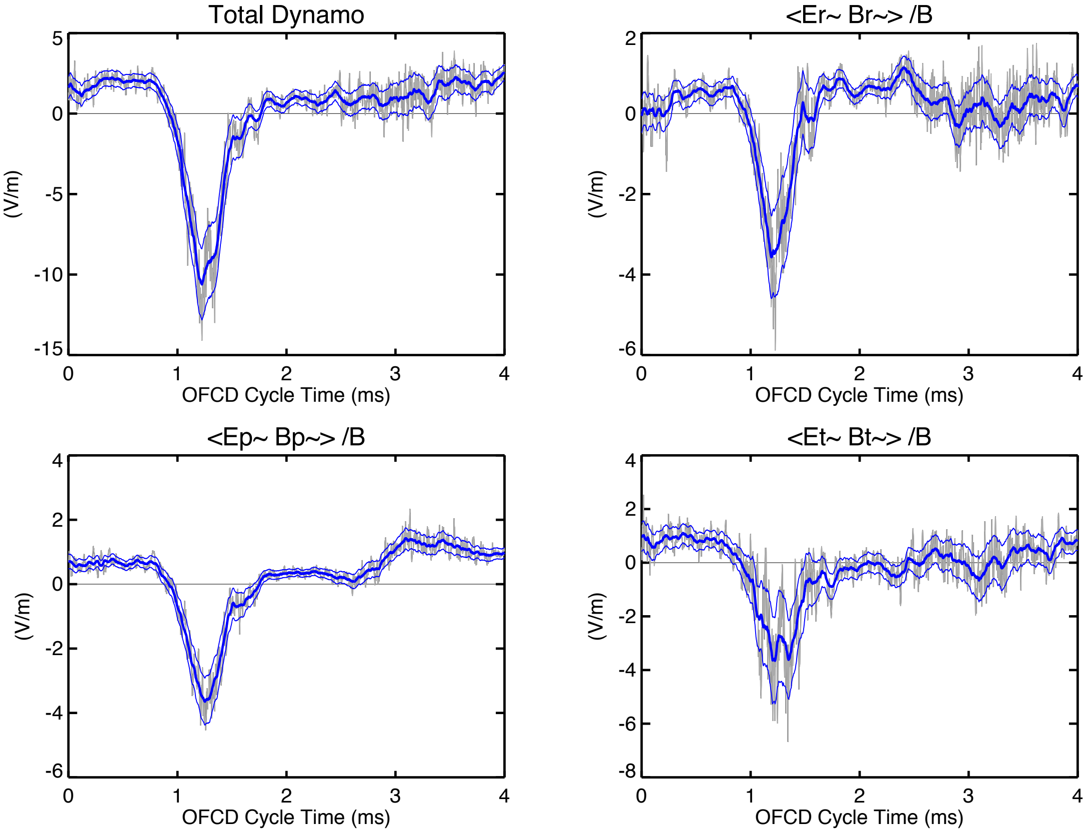

Figure D.39: Dynamo contributions from $\tilde{\mathbf{E}}$ and $\tilde{\mathbf{B}}$ components, OFCD $\delta = 0$ cycle.

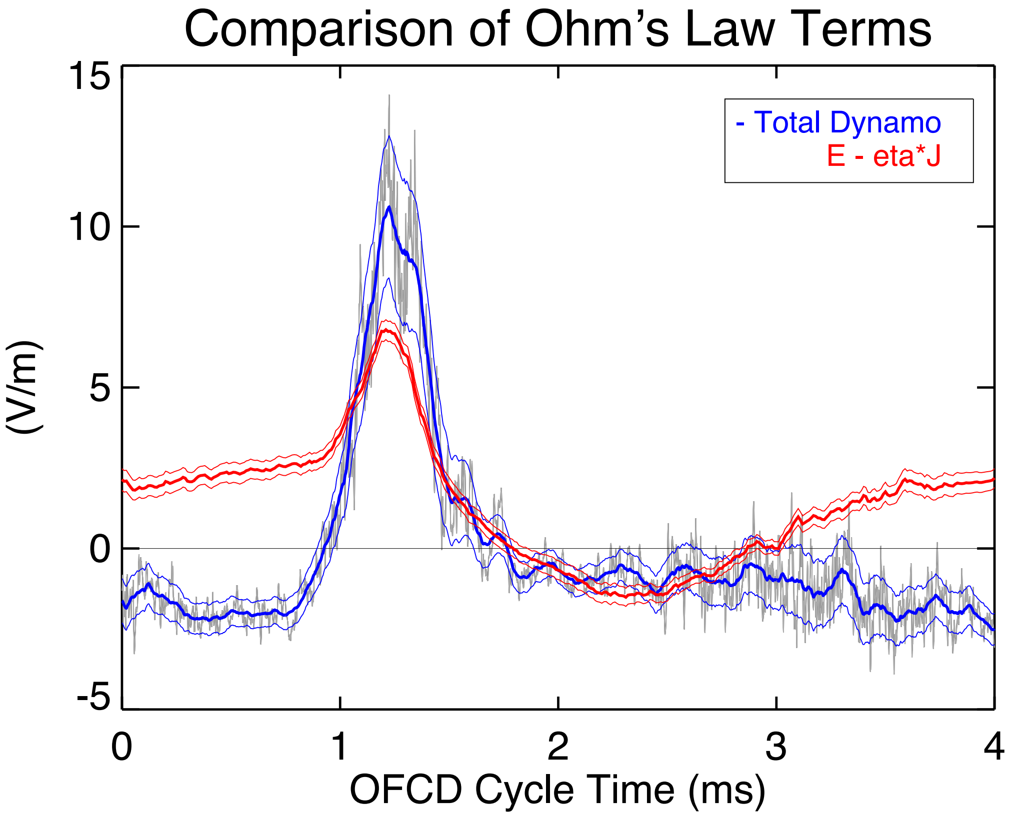

Figure D.40: Ohm's law ($\mathbf{E} - \eta \mathbf{J}$ and $- < \tilde{\mathbf{E}} \cdot \tilde{\mathbf{B}} > /B$), OFCD $\delta = 0$ cycle.

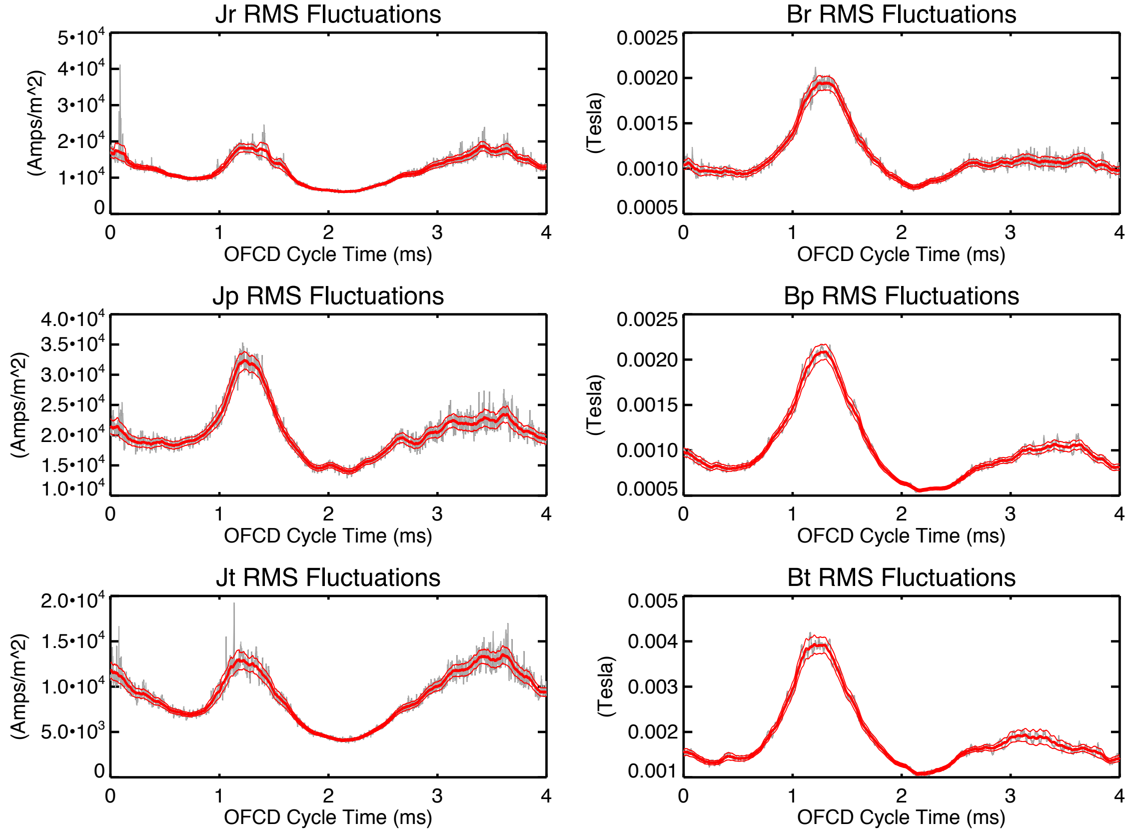

Figure D.41: Dynamo Probe $\tilde{\mathbf{J}}_{RMS}$ and $\tilde{\mathbf{B}}_{RMS}$, highpass filtered, OFCD $\delta = 0$ cycle.

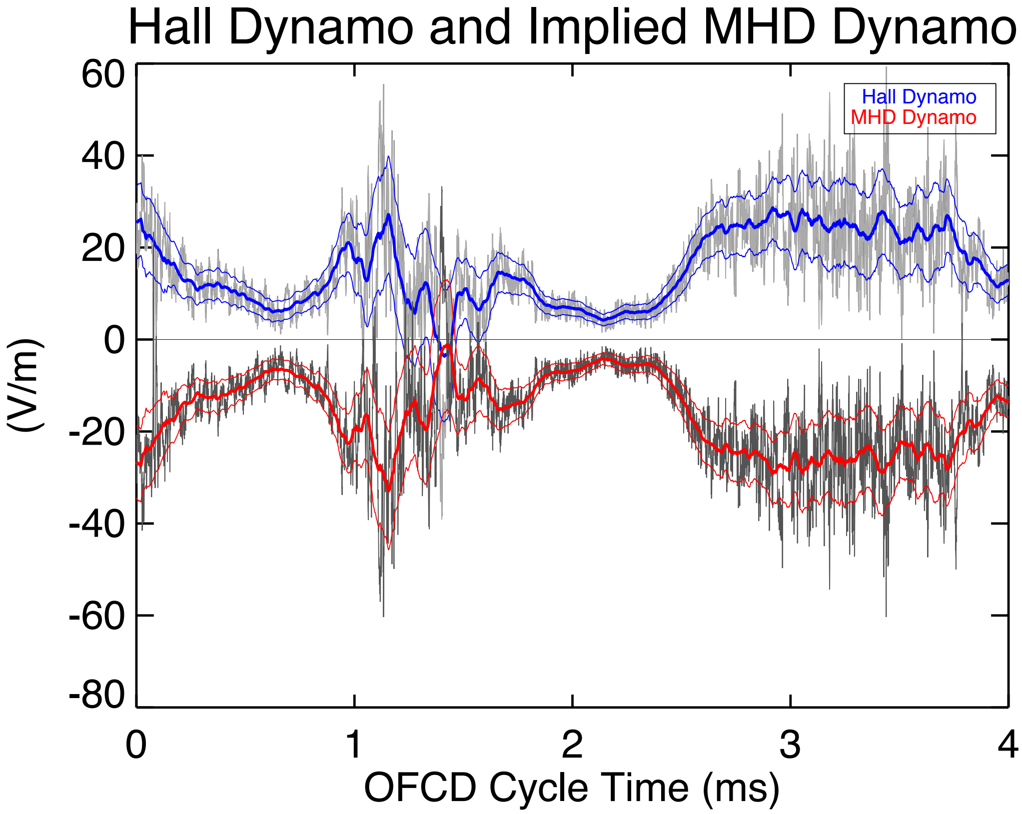

Figure D.42: Hall Dynamo and assumed MHD Dynamo (= Total Dynamo - Hall Dynamo) using highpass filtered data, OFCD $\delta = 0$ cycle.

D.3.2 Sawtooth Ensemble

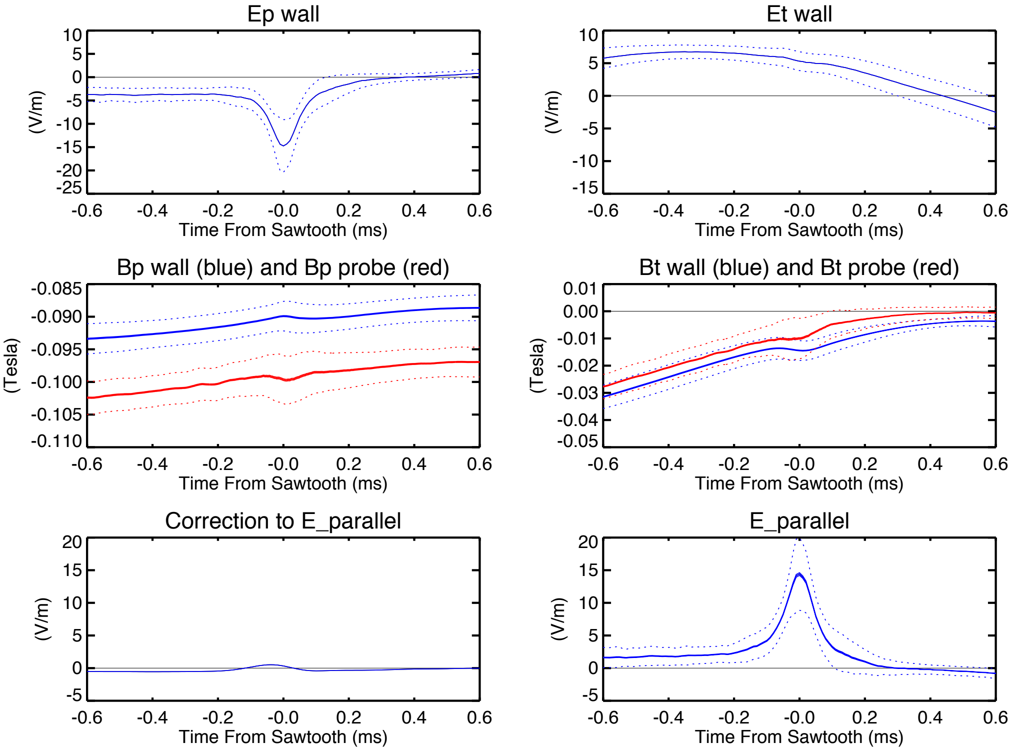

Figure D.43: Parallel electric field data, OFCD $\delta = 0$ sawtooth.

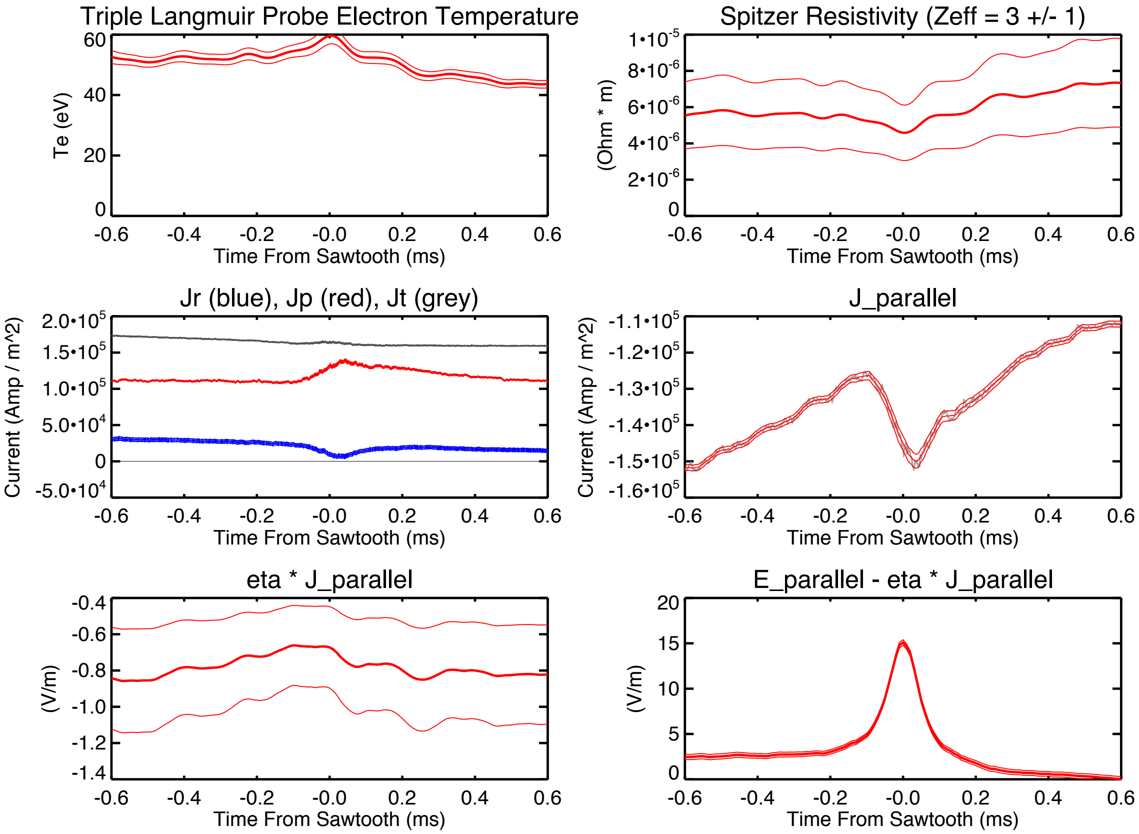

Figure D.44: Probe $\eta\mathbf{J}$ data, OFCD $\delta = 0$ sawtooth.

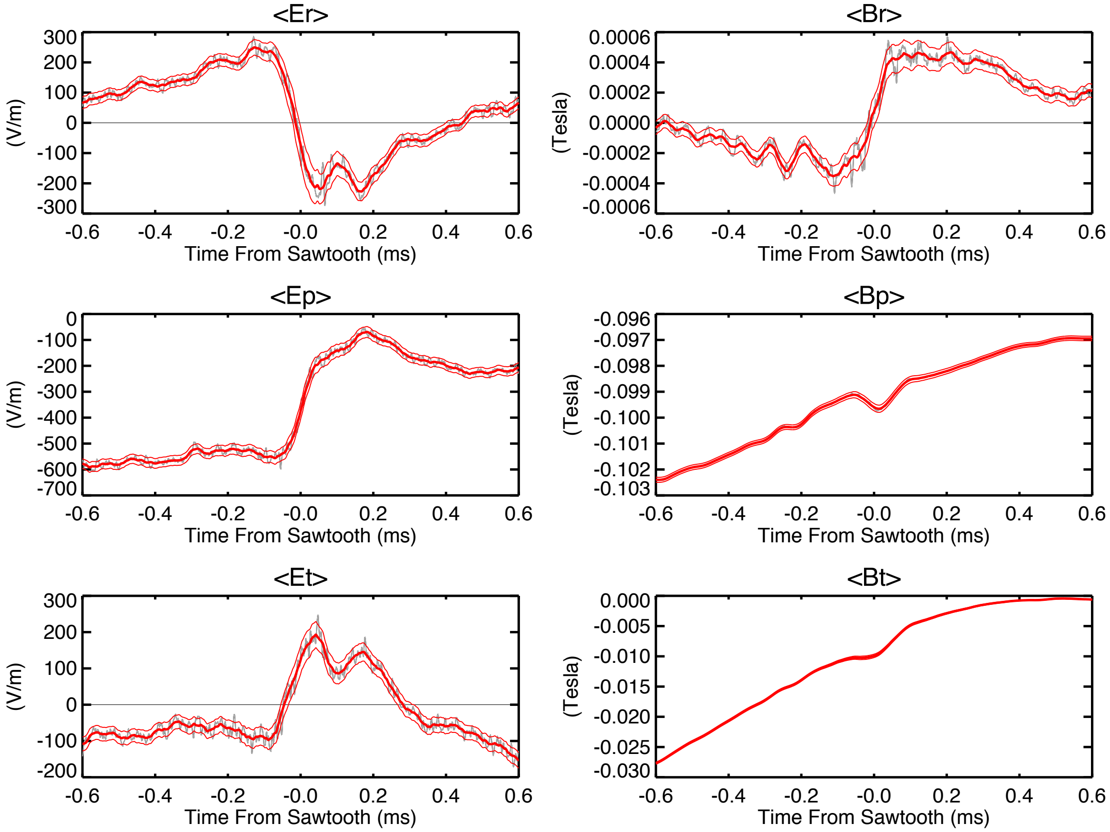

Figure D.45: Dynamo Probe $< \mathbf{E} >$ and $< \mathbf{B} >$, OFCD $\delta = 0$ sawtooth.

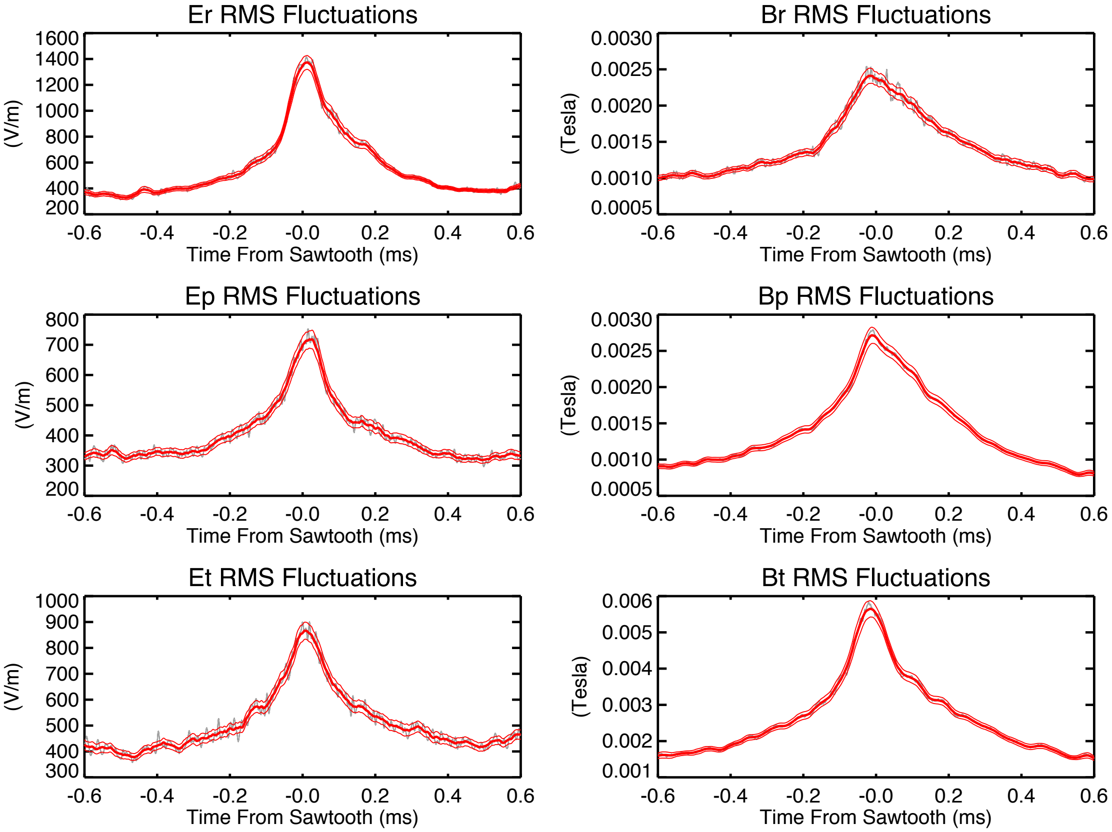

Figure D.46: Dynamo Probe $\tilde{\mathbf{E}}_{RMS}$ and $\tilde{\mathbf{B}}_{RMS}$, OFCD $\delta = 0$ sawtooth.

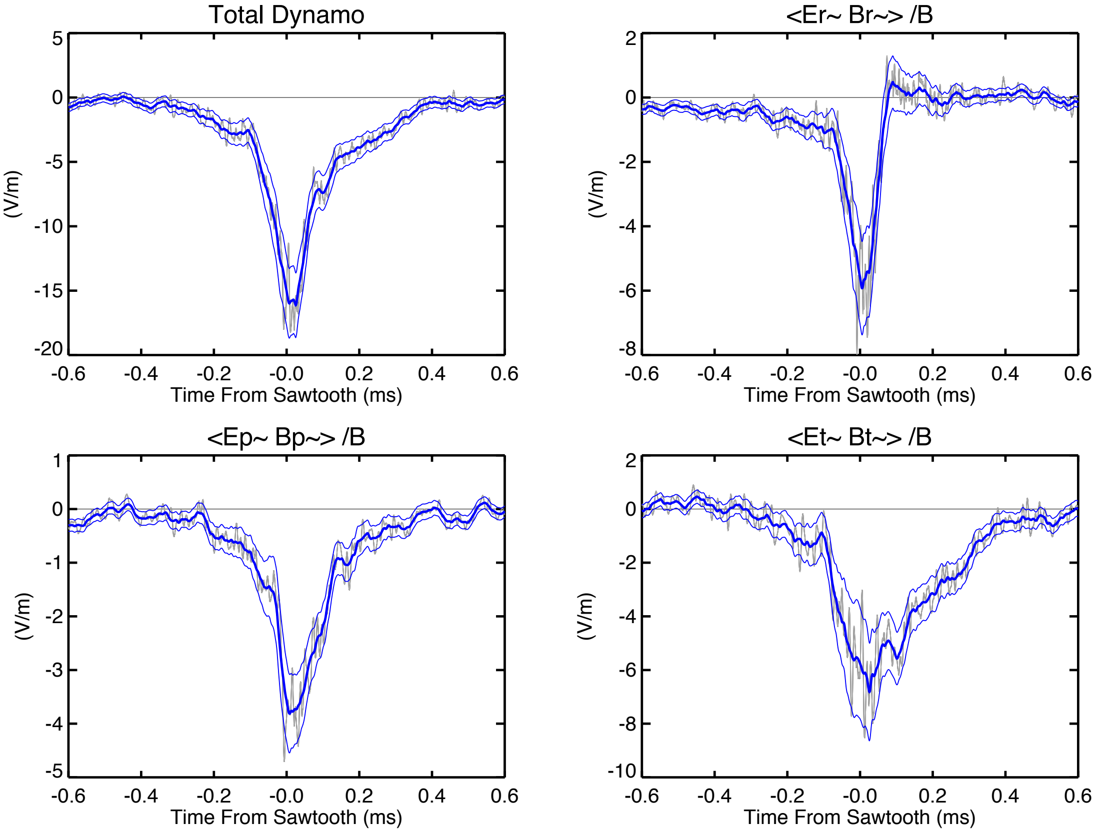

Figure D.47: Dynamo contributions from $\tilde{\mathbf{E}}$ and $\tilde{\mathbf{B}}$ components, OFCD $\delta = 0$ sawtooth.

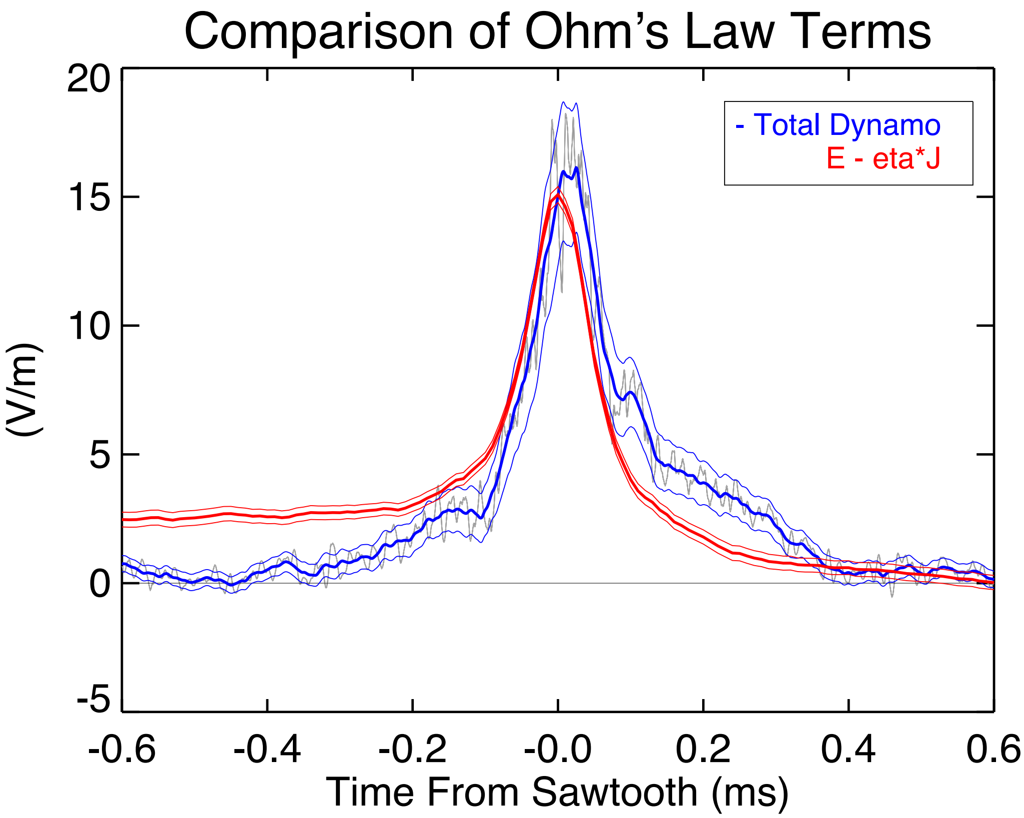

Figure D.48: Ohm's law ($\mathbf{E} - \eta\mathbf{J}$ and $- < \tilde{\mathbf{E}} \cdot \tilde{\mathbf{B}} > /B$), OFCD $\delta = 0$ sawtooth.

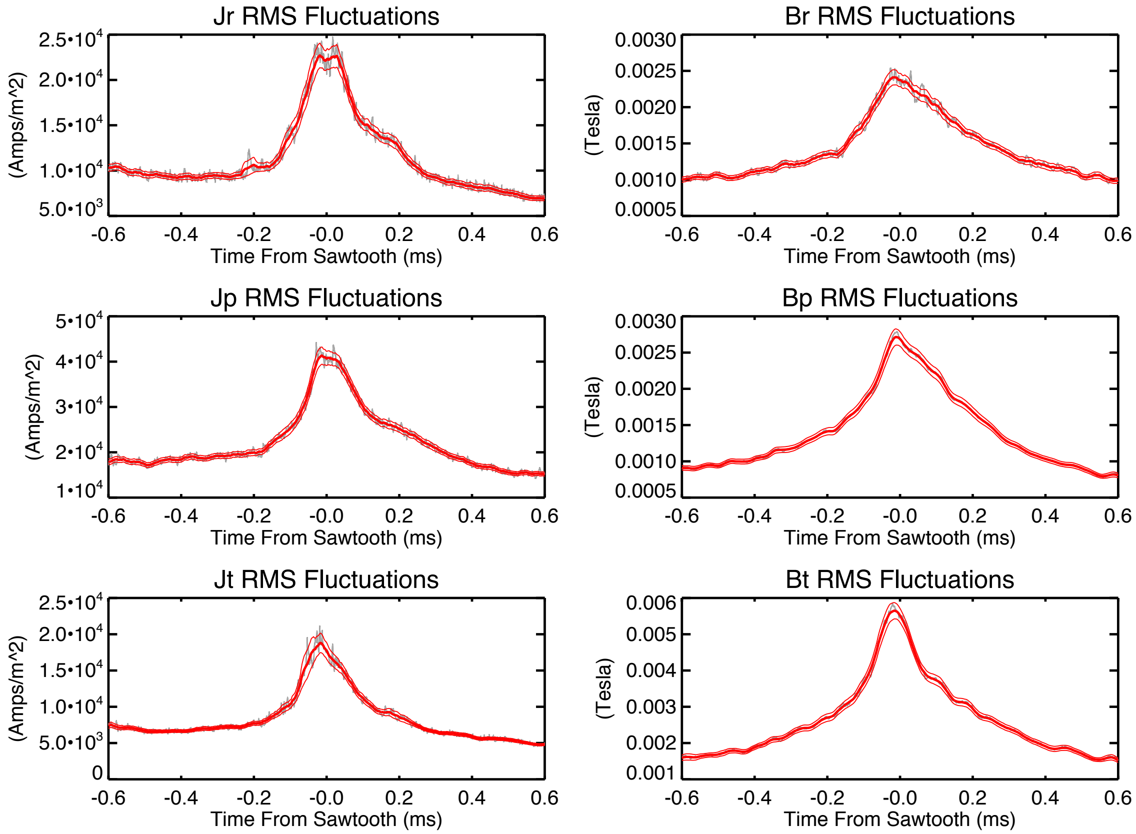

Figure D.49: Dynamo Probe $\tilde{\mathbf{J}}_{RMS}$ and $\tilde{\mathbf{B}}_{RMS}$, OFCD $\delta = 0$ sawtooth.

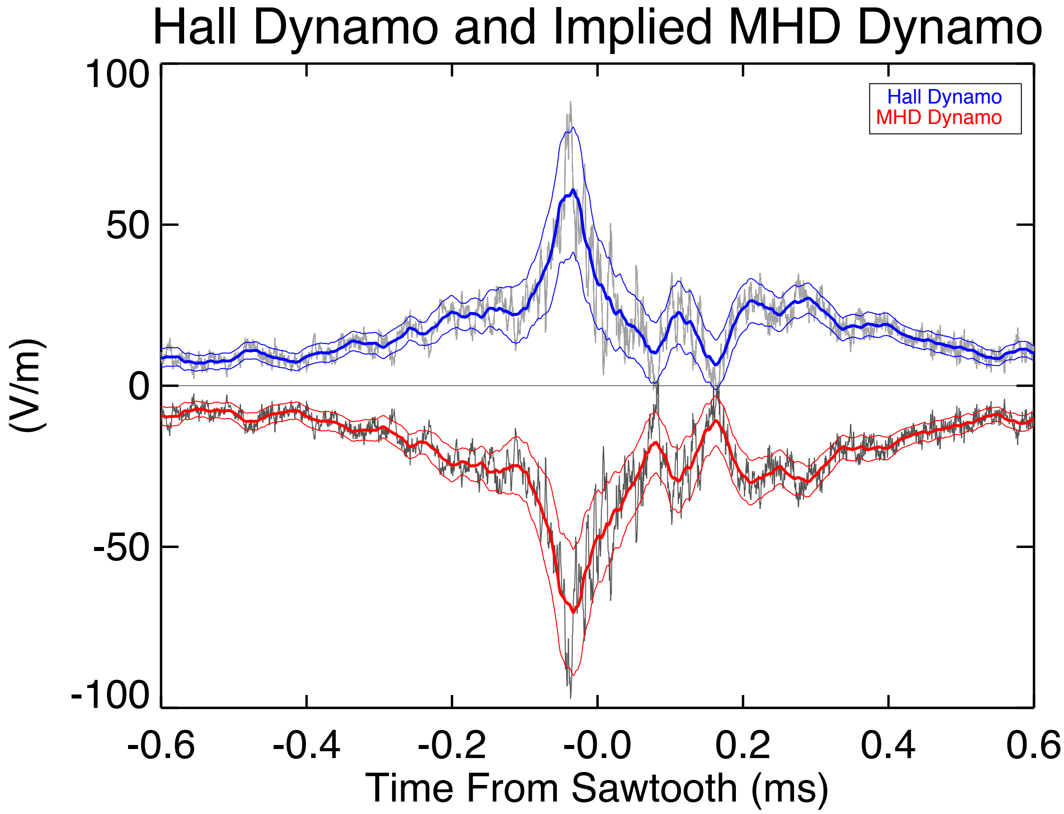

Figure D.50: Hall Dynamo and assumed MHD Dynamo (= Total Dynamo - Hall Dynamo), OFCD $\delta = 0$ sawtooth.

D.4 OFCD $\delta = -\pi/4$

D.4.1 Cycle Ensemble

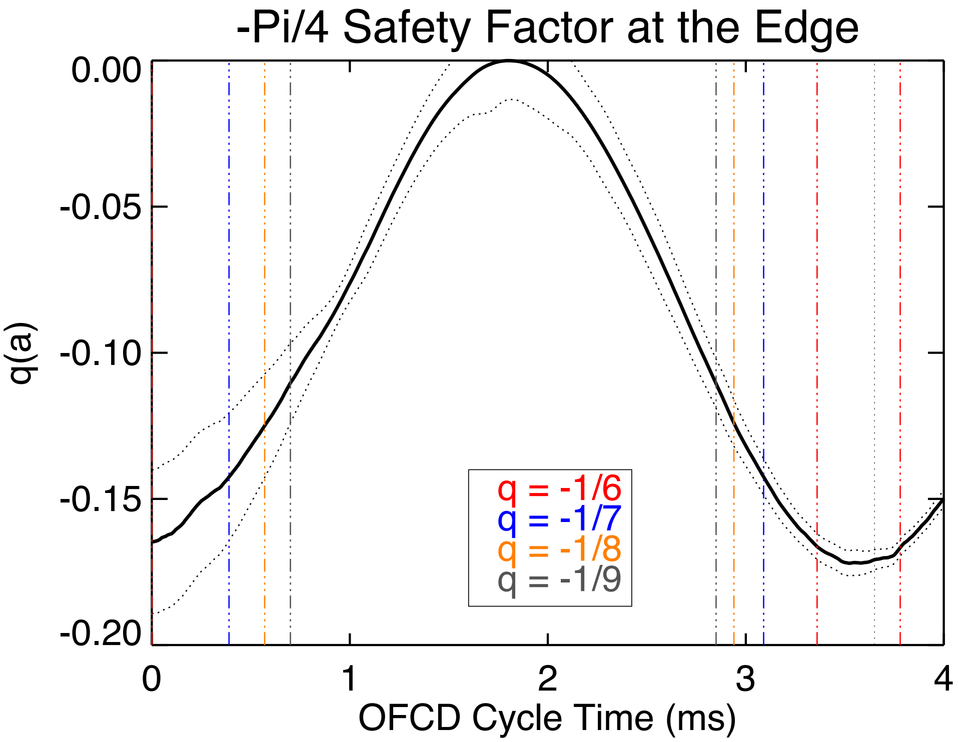

Figure D.51: Edge safety factor, OFCD $\delta = -\pi/4$ cycle.

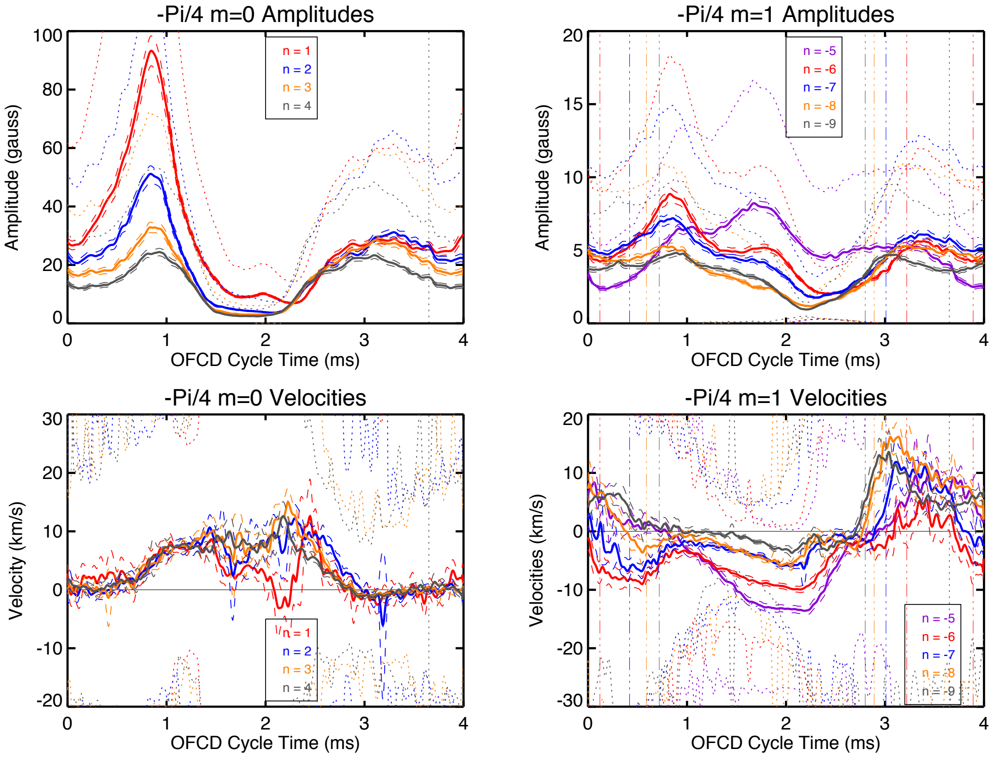

Figure D.52: Tearing mode amplitudes and velocities, OFCD $\delta = -\pi/4$ cycle.

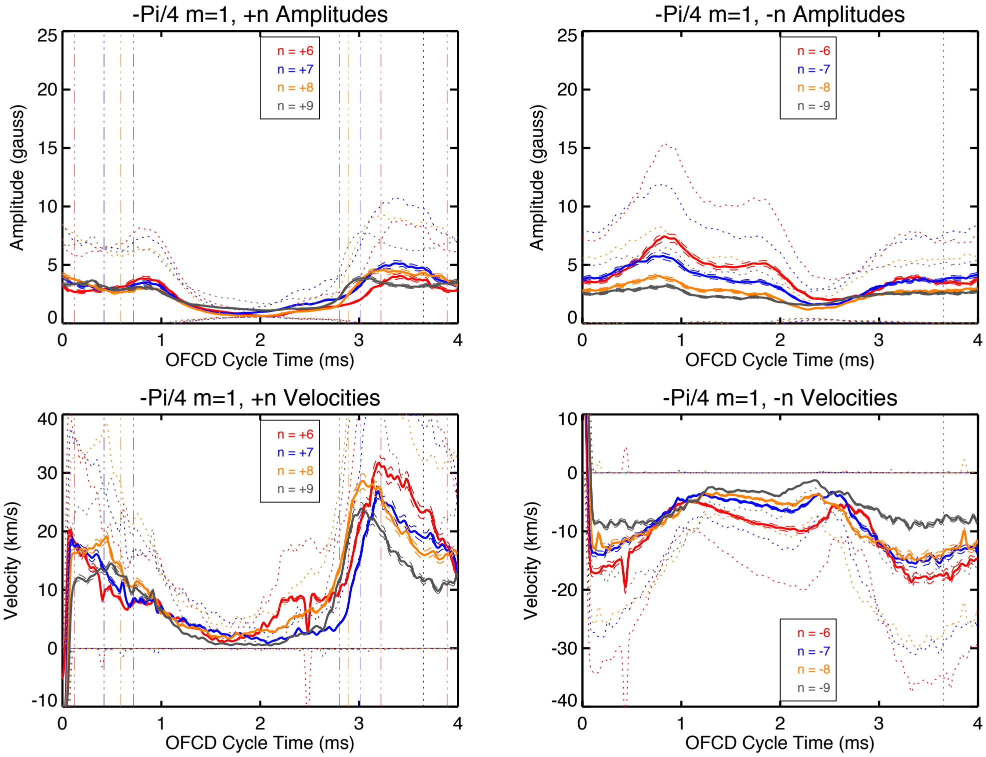

Figure D.53: Tearing mode +n and -n amplitudes and velocities, OFCD $\delta = -\pi/4$ cycle.

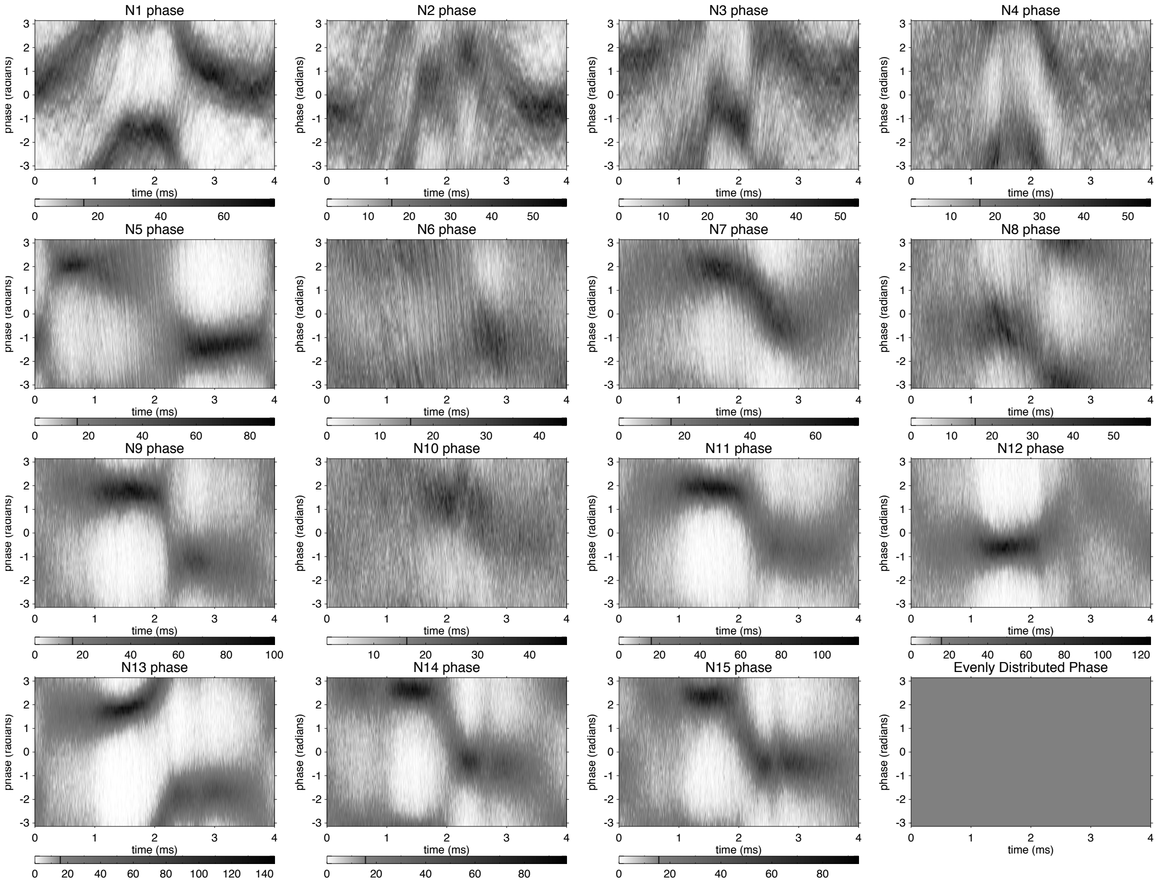

Figure D.54: Tearing mode phase distribution, OFCD $\delta = -\pi/4$ cycle.

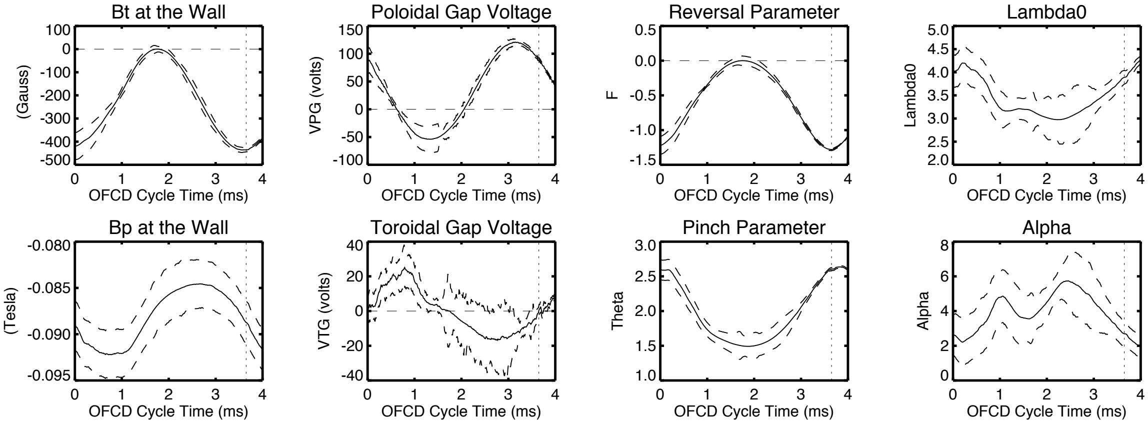

Figure D.55: Global and edge parameters, OFCD $\delta = -\pi/4$ cycle.

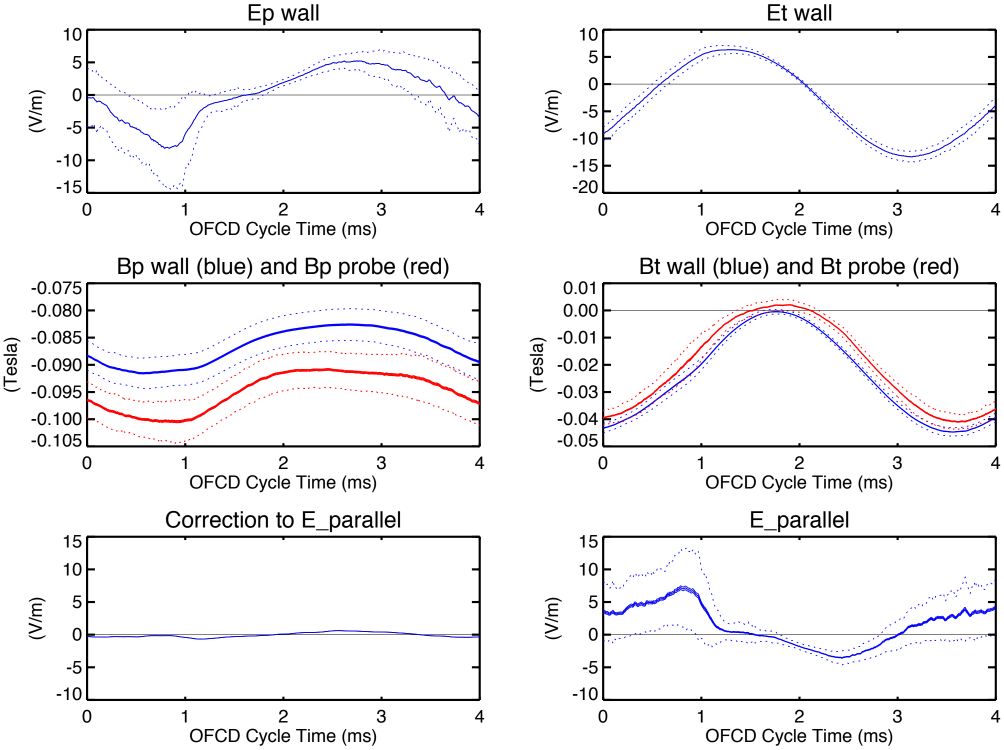

Figure D.56: Parallel electric field data, OFCD $\delta = -\pi/4$ cycle.

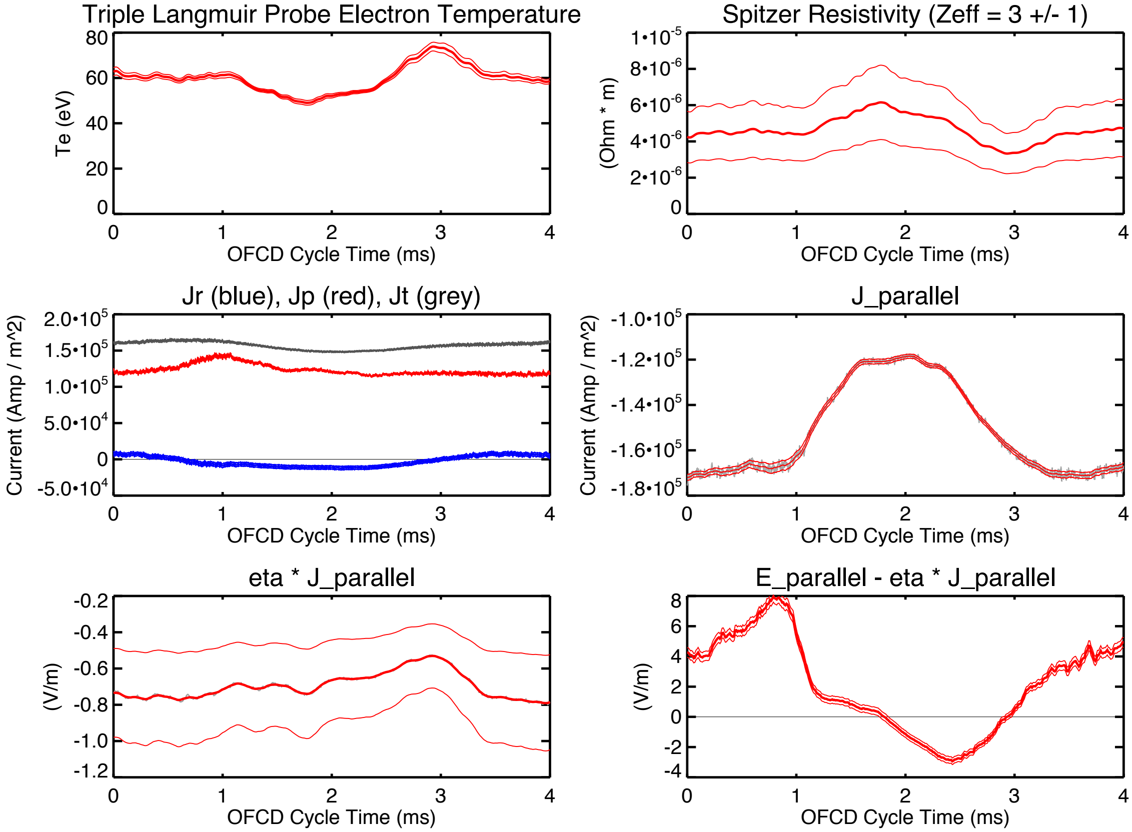
Triple Langmuir Probe Electron Temperature

Spitzer Resistivity (Zeff = 3 +/- 1)

Jr (blue), Jp (red), Jt (grey)

J_parallel

eta * J_parallel

E_parallel - eta * J_parallel

Figure D.57: Probe $\eta\mathbf{J}$ data, OFCD $\delta = -\pi/4$ cycle.

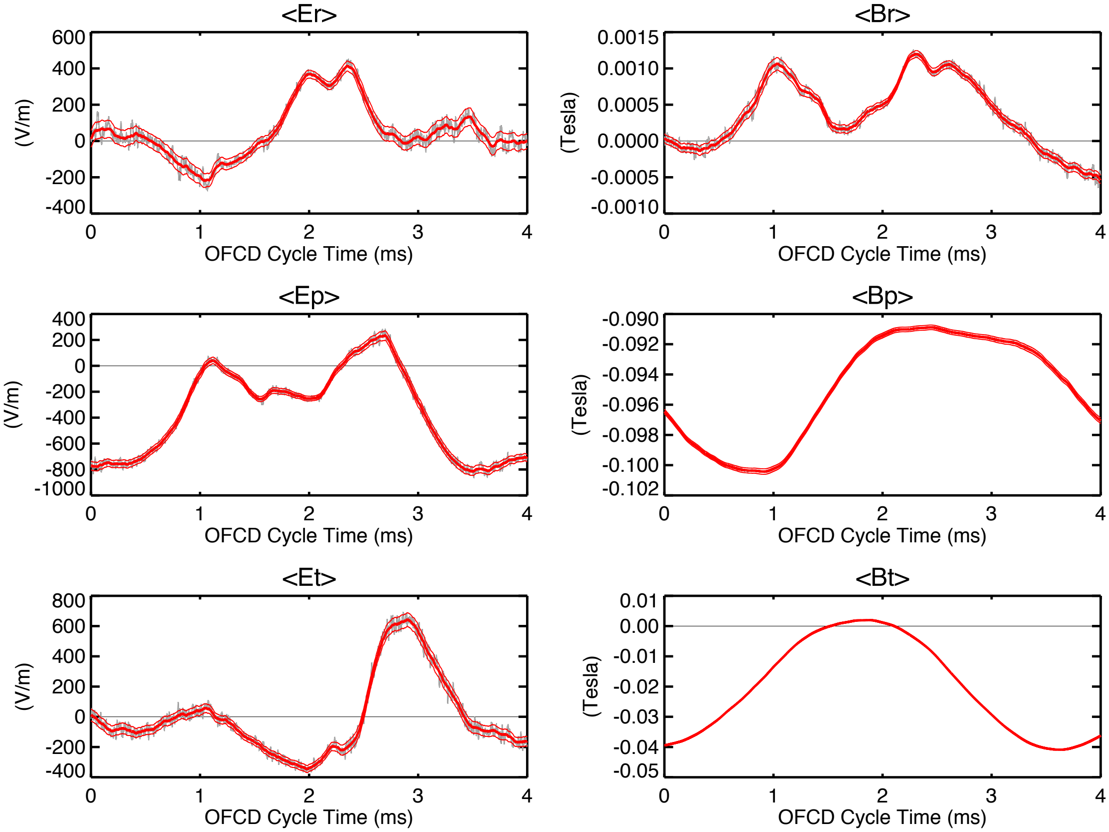

Figure D.58: Dynamo Probe $< \mathbf{E} >$ and $< \mathbf{B} >$, OFCD $\delta = -\pi/4$ cycle.

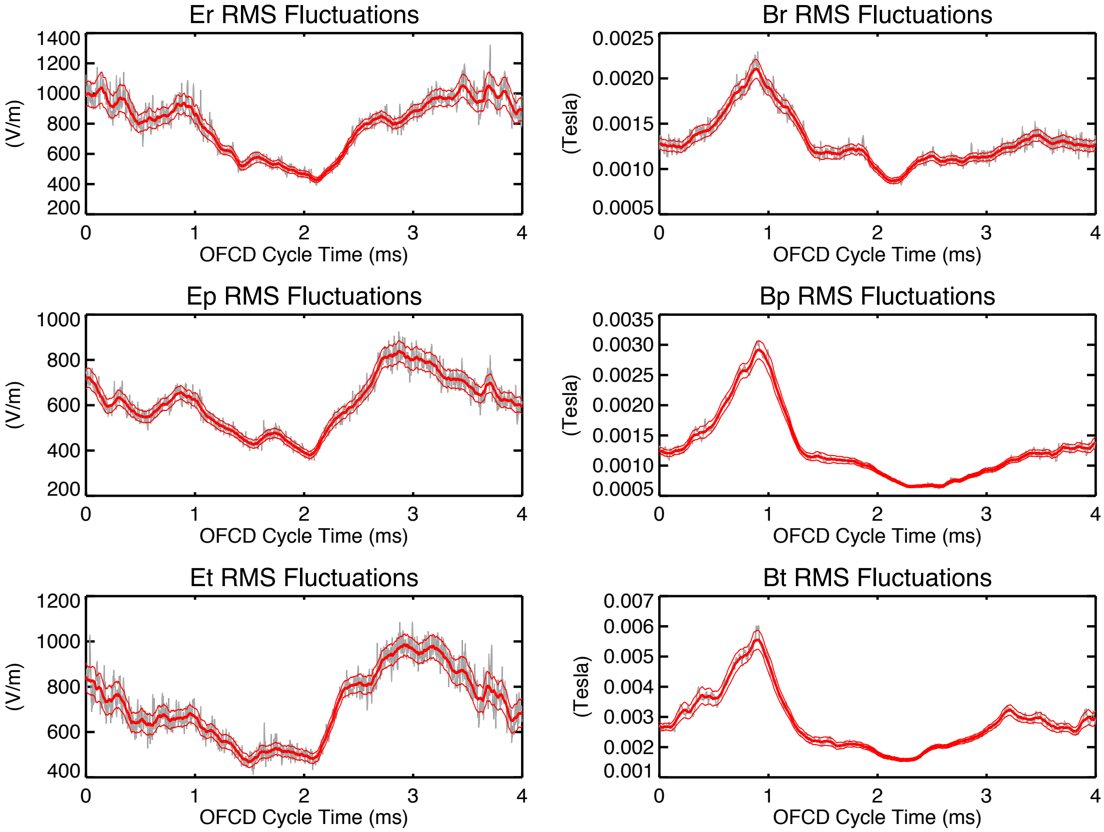

Figure D.59: Dynamo Probe $\tilde{\mathbf{E}}_{RMS}$ and $\tilde{\mathbf{B}}_{RMS}$, OFCD $\delta = -\pi/4$ cycle.

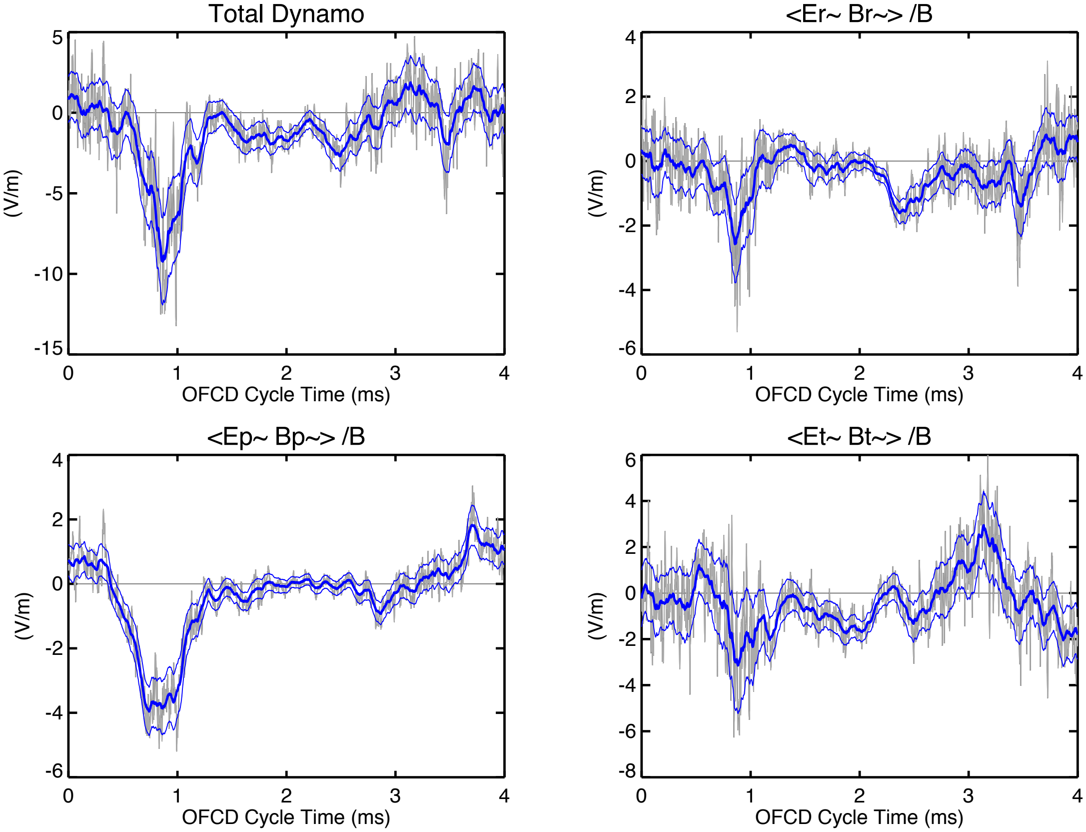

Figure D.60: Dynamo contributions from $\tilde{\mathbf{E}}$ and $\tilde{\mathbf{B}}$ components, OFCD $\delta = -\pi/4$ cycle.

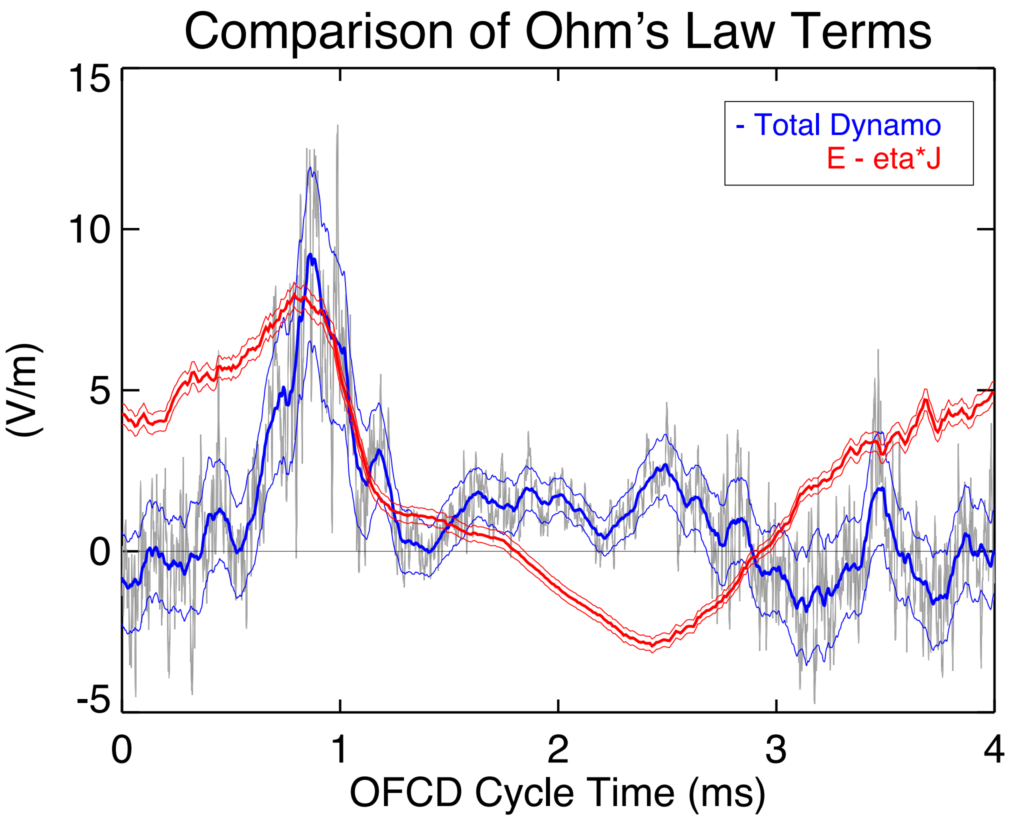

Figure D.61: Ohm's law ($\mathbf{E} - \eta\mathbf{J}$ and $- < \tilde{\mathbf{E}} \cdot \tilde{\mathbf{B}} > /B$), OFCD $\delta = -\pi/4$ cycle.

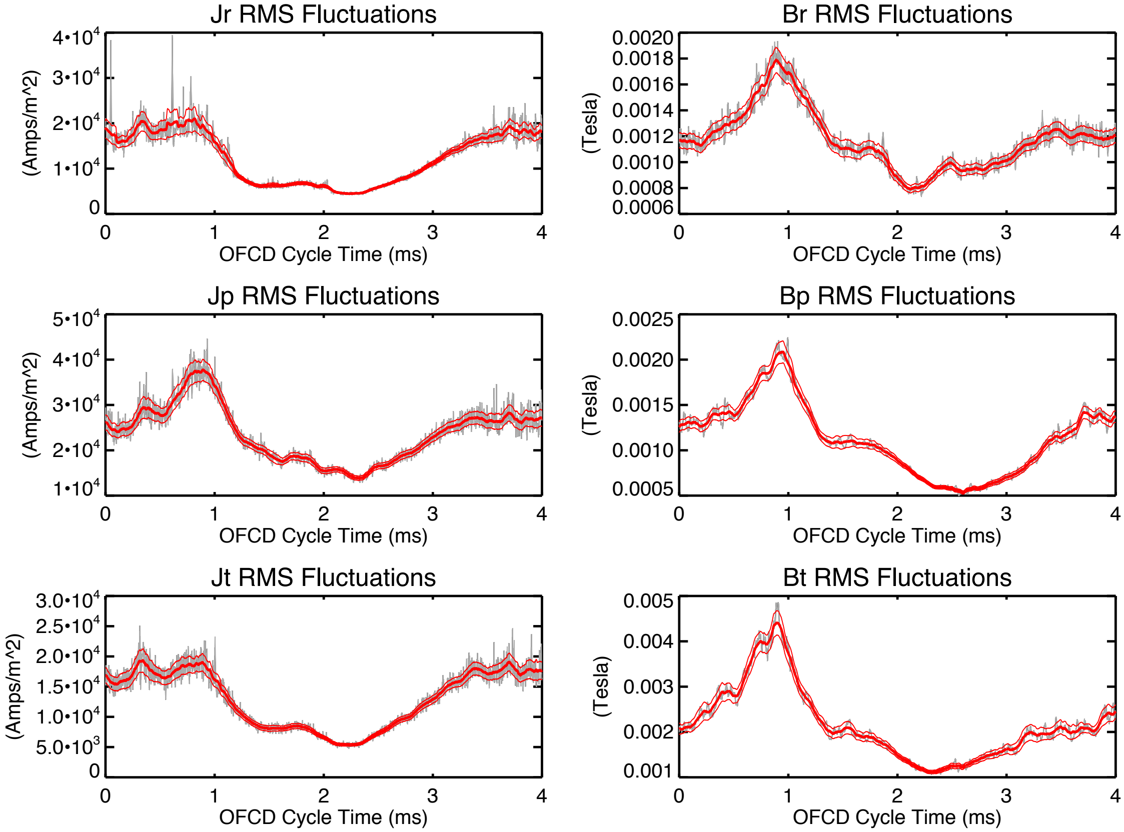

Figure D.62: Dynamo Probe $\tilde{\mathbf{J}}_{RMS}$ and $\tilde{\mathbf{B}}_{RMS}$, highpass filtered, OFCD $\delta = -\pi/4$ cycle.

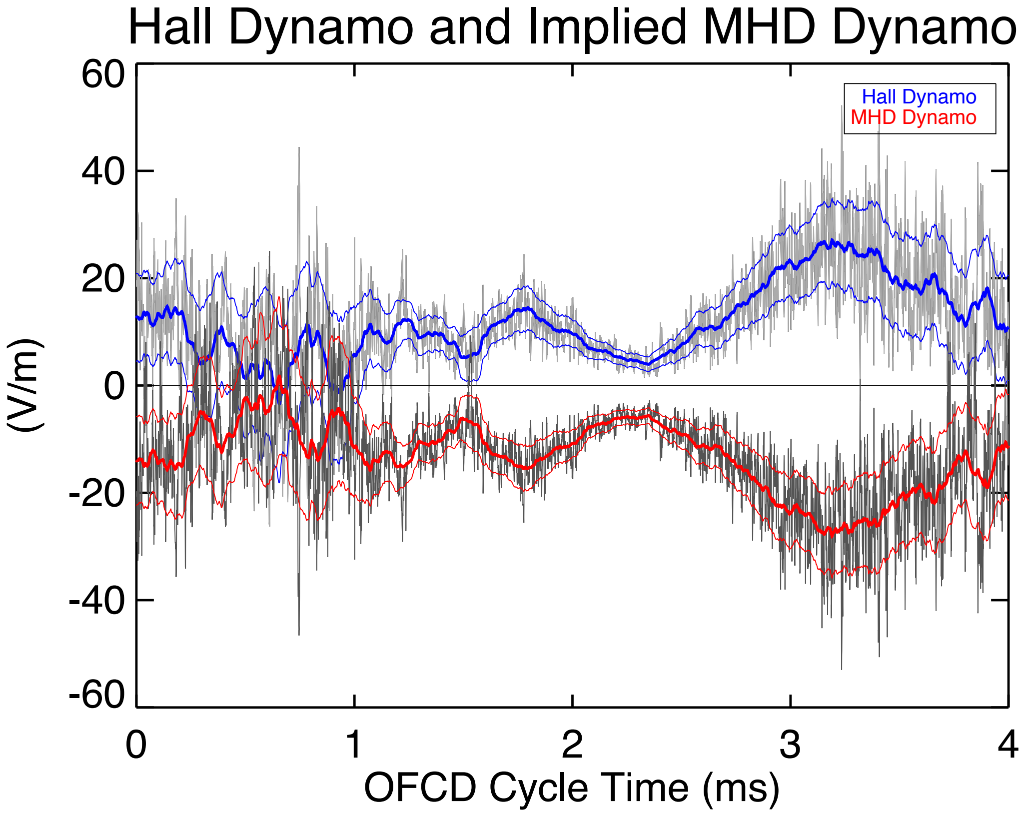

Figure D.63: Hall Dynamo and assumed MHD Dynamo (= Total Dynamo - Hall Dynamo) using highpass filtered data, OFCD $\delta = -\pi/4$ cycle.

D.4.2 Sawtooth Ensemble

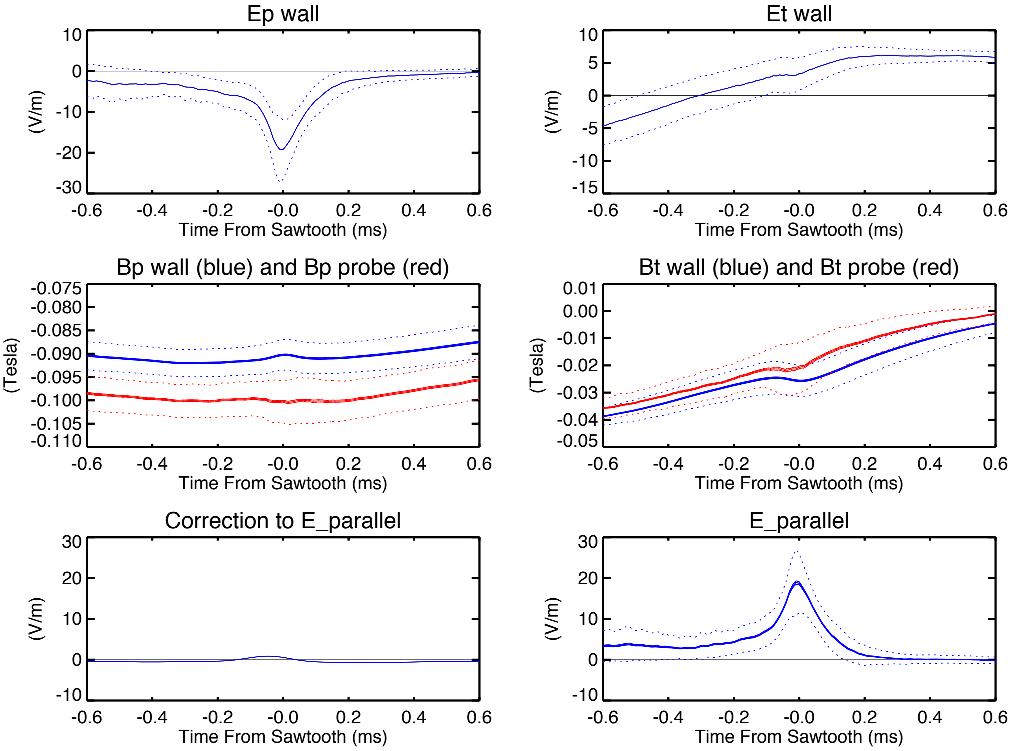

Figure D.64: Parallel electric field data, OFCD $\delta = -\pi/4$ sawtooth.

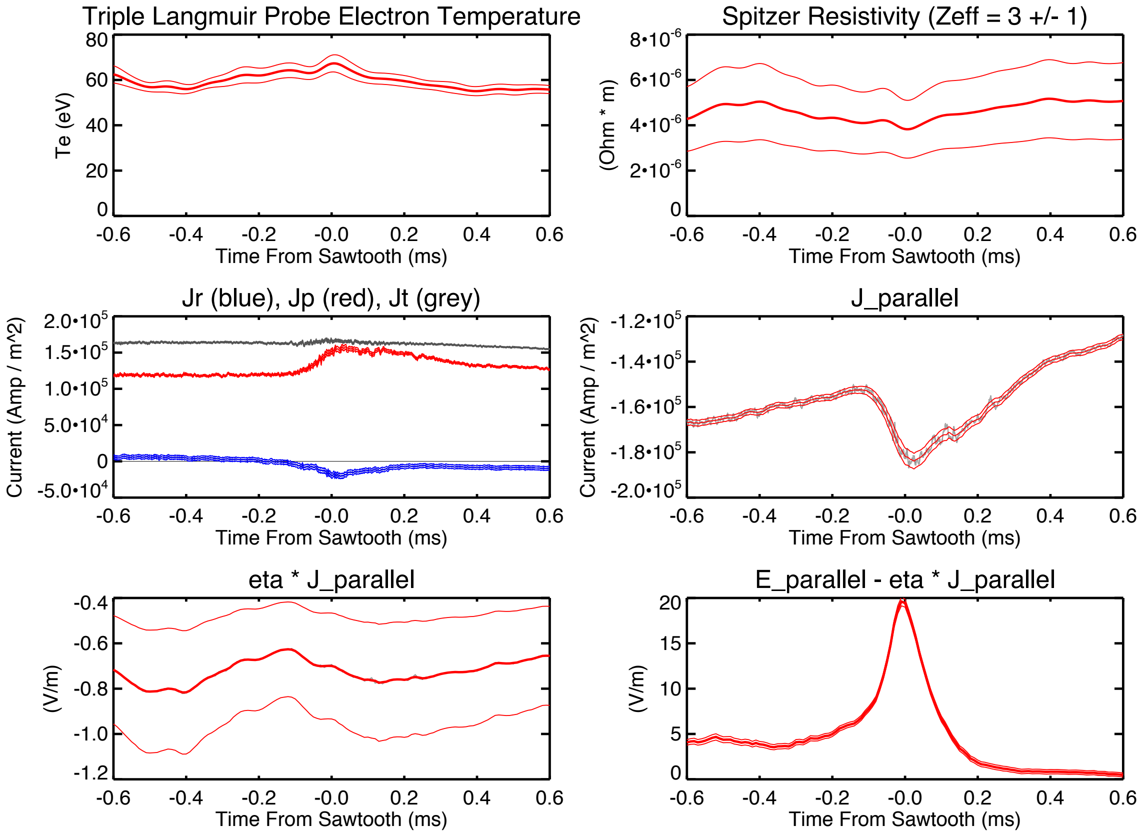

Figure D.65: Probe $\eta\mathbf{J}$ data, OFCD $\delta = -\pi/4$ sawtooth.

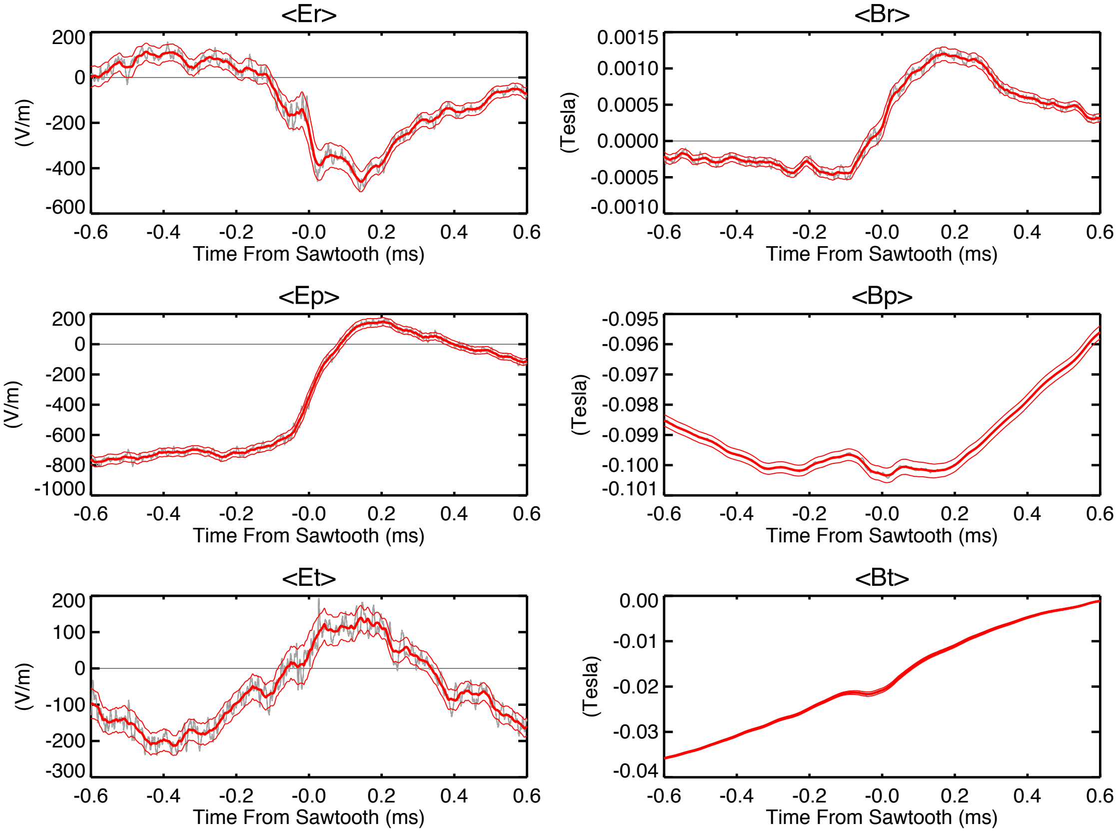

Figure D.66: Dynamo Probe $< \mathbf{E} >$ and $< \mathbf{B} >$, OFCD $\delta = -\pi/4$ sawtooth.

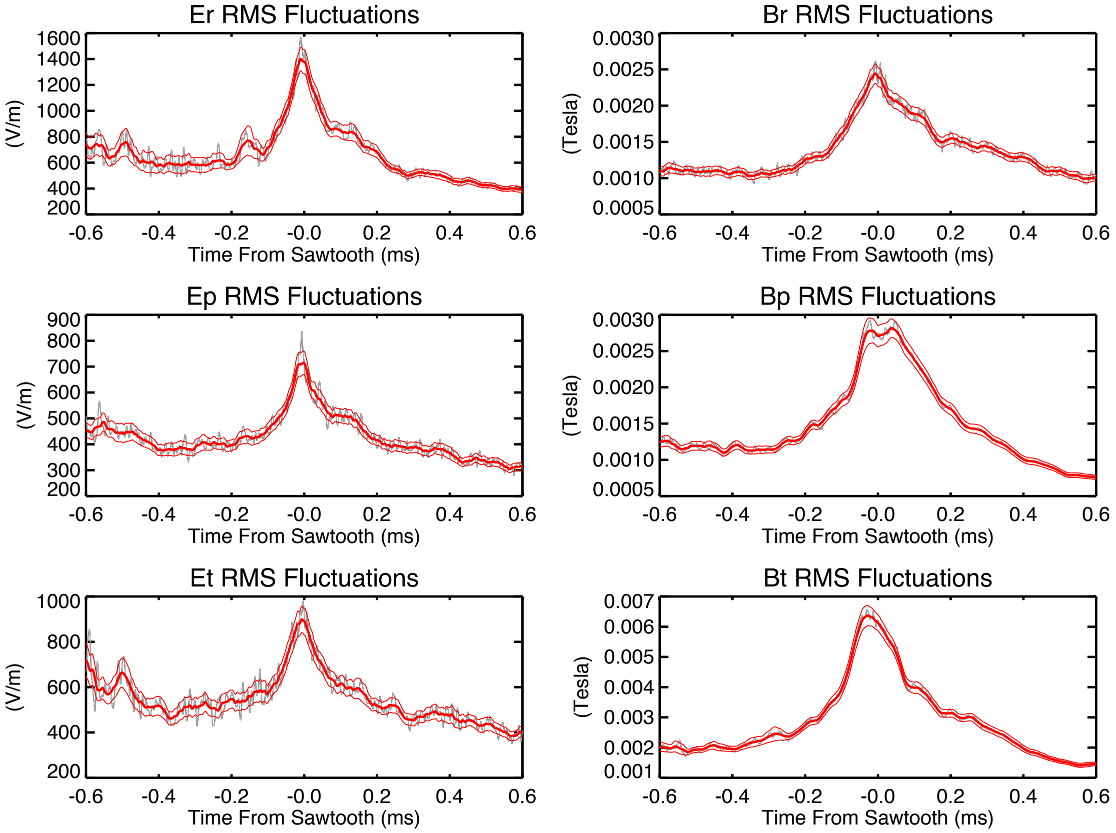

Figure D.67: Dynamo Probe $\tilde{\mathbf{E}}_{RMS}$ and $\tilde{\mathbf{B}}_{RMS}$, OFCD $\delta = -\pi/4$ sawtooth.

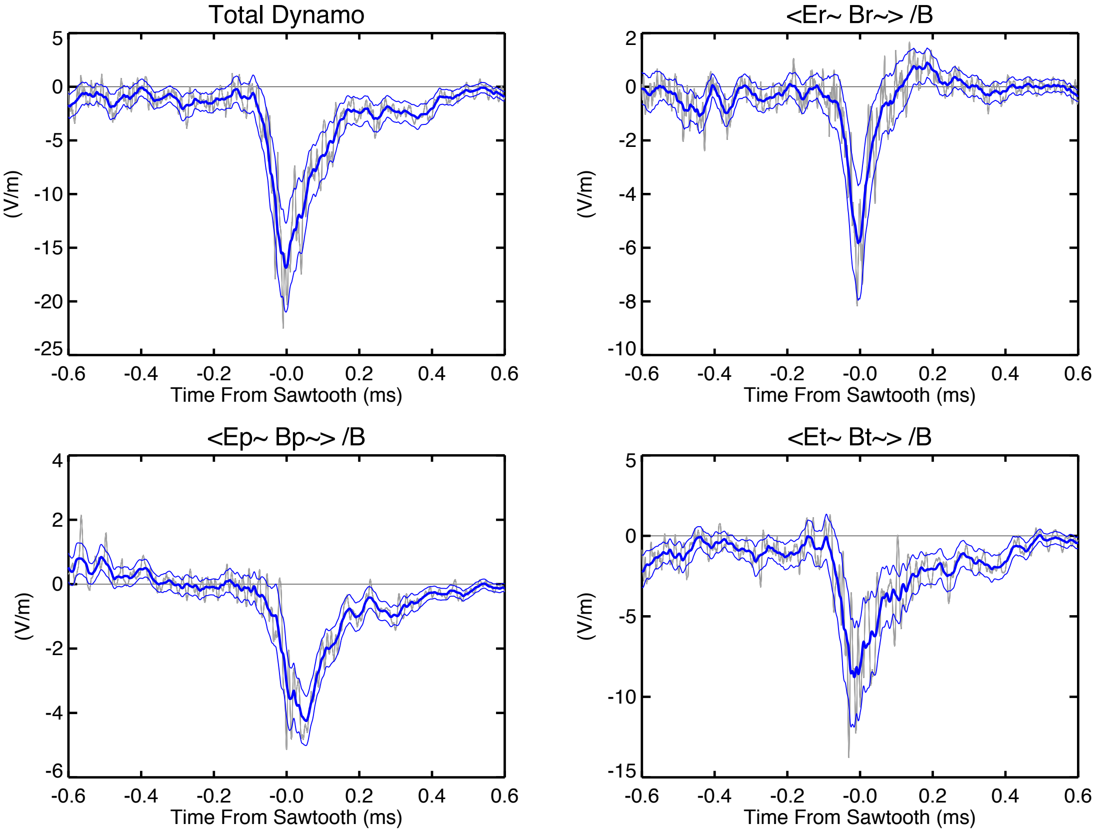

Figure D.68: Dynamo contributions from $\tilde{\mathbf{E}}$ and $\tilde{\mathbf{B}}$ components, OFCD $\delta = -\pi/4$ sawtooth.

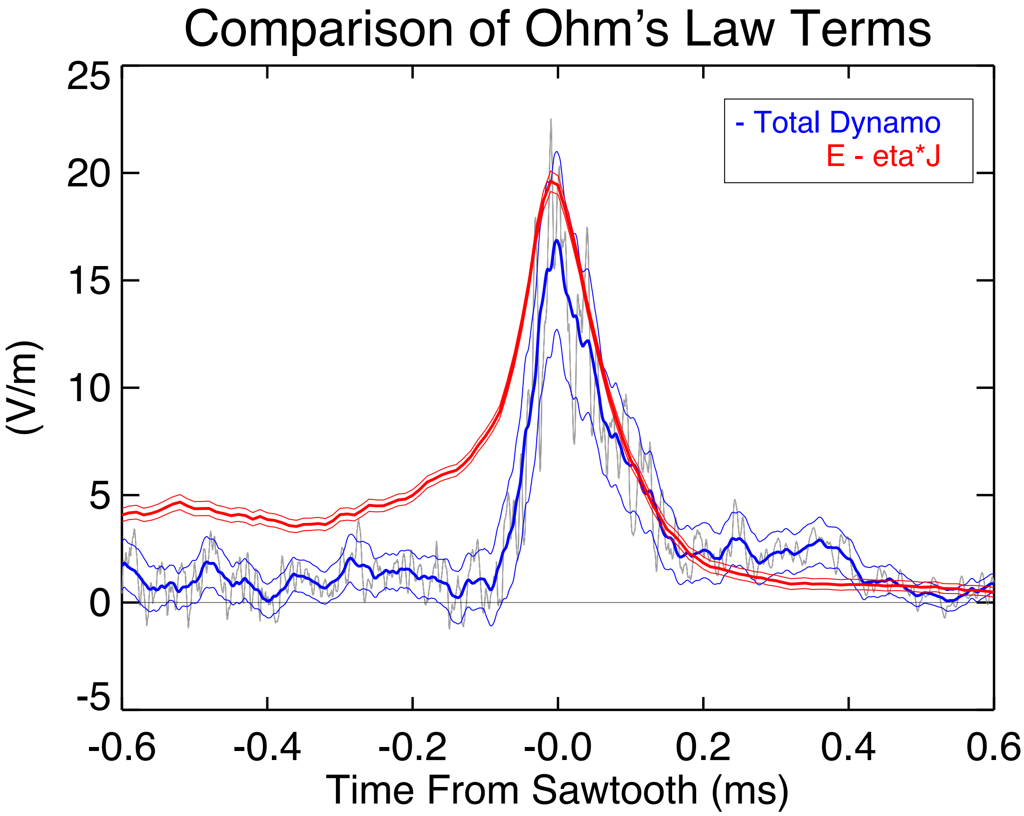

Figure D.69: Ohm's law ($\mathbf{E} - \eta \mathbf{J}$ and $- < \tilde{\mathbf{E}} \cdot \tilde{\mathbf{B}} > /B$), OFCD $\delta = -\pi/4$ sawtooth.

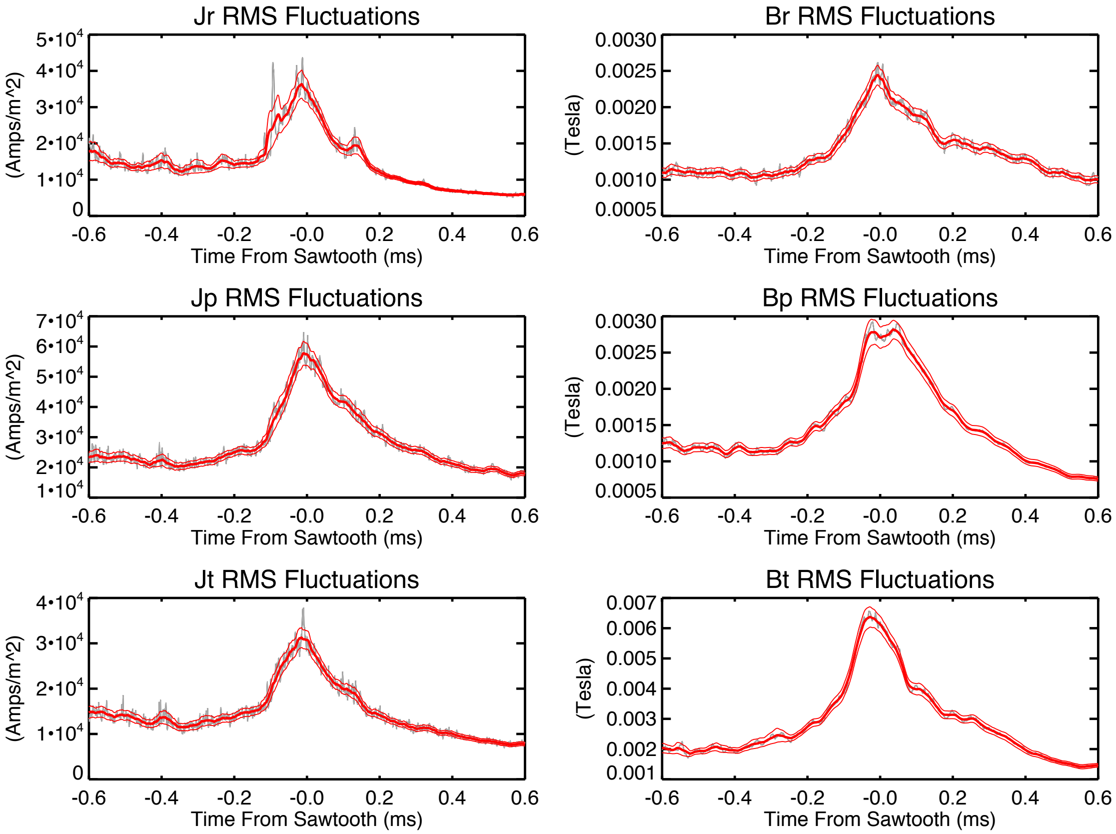

Figure D.70: Dynamo Probe $\tilde{\mathbf{J}}_{RMS}$ and $\tilde{\mathbf{B}}_{RMS}$, OFCD $\delta = -\pi/4$ sawtooth.

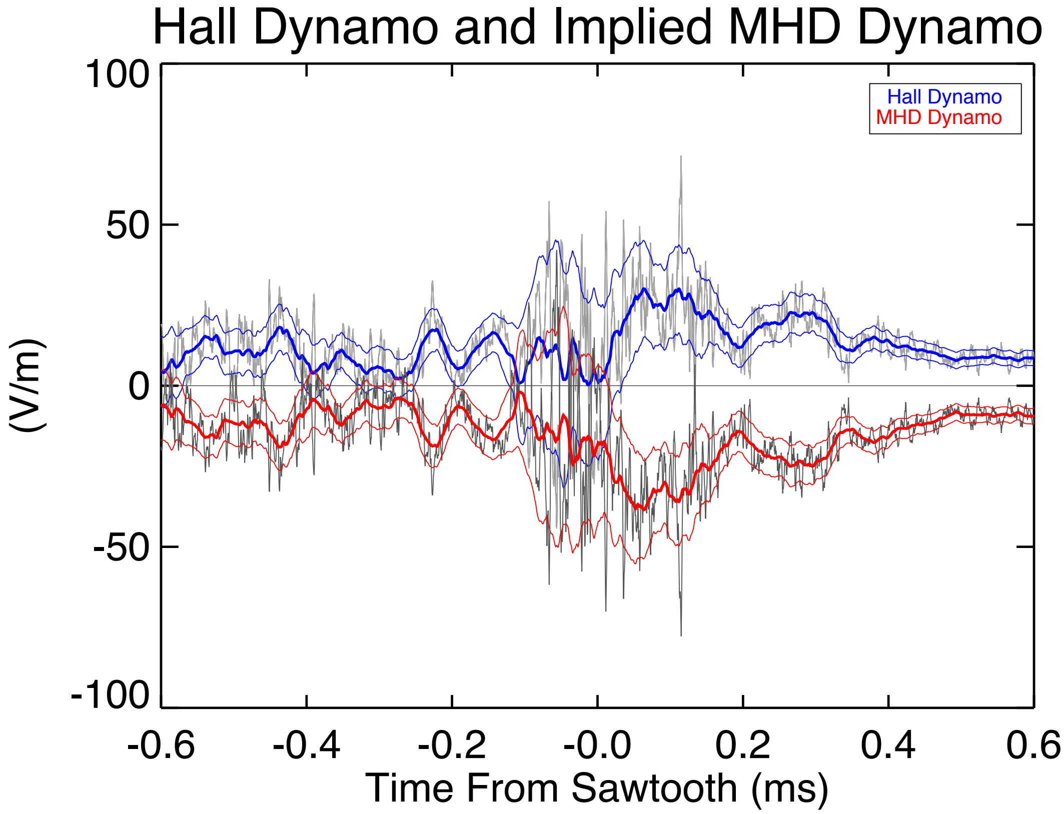

Figure D.71: Hall Dynamo and assumed MHD Dynamo (= Total Dynamo - Hall Dynamo), OFCD $\delta = -\pi/4$ sawtooth.

D.5 Standard 250 kA, $F \approx -0.5$

This section will summarize results from a deeply reversed, standard RFP ensemble with MST settings identical to the MST settings used for the ensembles of OFCD results presented in Chapter 6. The resulting RFPs have a plasma current of $I_p = 250 \pm 10$ kA and reversal of $F = -0.5 \pm 0.05$. During this ensemble the OFCD poloidal (B_θ) transformer secondary inductance is added to the MST circuit in order to match the MST circuit configuration during partial OFCD experiments. The OFCD B_ϕ secondary inductance does not need to be added to the MST circuit because the OFCD B_ϕ circuit uses an inductor normally in the MST circuit (the F-ductor) as its secondary.

This ensemble is a good match for I_{plasma} during the OFCD ensembles but only matches the cycle-average value of F, which oscillate over a range of approximately $-1.2 < F < 0$ during the OFCD ensembles. The reversal parameter of this ensemble matches F for the OFCD sawtooth region for the OFCD phases $\delta = 0$ and $\delta = -\pi/4$ fairly well, but the reversal parameter during the OFCD $\delta = \pi/2$ and $\delta = \pi/4$ sawteeth is less negative than this standard ensemble. In addition, the mean magnetic fields are constantly changing during OFCD but are fairly constant away from the crash during this ensemble. Therefore, this deeply reversed ensemble is decent but not perfect for comparing to the OFCD ensembles.

The results for the deeply reversed standard sawtooth ensemble are shown below. The probe signal fluctuations are calculated using signals that are highpass filtered with a cutoff at 1 kHz. The results are questionable. The dynamo is not a very good match for $\mathbf{E} - \eta\mathbf{J}$. The Hall dynamo and implied MHD dynamo are perhaps too large but look fairly reasonable otherwise. The helicity flux is mostly the wrong direction.

The results obtained by not highpass filtering the probe signals (not shown) are even less believable. It is possible that some other unmeasured term from Ohm's law, such as the diamagnetic dynamo, is significant during the sawtooth for the deeply reversed standard RFP plasma. Alternately, there could be issues with the application of the analysis to this ensemble.

There are two possible problems with the analysis. One problem is that there is substantial variations of the equilibrium during the sawtooth from event to event. The sawtooth amplitudes and shapes have a much larger variation in the deeply reversed case than in the case of $F = -0.18$. This could result in $\bar{X} \neq < X >$ at the crash. Another potential problem is that the selection of $t = 0$ for each sawtooth might not be as exact for the deeply reversed ensemble as it is for the standard ensemble with normal reversal, again due to variations in the sawtooth shape. The wider spike in $\mathbf{E} - \eta\mathbf{J}$ ($\sim 200\mu s$ vs. $\sim 100\mu s$ for normal reversal) hints at this possibility.

Ideally, this 250 kA deeply reversed RFP ensemble would serve as a comparison to the OFCD case. In this ensemble, it is expected that the dynamo would match $\mathbf{E} - \eta\mathbf{J}$, which comes from a measurement that requires far fewer assumptions. For comparing to OFCD, the best that can be done is to assume the dynamo is equal and opposite to $\mathbf{E} - \eta\mathbf{J}$ shown in this section.

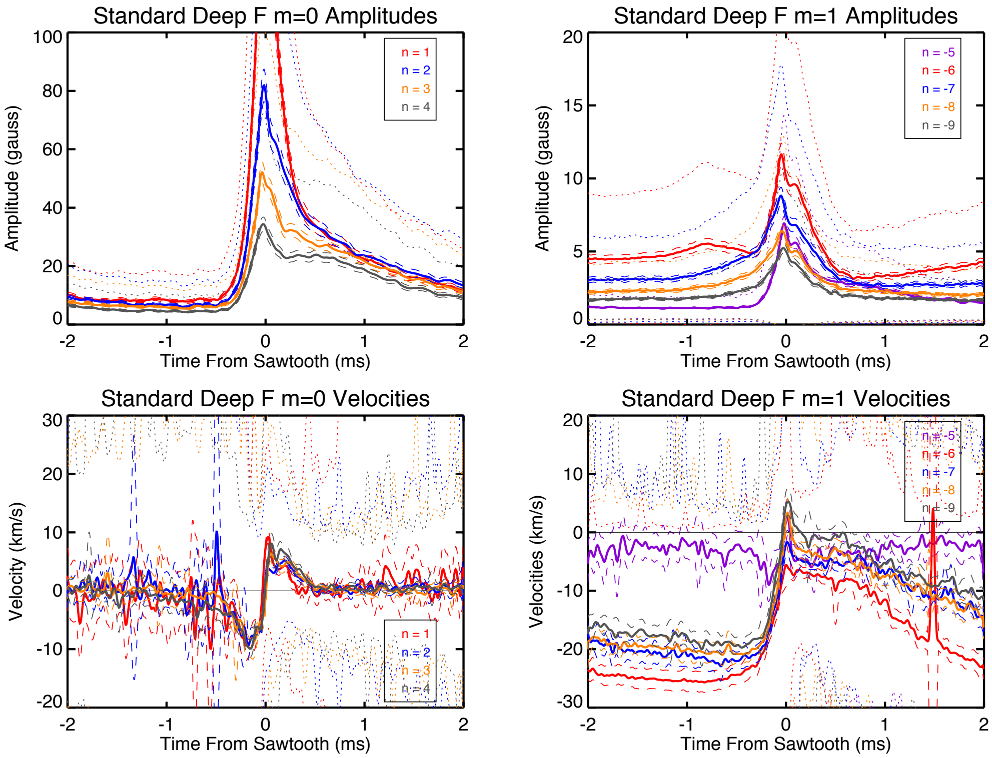

Figure D.72: Tearing mode amplitudes and velocities, deeply reversed standard sawtooth.

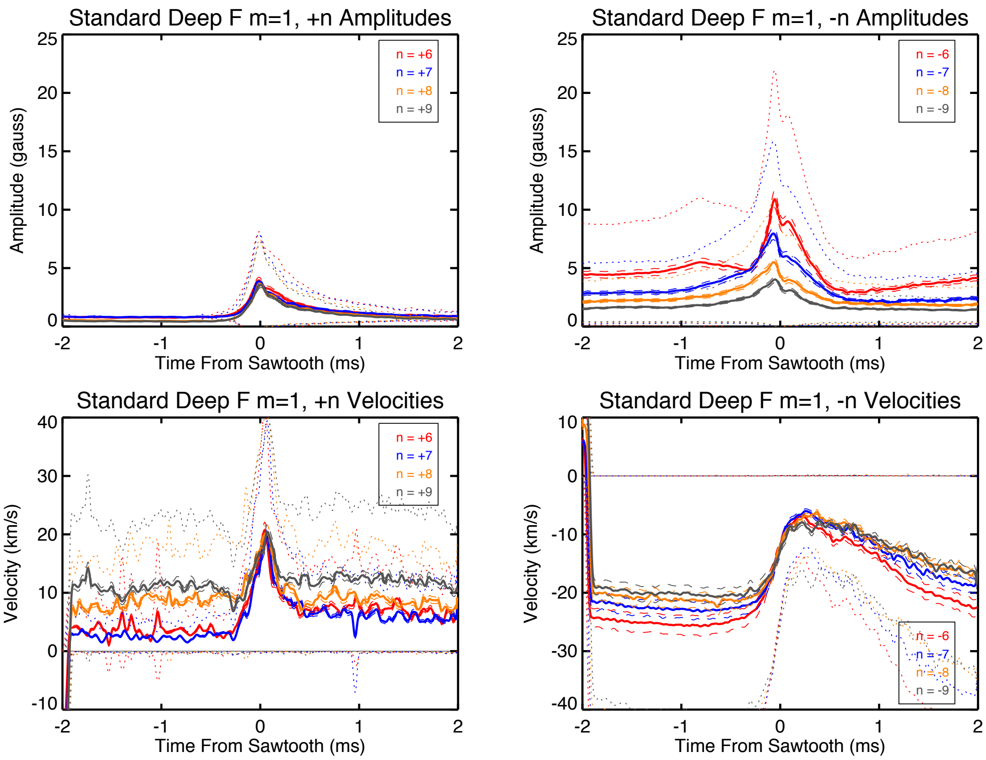

Figure D.73: Tearing mode +n and -n amplitudes and velocities, deeply reversed standard sawtooth.

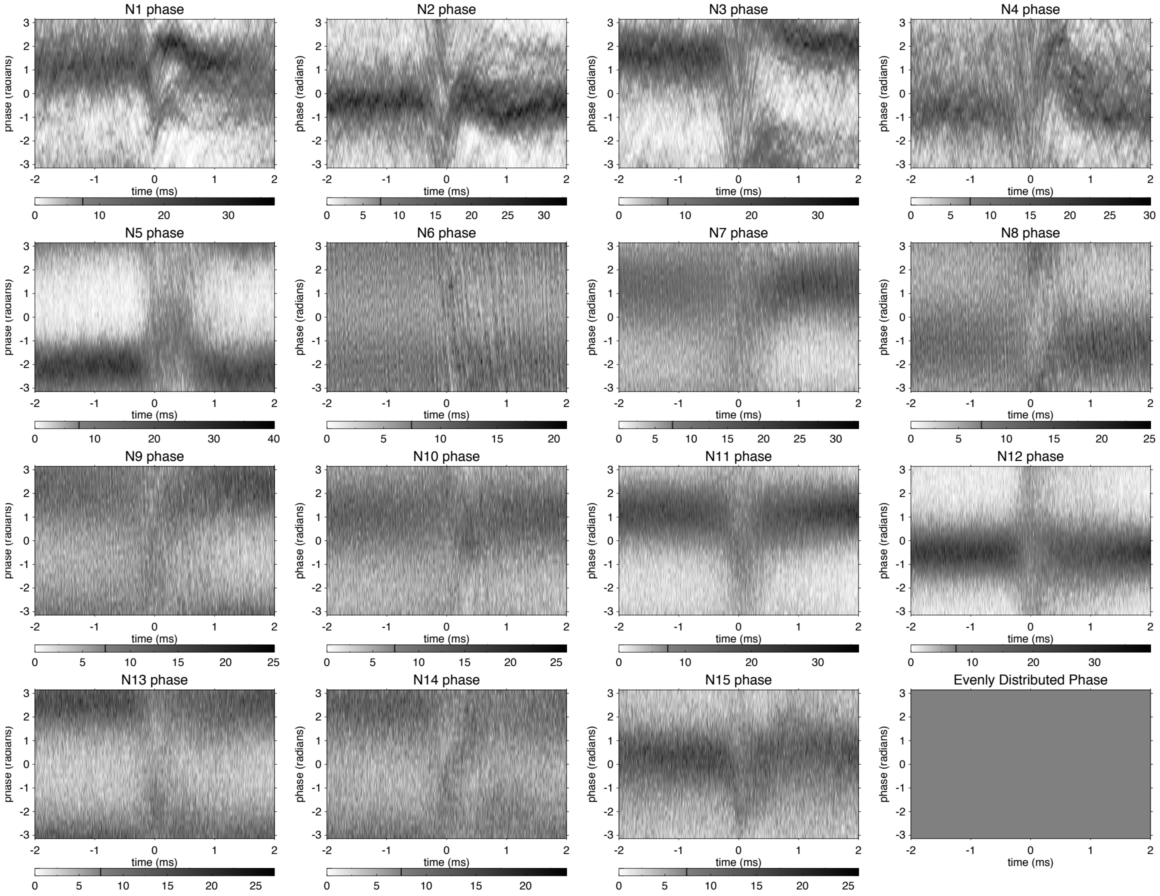

Figure D.74: Tearing mode phase distribution, deeply reversed standard sawtooth.

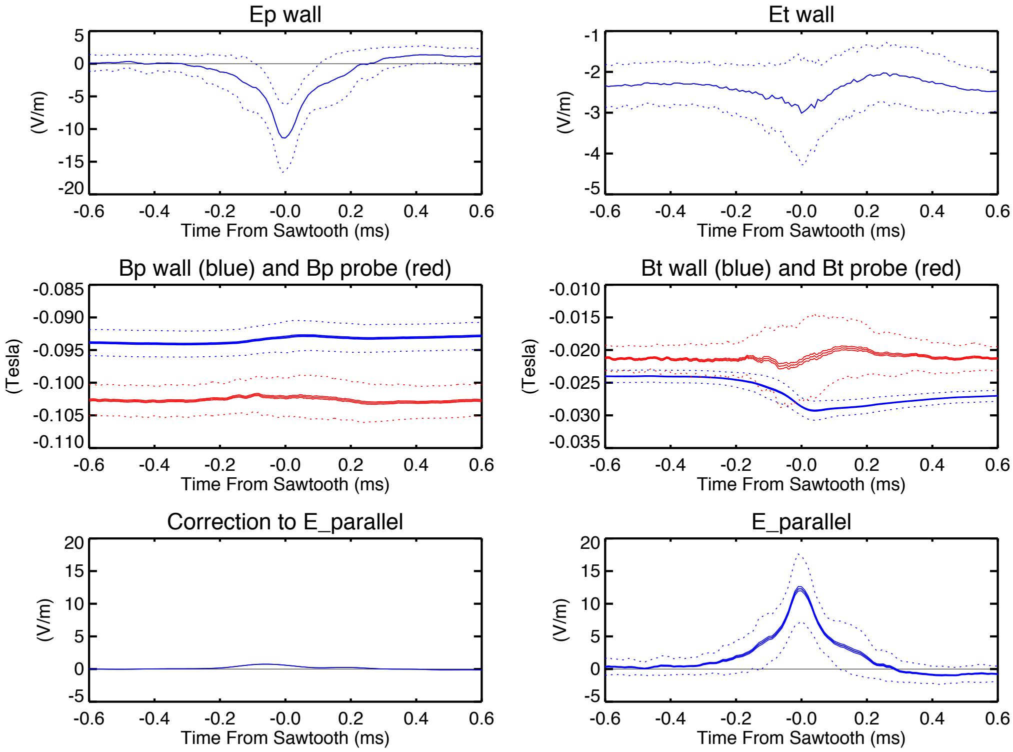

Figure D.75: Parallel electric field data, deeply reversed standard sawtooth.

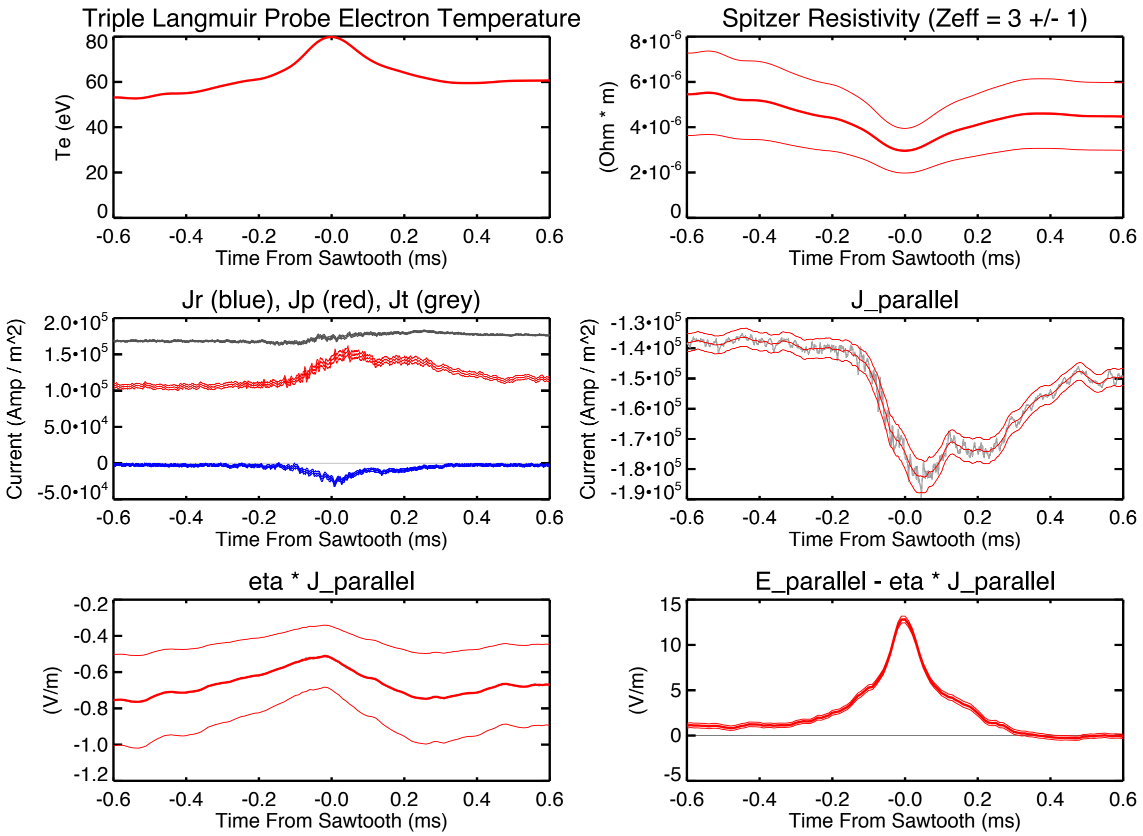

Figure D.76: Probe $\eta\mathbf{J}$ data, deeply reversed standard sawtooth.

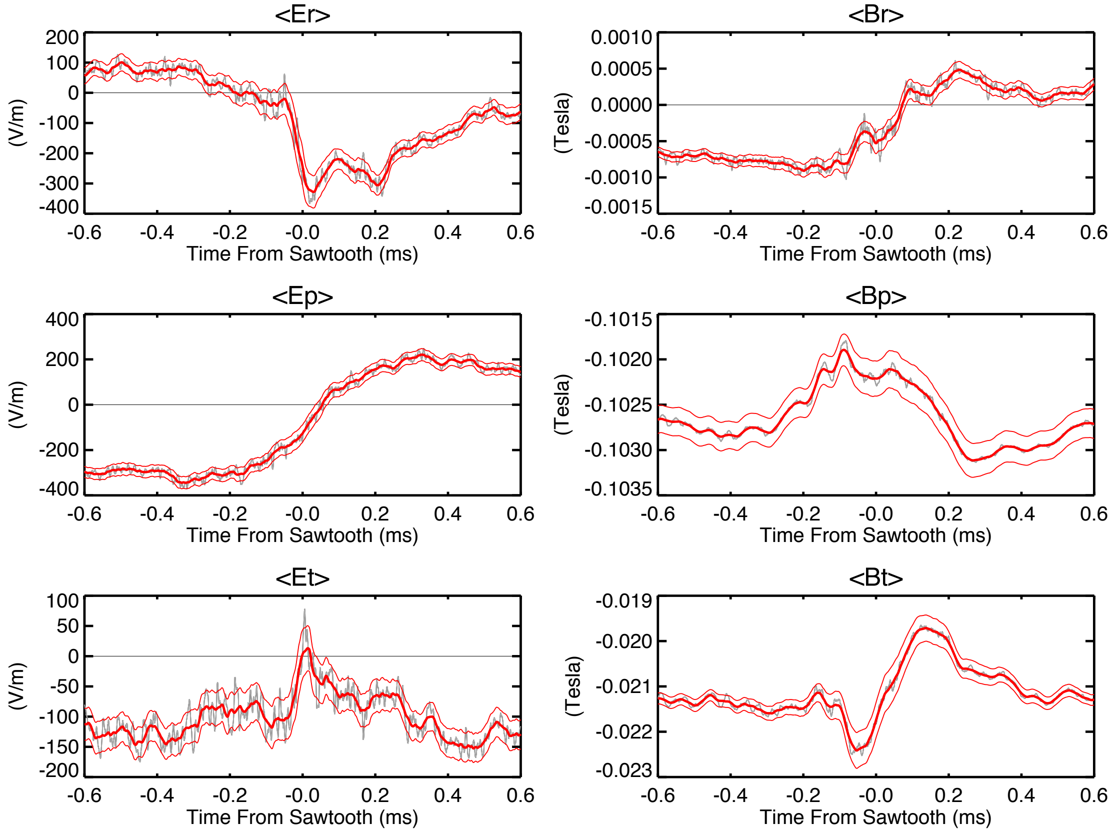

Figure D.77: Dynamo Probe < **E** > and < **B** >, deeply reversed standard sawtooth.

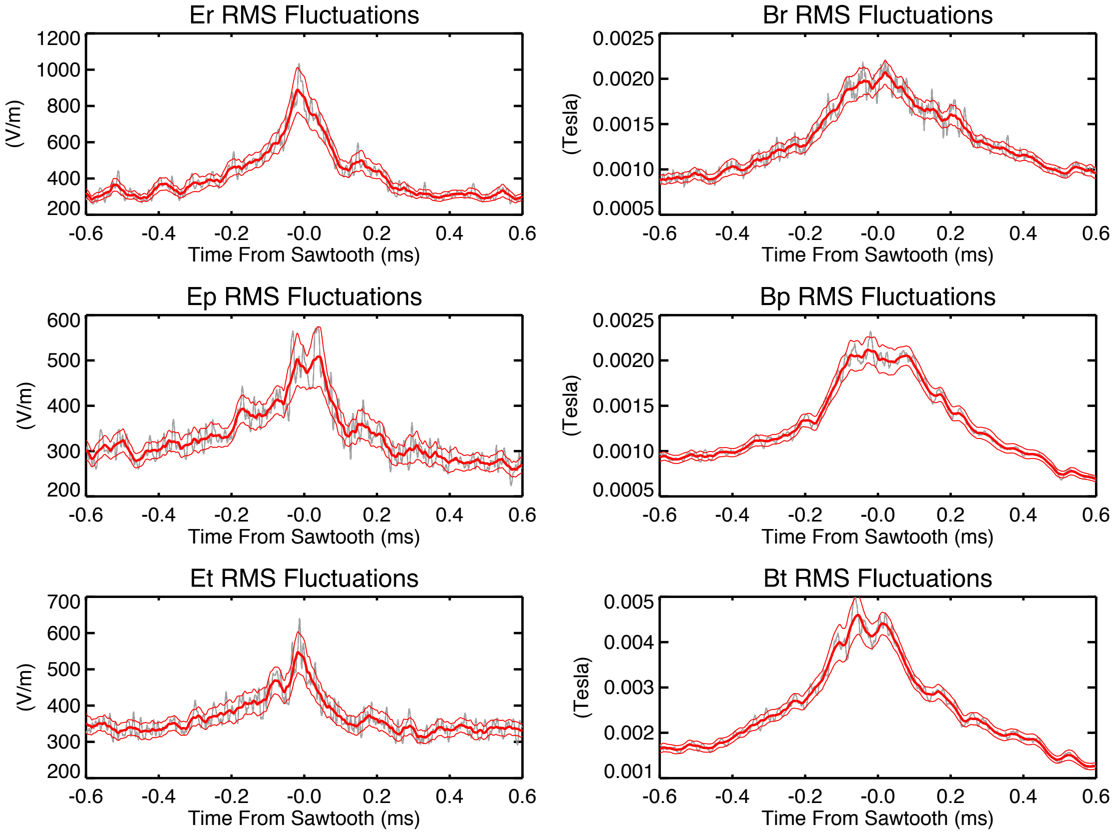

Figure D.78: Dynamo Probe $\tilde{\mathbf{E}}_{RMS}$ and $\tilde{\mathbf{B}}_{RMS}$, deeply reversed standard sawtooth.

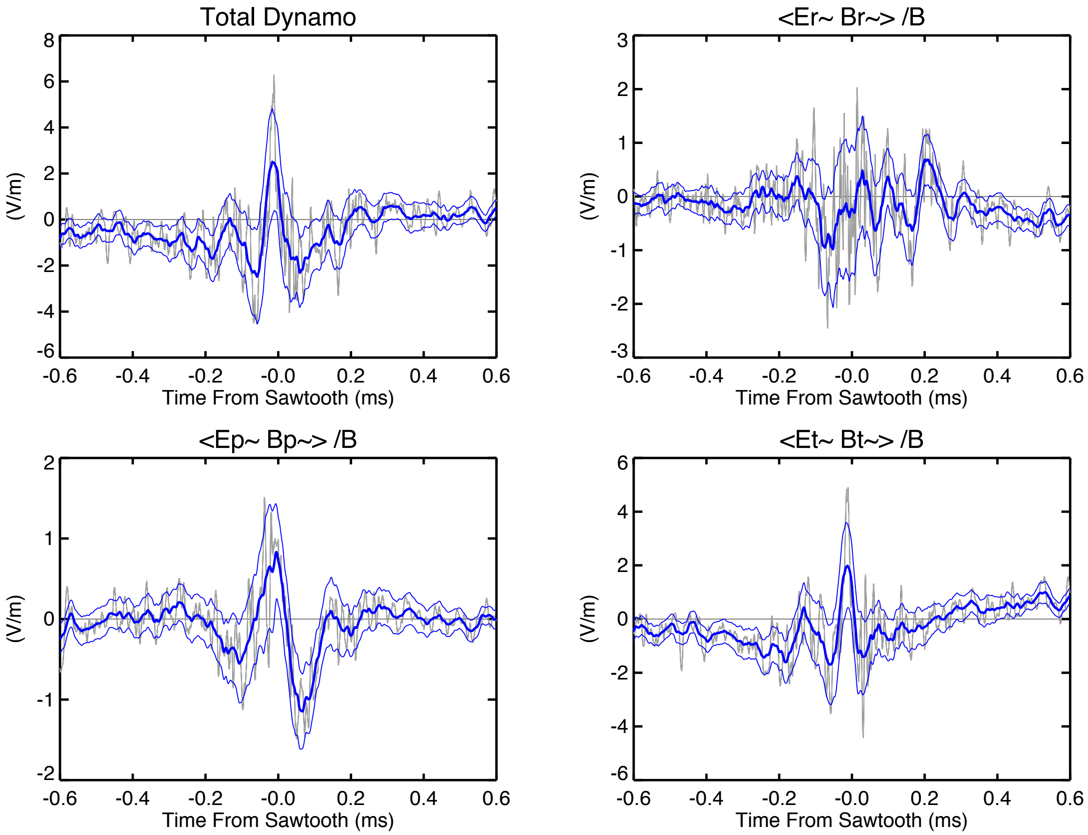

Figure D.79: Dynamo contributions from $\tilde{\mathbf{E}}$ and $\tilde{\mathbf{B}}$ components, deeply reversed standard sawtooth.

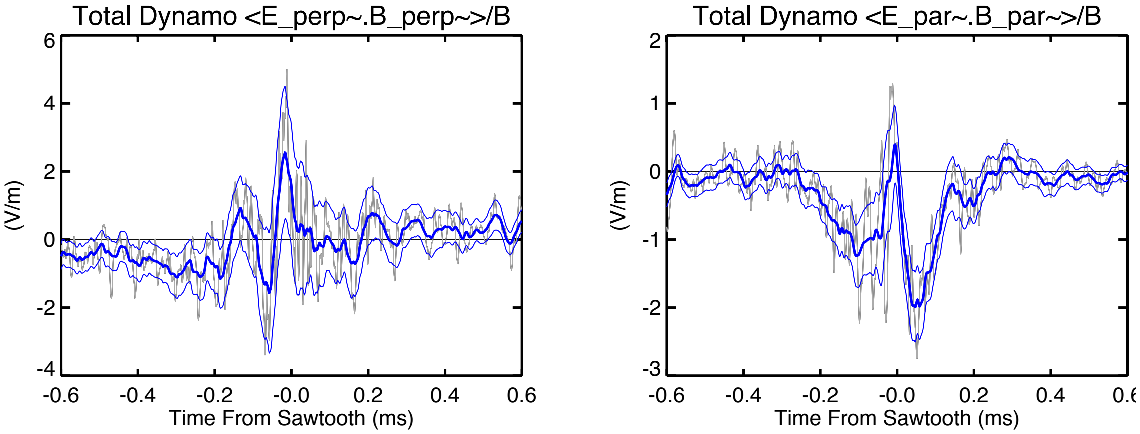

Figure D.80: Dynamo contributions from $< \tilde{\mathbf{E}}_\perp \cdot \tilde{\mathbf{B}}_\perp > / B_0$ and $< \tilde{\mathbf{E}}_\parallel \cdot \tilde{\mathbf{B}}_\parallel > / B_0$, deeply reversed standard sawtooth.

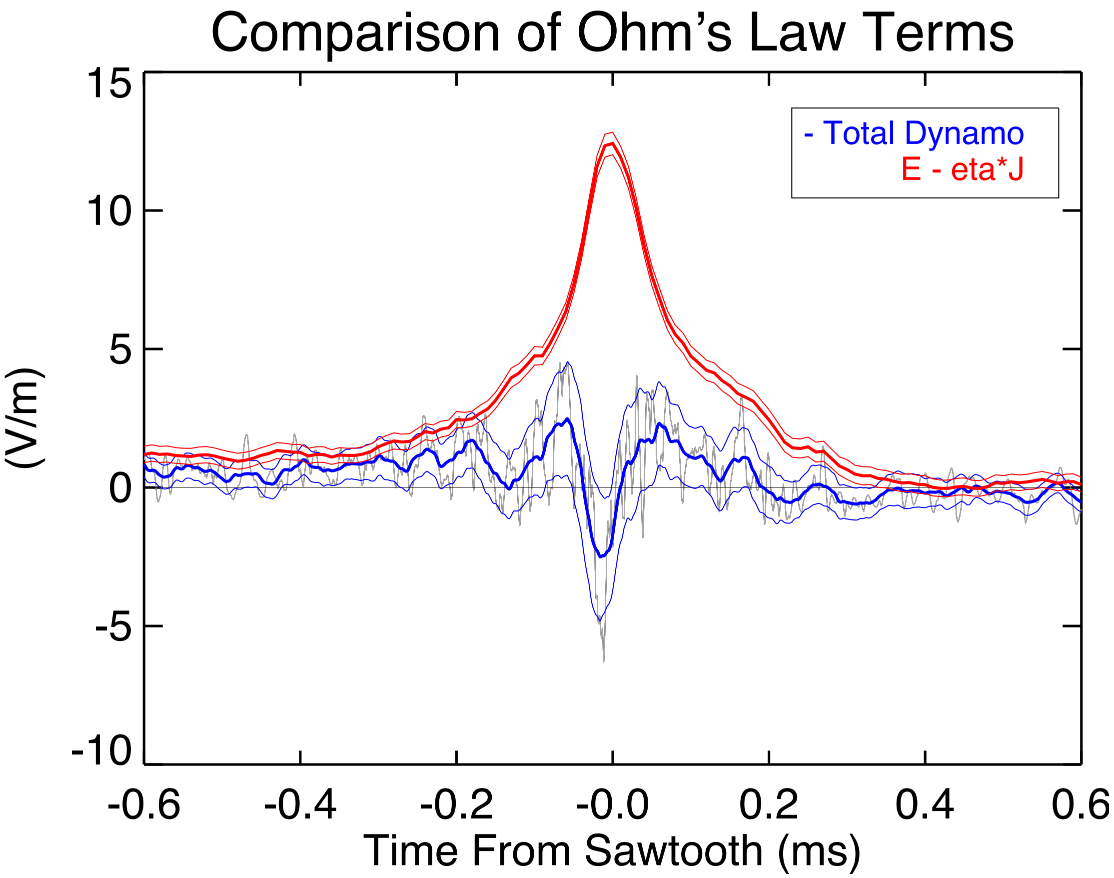

Figure D.81: Ohm's law ($\mathbf{E} - \eta\mathbf{J}$ and $- < \tilde{\mathbf{E}} \cdot \tilde{\mathbf{B}} > /B$), deeply reversed standard sawtooth.

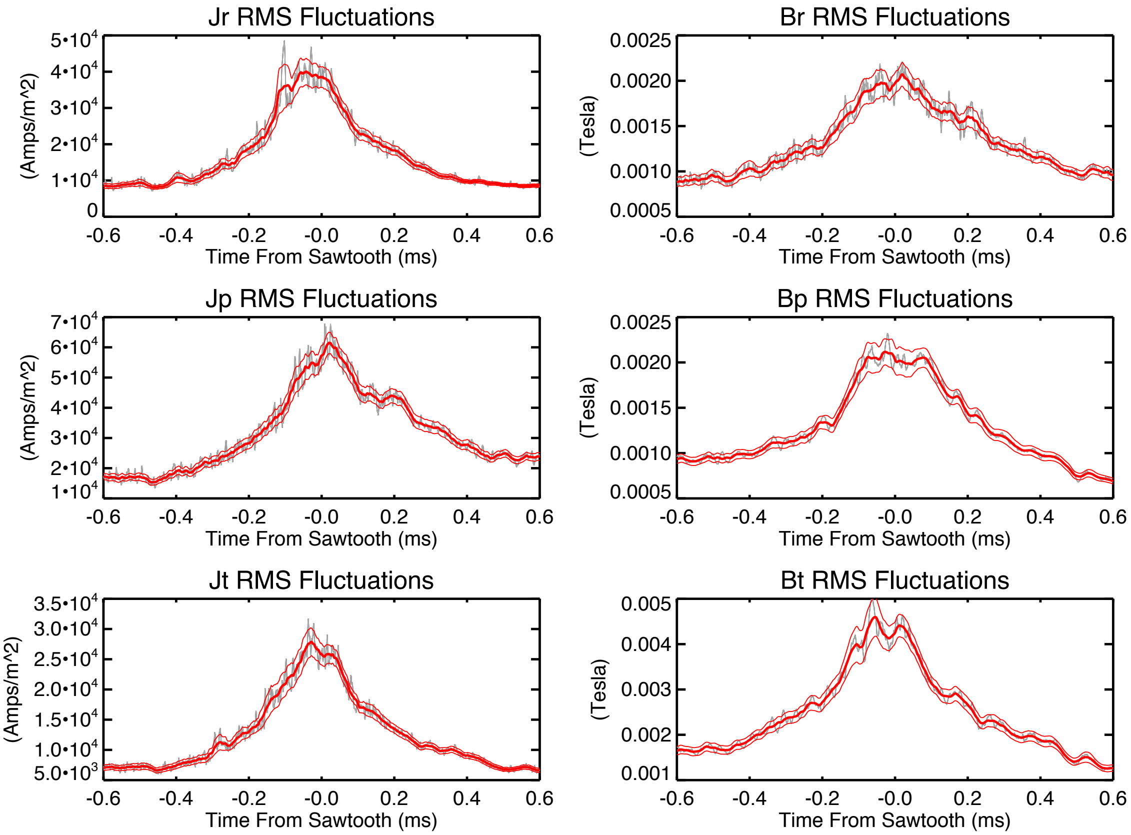

Figure D.82: Dynamo Probe $\tilde{\mathbf{J}}_{RMS}$ and $\tilde{\mathbf{B}}_{RMS}$, deeply reversed standard sawtooth.

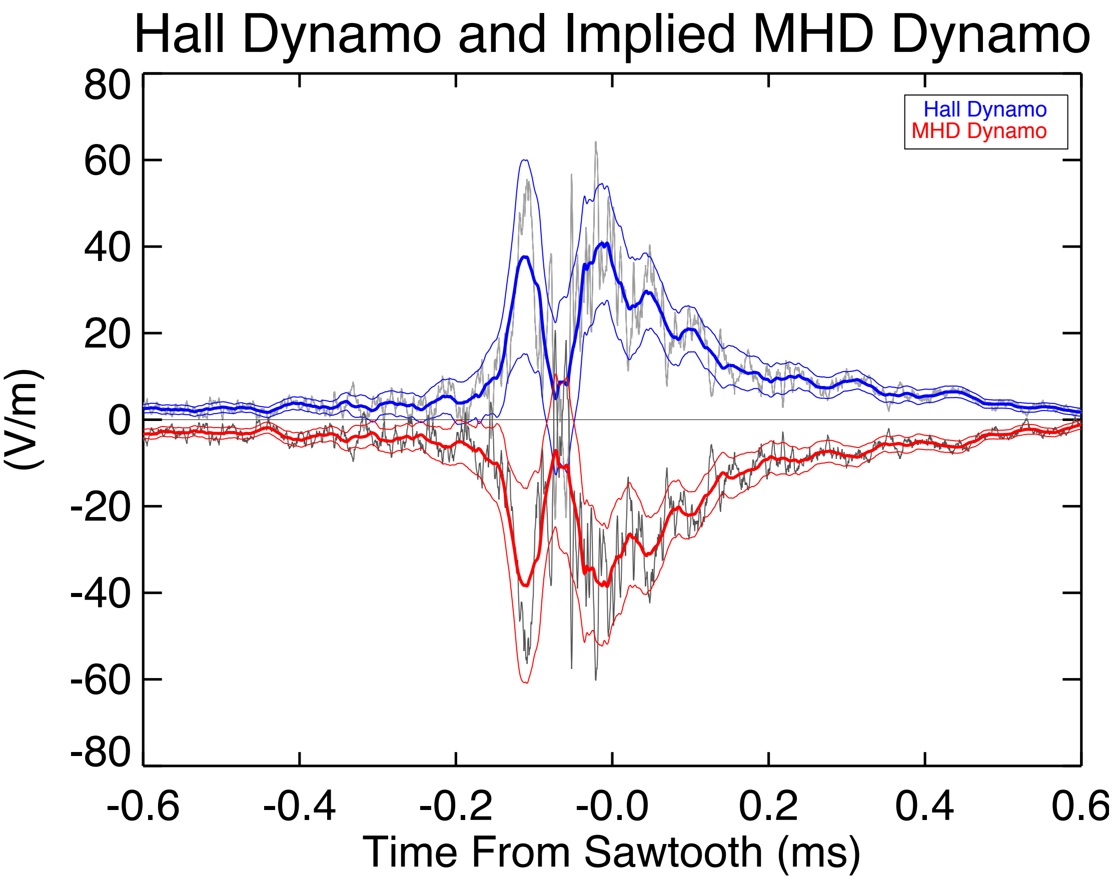

Figure D.83: Hall Dynamo and assumed MHD Dynamo (= Total Dynamo - Hall Dynamo), deeply reversed standard sawtooth.

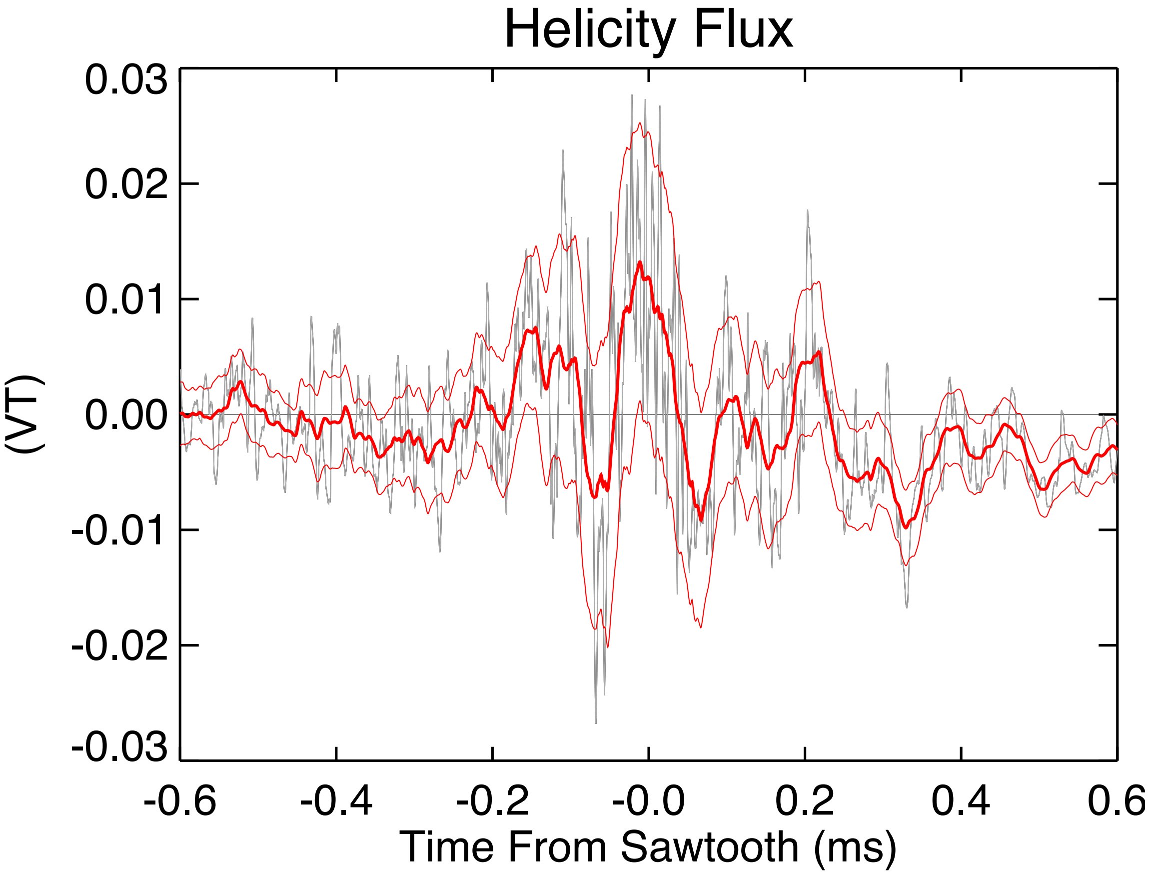

Figure D.84: Magnetic helicity flux, deeply reversed standard sawtooth.